EUROPIUM REDUCTION AND LANTHANIDE COORDINATION IN POLYOXOMETALATES

By

Jing Jing

A dissertation submitted to the Graduate Faculty in Chemistry in partial fulfillment of the requirement for the degree of Doctor of Philosophy, The City University of New York

2010

This manuscript has been read and accepted for the Graduate Faculty in Chemistry in satisfaction of the dissertation requirement for the degree of Doctor of Philosophy.

	Lynn C. Francesconi
Date	Chair of Examining Committee
	Mahesh K. Lakshman
Date	Executive Officer

Mark R. Antonio

Klaus Grohmann

Charles M. Drain

Harry D. Gafney

Supervisory Committee

THE CITY UNIVERSITY OF NEW YORK

Abstract

EUROPIUM REDUCTION AND LANTHANIDE COORDINATION IN POLYOXOMETALATES

By

Jing Jing

Advisers: Professor Lynn C. Francesconi

Dr. Mark R. Antonio

Polyoxometalates (POMs) are a unique class of metal-oxygen cluster anions in which the early transition metals are in their highest oxidation states. POMs have applications in quite diverse disciplines including catalysis, medicine and material sciences, many of which are based upon their reduction-oxidation (redox) properties. The variation of metal coordination environments and metal-oxygen framework architectures influences redox properties of POMs, and the extent of that influence depends on the nature of the incorporated metal ion. When combined with lanthanide (Ln) ions, Ln-POMs form new structures, exhibit catalytic properties, and offer unique functionality, such as the creation of luminescent and Lewis acid catalytic centers. Because of this, Ln-POM derivatives have attracted increasing attention in recent years.

The first project focused on Europium (Eu) and Wells-Dawson Heteropolytungstates because of their prospects in electroanalytical chemistry. Eu is redox-active. Wells-Dawson Heteropolytungstates contain electroactive, lacunary P-W-O anions that, upon reduction in aqueous and organic media, form heteropoly blue species

that retain the same structures as the parent anions. The combination of the electrochemical properties of both the Eu and the ligands in one molecule produces a two-center, multielectron redox. We wish to investigate multi-electron redox processes so as to derive some information about the interaction between the Ln f orbitals and the tungsten d-band LUMO. To this end, electrochemical techniques (cyclic voltammetry and bulk electrolysis), in situ XAFS (X-ray absorption fine structure) spectroelectrochemistry, NMR spectroscopy and optical luminescence were used. The cyclic voltammograms show concentration dependence. The reduced form of $K_7[(H_2O)_4Eu(\alpha\text{-}1\text{-}P_2W_{17}O_{61})]$ was probed by Eu L_{III} edge XANES and confirmed that Eu(III) is reduced to Eu(II). EXAFS data for the reduced Eu(II)-POM shows the average Eu-O bond length is 2.55(4) Å, which is 0.17 Å longer than that for the oxidized anion, and consistent with the 0.184 difference between the Eu(II) and Eu(III) ionic radii.

In the second project, the Nd^{3+}, Sm^{3+}, Eu^{3+}, Tb^{3+}, Dy^{3+}, and Yb^{3+} complexes with $\alpha\text{-}1\text{-}[P_2W_{17}O_{61}]^{7-}$ of 1:1 Ln:α-1-ligand stoichiometries, $[(H_2O)_nLn(\alpha\text{-}1\text{-}P_2W_{17}O_{61})]^{7-}$, as the tetra-*n*-butylammonium solid salts as well as their solutions in dry and wet acetonitrile were probed through use of voltammetry, electrolysis, and EXAFS. The comparative metrical data obtained about the inner-sphere Eu coordination environments in the solid salt of TBA^+-Eu-α-1 and upon its dissolution in dry MeCN with a 0.1 M $TBAPF_6$ electrolyte suggest that MeCN binds to Eu(III) in part ($0 < \delta < 4$) and in exchange with H_2O, forming a mixed H_2O-MeCN solvate. These results, in combination with the EXAFS results for the TBA^+-Ln-α-1 systems across the 4f period provide a fresh perspective on the variation of Ln(III) coordination in MeCN, including the effects of the lanthanoid contraction as well as known variations of MeCN and H_2O residence times.

The third project, the SAXS measurements for potassium salts of [α-1-$P_2W_{17}O_{61}]^{10-}$, [Eu(α-1-$P_2W_{17}O_{61}$)]$^{7-}$ and [Yb(α-1-$P_2W_{17}O_{61}$)]$^{7-}$ at different concentrations, is presented in Appendix. The Guinier plots showing linear and parallel response suggest that the cluster size for each compound is independent of concentration and the clusters remain monodisperse without aggregation at high concentrations. The R_gs obtained from the Guinier fit over the low Q range and P(r) analysis over the entire Q rang exhibit good consistence with each other, which again indicates that the clusters remain intact and monodisperse with no interparticle interactions and no aggregation at high concentrations.

Acknowledgements

First of all, I want to express my sincere gratitude to my two mentors - Professor Lynn C. Francesconi and Dr. Mark R. Antonio for their support, guidance and encouragement. Their attitudes towards science make them great scientists and have a tremendous influence on my research. The completion of this thesis would not have been possible without their help.

I want to thank Professor Grohmann, Professor Drain and Professor Gafney for serving on my committee and giving me guidance and suggestions. Especially, Professor Grohmann, being one of my committee members and the graduate student advisor at Hunter, has given me lots of very useful advice, support and help.

Moreover, I would like to thank Graduate Center of the City University of New York and Chemistry Department at Hunter College for offering me different grants and awards, and providing me a comfortable working environment. Thank Advanced Photon Source (APS) at Argonne National Laboratory for giving me beam times to complete all my XAS and SAXS data collection. My special gratitude goes to Dr. Benjamin P. Burton-Pye for his useful comments, advice and support; To Dr. Beau, Donna, Fang and Laurence for their help in the lab. My thanks also go to Dr. Nadia Leyarovska for her generous assistance at the APS Sector 12 beam line.

I also want to make special mention to my friends in Hunter: Junyi Wang, Jialiang Li, Youyu Chen, Youchun Wu, Medis, Yijia Yang, Haiying Bai and Fen Xu for helping me in different way from the first day I arrived in the US.

Furthermore, I want to express my gratitude to Dr. Rose K. Rose for the Rose Kfar Rose Dissertation Award, Dr. Gertrude Elion for Gertrude Elion Fellowship Award and Dr. Helen S. Schectman for Helen S. Schectman award. Their generous supports are so important to me and other recipients from CUNY especially during these difficult economic times. Their spirit encourages me to keep working hard.

Last, but not least, I am deeply and completely grateful to my parents, my husband and my daughter, and my parents-in-law. Their love, encouragement, understanding and tremendous support enabled me to focus on my PhD research for all the time and travel to Chicago (Argonne National Laboratory) for my experiments periodically. Especially to my husband, I am so grateful for his assistance and encouragement.

Table of Contents

List of Figures

Chapter 1.

R_g value obtained from Guinier and P(r) analysis of the Experimental SAXS data for for (a) α1 ligand, (b) Eu- α1 and (c) Yb- α1 at different concentrations.

List of Tables

Chapter 2.

residual squared. Error of measurement is ±10%. The weights are representative of the percentage contribution of each of the emitting species at that wavelength.

Chapter 3.

Appendix.

Chapter 1. Overview

1.1 Polyoxometalates (POMs)

1.1.1 General Introduction

Polyoxometalates [1, 2](POMs) are a unique class of early transitional metal-oxygen clusters in which the transition metals are in high oxidation state. POMs have attracted significant and increasing attention since Berzelius[2] reported the synthesis of the first POM, phosphomolybdate of formula $[PMo_{12}O_{40}]^{3-}$ in 1826. The attention was aroused by the electronic versatility, the enormous diversity of structures, flexible redox behaviors and the potential application in catalysis as well as in medicine and material science.[3]

Generally, there are two types of POM species based on their chemical composition- Isopolyanions and Heteropolyanions. Isopolyanions contain only the d0 metal cations and oxide anions. They are obtained by condensation reactions in acidic aqueous solutions, as demonstrated by equation 1.1:[4]

Isopolyanions (IPAs) $[M_nO_y]^{p-}$

$$7WO_4^{2-} + 8H^+ \longrightarrow [W_7O_{24}]^{6-} + 4H_2O \qquad \text{Equation 1.1}$$

Heteropolyanions contain one or more p-, d-, or f-block "heteroatoms" in addition to the other ions.[5] They are obtained when the condensation occurs in the presence of an other oxo/hydrooxoanion, $[XO_o^6{}_z]^{p-}$, as shown in equation 1.2:[4]

Heteropolyanions (HPAs) $[X_zM_nO_y]^{q-}$, with $z \leq n$

$$12MoO_4^{2-} + H_3PO_4 + 21H^+ \longrightarrow [PMo_{12}O_{40}]^{3-} + 12\ H_2O \qquad \text{Equation 1.2}$$

Where M is the so called secondary, peripheral or *addenda* atoms and X is the primary, central or *heteroatoms*. The most common addenda atoms are Mo or W.

Heteroatoms have much broader range: Over half of the elements in the periodic table are known to function as heteroatoms in heteropolyanions,[7] most typical ones being P^{5+}, As^{5+}, Si^{4+}, Ge^{4+} and B^{3+}, etc.

Compared to Isopolyanions (IPAs), heteropolyanions (HPAs) are more numerous, their structural and electronic properties are easier to modify synthetically, and they exhibit unusual combinations of properties in catalysis and medicine, therefore HPAs have been dominating the POMs area to date.[7, 8]

HPAs have different isomeric forms: the Keggin and the Wells−Dawson anions.

1.1.2 Keggin structure and its lacunary isomer

The Keggin anions, $XM_{12}O_{40}^{n-}$ (when M= W or Mo), are very stable, easily available and well characterized spectroscopically. They also exhibit a rich and well elaborated substitution chemistry in which one or more of the addenda W(VI)[9] or Mo(VI) ions can be substituted by other early transition metal (addenda) ions, d-electron transition metal ions, or organometallic or organic groups.[10]

The name "Keggin" is from the structure of $[PW_{12}O_{40}]^{3-}$ which was determined by Keggin using X-ray diffraction in 1933.[11] The Keggin anion, $XM_{12}O_{40}^{n-}$, is composed of four M_3O_{13} groups. Two M_3O_{13} are in the belt, and one M_3O_{13} is in the cap position, respectively. Each of these M_3O_{13} groups can be turned by 60º around its C_3 axis.[12]

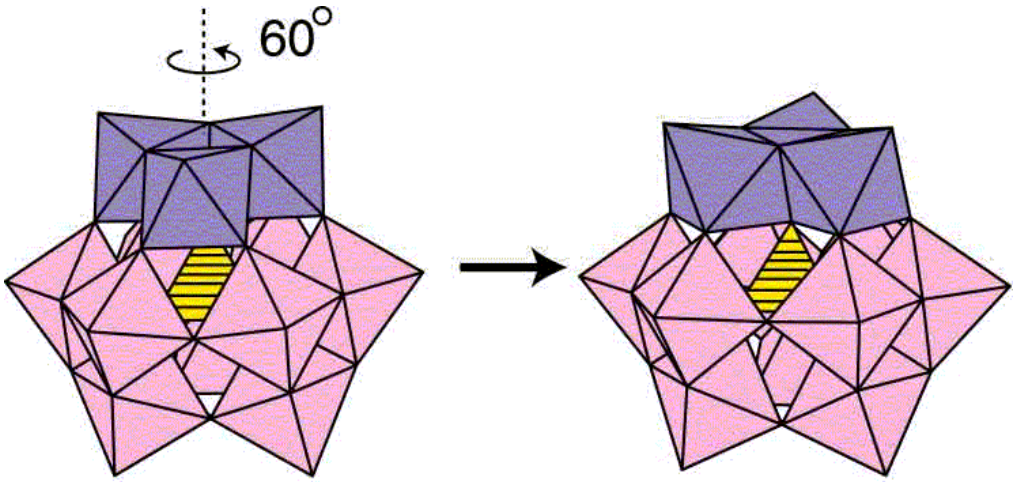

Figure 1a and 1b. α and β isomer of Keggin structure

The structure illustrated in Figure 1a is the most common α isomer of the Keggin structure. Rotation of one of its M_3O_{13} groups produces the β isomer shown in Figure 1b. Rotation of two, three or all four M_3O_{13} groups produces the γ, δ, ε isomers, respectively.[5, 13]

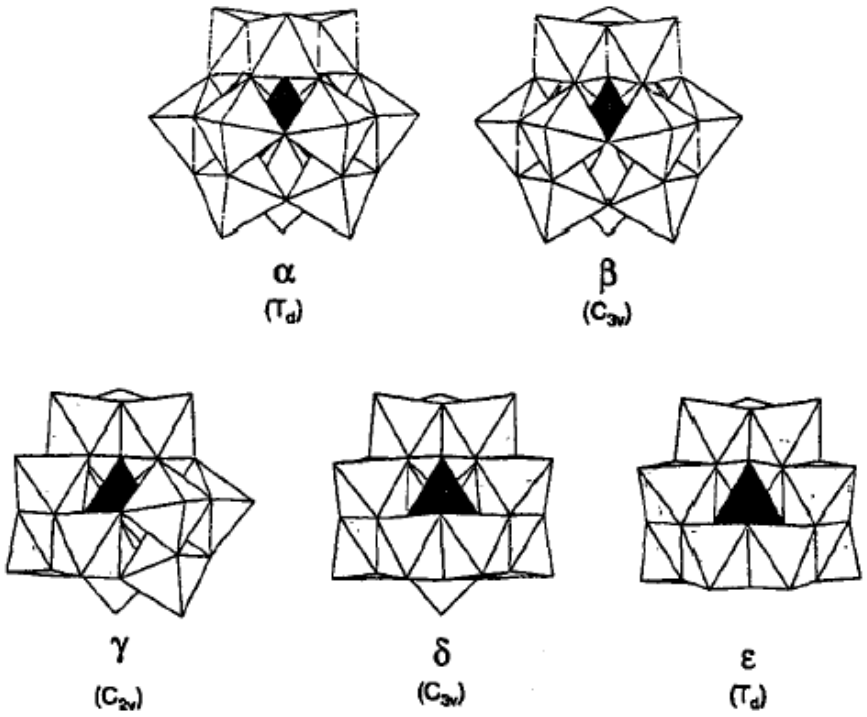

Figure 2. The five Baker-Figgis isomers of the Keggin anions

Lacunary derivatives of the Keggin anions can be obtained by removal of one or more M atoms. Figure 3 shows three lacunary derivatives (one monovacant and two trivacant) of the α-Keggin. The two trivacant species correspond to loss of a corner-shared group of MO_6 octahedar or an edge-shared group. Such species can assemble into larger polyoxometalate structures, either directly or with incorporation of metal ion linkers.[14]

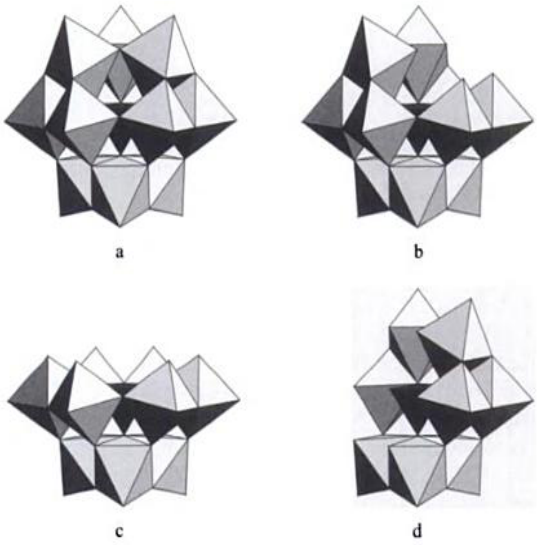

Figure 3. The structures of the α-Keggin anion $XM_{12}O_{40}^{n-}$ (a) and its lacunary derivatives: (b) monovacant, (c) trivacant A-{XM_9}, and (d) trivacant B-{XM_9}.

1.1.3 Wells-Dawson structure and the lacunary isomer

After the Keggin structure, the Wells-Dawson complexes are the most well known polyoxometalates. The structure of one well-Dawson, α-$P_2W_{18}O_{62}^{6-}$, is shown in Figure 4. The anion consists of two trivacant lacunary Keggin species A-PW_9 linked directly across the lacunae.[14]

Lacunary derivatives of Wells-Dawson anions can be obtained by removal of a $[WO]^{4+}$ unit from a WO_6 polyhedron of the parent $[\alpha\text{-}P_2W_{18}O_{62}]^{6-}$. Removing the $[WO]^{4+}$ unit from the belt region will produce lacunary $[\alpha1\text{-}P_2W_{17}O_{61}]^{10-}$ isomer shown in Figure 5b, while removing $[WO]^{4+}$ unit from the cap region will produce lacunary $[\alpha2\text{-}P_2W_{17}O_{61}]^{10-}$ isomer in Figure 5a.

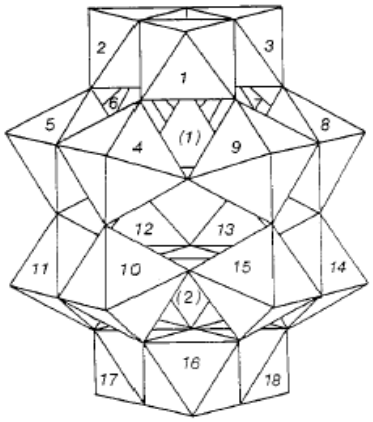

Figure 4. Numbering scheme of $\alpha\text{-}P_2W_{18}O_{62}^{6-}$ (Dawson structure). The tungsten atoms (9 atoms are in the upper and the lower halves of the molecule, respectively) are numbered according to the IUPAC recommendations. The two P atoms are numbered (1) and (2) for the upper and the lower halves of the molecule, respectively.

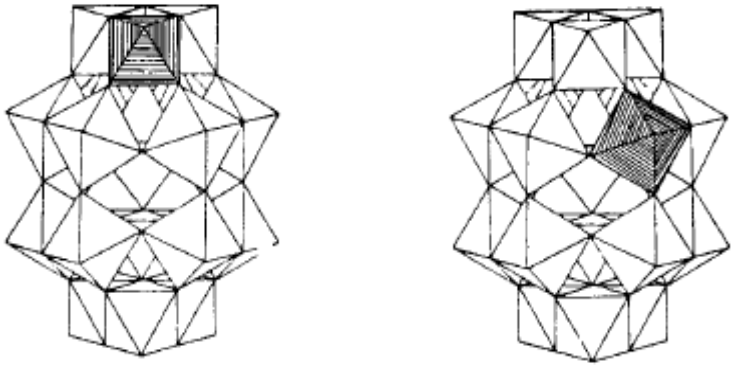

Figure 5(a) and 5(b). α-2 $[P_2W_{17}O_{61}]^{8-}$ and α-1 $[P_2W_{17}O_{61}]^{8-}$ isomers.

Lacunary Wells-Dawson anions are generally good ligands for transition metals, lanthanides and actinides. Subsequent work has been done to investigate [α2-$P_2W_{17}O_{61}]^{10-}$. In contrast, there have been fewer reports of metal complexes of [α1-$P_2W_{17}O_{61}]^{10-}$, probably due to the instability of the α1 lacunary isomer.

1.1.4 Transition Metal substituted-POMs

Lacunary POMs easily bind to metal ions to form derivatives due to their negative charges and geometry. In particular, transition metal substituted-POMs have been heavily investigated for the purpose of generating new catalysts and functional materials with interesting optical and magnetic properties. Synthesis of such compounds is usually accomplished by reaction of a transition metal ion (e.g. Fe^{2+}, Cu^{2+} , Mn^{2+}) with the appropriate lacunary POM precursor (e.g. $[AsW_9O_{33}]^{9-}$, $[GeW_9O_{34}]^{10-}$, and $[P_2W_{15}O_{56}]^{12-}$). Stimulated by Baker's early work,[6] many researchers have focused their research in the synthesis and characterization of transition metal-substituted POMs to explore the redox chemistry and catalytic and electrocatalytic abilities.[15-17] In most cases the incorporated metal is the active site for the reactions. In this area, Fe-substituted POMs for catalytic applications has become a popular area due to the easily accessible $Fe^{2+/3+}$ redox couple and have been used as catalysts for the reduction of H_2O_2 and NO^{2-} [18-20]and other reactions. The substitution by transition meal modifies the property of POMs and facilitates the catalysis. For example, Mizuno et al studied the activity of non-, mono-, di-, and triiron substituted Keggin type silicotungstates (α-$[SiW_{12}O_{40}]^{4-}$, α-$[SiW_{11}Fe(OH_2)O_{39}]^{5-}$, γ-$[SiW_{10}\{Fe(OH_2)\}_2O_{38}]^{6-}$, and α-$[SiW_9\{Fe(OH_2)\}_3O_{37}]^{7-}$) as catalysts for the oxygenation of alkanes in homogeneous reaction media. The results

showed that incorporation of iron centers into the POM framework remarkably influences the catalytic activity.[21]

1.1.5 Lanthanide substituted-POMs

As one of the subjects of our ongoing research in Hunter College, Lanthanide substituted-POMs have also attracted considerable attention from other POMs groups owing to their characteristic luminescence properties and electrochemistry properties.

This was initiated by Peacock and Weakley's work investigating the interaction of the Keggin $[PW_{11}O_{39}]^{7-}$ and the Wells-Dawson $[P_2W_{17}O_{61}]^{10-}$ monovacant POMs with Ln cations.[22] Since then, numerous Ln-POMs, especially Eu^{3+}, have been synthesized and characterized, such as $[EuP_5W_{30}O_{110}]^{12-}$,[23] $[Eu(H_2O)_3(\alpha_2\text{-}P_2W_{17}O_{61})(Eu_2(H_2O)_7)]_4^{4-}$,[24] $[EuW_{10}O_{36}]^{9-}$,[25] $[Eu_2CeMo_{12}O_{42}]^{6-}$,[26] $[Eu(SiW_{11}O_{39})_2]^{13-}$,[27] $[EuAs_4W_{40}O_{140}]^{25-}$,[27] and $[EuSb_9W_{21}O_{86}]^{16-}$,[27] etc. All these Eu-substituted POMs are shown luminescent, in which, the Europium decatungstates, $[EuW_{10}O_{36}]$9-, shows the best luminescence performance.[25]

Besides the luminescence and electrochemistry properties exhibited by Ln-POMs, a novel feature has recently aroused attention since the first example of a POM ($[ErW_{10}O_{36}]^{9-}$, structure in Figure 6) showing single-molecule magnet (SMM) behavior was published in 2008.[28] AlDamen M.A. etc also reported the magnetostructural characterization for the whole family $[Ln(W_5O_{18})_2]^{9-}$ (Ln^{III} = Tb, Dy, Ho, and Er) and $[Ln(SiW_{11}O_{39})_2]^{13-}$ (Ln^{III} = Tb, Dy, Ho, Er, Tm, and Yb) which are exhibiting SMM behaviors.[29] This new property renders POMs a potential candidate for the development of high-density magnetic memories and quantum computing devices.[28]

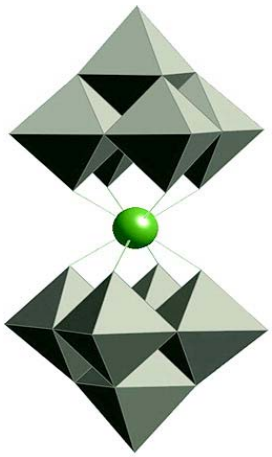

Figure 6. Structure of the $[ErW_{10}O_{36}]^{9-}$ POM.[28]

1.1.6 POMs application

POMs have found a variety of applications in many fields such as catalysis, electrocatalysis, material science, medicine and analytical chemistry.[1, 10, 30-32] The majority of the applications of POMs are found in the area of catalysis. This was stimulated by Baker's pioneering work in which he found that monosubstituted heteropolyanions can be used in catalytic processes with advantage of thermal stability and resistance toward oxidation, compared to their organic counterparts.

Catalysis: Heteropoly acids (HPAs) composed of heteropoly anions and protons are the most important type of POMs for catalysis. Such examples are $H_3[PW_{12}O_{40}]$, $H_4[SiW_{12}O_{40}]$, etc. HPAs have been applied in homogeneous and heterogeneous systems especially for purpose of acid catalysis and oxidation catalysis due to some advantages over other catalyst: 1. HPAs are very strong Bronsted acids. The strong acidity has made HPAs higher catalytic activity than mineral acids and conventional solid-acid catalysts. In particular in organic media, the molar catalytic of HPA is often 100-1000 times higher than that of H_2SO_4. Also, HPA catalysis lack side reactions which often happen in the

mineral acids catalysis.[31, 33] 2. They are efficient oxidants, exhibiting the ability to undergo multiple, consecutive and reversible multielectron reductions without affecting their structures.[32] 3. Many POMs are thermally stable and highly soluble in polar solvents. Because of these unique properties, HPAs are promising acid and oxidation catalysts.

Medicine: The biomedical studies of POMs have been focused on two main types of activities: antiviral and antitumoral. The early work about the antiviral activity of POMs was published in 1971.[34] Raynaud et al. noted that polytungstosilicate heteropoly compounds inhibited murine leukemia sarcoma virus in vitro.[7] The Table 1 in review[7] by Rhule J.T. etc summarizing the data on the antiviral activity and toxicity of POMs in cell culture shows most POMs are highly effective against HIV-1 and HIV-2. Although a great number of POMs have been reported to be useful for inhibition of viruses and it was known that POMs can penetrate cell membranes and localize intracellularly, the main mechanism for antiviral and antitumoral actions still remain unclear.

Material sciences: Due to their ability to act as an electron reservoir and produce colored species(heterpolyblue) while retaining the structure, POMs are promising candidates for electrochromic materials.[35] Although a wide range of electrochromic materials, such as conduction polymers,[36] Prussian blue[37] and metal phthalocyanines[38] have been investigated, these materials still show drawbacks in terms of response time, reliability, costs and device fabrication. The thin-film electrochromic devices based on various POMs, such as Eu-Preyssler ($[Eu\text{-}(H_2O)P_5W_{30}O_{110}]^{12-}$)[35] and $K_{17}[Ce(P_2W_{17}O_{61})_2 \cdot 30H_2O[Ce(P_2W_{17})_2]$[39] were fabricated and showed suitable response times and high optical contrast. Some POMs combined with polyelectrolytes even exhibit both photochromism and electrochromism.[40, 41] Such combination is of importance for

applying polyoxometalates-based functional materials as optical and electronic memory system, smart windows and chemical sensors.[42, 43]

As it shows in the earlier section, some POMs also exhibit luminescence and magnetic properties.

1.2 Electrochemistry

1.2.1 Cyclic Voltammetry (CV)

Electrochemistry deals with chemical reactions involving electron transfers. The determination of the mechanisms and rates of redox (oxidation/reduction) reactions can be achieved through various electrochemical methods. The most common and perhaps most versatile electroanalytical technique used is cyclic voltammetry.[44, 45] In CV, an external voltage is applied to the electrochemical cell, the current in the cell is measured while cycling the potential of the electrode. The resulting current (i) versus applied potential (E) gives a cyclic voltammogram (i-E curve). Typically three electrodes are used: a working electrode, a reference electrode and an auxiliary electrode. The working electrode (where the reactions occur) is immersed in a solution containing analyte, electrolyte, the reference electrode and the auxiliary electrode. The current passes between the working electrode and the auxiliary electrode. The potential is controlled by a potentiostat.

CV's versatility combined with ease of measurement has resulted in extensive use by electrochemists as well as physical, organic, and inorganic chemists.[46, 47]

1.2.2 Electrochemistry of POMs

The electrochemical properties of POMs have been extensively investigated by using Cyclic Voltammetry.[1, 32] The most important reason is that POMs have the ability to participate in multiple and reversible multi-electron reductions without decomposition, which makes POMs suitable candidates in electrocatalytic research.

1.2.2.1 Electrochemical behavior of POMs

The review[32] by Steckhan E. describes in detail the electrochemical behavior of different types of POMs. Different POMs generally exhibit different features. Keggin-type heteropolyanions can accept a limited number of electrons without decomposition. The reduction potentials of the Keggin-type heteropolytungstates and heteropoly molybdates are controlled by some factors such as the nature of isomers: the reducibility increases in the sequence α-β-γ as the number of rotated M_3O_{13} groups;[48, 49] The reduction potential of one-electron waves is found to decrease linearly with a decrease in the valence of the central metal or an increase in the negative charge of the heteropolyanions.[50, 51] Dawson-Type Heteropolyanions were investigated in the aqueous and organic solvents and were found the pH of the solution affects the electrochemical behavior of POMs. For instance, in aqueous media, the CV of $P_2W_{18}O_6^{26-}$ exhibits four reversible reductions following an irreversible reduction.[52, 53] By adding acid to the solution, the 2nd, 3rd and 4th reduction waves shift to more positive potentials, while the 1st wave remains the same. In organic media, $P_2W_{18}O_6^{26-}$ undergoes four redox pairs. When adding acid, new features appear at more positive potential than the first wave and they grow as the acid concentration increases.

1.2.2.2 Electroanalytic Reduction

Some promising results have been reported that POMs can be used for the activation of electroreduction reactions. POMs are readily reversibly reduced, and the reduction products(known as the "heteropoly blues") are the active species.[32] They are used for catalysis of the hydrogen evolution reaction,[52, 54, 55] the reduction of bromate, [56]nitrite[16, 53] and hydrogen peroxide. As reductive electrocatalysts, POMs are usually used in either homogeneously dissolved in the electrolyte solution or attached to the electrode surface.

1.2.2.3 Electroanalytic Oxidation

Research investigating electroanalytic oxidation of POMs mostly involves the transition metal-substituted POMs and the majority of them highlight the prominent role of the metal substituted into the POM framework. These complexes have been applied as oxidation catalysts in both organic and aqueous phase. The POMs are robust under strong oxidative conditions and therefore have important advantage, relative to their organic counterparts which often decompose under these conditions.[1, 32]

1.3 Synchrotron, XAS and in situ Spectroelectrochemistry

1.3.1 Synchrotron

As a new source of X-rays, synchrotron radiation has revolutionized many branches of science. In comparison with other X-ray sources, synchrotron radiation has obvious advantages:[57, 58] 1) high intensity (hundreds of thousands of times higher than conventional X-ray tubes) and highly collimated; 2) It is emitted with a wide energy

range(continuous spectrum); 3) highly polarized; 4) It is emitted in very short pulses, typically less that a nano-second. Because of these characteristics, synchrotron has been extensively utilized in a wide range of scientific research.

Currently the most brilliant sources of X-rays available are called "Third Generation" synchrotrons. Figure 7[59] shows one of the third-generation synchrotrons- the Advance Photon Source (APS) at Argonne National Laboratory, where all my XAS(X-ray Absorption Spectroscopy) data were collected. This facility has 1,104-meter circumference and includes 34 bending magnets and 34 insertion devices, which generate a capacity of 68 beamlines for experimental research. The high-quality, reliable X-ray beams at APS has attracted scientists to study the structure and dynamics of materials in a variety of disciplines.[60, 61]

1.3.2 XAFS, XANES and EXAFS

With the development of the synchrotron radiation, XAS (X-ray absorption spectroscopy technique) has been used as a powerful tool for the structure research of materials. XAS is a spectroscopic technique that uses X-rays to probe the physical and chemical structure of matter at an atomic scale. It measures the absorption of X-rays as a function of incident X-ray energy E. XAS is element-specific, since each element in the periodic table exhibits an X-ray absorption edge at a different energy. Nearly all elements except for the lightest elements can be studied with XAS.[62] Figure 8 shows the relative cross-sections for photoelectric absorption as a function of photon energy. The saw-tooth-like feature with a sharp rise is called absorption edges. The absorb ion edges (K, L_I, L_{II}, L_{III} etc.) correspond to the excitation of an electron from the 1s, 2s, $2p_{1/2}$, $2p_{3/2}$, etc. respectively. For example, L_{III} edge refers to transition from $2p_{3/2}$ to the corresponding

higher lying bound core shells.[57, 63] My research focused on the L_{III} edge of Lanthanide elements.

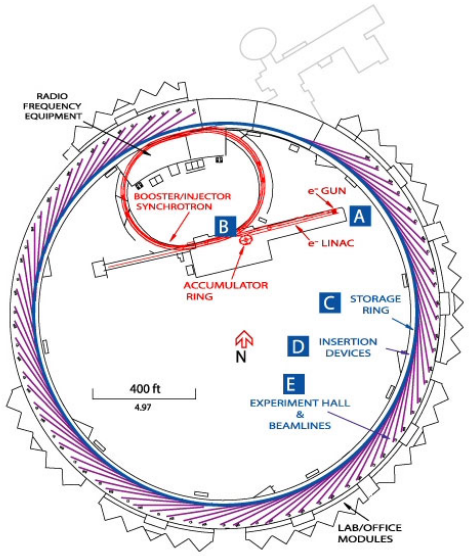

Figure 7. (a) Up: the aerial photo of Advance Photon Source(APS) at Argonne National Laboratory. From the website of Argonne National Lab. (b) Left: the layout of APS.

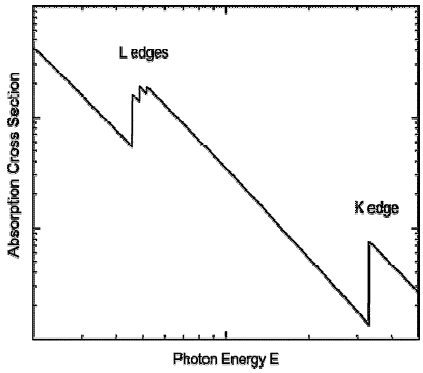

Figure 8. Variation of the linear X-ray absorption coefficient of an atom as a function of the photon energy.[63]

As illustrated in Figure 9, a typical X-ray absorption spectrum is generally divided into three regions: 1) Pre-edge. 2) X-ray absorption near-edge structure (XANES). 3) Extended X-ray absorption fine structure spectroscopy (EXAFS).

The combination of XANES and EXAFS is referred to as XAFS (X-ray Absorption Fine Structure).The XANES region with a rising edge provides information about the oxidation state of the atom and the local geometry around the atom. For instance, Eu^{2+} and Eu^{3+} have 8eV difference in the energy. The peak at 6.9829 keV in the X-ray absorption spectrum indicates the presence of Eu^{3+}, while peak at 6.9749 keV is the characteristic of Eu^{2+}. EXAF region corresponds to the scattering of the ejected photoelectron off neighboring atoms and provides detailed coordination information: coordination numbers, bond lengths and identity of neighboring atoms.[64, 65]

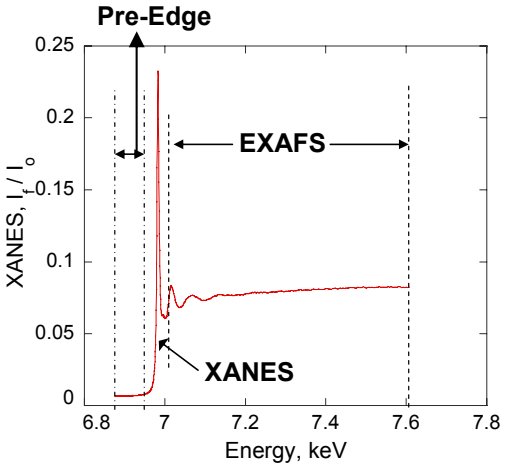

Figure 9. An X-ray absorption spectrum from my experiment.

1.3.3 In situ XAS Spectroelectrochemistry

Spectroelectrochemistry combines the techniques of spectroscopy and electrochemistry.[66] In a specially-built electrochemical cell, by applying a potential, the changes in the redox active compounds are monitored in situ by spectroscopic techniques. We have used bulk electrolysis in combination with XAS to investigate the structural changes of Ln-POMs. All the measurements were carried out with a BAS 100B/W electrochemical workstation (West Lafayette, IN) and a purpose-built electrochemical cell[67] which was designed by my mentor, Dr. Mark Antonio at Argonne National Lab. All these experiments were performed at the BESSRC CAT station 12-BM-B of Advanced Proton Source. The general description of experimental arrangement is shown in Figure 10. An electrochemical sample cell shown in Figure 11 was held in an outer cell. The solution in the sample cell was continuously sparged with argon gas and the outer cell was continuously sparged with helium gas.

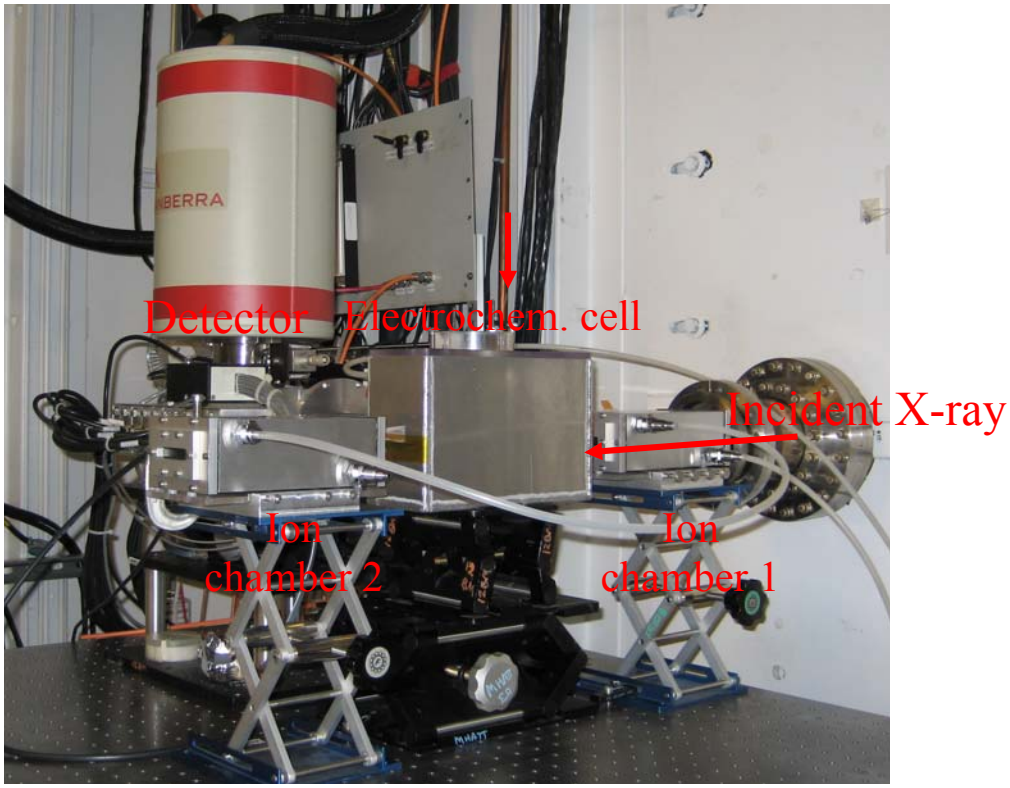

Figure 10. The diagram of the apparatus for in situ XAS spectroelectrochemistry.

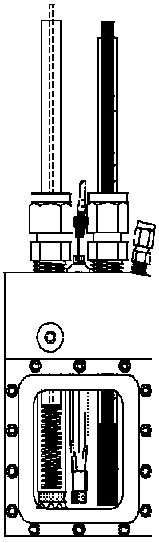

Figure 11. The electrochemical cell designed by Dr. Mark Antonio.

1.4 References

1. Pope, M. T. *Heteropoly and Isopoly Oxometalates*; Springer-Verlag: Berlin, 1983.
2. Berzelius, J.; Poggendorfs, A. *Phys. Chem.* **1826,** *6,* 369-380.
3. Topical issue on polyoxometalates: Hill, C. L., Guest Ed. *Chem. Rev.* **1998,** *98,* 1-389.
4. Herve, G.; Teze, A. In *Polyoxometalate molecular science*; Borras-Almenar, J. J.; Coronado, E.; Muller, A.; Pope, M. T., Eds; Kluwer Academic Publishers: Dordrecht, 2001; Vol. 98; pp 33-54.
5. Pope, M. T. *Inorg. Chem.* **1976,** *15,* 2008-2010.
6. Baker, L. C. W.; Baker, V. S.; Eriks, K.; Pope, M. T.; Shibata, M.; Rollins, O. W.; Fang, J. H.; Koh, L. L. *J. Am. Chem. Soc.* **1966,** *88,* 2329-2331.
7. Rhule, J. T.; Hill, C. L.; Judd, D. A. *Chem. Rev.* **1998,** *98,* 327-357.
8. Jeannin, Y. P. *Chem. Rev.* **1998,** *98,* 51-76.
9. Kishore, P. S.; Viswanathan, B.; Varadarajan, T. K. In *Electrochemical Oxygen Reduction Reaction by Pt Nanoparticles on Carbon Support Stabilized by Polyoxometalates*, 2009; 2009; pp 5188-5197.
10. Hill, C. L.; Prossermccartha, C. M. *Coord. Chem. Rev.* **1995,** *143,* 407-455.
11. Keggin, J. F. *Nature* **1933,** *131,* 908-909.
12. Massart, R.; Contant, R.; Fruchart, J. M.; Ciabrini, J. P.; Fournier, M. *Inorg. Chem.* **1977,** *16,* 2916-2921.
13. Weinstock, I. A.; Cowan, J. J.; Barbuzzi, E. M. G.; Zeng, H. D.; Hill, C. L. *J. Am. Chem. Soc.* **1999,** *121,* 4608-4617.

14. Kozhevnikov, I.; Roberts, S. M. *Catalysis by polyoxometalates* John Wiley and Sons: Chichester, 2002.

15. Ciabrini, J. P.; Contant, R.; Fruchart, J. M. *Polyhedron* **1983,** *2,* 1229-1233.

16. Toth, J. E.; Anson, F. C. *J. Am. Chem. Soc.* **1989,** *111,* 2444-2451.

17. Toth, J. E.; Melton, J. D.; Cabelli, D.; Bielski, B. H. J.; Anson, F. C. *Inorg. Chem.* **1990,** *29,* 1952-1957.

18. Toth, J. E.; Anson, F. C. *J. Electroanal. Chem.* **1988,** *256,* 361-370.

19. Anderson, T. M.; Zhang, X.; Hardcastle, K. I.; Hill, C. L. *Inorg. Chem.* **2002,** *41,* 2477-2488.

20. Zhang, X.; Chen, Q.; Duncan, D. C.; Lachicotte, R. J.; Hill, C. L. *Inorg. Chem.* **1997,** *36,* 4381-4386.

21. Mizuno, N.; Nozaki, C.; Kiyoto, I.; Misono, M. *J. Am. Chem. Soc.* **1998,** *120,* 9267-9272.

22. Peacock, R. D.; Weakley, T. J. R. *J. Chem. Soc. A* **1971,** 1836-1838.

23. Soderholm, L.; Liu, G. K.; Muntean, J.; Malinsky, J.; Antonio, M. R. *J. Phys. Chem.* **1995,** *99,* 9611-9616.

24. Zhang, C.; Howell, R. C.; McGregor, D.; Bensaid, L.; Rahyab, S.; Nayshtut, M.; Lekperic, S.; Francesconi, L. C. *C. R. Chim.* **2005,** *8,* 1035-1044.

25. Binnemans, K. *Chem. Rev.* **2009,** *109,* 4283-4374.

26. Blasse, G. *Eur. J. Solid State Inorg. Chem.* **1991,** *28,* 719-726.

27. Lis, S. *J. Alloy. Compd.* **2000,** *300,* 88-94.

28. AlDamen, M. A.; Clemente-Juan, J. M.; Coronado, E.; Marti-Gastaldo, C.; Gaita-Arino, A. *J. Am. Chem. Soc.* **2008,** *130,* 8874-8875.

29. AlDamen, M. A.; Cardona-Serra, S.; Clemente-Juan, J. M.; Coronado, E.; Gaita-Arino, A.; Marti-Gastaldo, C.; Luis, F.; Montero, O. *Inorg. Chem.* **2009,** *48,* 3467-3479.

30. Corma, A. *Chem. Rev.* **1995,** *95,* 559-614.

31. Kozhevnikov, I. V. *Chem. Rev.* **1998,** *98,* 171-198.

32. Sadakane, M.; Steckhan, E. *Chem. Rev.* **1998,** *98,* 219-237.

33. Okuhara, T.; Mizuno, N.; Misono, M. Catalytic chemistry of heteropoly compounds. In *Advances in Catalysis, Vol 41*; Academic Press Inc: San Diego, 1996; Vol. 41; pp 113-252.

34. Raynaud, M.; Chermann, J. C.; Plata, F.; Jasmin, C.; Mathe, G. **1971,** *272,* 347-348.

35. Liu, S. Q.; Kurth, D. G.; Mohwald, H.; Volkmer, D. *Adv. Mater.* **2002,** *14,* 225-227.

36. Groenendaal, B. L.; Jonas, F.; Freitag, D.; Pielartzik, H.; Reynolds, J. R. *Adv. Mater.* **2000,** *12,* 481-494.

37. DeLongchamp, D. M.; Hammond, P. T. *Adv. Funct. Mater.* **2004,** *14,* 224-232.

38. Trombach, N.; Hild, O.; Schlettwein, D.; Wohrle, D. *J. Mater. Chem.* **2002,** *12,* 879-885.

39. Gao, G. G.; Xu, L.; Wang, W. J.; An, W. J.; Qiu, Y. F. *J. Mater. Chem.* **2004,** *14,* 2024-2029.

40. Liu, S. Q.; Mohwald, H.; Volkmer, D.; Kurth, D. G. *Langmuir* **2006,** *22,* 1949-1951.

41. Xu, B. B.; Xu, L.; Gao, G. G.; Jin, Y. N. *Appl. Surf. Sci.* **2007,** *253,* 3190-3195.

42. Kawata, S.; Kawata, Y. *Chem. Rev.* **2000,** *100,* 1777-1788.

43. Rosseinsky, D. R.; Mortimer, R. J. *Adv. Mater.* **2001,** *13,* 783-789.

44. Bard, A. J.; Faulkner, L. R. *Electrochemical Methods: Fundamentals and Applications*; John Wiley & Sons: New York, 1980.

45. Kissinger, P. T.; Heineman, W. R. *Laboratory Techniques in Electroanalytical Chemistry*; Marcel Dekker: New York, 1984.

46. Rudolph, M.; Reddy, D. P.; Feldberg, S. W. **1994,** *66,* A589-A600.

47. Kissinger, P. T.; Heineman, W. R. *J. Chem. Educ.* **1983,** *60,* 702-706.

48. Teze, A.; Canny, J.; Gurban, L.; Thouvenot, R.; Herve, G. *Inorg. Chem.* **1996,** *35,* 1001-1005.

49. Pope, M. T.; Muller, A. *Angew. Chem.-Int. Edit. Engl.* **1991,** *30,* 34-48.

50. Altenau, J. J.; Pope, M. T.; Prados, R. A.; So, H. *Inorg. Chem.* **1975,** *14,* 417-421.

51. Maeda, K.; Katano, H.; Osakai, T.; Himeno, S.; Saito, A. *J. Electroanal. Chem.* **1995,** *389,* 167-173.

52. Keita, B.; Nadjo, L. *J. Electroanal. Chem.* **1987,** *227,* 77-98.

53. Xi, X. D.; Dong, S. J. *J. Mol. Catal. A-Chem.* **1996,** *114,* 257-265.

54. Keita, B.; Nadjo, L.; Krier, G.; Muller, J. F. *J. Electroanal. Chem.* **1987,** *223,* 287-294.

55. Shen, Y.; Liu, J. Y.; Jiang, J. G.; Liu, B. F.; Dong, S. J. *J. Phys. Chem. B* **2003,** *107,* 9744-9748.

56. Papadakis, A.; Souliotis, A.; Papaconstantinou, E. *J. Electroanal. Chem.* **1997,** *435,* 17-21.

57. Teo, B. K. *EXAFS: Basic Principles and Data Analysis*; Springger-Verlag: Berlin, 1985.

58. Antonio, M. R.; Soderholm, L. X-ray absorption spectrocopy of the actinides. In *The Chemistry of the Actinide and Transactinide Elements*; Morss, L. R.; Edelstein, N. M.; Fuger, J., Eds; Springer: Dordrecht, 2006; Vol. 5; pp 3086-3198.

59. Chiang, M. H.; Soderholm, L.; Antonio, M. R. *Eur. J. Inorg. Chem.* **2003,** 2929-2936.

60. http://www.aps.anl.gov/.

61. Chiang, M. H.; Williams, C. W.; Soderholm, L.; Antonio, M. R. *Eur. J. Inorg. Chem.* **2003,** 2663-2669.

62. Yano, J.; Yachandra, V. K. *Photosynth. Res.* **2009,** *102,* 241-254.

63. Bressler, C.; Chergui, M. *Chem. Rev.* **2004,** *104,* 1781-1812.

64. Teo, B. K.; Antonio, M. R.; Averill, B. A. *J. Am. Chem. Soc.* **1983,** *105,* 3751-3762.

65. Antonio, M. R.; Teo, B. K.; Averill, B. A. *J. Am. Chem. Soc.* **1985,** *107,* 3583-3590.

66. Sharpe, L. R.; Heineman, W. R.; Elder, R. C. *Chem. Rev.* **1990,** *90,* 705-722.

67. Antonio, M. R. *Mat. Res. Soc. Symp. Proc.* **2004,** *8002,* 157-168.

Chapter 2. Europium (III) reduction and speciation within a Wells-Dawson heteropolytungstate

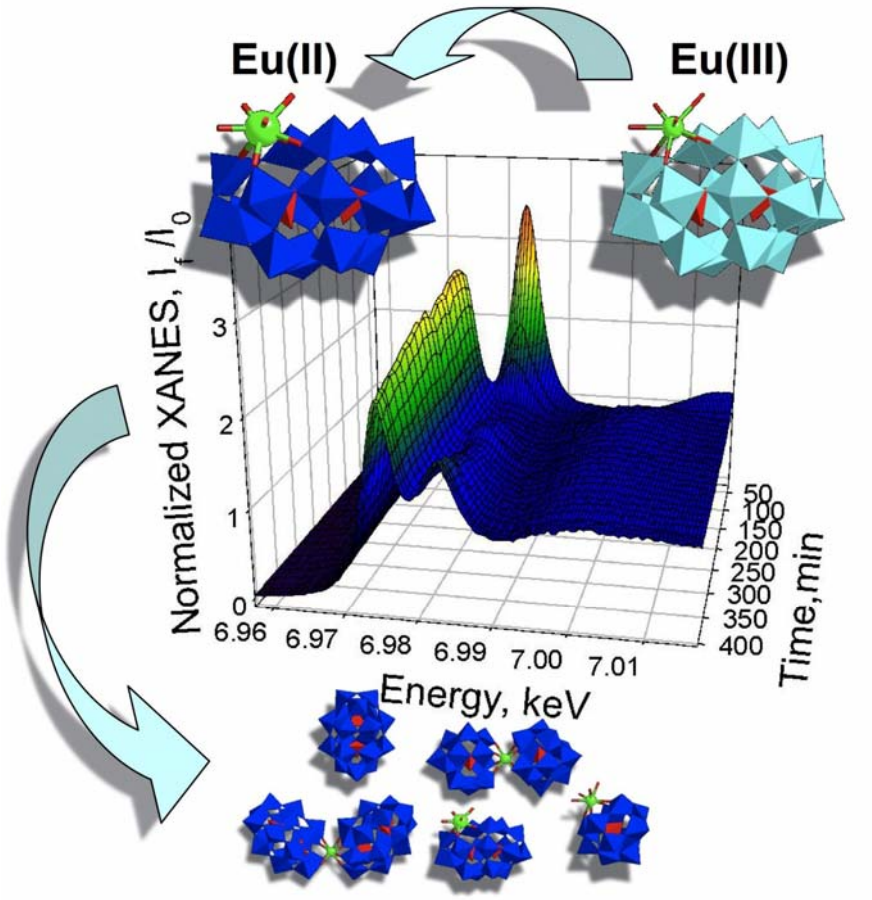

2.1 Introduction

Lanthanide (Ln) interactions with polyoxometalate (POM) anions are of contemporary interest, both fundamental and practical, as a consequence of the formation of high-nuclearity clusters with complex architectures assembled from oxo linkage connectivities of f and d elements, -Ln(III)-O-M(VI)- for M ≡ Mo and W.[1-8 12 20, 9-17] The resulting Ln-POM clusters offer unique functionalities and properties as luminescent materials, particularly the Eu-POMs,[18,19] and as selective and recoverable Lewis acid catalysts.[20,21] Moreover, prospective and realized applications in areas of separations science, photophysics, and electroanalytical chemistry are founded upon the renown reduction-oxidation (redox) properties of POMs.[22,23] As such, the fusion of redox-active Ln ions, specifically the reducible Eu(III) ion and the oxidizable Ce(III) ion, with POMs provides molecular systems with hybrid electrochemical properties, such as seen in other hybrid systems that combine, for example, metallocenes , fullerenes[24,25] and multinuclear exohedral metallofullerenes.[26] For Ln-POMs the combination of the key electro-functional properties of both metal and ligand in one molecule produces two-center, multielectron redox systems in which basic information about the interactions between the atomic-like Ln f-orbitals and the band-like M d-orbitals of POM ligands is largely unknown.

Although there are numerous reports about Eu-POMs,[1-3,9,17,19,27-33] the reduction of Eu(III) in these cluster anions is an unusual phenomenon, and has only been observed for the Preyssler anion, $[EuP_5W_{30}O_{110}]^{12-}$.[34] This may be due to experimental difficulties of probing the Eu ion valence in opaque, heteropoly blue solutions of Eu-POMs or, alternatively, that the energetics of the Eu 4f orbital interactions with LUMO states of

essentially d-orbital character are unfavorable. The first hurdle has been cleared by the application of in situ X-ray absorption near edge structure (XANES) spectroelectrochemistry to Ln- and actinide-POM science.[32,33,35] The second vis-à-vis the interaction of the localized Eu f states and the W-O d states may be due to stereochemical effects that either favor or hinder metal-ligand orbital mixing. For example, the connectivity of Eu(III) with the ligand LUMO is pivotal to reductive electrochemistry and, for the case of $[EuP_5W_{30}O_{110}]^{12-}$, experimental[36] and theoretical[37] results indicate that the spatial association of Eu(III) with the W ions that comprise the LUMO states is a principal factor in f-d electron coupling and non-Nernstian electrochemical behavior.[34]

In similar regard, geometric factors concerning the complexation of Eu(III) by isomers of the monovacant Wells-Dawson anion, $[P_2W_{17}O_{61}]^{10-}$, may influence Eu reduction. In complexes with both the α-1 and α-2 isomers, Eu is bonded to the P-W-O ligands by four O atoms, which serve as μ-oxo bridges between Eu(III) and 4 W(VI) sites of which, for the α-1 isomer, 3 occupy belt positions and 1 occupies a cap position and, for the α-2 isomer, 2 are in belt and 2 are in cap positions, see Figure 1. Each of the 17 W(VI) ion positions in the P-W-O framework structures of the α-1 isomer are magnetically inequivalent.[30,38-41] Of particular significance here is that upon reduction of the fully oxidized anions, electrons are injected into the LUMO states that are centered on the W ions in the belt regions of the anions.[42,43] As such, heterometal cations, i.e., Ln and transition metals, bound in the vacancies of the α-1 POM have one more direct connection with the W-centered LUMO states than do the heterometal complexes of the α-2 POM. A physical manifestation of these oxo linkage connectivities relates to reduction processes, wherein electroactive transition metal cations at the α-1 site are more

readily reduced than when substituted at the α-2 position.[44-49] The orientation of a basic oxygen atom—pointing at the α-1 site—from the adjoining $[PO_4]^{3-}$ tetrahedron around which the W-O framework is assembled also favors stronger coupling of heterometal ions with the W atoms in the belt (LUMO) of the α-1 ligand than in the α-2 ligand. The results from theoretical treatments, showing that the LUMO in the frontier molecular orbitals of $[\alpha\text{-}P_2W_{18}O_{62}]^{6-}$ consists of 96% α-1 character,[50-52] are consistent with experimental observations, including those showing that Eu(III) in an α-2 site, such as in $[Eu(\alpha\text{-}2\text{-}As_2W_{17}O_{61})_2]^{17-}$, is not reduced in an aqueous supporting electrolyte of 0.1 M CH_3CO_2Na + 0.1 M $NaClO_4$ at pH = 5.0.[33,53]

The information about structural and electronic properties suggests to us that the $[\alpha\text{-}1\text{-}P_2W_{17}O_{61}]^{10-}$ lacunary POM would be an obvious system with which to deliberately couple Eu f-states and POM-ligand d-states by electrochemical means. In so doing, the reduction of Eu(III) in a complex molecular anion with dual centers of redox activity provides an opportunity for observation of correlated electron behaviors and otherwise interesting electrochemistry that would advance knowledge about the energetics of Eu-POMs, in general, and their applications in europium hydrometallurgy and electrocatalysis, in particular. The objective of this study is the investigation of the spectroscopy and electrochemistry for solutions of $K_7[(H_2O)_4Eu(\alpha\text{-}1\text{-}P_2W_{17}O_{61})]$ dissolved in aqueous electrolytes. Toward this end, we used the electrochemical techniques of cyclic voltammetry (CV) and bulk electrolysis (BE) as well as XAFS (X-ray absorption fine structure) spectroelectrochemistry. In particular, the Eu valence and coordination environment were probed through use of Eu L_3-edge XANES and EXAFS (extended X-ray absorption fine structure) obtained for the fully oxidized (colorless)

complex anion, $[(H_2O)_4Eu(\alpha\text{-}1\text{-}P_2W_{17}O_{61})]^{7-}$, and for several, multielectron reduced (heteropoly blue) forms, $[(H_2O)_4Eu(\alpha\text{-}1\text{-}P_2W_{17}O_{61})]^{n-}$, produced by exhaustive electrolysis at controlled electrode potentials simultaneously with the XAFS data acquisition. It is shown that Eu(III) in $[(H_2O)_4Eu(\alpha\text{-}1\text{-}P_2W_{17}O_{61})]^{7-}$ as dilute solutions (0.25 and 5.0 mM) in aqueous electrolytes of 0.2 M Li_2SO_4 at pH = 3.0 is reduced to Eu(II) at sufficiently negative electrode potentials. The species containing Eu(II) and the reduced ligand is unstable with respect to autooxidation of Eu(II), fragmentation and rearrangement of the POM ligand, leading to the reconstitution of the plenary anion, $[\alpha\text{-}P_2W_{18}O_{62}]^{6-}$, and the formation of Eu(III) complexes of $[\alpha\text{-}2\text{-}P_2W_{17}O_{61}]^{10-}$ and $[PW_{11}O_{39}]^{7-}$ at negative electrode potentials. The mixed solution speciation was confirmed by ^{31}P NMR spectroscopy and optical luminescence measurements.

2.2 Experimental Section

2.2.1 Solution and Sample Preparation

$K_7[(H_2O)_4Eu(\alpha\text{-}1\text{-}P_2W_{17}O_{61})]$, $K_7[(H_2O)_4Y(\alpha\text{-}1\text{-}P_2W_{17}O_{61})]$, $Al(H_3O)[(H_2O)_2Eu(PW_{11}O_{39})]$, $Cs_{11}[Eu(PW_{11}O_{39})_2]$, $K_7[Eu(\alpha\text{-}2\text{-}P_2W_{17}O_{61})]$, and $K_{17}[Eu(\alpha\text{-}2\text{-}P_2W_{17}O_{61})_2]$ were synthesized as previously described.[27,30,40] The plenary Wells-Dawson POM, $K_6[\alpha\text{-}P_2W_{18}O_{62}]$, and its lacunary, monovacant form, $K_9Li[\alpha\text{-}1\text{-}P_2W_{17}O_{61}]\cdot 20H_2O$, were prepared according to literature procedures.[54] $EuCl_3$, Eu_2O_3, YCl_3, and Li_2SO_4 were purchased from Aldrich Chemical Co. Aqueous supporting electrolyte solutions of 0.2 M Li_2SO_4 adjusted to pH = 3.0 with H_2SO_4 (Fisher Optima) were used for all electrochemical and spectroscopic experiments in accordance with previous studies showing that this medium imparts stability to metal complexes of [α-1-

$P_2W_{17}O_{61}]^{10-}$.[45] Indeed, we have found through use of ^{31}P NMR that the stabilities of all fully oxidized Ln-POMs, $K_7[(H_2O)_4Ln(\alpha\text{-}1\text{-}P_2W_{17}O_{61})]$, in this aqueous supporting electrolyte are good (48 hours before onset of decomposition). A solution of $Eu_2(SO_4)_3$ was prepared by dissolving Eu_2O_3 (9 mg) in the 0.2 M Li_2SO_4 solution electrolyte (10 mL). All chemical reagents were used as received. Deionized water (18 MΩ cm) was used for the preparation of all solutions.

2.2.2 ^{31}P Nuclear Magnetic Resonance (NMR)

^{31}P NMR (161.8 MHz) spectra were recorded in 10 mm tubes with a volume of 3 mL on a JEOL GX-400 spectrometer. Typical acquisition parameters are as follows: spectral width, 10000 Hz; acquisition time, 0.8 s; pulse delay, 1 s; pulse width, 15 μs (50° tip angle). 2000 scans were accumulated. A 85% H_3PO_4 solution was used as a chemical shift reference. The preparation of isomerically-pure $K_7[(H_2O)_4Ln(\alpha\text{-}1\text{-}P_2W_{17}O_{61})]$ samples(5.0 mM) was established by their two-line spectra with δ(P1) and δ(P2) values of 6.42 and -11.41, -9.97 and -13.01 ppm for the complexes with Ln ≡ Eu and Y, respectively. All chemical shifts are reported on the δ scale with upfield resonances as negative.

2.2.3 Electrochemical Measurements

A BAS 100B/W potentiostat (West Lafayette, IN) was used for the acquisition of all electroanalytical data, which were obtained from POM solutions (0.25 and 5.0 mM) at room temperature in 0.2 M Li_2SO_4 (pH = 3.0). All reported potentials are given with respect to the Ag/AgCl reference electrode (BASi MF-2052). CV data for the lacunary ligand, $K_9Li[\alpha\text{-}1\text{-}P_2W_{17}O_{61}]$, its Ln complexes $K_7[(H_2O)_4Ln(\alpha\text{-}1\text{-}P_2W_{17}O_{61})]$ (Ln ≡ Eu^{3+}

and Y^{3+}), and $Eu(ClO_4)_3$ were obtained in one-compartment glass vials using a standard three-electrode system consisting of either glassy carbon (GC) (BASi MF-2012, geometrical area 0.071 cm^2) or 6.15 mm diam. graphite rod (GR) (Alfa 14739) working electrodes; 6.15 mm diam. GR auxiliary electrodes; the aforementioned Ag/AgCl reference electrodes. Each solution was deaerated with dinitrogen gas for 10–15 min prior to the CV measurement and subsequently blanketed with dinitrogen during all sweeps. Bulk electrolyses data for 5.0 mM solutions of $K_7[(H_2O)_4Ln(\alpha\text{-}1\text{-}P_2W_{17}O_{61})]$ (Ln ≡ Eu and Y) were obtained in two-compartment electrochemical cell vials separated by a medium porosity glass frit to isolate the auxiliary and working GR electrodes. The solutions were step polarized from rest potential (+0.054 V) to an electrode potential of -1.30 V as they were vigorously sparged with dinitrogen throughout the course of exhaustive electrolysis, from which the net charge was used to calculate the number of electrons transferred/molecule through Faraday's law.

2.2.4 XAFS Data Acquisition and Analysis

Europium L_3-edge (6.977 keV) X-ray absorption spectroscopy (XAS) was performed at beamline 12-BM-B[55] at the Advanced Photon Source. The incident X-ray energy was calibrated by the first inflection point energy for the K-edge XANES of Fe foil, 7.112 keV. All measurements were made in fluorescence mode at ambient conditions with a multielement (Canberra) detector. The neat powder of $K_7[(H_2O)_4Eu(\alpha\text{-}1\text{-}P_2W_{17}O_{61})]$ was pressed into a micro X-ray cell (SPEX 3577) with Prolene® X-Ray film windows (4 μm gauge, Chemplex Industries), and its solutions of 0.25 mM and 5.0 mM POM concentrations (5 mL in 0.2 M Li_2SO_4 electrolyte, pH = 3.0) were injected into purpose-built electrochemical cells for measurement.[56,57] The data from 3 one-hour scans

of the white powder sample and the 5.0 mM solution (in its colorless-oxidized state as well as blue-reduced form) were averaged for analysis of EXAFS, which was performed in consistent fashion in the usual manner[58] with EXAFSPAK[59] and WinXAS 3.1[60] and theoretical phase and amplitude functions calculated with FEFF8.0.[61] Conventional metrical treatments of the Eu $k^3\chi(k)$ EXAFS with a fixed scale factor ($S_0^2 = 0.9$) entailed a series of step-wise fits of increasing complexity, from single- to multi-shell coordination models based upon the crystallographic data available for the structure of the corresponding lutetium POM, $[(H_2O)_4Lu(\alpha\text{-}1\text{-}P_2W_{17}O_{61})]^{7-}$.[62] Ultimately, the EXAFS spectra were precisely modeled with either three or four-shell fits that included contributions from the nearest O atoms as well as the distant neighbors of O, P, and W. The number of refined parameters (10) was less than the number of relevant independent data points, $N_I = 15$, available in the primary spectra, with $k_{max} = 10.2$ Å^{-1} and $\Delta r = 3$ Å.[63] The in situ X-ray absorption spectroelectrochemical data were collected on the deaerated and continuously N_2-sparged solution of the fully oxidized $[(H_2O)_4Eu(III)(\alpha\text{-}1\text{-}P_2W_{17}O_{61})]^{7-}$ anion in the aqueous electrolyte at the electrode open circuit potential, +0.054 V. This was followed by bulk electrolysis at -1.30 V and at -0.90 V for the concentrated (5.0 mM) and dilute (0.25 mM) solutions, respectively, of $[(H_2O)_4Eu(III)(\alpha\text{-}1\text{-}P_2W_{17}O_{61})]^{7-}$ to produce the corresponding reduced anions containing Eu(II). XANES data were recorded with respect to time while electrode polarization was maintained to probe the stability of the reduced species. The time-dependent spectra obtained at each electrode potential were fit using linear combination analyses with the end member spectra for the oxidized, Eu(III), and reduced, Eu(II), POMs as well as with pseudo-Voigt and arctangent functions.

2.2.5 Optical Luminescence

$K_7[(H_2O)_4Eu(\alpha\text{-}1\text{-}P_2W_{17}O_{61})]$ (0.233 g, 46.6 μmol) was dissolved in 10 mL Li_2SO_4 (0.2 M, pH 3.0) and placed in an electrochemical cell. The solution was reduced at a potential of -1.30 V for 4 hours under an atmosphere of dinitrogen. An aliquot of this reduced solution was taken for analysis (200 μL in 2000 μL Li_2SO_4 buffer, 0.466 mM).

The remaining solution was oxidized at a potential of +1.00 V for 5 hours (until the solution was completely clear) and a sample was taken for the final spectroscopic analysis. Standard solutions of $K_7[Eu(\alpha\text{-}2\text{-}P_2W_{17}O_{61})]$, $K_{17}[Eu(\alpha\text{-}2\text{-}P_2W_{17}O_{61})_2]$, $Al(H_3O)[(H_2O)_2Eu(PW_{11}O_{39})]$, $Cs_{11}[Eu(PW_{11}O_{39})_2]$, and $Eu_2[SO_4]_3$ were prepared at a working concentration of ~ 0.5 mM also in Li_2SO_4 (0.2 M, pH = 3.0) and placed in a quartz cuvettes for analyses. Eu(III) excitation spectra and excited state lifetimes were obtained using a Spectra-Physics Quanta Ray PRO-270-10 Q-switched Nd:YAG pump laser (10 Hz, 60-70 mJ/pulse) and a MOPO SL for all luminescence measurements as reported.[64] The non-degenerate $^7F_0 \rightarrow {}^5D_0$ transition of the Eu(III) ion was scanned between 578 and 582 nm while the $^5D_0 \rightarrow {}^7F_2$ emission band was monitored at 614 nm. Excitation spectra were deconvoluted by using the program PeakFit 4.12 (Jandel). Time resolved luminescence measurements were collected by using a digital Tektronix TDS 3034B oscilloscope. Data were fit to single and double exponential decays by using Sigmaplot version 10 (Systat).

2.3 Results and Discussion

2.3.1 Electrochemical Studies

Cyclic voltammograms obtained for two concentrations—0.25 and 5.0 mM—of three analytes—$[\alpha\text{-}1\text{-}P_2W_{17}O_{61}]^{10-}$, $[Eu(\alpha\text{-}1\text{-}P_2W_{17}O_{61})]^{7-}$ and $[Y(\alpha\text{-}1\text{-}P_2W_{17}O_{61})]^{7-}$ (abbreviated hereafter as α-1, Eu-α-1, and Y-α-1, respectively)— and two concentrations—1.0 and 5.0 mM—of Eu(III) in the pH = 3.0 aqueous electrolyte of 0.2 M Li_2SO_4 are shown in Figure 2. The data of Figure 2a (solid black line) for the 0.25 mM Ln-free lacunary anion shows three well-resolved processes with $E_{½}$ = -0.22, -0.47, and -0.81 V (identified as I, II, and III), which are attributed to W-based redox chemistry involving three successive two-electron couples.[65] The response is essentially the same as reported beforehand for 0.25–0.5 mM solutions of $K_9Li[\alpha\text{-}1\text{-}P_2W_{17}O_{61}]$ in 0.2 M Na_2SO_4 aqueous electrolytes of pH = 3.0.[45-47] Repetitive sweeps between -0.90 and +0.20 V showed reproducible behavior even though the original, colorless solution changed to light blue during the course of experimentation with different scan rates (see Figure S0, Supporting Information). The blue color arises from the reductive electrochemistry and delocalization of the added electrons in the LUMOs that consist of W (α-1, belt site of Figure 1, left) and O character.[66-69]

The data of Figure 2a (black dashed line) for a 1.0 mM Eu(III) solution shows a single process with $E_{½}$ = -0.63 V, which is attributed to the one-electron Eu(III)/Eu(II) couple. The standard electrode potential for this process is -0.55 V vs. Ag/AgCl.[70] The more negative experimental value is attributed to stabilizing effects of sulfate complexation with Eu(III) in much the same manner as the electrode potential of the

Ce(III)/Ce(IV) couple is lowered by complexation with $[SO_4]^{2-}$.[71] Of essence here is that the Eu redox activity occurs within the electrode potential region for the ligand-centered reduction of the W-O POM framework alone. As such, the CV data for Eu-α-1 shown in Figure 2b (solid black line) may be an amalgamation of Eu- and ligand-centered redox activities. The values of $E_{½}$ for the 4 redox couples are provided in Table 1. These show that Eu(III) complexation with $[\alpha\text{-}1\text{-}P_2W_{17}O_{61}]^{10-}$ results in a negative shift of 0.11 V of the first redox couple, I, equivalent to the effects observed upon transition-metal-ion complexation with α-1.[47] The second and the third couples of the anionic ligand alone (II and III, respectively, in Table 1) are effectively preserved in the response of Eu-α-1 as couples II and IV. The principal variation between the ligand and Eu-α-1 is the presence of a new feature at $E_{½}$ = -0.65 V, which is nearly coincident with the response of free Eu and with a peak separation, ΔE_p, of 0.058 V, indicating one-electron Eu(III)/Eu(II) redox activity in Eu-α-1. The presumed mixing of Eu- and W-centered electrochemical processes in the complex anion parallels the heterobinuclear reductive response of Fe(III) and α-1 in the Fe(III)-α-1 system.[46]

To provide insight into this issue, the CV data for a 0.25 mM solution of Y-α-1 was recorded and is shown in Figure 2b as the black dashed line. Because Y(III) is not reducible to Y(II) in aqueous electrolytes, the electrochemical response will be that of the ligand alone as modified by Y(III) complexation, so a difference between Y-α-1 and Eu-α-1 stands to be an indicator of Eu redox activity. Three couples are evident for Y-α-1 with $E_{½}$ values (I–III, Table 1) that are in agreement with three of the four processes observed for Eu-α-1. This comparison indicates that waves I, II, and IV of Eu-α-1 are attributable to W electrochemistry. Couple III at $E_{½}$ = -0.65 V is unique to Eu-α-1—there

is no wave between -0.60 and -0.70 V in the CV for Y-α-1—and is evidence to support the assignment of Eu redox activity in the bulk voltammetric response for Eu-α-1. Confirmation of the Eu valence switching is provided through use of XANES spectroelectrochemisty, vide infra.

The CV data for the 5.0 mM solution analyte concentrations are shown in Figure 2 (c, d) in identical fashion to the presentation of the data for the 0.25 mM analytes of Figure 2 (a, b). In comparing the CVs in the left and right panels of Figure 2, two differences are obvious vis-à-vis the negative electrode potential switching limits and the current response itself. The negative limits of -0.90 and -1.30 V for the 0.25 and 5.0 mM analyte concentrations, respectively, are determined by the onset of the hydrogen evolution reaction, which appears to be promoted by surface derivatization by the analytes at low concentrations in the acidic medium.[72] The rather dramatic and detrimental changes of appearance, in terms of peak broadening and poor peak separations, for the CVs obtained at the high (5.0 mM) POM concentrations are indicators of, in part, solvent and solute effects, esp. interion-associations, such as have become commonplace in organic[73-75] and aqueous[76-80] POM electrochemistry. Nevertheless, in considering the 1st redox couple, which is the only one with clear resolution even in the corresponding semi-differential data (see Figure S1, Supporting Information), the trends in the $E_{½}$ values for the 0.25 mM analytes are consistent with the 5.0 mM solutions, see Table 1. In particular, the couples for Eu-α-1 and Y-α-1 are 0.13–0.15 V less than that for the ligand itself. Whereas there are subtle differences between the data for Y-α-1 and Eu-α-1, shown in Figure 2d, it is not possible to disentangle the ligand, W-centered processes from one for the Eu(III)/Eu(II) couple as was possible with

the CV data for 0.25 mM Eu-α-1 (Figure 2b). The same systematic comparison of the CV data for the 5.0 mM α-1 and Ln-α-1 POMs reveal complicated behaviors that may arise from combined effects of interion associations, polydispersity, protonation, isomerization, analyte instabilities, etc. For instance, although the $E_{½}$ values for the 5.0 mM analytes are slightly (0.005–0.09 V) more negative than the corresponding values obtained at 0.25 mM, the ΔE_p values for the 5.0 mM analytes at 49 mV s^{-1} are large, 0.10–0.20 V see Table 1, and significantly (1.8–5.4 ×) greater than those for the 0.25 mM analytes at the same scan rate. This suggests that the electron transfer kinetics are slower for the species in the concentrated analytes than for those in the dilute ones.

Information about the redox kinetics of α-1 and Ln-α-1 at the GR electrode surface is provided by plots of the peak currents for the cathodic and anodic processes of couple I (i_{pc} and i_{pa}, respectively) vs. the square roots of the scan rates, $\nu^{½}$. Figure 3 shows that a linear proportionality exists between the currents and $\nu^{½}$ for both analyte concentrations—0.25 (a, b) and 5.0 (c, d) mM. The primary data (shown as symbols) are adequately described by the linear fits (R^2 = 0.86–0.99, shown as lines) with intercepts of zero according to the Randles-Sevcik equation, indicating that the electron transfer kinetics are mass transport controlled.[81] The individual slopes and regressions coefficients, tabulated in the Supporting Information (Table S0), show that the ratio of average peak currents, i_{pa}/i_{pc}, is less than unity (0.8–0.9) for the dilute, 0.25 mM analyte concentrations, and is greater than unity (1.1–1.6) for the 5.0 mM analyte concentrations for all 4 scan rates, 9, 25, 49, and 100 mV s^{-1}. These deviations indicate irreversible behaviors, which are corroborated by the plots of ΔE_p vs. ν, showing (See Figure S2, Supporting Information) that the peak potential separations increase with increasing scan

rates for both the 0.25 and 5.0 mM analyte concentrations and, consequently, that electron transfer kinetics are slow relative to the aforementioned scan rates. The combined deviations of peak currents and potentials from ideal, Randles-Sevcik and Nernst behaviors suggest electrochemical irreversibilities, such as may result from redox processes that are coupled to chemical reactions involving the electrolyzed species, may also be at play.

We sought to obtain additional information about the electrochemical processes by use of controlled potential electrolysis of fully-oxidized α-1 and Ln-α-1 POM solutions. In agreement with the literature,[47,65] a 5.0 mM solution of the α-1 ligand was found to consume 6.1 electrons/molecule upon exhaustive electrolysis at -1.30 V. The comparable experiments with 5.0 mM and 0.25 mM solutions of Eu-α-1 and Y-α-1 were less conclusive. The results show the transfer of 5.8–10.2 electrons for Eu-α-1 and 6.0–7.9 electrons for Y-α-1. We attribute this unusually high dispersion of results from repeated measurements performed under identical conditions to interferences from chemical reactions, particularly those resulting from the reactivity of the reduced Ln-α-1 complexes toward isomerization and rearrangement, forming electroactive species in addition to Ln-α-1. As pointed out beforehand,[46] such chemical interferences in the labile α-1 system can complicate the overall count of charge (electrons) consumed throughout the timescale of a bulk electrolysis experiment. Whereas the results from BE are inconclusive regarding evidence about Eu redox activity in Eu-α-1, as indicated by the CV measurements of the 0.25 mM analyte, and its structural chemistry, direct and definitive insights about both issues were obtained by the use of in situ Eu XAFS.

2.3.2 Eu L_3-edge XAFS

Spectra were first acquired for the solid salt of Eu-α-1 and for a freshly-prepared 5.0 mM solution of it in fully oxidized form at rest potential (+0.054 V) to confirm that the coordination environment about Eu(III) in the solid state does not change upon dissolution in the 0.2 M Li_2SO_4 electrolyte. The XANES and EXAFS data are shown as Figures 4 and 5, respectfully. The intense edge peaks at 6.9829 keV observed in the XANES are characteristic of Eu(III),[57,62,82] and the coincident responses suggests that the Eu coordination for the solution species is stable and equivalent to that of the solid. The experimental $k^3\chi(k)$ EXAFS and the corresponding Fourier transform (FT) data of Figure 5 (without phase correction) confirm the structural identity. In the absence of single-crystal X-ray diffraction data for Eu-α-1, the fitting of the primary Eu EXAFS (solid lines) was modeled upon the known structure of $K_7[(H_2O)_4Lu(\alpha\text{-}1\text{-}P_2W_{17}O_{61})]$ (abbreviated hereafter as Lu-α-1), which shows that Lu(III) is 8-coordinated with O atoms at an average distance of 2.36(6) Å.[62] The average bond length between Lu and the four O atoms of the tetradentate α-1 ligand is 2.30(4) Å. The square antiprism of O around Lu(III) is completed by complexation of four water molecules with an average distance of 2.42(5) Å. Our Eu EXAFS is of insufficient resolution (Δk = 8.2 $Å^{-1}$; Δr = 0.19 Å) to show two separate O peaks in the FT data, which instead reveal a single intense peak at 1.86 Å (before phase shift, part b of Figure 5) containing the combined O backscattering contributions.

The EXAFS for the solid salt and aqueous solution of Eu-α-1 were fit to reveal 7.6 ± 1 nearest O at 2.37(1) Å and 7.8 ± 1 O at 2.38(1) Å, respectively. The O coordination numbers (CNs) agree with those obtained for the solid salt of Lu-α-1 (8) and

for an aqueous solution of Eu-α-1 (7.8). The latter value was obtained as the sum of 4 O, from the α-1 ligand, and 3.8 bound H_2O, as determined from luminescence lifetimes of Eu-α-1 measured in H_2O and D_2O.[30] The EXAFS results for the solid and solution of Eu-α-1 are in agreement with the 1:1 formulation of the $[(H_2O)_4Eu(\alpha\text{-}1\text{-}P_2W_{17}O_{61})]^{7-}$ complex wherein Eu(III) binds to four O atoms of the POM ligand and four other coordination sites are occupied by water molecules, possibly with the stereochemistry that obtains for the Lu-α-1 crystal structure. The fact that the average Eu-O distances, 2.37–2.38 Å, are only 0.01–0.02 Å longer than the average Lu-O distance is unexpected in view of the 0.089 Å larger ionic radius for Eu(III), 1.066 Å, vs. Lu(III), 0.977Å, for CN = VIII.[83]

Additional evidence that the Eu-α-1 molecular complex remains stable and intact upon dissolution of the solid and throughout the course of the measurements is provided by the analysis of the three distant peaks—2.86, 3.26, and 3.72 Å—in the FT data of Figure 5b. The fits (shown as dashed lines in Figure 5) to the Eu EXAFS data of the solid and solution samples obtained from the 4-shell model with fixed CNs for the distant interactions based upon the Lu-α-1 environment are convincing. The three small peaks correspond to backscattering from 1 O at 3.36–3.37 Å, 4 W at 3.74 Å, and 4 O at 4.37–4.39 Å. The complete metrical parameters are provided in Table 2. These distances compare favorably with those—3.41(1), 3.97(8), and 4.33(9) Å, respectively—from the X-ray crystallographic investigation of the Lu-α-1 system.[62]

Following acquisition of the solution EXAFS for the oxidized Eu-α-1 at rest potential described above, the electrode potential was step polarized to -1.30 V to produce the reduced species. Upon achieving exhaustive electrolysis after 125 min, the

Eu L_3-edge XANES of Figure 4 (blue dashed line) for the heteropoly blue, reduced analyte reveals a new edge peak at 6.9749 keV, approximately 8 eV below the Eu(III) peak for the oxidized analyte, that is diagnostic of Eu(II).[57,84,85] This in situ XANES spectroelectrochemistry experiment provides direct confirmation of the independent results from CV alone, vide supra, by demonstrating that Eu(III) is, indeed, reduced along with the P-W-O ligand. With the possible exception of $[Eu(III)(W_5O_{18})_2]^{9-}$,[86] it is only the second known example of such behavior in Eu-POMs, the first being the Eu(III)-Preyssler POM.[32]

During the subsequent campaign to obtain high-quality EXAFS for the pure Eu(II)-α-1 solution species, we observed an autooxidation process—with the electrode continuously polarized at -1.30 V—commencing some 15 min after producing the Eu(II) solution species. The XANES data of Figure 6a show the time evolution of the autooxidation to Eu(III). This dynamic behavior demonstrates that the electrochemical interconversion between the fully oxidized Eu(III)-α-1 anion and its multi-electron-reduced species, Eu(II)-α-1, is an irreversible, non-Nernstian process. The EXAFS data obtained within the ca. 50 min time-frame (110–160 min, see Figure 6b) when there is ≤ 5 % of the autooxidized Eu(III) species formed were analyzed in terms of its Eu-O bonding. A single-shell fit to the data for the metastable, reduced POM indicates that there are 7.7±1.0 O atoms about Eu(II) with an average distance of 2.55(4) Å (see Supporting Information, Figure S3). This bond length is 0.17 Å longer than that (2.38(1) Å) for the original solution of Eu(III)-α-1. The increase is consistent with the 0.184 Å larger IR of Eu(II), which is 1.25 Å for CN = VIII, versus Eu(III).

The in situ Eu XANES acquired following exhaustive electrolysis of the fully oxidized, dilute (0.25) mM Eu-α-1 solution with the electrode polarized at -0.90 V confirms the response observed with the 5.0 mM analyte. That is, the reduced Eu(II)-α-1 anion is a labile species prone to autooxidation and structural transformations, which were addressed by subsequent experimentation described here. Some 30 % the fully-reduced Eu(II)-α-1 species in the 5.0 mM analyte is autooxidized to Eu(III) after 6.7 hours with the electrode at -1.30 V (part b of Figure 6). To accelerate the oxidation of the remaining Eu(II), the solution was electrolyzed with an electrode potential of -1.00 V. The Eu XANES obtained for the heteropoly blue solution following exhaustive electrolysis, Figure 4 (blue solid line), shows the presence of only Eu(III), confirming the complete oxidation of Eu(II). The corresponding EXAFS and FT data of the blue, Eu(III) solution maintained at -1.00 V are shown in Figure 7. This FT, with three peaks at 1.91, 2.76, and 3.67 Å, is significantly different from that for the original, colorless, oxidized solution of Eu-α-1 shown in Figure 5. The fit to the $k^3\chi(k)$EXAFS with a three-coordination shell model with O nearest neighbors and distant P neighbors is quite good (dashed line in Figure 7). Fitting with S in place of P, to account for the possibility that the electrolyte, 0.2 M $[SO_4]^{2-}$, coordinates with Eu(III) produces equivalent fits and metrical parameters. Because P (Z = 15) and S (Z = 16) are adjacent elements, the use of EXAFS alone provides insufficient contrast to distinguish between combination of P/S backscattering. The coordination of Eu(III) in the blue solution at -1.00 V is well-described by a first shell of 9.0 ± 1 O atoms at 2.42(2) Å, a second shell of 3.9 ± 0.9 P/(S) atoms at 3.16(3) Å, and a third shell of 1.8 ± 0.8 P/(S) atoms at 4.15(3) Å. All the fitting parameters are provided in Table 2.

Despite the availability of such structural detail, the exact speciation of Eu(III) in terms of the identity, nature, and number of different species is impossible to ascertain. The EXAFS data are consistent with a combination of P-containing species that are known decomposition products of α-1 and chelants of Eu, including $[P_2W_{18}O_{62}]^{6-}$, [α-2-$P_2W_{17}O_{61}]^{10-}$, $[H_2P_2W_{12}O_{48}]^{12-}$,[45] as well as Eu phosphate/(sulfate) materials.[87,88] Additional spectroscopic evidence obtained by use of optical luminescence and ^{31}P NMR spectroscopy was applied to disentangle the identities of the individual species produced following the complete reduction and subsequent oxidation of Eu-α-1. This combination of techniques, wherein luminescence opens a window on the speciation of Eu only, and NMR on P speciation, provides information that complements and is otherwise not available from CV and Eu XANES.

2.3.3 Optical Luminescence

The bulk electrolysis experiment monitored by XANES was replicated and probed by luminescence spectroscopy to interrogate the Eu(III) speciation upon reduction and oxidation. The excitation spectrum of a fresh solution of Eu-α-1 in its oxidized (colorless) form prepared by dissolution of a spectroscopically-pure solid salt, as determined by ^{31}P NMR (Table 3), in 0.2 M Li_2SO_4 (pH = 3.0) is shown in Figure 8 (pink trace). The intense peak at 580.0 nm with a single-exponential lifetime of 215 ± 21 μs is in agreement with previous results for the tetrahydrated anion, $[(H_2O)_4Eu(\alpha\text{-}1\text{-}P_2W_{17}O_{61})]^{7-}$.[30] The spectrum shows two characteristic shoulders on the left and right flanks (579.8 and 580.5 nm, respectively) of the peak that exhibit bi-exponential lifetimes with components arising from $[(H_2O)_4Eu(\alpha\text{-}1\text{-}P_2W_{17}O_{61})]^{7-}$, and those attributed to the

presence of isomeric species $[(H_2O)_nEu(\alpha\text{-}2\text{-}P_2W_{17}O_{61})]^{7-}$ and $[Eu(\alpha\text{-}2\text{-}P_2W_{17}O_{61})_2]^{17-}$ respectively.[30] The relatively small amount of isomerization (Figure S4, Supporting Information, for deconvolved spectrum) arises from the dilution induced dissociation of Eu-α-1 at the extremely low concentration (47 μM) necessary to avoid quenching artifacts.[30]

The excitation spectrum of an aliquot of the blue, reduced solution removed from the electrochemical cell upon completion of exhaustive BE at -1.30 V in identical manner to the in situ XAFS spectroelectrochemistry is shown in Figure 8 (blue trace). The dramatic decrease in signal intensity compared with that for the oxidized starting solution (pink trace) is attributed to the combination of two factors. First, the sample excitation and emission is attenuated by the deep blue color of the solution, and second, the reduction of Eu(III) to Eu(II) lowers the Eu(III) concentration, which in turn lowers the luminescence intensities. Also the relative intensity of the shoulder at 579.7 nm on the left flank of the main peak at 580.0 nm increases to ca. two-thirds of the maximum peak value, consistent with the notion that reduction is correlated with decomposition. The lifetime, 320 ± 32 μs, of this shoulder is significantly longer than for the similar feature in the oxidized solution, 226 ± 22 μs, and suggests that a different species, notably $[(H_2O)_nEu(PW_{11}O_{39})]^{4-}$, forms upon reduction (Figure S5, Supporting Information).

The excitation spectrum for the solution following complete oxidation to its clear and colorless state is shown in Figure 8 (teal trace). The doublet spectrum with peaks of equal intensities at 579.8 and 580.0 nm and equal lifetimes, 258 ± 25 μs, indicates that the reduction-oxidation process induces the formation of bulk quantities of $[(H_2O)_nEu(PW_{11}O_{39})]^{4-}$. Because we thought it likely that the 0.2 M sulfate electrolyte

would form an inner-sphere complex with any Eu(III) that disincorporates from the POMs, an excitation spectrum for a $Eu_2(SO_4)_3$ solution standard was obtained. As evident in Figure 8 (tan trace), the peak maximum for the excitation of $Eu_2(SO_4)_3$ occurs at 579.0 nm, which is well separated from the luminescence of the oxidized solution (teal trace). Therefore, we conclude that Eu(III)-$[SO_4]^{2-}$ complexation,[89,90] does not pertain to the Eu-α-1 system as treated here, see Figure S6, Supporting Information. Nevertheless, other isomeric Eu-POMs, besides $[(H_2O)_nEu(PW_{11}O_{39})]^{4-}$, are likely to contribute to the luminescence of the oxidized solution, Figure 8 (teal trace), as well. In view of uncertainties with multicomponent-lifetime analyses for such a polydisperse mixture, ^{31}P NMR was brought to bear upon the solution speciation.

2.3.4 NMR

A reduced and oxidized replication of the XANES experiment was monitored by ^{31}P NMR. The results of ^{31}P NMR measurements (Table 3 and Supporting Information) (Figure S7)), demonstrate the presence of six POM species in the oxidized solution. These include the original Eu-α-1 complex and the free α-1 ligand as well as one product that results from isomerization and complexation, $[Eu(\alpha\text{-}2\text{-}P_2W_{17}O_{61})_2]^{17-}$, and three products that result from fragmentation and reconstitution, $[(H_2O)_nEu(PW_{11}O_{39})]^{4-}$, $[Eu(PW_{11}O_{39})_2]^{11-}$, and $\alpha\text{-}[P_2W_{18}O_{62}]^{6-}$. In view of the known chemical instabilities of the α-1 ligand,[45] the transformations to the Eu-α-2 and plenary Wells-Dawson anions are not unexpected. It is the formation of the two lacunary Keggin complexes of Eu(III) that are unusual and possibly driven by the combined Eu- and ligand-centered reductive electrochemistry of $[(H_2O)_4Eu(III)(\alpha\text{-}1\text{-}P_2W_{17}O_{61})]^{7-}$.

2.4 Conclusions

The Eu-α-1 POM combines an electroactive lanthanide ion, Eu(III), and an electroactive ligand, $[\alpha\text{-}1\text{-}P_2W_{17}O_{61}]^{10-}$, in a single, heterobinuclear molecular anion. The two redox-active centers involve valence orbitals of dissimilar character—localized 4f-states of Eu and d-band states of W. The prospect of dual redox activity, although not always realized in Eu complexes with other electroactive ligands,[91,92] including POMs,[33,53] is demonstrated here for Eu-α-1, wherein the Eu(III)/Eu(II) couple occurs within the range of electrode potentials that drive the multielectron reduction of the P-W-O anion and the formation of a heteropoly blue species. Whereas the redox chemistry of the α-1 ligand is affected by its complexation with Eu(III), the redox chemistry of Eu is only slightly perturbed by its complexation with the ligand. Namely, for a dilute, 0.25 mM solution of Eu-α-1, the Eu(III)/Eu(II) couple is found at $E_{½}$ = -0.65 V, which although deep within the domain of the W-centered redox processes (the first reduction occurs with $E_{½}$ = -0.33 V) is essentially coincident with the electrode potential for the POM-free Eu(III) ion ($E_{½}$ = -0.63 V) in the same supporting electrolyte of 0.2 M Li_2SO_4 at pH = 3.0. The absence of a significant difference suggests that the energetics of the f-orbital interactions with the LUMO of essentially W d-orbital character are unfavorable and uncooperative, a possible result of insufficient interconnectivity. In this regard, the inner-sphere Eu coordination environment in the solid salt of Eu-α-1 and after its dissolution in the aqueous electrolyte were shown to be the same, consisting of 4 water molecules and the 4 O atoms from the tetradentate ligand with an average Eu-O_8 distance of 2.37–2.38 Å. The fact that the Eu cation is directly exposed to the solvent medium, although ideal for facile water-exchange and electron-transfer at an electrode surface,

may account for its ligand-independent and labile behaviors, wherein the exhaustive, multi-electron reduction of $[(H_2O)_4Eu(III)(\alpha\text{-}1\text{-}P_2W_{17}O_{61})]^{7-}$ to its metastable $[(H_2O)_nEu(II)(\alpha\text{-}1\text{-}P_2W_{17}O_{61})]^{n-}$ species leads to dynamic processes of Eu-disincorporation, cluster isomerization, fragmentation, and reconstitution to four other POMs, including $[Eu(\alpha\text{-}2\text{-}P_2W_{17}O_{61})_2]^{17-}$, $[(H_2O)_nEu(PW_{11}O_{39})]^{4-}$, $[Eu(PW_{11}O_{39})_2]^{11-}$, and $\alpha\text{-}[P_2W_{18}O_{62}]^{6-}$. Despite the apparent stability of the reduced species under conditions and on time scales typical of voltammetric measurements that show evidence of quasi-reversible redox chemistry, the significant instability of the fully-reduced anion following controlled-potential bulk electrolysis leads to irreversible electroanalytical behaviors. A more suitable medium, such as aprotic nonaqueous solvents may improve the stability of the electrolyzed species. In that case, efforts to understand the mechanism of the independent, reductive electrochemistry of the Eu(III) and polyoxotungstates.

Supporting Information Available: Figures S0–S7 and Tables S0 and S1 containing details about cyclic voltammetry, optical luminescence, and NMR spectroscopy.

2.5 Figures

Figure 1. Local environments of Eu(III) (red spheres) in Eu-α-1 (top) and Eu-α-2 (bottom) showing the μ-O atom (open teal blue circles) connectivities with the W atoms in the belt, α-1 sites (striped black circles) and in the cap, α-2 sites (hatched black circles) of the tetradentate ligands.[46] In these two illustrations of the projected structures of 1:1 $[(H_2O)_4Eu(\alpha\text{-}1\text{-}P_2W_{17}O_{61})]^{7-}$ and 1:2 $[Eu(\alpha\text{-}2\text{-}P_2W_{17}O_{61})_2]^{17-}$, which are based upon the structures of the corresponding Lu(III) complexes,[62], the 4 terminal O atoms from H_2O molecules that complete the innermost Eu-O_8 coordination spheres are omitted for clarity, as are the majority of the atoms that constitute the framework structures. For the solid salt and solution of Eu-α-1 (top), the next-nearest interaction with the O atom (teal blue sphere) behind and to the left of the Eu ion as well as the more distant interactions with 4 W (3 striped and 1 hatched black circles) and 4 O (hatched teal blue circles) were refined in the EXAFS data Phosphorus atoms are shown as yellow spheres.

Figure 2. Cyclic voltammograms, ν = 49 mV s^{-1}, of 0.25 mM (left panel) and 5.0 mM (right panel) analytes (a, c) $[\alpha\text{-}1\text{-}P_2W_{17}O_{61}]^{10-}$ (solid line) and $Eu(ClO_4)_3$ (dashed line: left panel 1.0 mM, right panel 5.0 mM)); (b, d) background scan (grey dashed line), Eu-α-1 (solid line), and Y-α-1 (black dashed line) on GR electrodes in 0.2 M Li_2SO_4 electrolyte at pH = 3.0. The data in parts a and c are offset for clarity.

Figure 3. Anodic and cathodic peak current, i_{pa} and i_{pc}, variations of the first redox couple (I, Table 1) with the square roots of scan rates from CVs of 0.25 mM (left panel) and 5.0 mM (right panel) analytes (a, c) $[\alpha1\text{-}P_2W_{17}O_{61}]^{10-}$; (b, d) Eu-α-1 (solid squares

and solid lines) and Y-α-1 (open squares and dashed lines) on GR electrodes in 0.2 M Li_2SO_4 electrolyte at pH = 3.0 and v = 9, 25, 49, and 100 mV s^{-1} (see Supporting Information). The fitted lines are based upon the Randles-Sevcik equation, $i_p = (5.02RT)^{-½}(nF)^{3/2}ACD^{½}v^{½}$ with the conventional symbol meanings.[81] All slopes, which are negative for the i_{pc} response and positive for i_{pa}, and regression coefficients are provided as Supporting Information, Table S0.

Figure 4. Normalized Eu L_3-edge XANES spectra of Eu-α-1 solid salt (solid black line) and its freshly prepared, fully-oxidized 5.0 mM Eu-α-1 solution at rest potential, +0.054 V (dashed black line), in the in 0.2M Li_2SO_4 electrolyte of pH = 3.0; reduced, heteropoly blue solution with the GR electrode polarized at -1.30 V (dashed blue line); and after oxidation at -1.00 V (solid blue line, offset for clarity). The Eu(III) edge peaks at 6.9829 eV have a FWHM of 6.4 eV, and the Eu(II) edge peak at 6.9749 eV has a FWHM of 5.0 eV, consistent with the inverse relationship between linewidth and IR.[57]

Figure 5. Eu L_3-edge $k^3\chi(k)$ EXAFS data (a) and corresponding Fourier transform data (b) for Eu-α-1 solid salt (top, offset for clarity) and its freshly prepared, fully-oxidized 5.0 mM Eu-α-1 solution at rest potential, +0.054 V, (bottom) as described in Figure 4. The solid lines illustrate the experimental data, and the dashed lines show the fits.

Figure 6. (a) Normalized Eu L_3-edge XANES for the 5.0 mM Eu-α-1 solution from one hour after starting electrode polarization at -1.30 V to the final scan some 7 hours later showing the initial reduction of Eu(III) and the subsequent autooxidation of Eu(II) while

under potential control. (b) Time evolution of the Eu(III) valence in Eu-α-1 throughout the bulk electrolysis experiment of part (a).

Figure 7. Eu L_3-edge $k^3\chi(k)$ EXAFS data (a) and corresponding Fourier transform data (b) for the blue solution of Eu-α-1 obtained by oxidation at -1.00 V of the fully reduced 5.0 mM analyte. The solid lines illustrate the experimental data, and the dashed lines show the fit.

Figure 8. $^7F_0 \rightarrow {}^5D_0$ excitation spectrum (λ_{em} = 614 nm) of 47 μM solution of Eu-α-1 in 0.2 M Li_2SO_4 (pH = 3.0) before reduction (pink trace), after reduction (blue trace), and after oxidation (teal trace). The corresponding excitation spectrum for $Eu_2(SO_4)_3$ is shown as the tan trace.

Figure 1

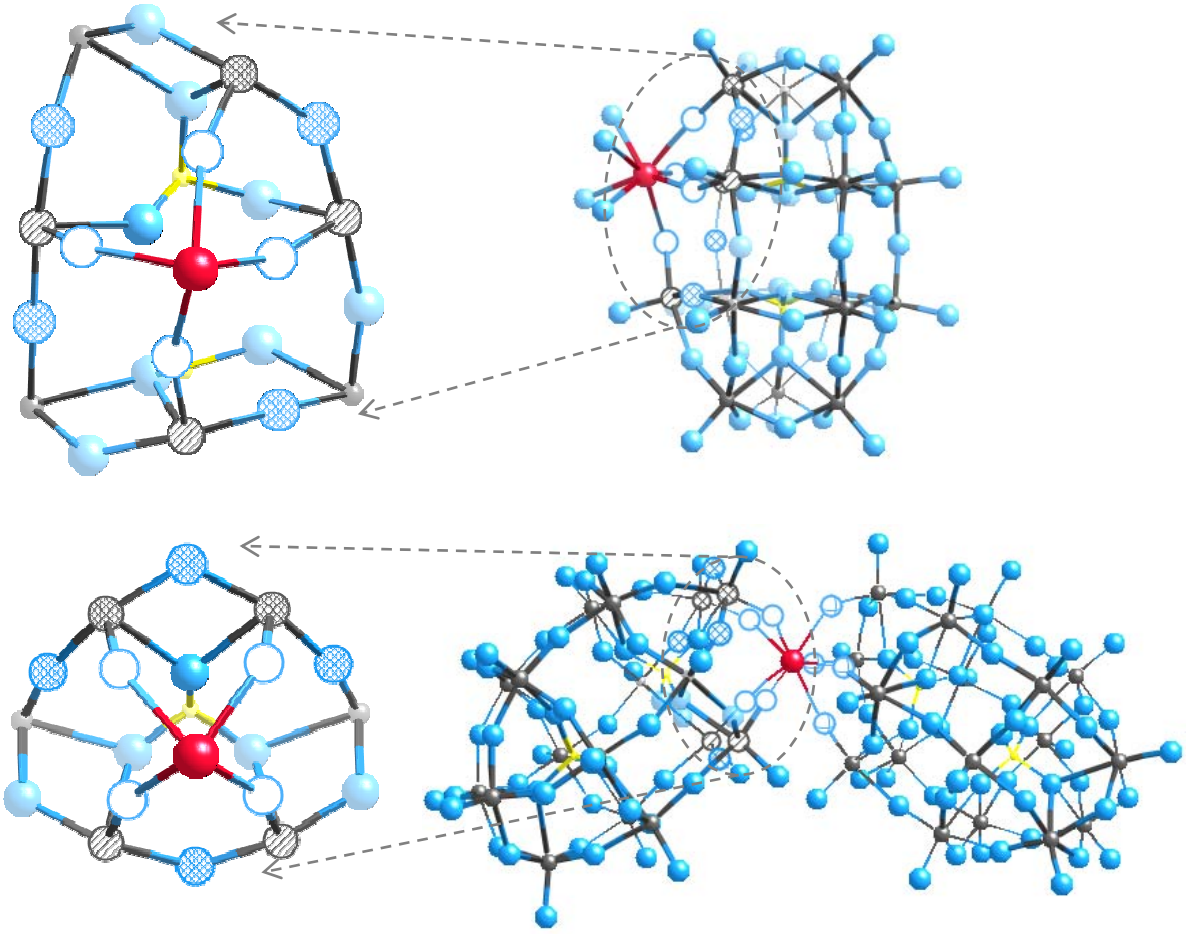

Figure 2

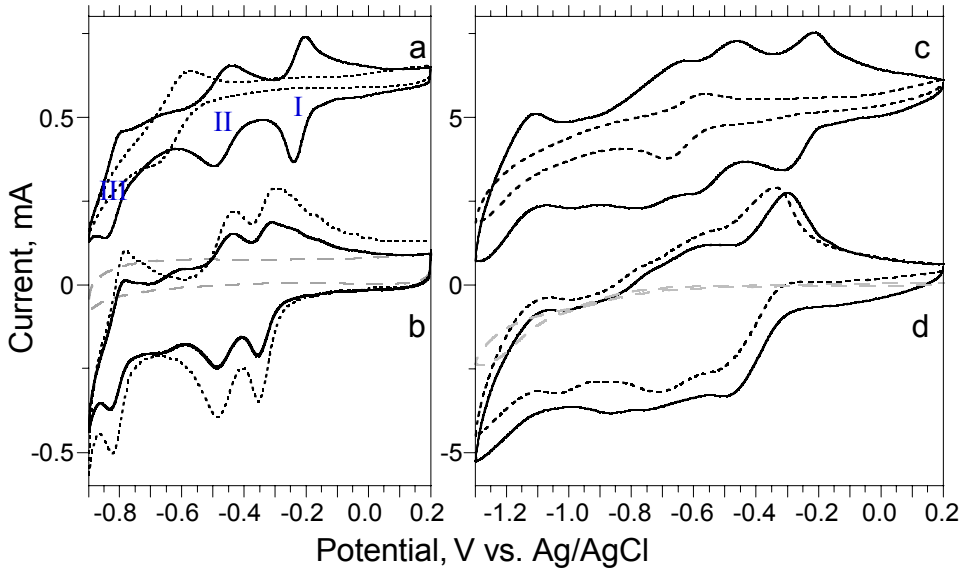
a
b
c
d
I
II
III
0.5
0
-0.5
5
0
-5
Current, mA
-0.8 -0.6 -0.4 -0.2 0.0 0.2
-1.2 -1.0 -0.8 -0.6 -0.4 -0.2 0.0 0.2
Potential, V vs. Ag/AgCl

Figure 3

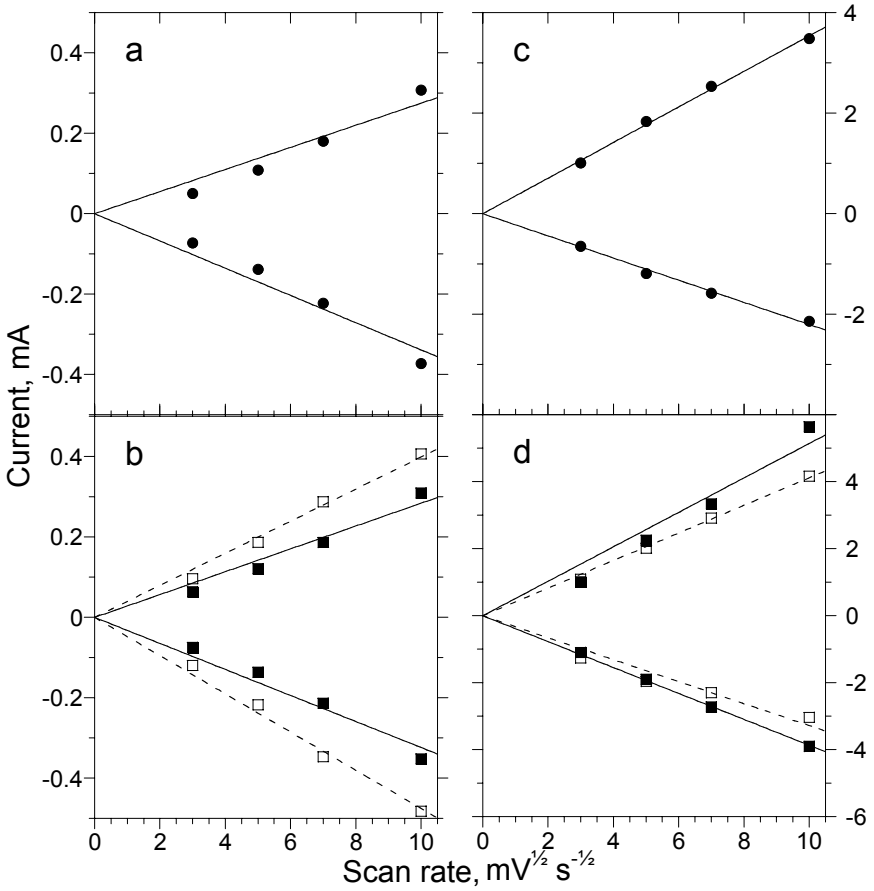

Figure 4

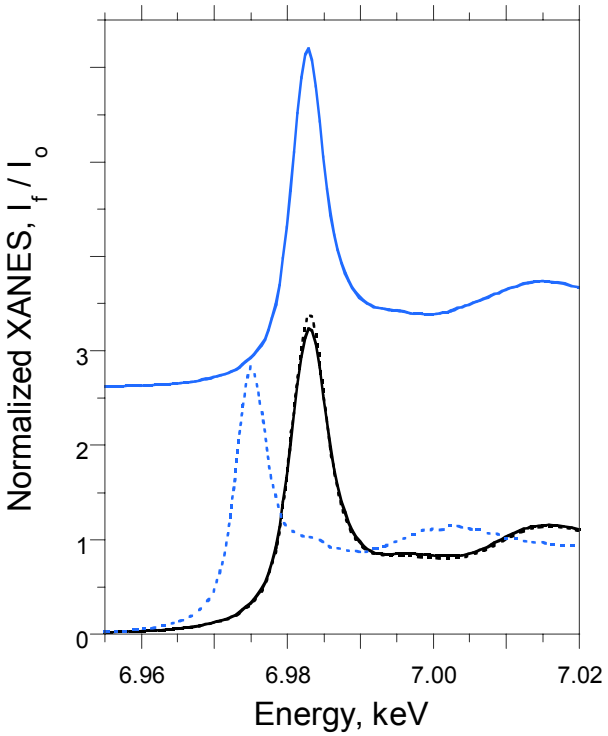

Figure 5

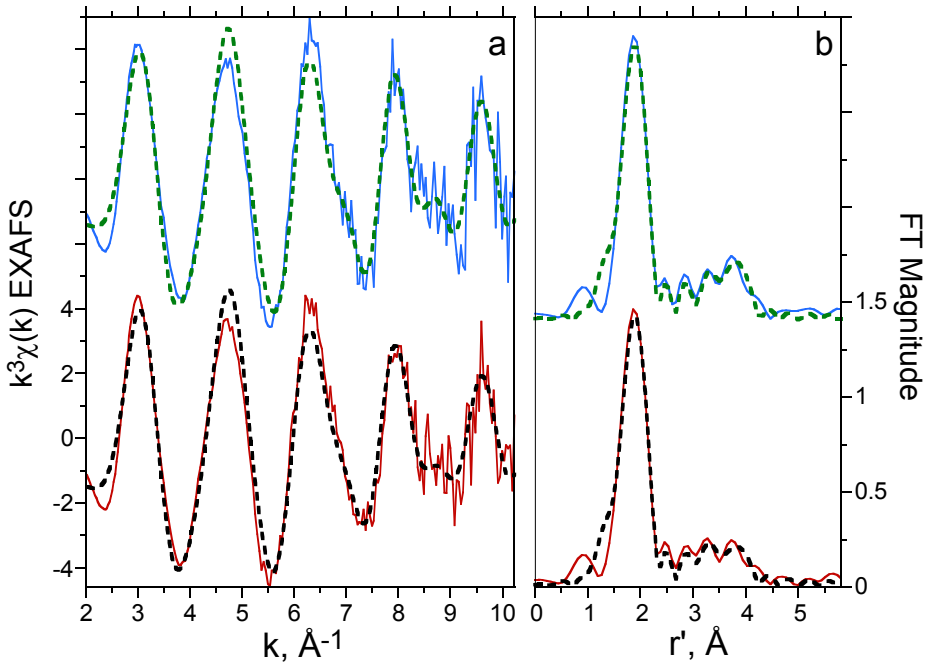

Figure 6a

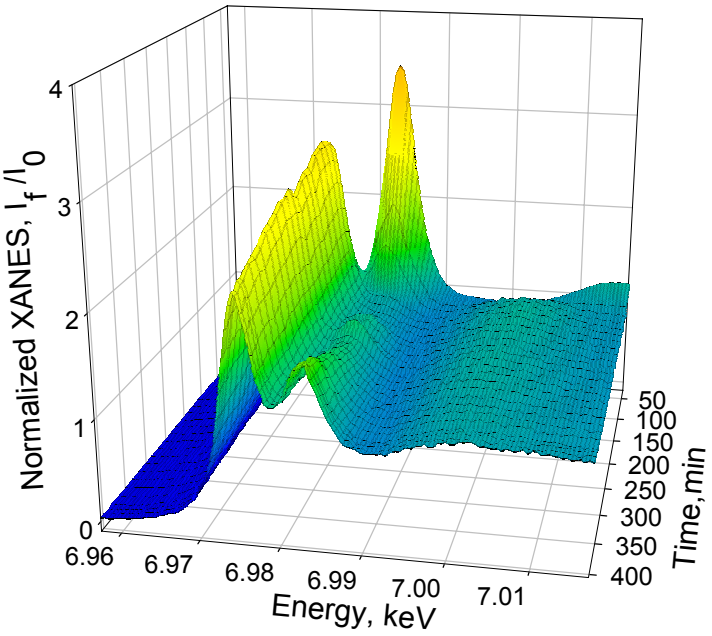

Figure 6b

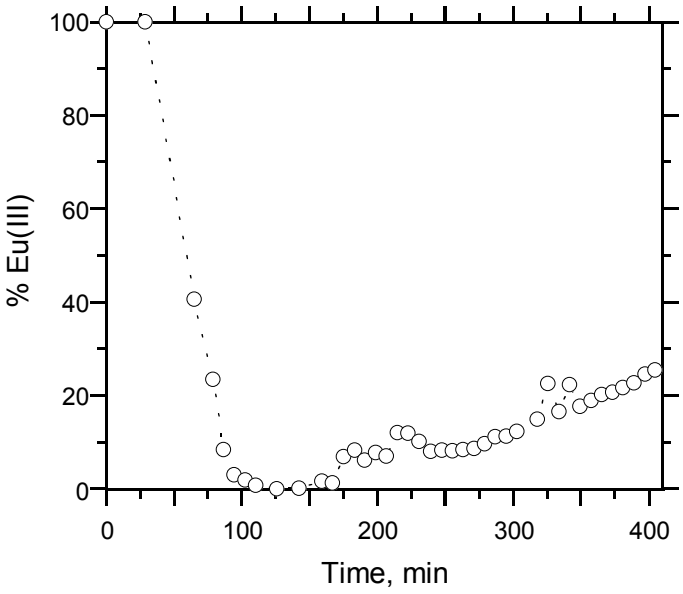

Figure 7

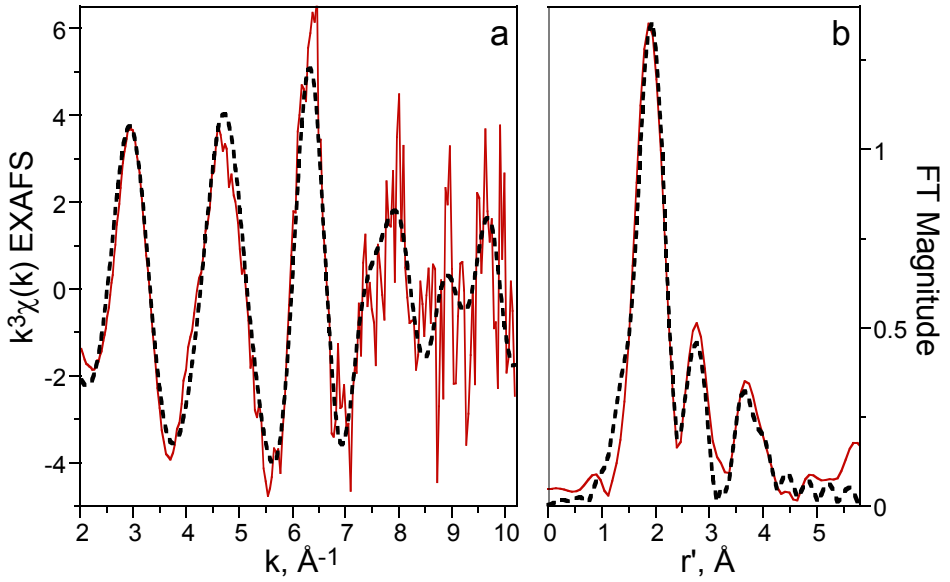

Figure 8

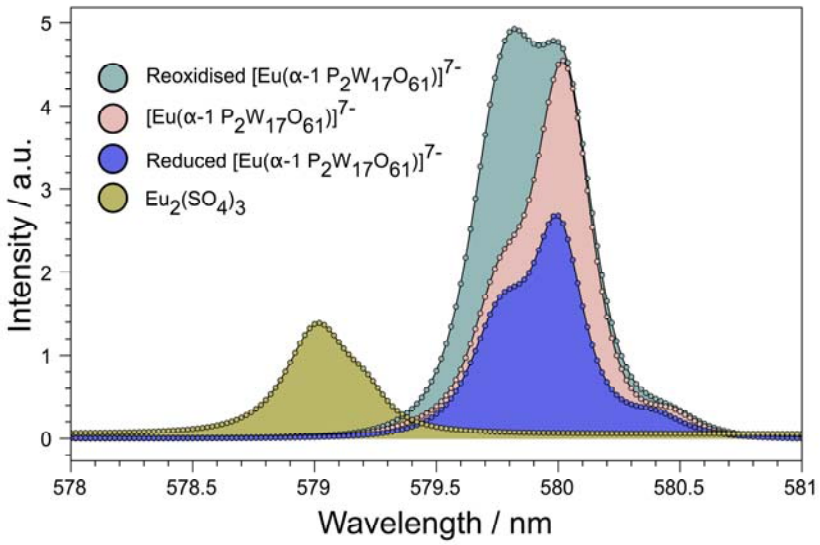

2.6 Tables

Table 1. Peak potentials (± 0.005 V) for the redox couples observed in the cyclic voltammograms of Figure 2 (left panel) for 0.25 mM $[\alpha\text{-}1\text{-}P_2W_{17}O_{61}]^{10-}$, Y-α-1, Eu-α-1,

and 1.0 mM for $Eu(ClO_4)_3$ on GR working electrodes at 49 mV s^{-1}. The peak potentials (± 0.01 V) for the first couple (I) in the CV data for the 5.0 mM analytes (Figure 2, right panel) are also given.

Anion	**Wave**	E_{pc}**[V]**[a]	E_{pa}**[V]**[b]	$E_{½}$**[V]**[c]	ΔE_p**[V]**[d]
——————————0.25 mM——————————					
$[\alpha\text{-}1\text{-}P_2W_{17}O_{61}]^{10-}$	I	-0.241	-0.204	-0.223	0.037
	II	-0.502	-0.436	-0.469	0.066
	III	-0.836	-0.783	-0.810	0.053
Y-α-1	I	-0.354	-0.298	-0.326	0.056
	II	-0.485	-0.431	-0.458	0.054
	III	-0.825	-0.780	-0.803	0.045
Eu-α-1	I	-0.356	-0.311	-0.334	0.045
	II	-0.487	-0.436	-0.462	0.051
	III	-0.675	-0.617	-0.646	0.058
	IV	-0.831	-0.782	-0.807	0.049
$Eu(ClO_4)_3$	I	-0.677	-0.572	-0.625	0.105
——————————5.0 mM——————————					
$[\alpha\text{-}1\text{-}P_2W_{17}O_{61}]^{10-}$	I	-0.32	-0.22	-0.27	0.10
Y-α-1	I	-0.49	-0.34	-0.42	0.15
Eu-α-1	I	-0.50	-0.30	-0.40	0.20
$Eu(ClO_4)_3$	I	-0.69	-0.57	-0.63	0.12

[a] E_{pc} is the electrode potential of peaks with cathodic current. [b] E_{pa} is the electrode potential of peaks with anodic current. [c] $E_{½} = (E_{pc} + E_{pa})/2$. [d] $\Delta E_p = E_{pa} - E_{pc}$.

Table 2. Results of curve-fitting analysis of the Eu L_3-edge $k^3\chi(k)$ EXAFS of Figures 5 and 7.[a]

Sample	**Shell**	**CN**[b]	***r*,**[c] **Å**	σ^2,[d] **Å**^{2}	ΔE_0 [e]
Solid salt Eu-α-1	Eu-O	7.6(10)	2.37(1)	0.009(2)	-0.2
	Eu-O	1	3.36(7)	0.004(9)	/[f]
	Eu-W	4	3.74(2)	0.009(3)	/
	Eu-O	4	4.4(1)	0.008(9)	/
Original Eu-α-1 solution	Eu-O	7.8(10)	2.38(1)	0.009(2)	-0.03
	Eu-O	1	3.37(9)	0.008(12)	/
	Eu-W	4	3.74(2)	0.011(3)	/
	Eu-O	4	4.4 (1)	0.02(2)	/
Oxidized Eu-α-1 solution	Eu-O	9.0(10)	2.42(2)	0.012(3)	1.4
obtained after reduction	Eu-P	3.9(9)	3.16(3)	0.013(9)	/
	Eu-P	1.8(8)	4.15(3)	0.001(9)	/

[a] The number in the parentheses represent the estimated standard deviations (3σ) obtained from the least-squares fits. [b] Coordination number. [c] Interatomic distance. [d] The Debye-Waller factor, the root-mean-square deviation of the average Eu-X bond length, for X ≡ O, P, W. [e] The energy difference between the experimental and theoretical values of E_0. [f] Parameter fixed to value in column above.

Table 3. ^{31}P NMR data for original Eu-α-1 solution (5.0 mM) before reduction and for the oxidized Eu-α-1 solution obtained after reduction to the heteropoly blue species with an electrode potential of -1.30 V. ^{31}P spectra were referenced to 85% H_3PO_4.

Solution	**Species**	**^{31}P NMR data (δ, ppm)**
Original Eu-α-1	$[(H_2O)_4Eu(\alpha\text{-}1\text{-}P_2W_{17}O_{61})]^{7-}$	6.42, -11.41
Oxidized Eu-α-1	$[(H_2O)_4Eu(\alpha\text{-}1\text{-}P_2W_{17}O_{61})]^{7-}$	6.687, -11.34
	$[(H_2O)_nEu(PW_{11}O_{39})]^{4-}$	5.413[27]
	$[Eu(PW_{11}O_{39})_2]^{11-}$	0.416[27]
	$[Eu(\alpha\text{-}2\text{-}P_2W_{17}O_{61})_2]^{17-}$	3.747, -12.711[40]
	$[\alpha\text{-}1\text{-}P_2W_{17}O_{61}]^{10-}$	-8.54, -12.853[45]
	$\alpha\text{-}[P_2W_{18}O_{62}]^{6-}$	-12.467

2.7 References

1. Cronin, L.; Beugholt, C.; Krickemeyer, E.; Schmidtmann, M.; Bogge, H.; Kogerler, P.; Luong, T. K. K.; Muller, A. *Angew. Chem., Int. Ed.* **2002,** *41,* 2805-2808.
2. Fukaya, K.; Yamase, T. *Angew. Chem., Int. Ed.* **2003,** *42,* 654-658.
3. Howell, R. C.; Perez, F. G.; Jain, S.; Horrocks, W. D.; Rheingold, A. L.; Francesconi, L. C. *Angew. Chem., Int. Ed.* **2001,** *40,* 4031-4034.
4. Muller, A.; Beugholt, C.; Bogge, H.; Schmidtmann, M. *Inorg. Chem.* **2000,** *39,* 3112-3113.
5. Muller, A.; Peters, F.; Pope, M. T.; Gatteschi, D. *Chem. Rev.* **1998,** *98,* 239-272.
6. Ostuni, A.; Pope, M. T. *Comptes Rendus Acad. Sci. Ser. II C* **2000,** *3,* 199-204.
7. Wassermann, K.; Dickman, M. H.; Pope, M. T. *Angew. Chem., Int. Ed.* **1997,** *36,* 1445-1448.
8. Zimmermann, M.; Belai, N.; Butcher, R. J.; Pope, M. T.; Chubarova, E. V.; Dickman, M. H.; Kortz, U. *Inorg. Chem.* **2007,** *46,* 1737-1740.
9. Bassil, B. S.; Dickman, M. H.; Von Kammer, B.; Kortz, U. *Inorg. Chem.* **2007,** *46,* 2452-2458.
10. Belai, N.; Sadakane, M.; Pope, M. T. *J. Am. Chem. Soc.* **2001,** *123,* 2087-2088.
11. Copping, R.; Gaunt, A. J.; May, I.; Sarsfield, M. J.; Collison, D.; Helliwell, M.; Denniss, I. S.; Apperley, D. C. *Dalton Trans.* **2005,** 1256-1262.
12. Lu, Y. W.; Keita, B.; Nadjo, L. *Polyhedron* **2004,** *23,* 1579-1586.
13. Mialane, P.; Lisnard, L.; Mallard, A.; Marrot, J.; Antic-Fidancev, E.; Aschehoug, P.; Vivien, D.; Secheresse, F. *Inorg. Chem.* **2003,** *42,* 2102-2108.
14. Ozeki, T.; Yamase, T. *Acta Crystallogr. Sect. B-Struct. Commun.* **1994,** *50,* 128-134.

15. Sadakane, M.; Dickman, M. H.; Pope, M. T. *Angew. Chem., Int. Ed.* **2000,** *39,* 2914-2916.

16. Shiozaki, R.; Inagaki, A.; Nishino, A.; Nishio, E.; Maekawa, M.; Kominami, H.; Kera, Y. *J. Alloys Compd.* **1996,** *234,* 193-198.

17. Sousa, F. L.; Ferreira, A.; Ferreira, R. A. S.; Cavaleiro, A. M. V.; Carlos, L. D.; Nogueira, H. I. S.; Rocha, J.; Trindade, T. *J. Nanosci. Nanotechnol.* **2004,** *4,* 214-220.

18. Yamase, T. *Chem. Rev.* **1998,** *98,* 307-326.

19. Yamase, T.; Kobayashi, T.; Sugeta, M.; Naruke, H. *J. Phys. Chem. A* **1997,** *101,* 5046-5053.

20. Boglio, C.; Lemiere, G.; Hasenknopf, B.; Thorimbert, S.; Lacote, E.; Malacria, M. *Angew. Chem., Int. Ed.* **2006,** *45,* 3324-3327.

21. Boglio, C.; Lenoble, G.; Duhayon, C.; Hasenknopf, B.; Thouvenot, R.; Zhang, C.; Howell R., C.; Burton-Pye B., P.; Francesconi L., C.; Lacote, E.; Thorimbert, S.; Malacria, M.; Afonso, C.; Tabet, J.-C. *Inorg. Chem.* **2006,** *45,* 1389-1398.

22. Keita, B.; Nadjo, L. In *Encyclopedia of Electrochemistry*; Scholz, F., Pickett, C. J., Eds.; Wiley-VCH: Weiheim, 2006; Vol. 7b; pp 607-700.

23. Weinstock, I. A. *Chem. Rev.* **1998,** *98,* 113-170.

24. Guldi, D. M.; Rahman, G. M. A.; Marczak, R.; Matsuo, Y.; Yamanaka, M.; Nakamura, E. *J. Am. Chem. Soc.* **2006,** *128,* 9420-9427.

25. Matsuo, Y.; Muramatsu, A.; Kamikawa, Y.; Kato, T.; Nakamura, E. *J. Am. Chem. Soc.* **2006,** *128,* 9586-9587.

26. Park, B. K.; Lee, G.; Kim, K. H.; Kang, H.; Lee, C. Y.; Miah, M. A.; Jung, J.; Han, Y. K.; Park, J. T. *J. Am. Chem. Soc.* **2006,** *128,* 11160-11172.

27. Zhang, C.; Howell, R. C.; Scotland, K. B.; Perez, F. G.; Todaro, L.; Francesconi, L. C. *Inorg. Chem.* **2004,** *43,* 7691-7701.

28. Zhang, C.; Howell, R. C.; McGregor, D.; Bensaid, L.; Rahyab, S.; Nayshtut, M.; Lekperic, S.; Francesconi, L. C. *C. R. Chim.* **2005,** *8,* 1035-1044.

29. Fukaya, K.; Yamase, T. *J. Alloy. Compd.* **2006,** *408,* 915-920.

30. Bartis, J.; Dankova, M.; Lessmann, J. J.; Luo, Q.-H.; De Horrocks, W., Jr.; Francesconi, L. C. *Inorg. Chem.* **1999,** *38,* 1042-1053.

31. Ozeki, T.; Yamase, T.; Naruke, H.; Sasaki, Y. *Inorg. Chem.* **1994,** *33,* 409-410.

32. Antonio, M. R.; Soderholm, L. *J. Cluster Sci.* **1996,** *7,* 585-591.

33. Antonio, M. R.; Soderholm, L.; Jennings, G.; Francesconi, L. C.; Dankova, M.; Bartis, J. *J. Alloys Compd.* **1998,** *275-277,* 827-830.

34. Soderholm, L.; Antonio, M. R.; Skanthakumar, S.; Williams, C. W. *J. Am. Chem. Soc.* **2002,** *124,* 7290-7291.

35. Antonio, M. R.; Soderholm, L.; Williams, C. W.; Ullah, N.; Francesconi, L. C. *Dalton Trans.* **1999,** 3825-3830.

36. Chiang, M. H.; Antonio, M. R.; Soderholm, L. *Dalton Trans.* **2004,** 3562-3567.

37. Fernandez, J. A.; Lopez, X.; Bo, C.; de Graaft, C.; Baerends, E. J.; Poblet, J. M. *J. Am. Chem. Soc.* **2007,** *129,* 12244-12253.

38. Bartis, J.; Kunina, Y.; Blumenstein, M.; Francesconi, L. C. *Inorg. Chem.* **1996,** *35,* 1497-1501.

39. Bartis, J.; Sukal, S.; Dankova, M.; Kraft, E.; Kronzon, R.; Blumenstein, M.; Francesconi, L. C. *Dalton Trans.* **1997,** 1937-1944.

40. Luo, Q.; Howell, R. C.; Bartis, J.; Dankova, M.; Horrocks, W. D., Jr.; Rheingold, A. L.; Francesconi, L. C. *Inorg. Chem.* **2002,** *41,* 6112-6117.

41. Lenoble, G.; Hasenknopf, B.; Thouvenot, R. *J. Am. Chem. Soc.* **2006,** *128,* 5735-5744.

42. Kozik, M.; Baker, L. C. W. *J. Am. Chem. Soc.* **1990,** *112,* 7604-7611.

43. Kozik, M.; Hammer, C. F.; Baker, L. C. W. *J. Am. Chem. Soc.* **1986,** *108,* 2748-2749.

44. Contant, R.; Abbessi, M.; Canny, J.; Belhouari, A.; Keita, B.; Nadjo, L. *Inorg. Chem.* **1997,** *36,* 4961-4967.

45. Contant, R.; Richet, M.; Lu, Y. W.; Keita, B.; Nadjo, L. **2002,** 2587-2593.

46. Keita, B.; Belhouari, A.; Nadjo, L.; Contant, R. *J. Electroanal. Chem.* **1998,** *442,* 49-57.

47. Keita, B.; Girard, F.; Nadjo, L.; Contant, R.; Canny, J.; Richet, M. *J. Electroanal. Chem.* **1999,** *478,* 76-82.

48. Keita, B.; Lu, Y. W.; Nadjo, L.; Contant, R. *Eur. J. Inorg. Chem.* **2000,** 2463-2471.

49. Keita, B.; Mbomekalle, I. M.; Nadjo, L.; Contant, R. *Eur. J. Inorg. Chem.* **2002,** 473-479.

50. Keita, B.; Jean, Y.; Levy, B.; Nadjo, L.; Contant, R. *New J. Chem.* **2002,** *26,* 1314-1319.

51. Lopez, X.; Bo, C.; Poblet, J. M. *J. Am. Chem. Soc.* **2002,** *124,* 12574-12582.

52. Lopez, X.; Bo, C.; Poblet, J. M. *Inorg. Chem.* **2003,** *42,* 2634-2638.

53. Xi, X. D.; Wang, G.; Liu, B. F.; Dong, S. J. *Electrochim. Acta* **1995,** *40,* 1025-1029.

54. Contant, R. Inorganic Syntheses; Ginsberg, A. P., Ed.; Wiley-Interscience: New York, 1990; Vol. 27; pp 104-107.

55. Beno, M. A.; Engbretson, M.; Jennings, G.; Knapp, G. S.; Linton, J.; Kurtz, C.; Rütt, U.; Montano, P. A. *Nucl. Instrum. Methods Phys. Res. A* **2001,** *467-468,* 699-702.

56. Soderholm, L.; Antonio, M. R.; Williams, C.; Wasserman, S. R. *Anal. Chem.* **1999,** *71,* 4622-4628.

57. Antonio, M. R.; Soderholm, L.; Song, I. *J. Appl. Electrochem.* **1997,** *27,* 784-792.

58. Gannaz, B.; Antonio, M. R.; Chiarizia, R.; Hill, C.; Cote, G. *Dalton Trans.* **2006,** 4553-4562.

59. George, G. N.; Hilton, J.; Temple, C.; Prince, R. C.; Rajagopalan, K. V. *J. Am. Chem. Soc.* **1999,** *121,* 1256-1266.

60. Ressler, T. *J. Phys. IV* **1997,** *7,* 269-270.

61. Rehr, J. J.; Albers, R. C. *Rev. Mod. Phys.* **2000,** *72,* 621-654.

62. Luo, Q. H.; Howell, R. C.; Dankova, M.; Bartis, J.; Williams, C. W.; Horrocks, W. D.; Young, V. G.; Rheingold, A. L.; Francesconi, L. C.; Antonio, M. R. *Inorg. Chem.* **2001,** *40,* 1894-1901.

63. Stern, E. A. *Phys. Rev. B* **1993,** *48,* 9825-9827.

64. Nwe, K.; Richard, J. P.; Morrow, J. R. *Dalton Trans.* **2007,** 5171-5178.

65. Contant, R.; Ciabrini, J. P. *J. Chem. Res. (S)* **1977,** 222.

66. Pope, M. T. In *Mixed-Valence Compounds. Theory and Applications in Chemistry, Physics, Geology, and Biology;* Brown, D.B., Ed.; D.Reidel: Dordrecht, 1980; pp 365-386

67. Papaconstantinou, E.; Pope, M. T. *Inorg. Chem.* **1970,** *9,* 667-669.

68. Varga, G. M., Jr.; Papaconstantinou, E.; Pope, M. T. *Inorg. Chem.* **1970,** *9,* 662-667.

69. Pope, M. T.; Papaconstantinou, E. *Inorg. Chem.* **1967,** *6,* 1147-1152.

70. Bratsch, S. G. *J. Phys. Chem. Ref. Data* **1989,** *18,* 1-21.

71. Wadsworth, E.; Duke, F. R.; Goetz, C. A. *Anal. Chem.* **1957,** *29,* 1824-1825.

72 Keita, B.; Nadjo, L. *Mater. Chem. Phys.* **1989,** *22,* 77-103.

73 Maeda, K.; Katano, H.; Osakai, T.; Himeno, S.; Saito, A. *J. Electroanal. Chem.* **1995,** *389,* 167-173.

74. Osakai, T.; Katano, H.; Maeda, K.; Himeno, S.; Saito, A. *Bull. Chem. Soc. Jpn.* **1993,** *66,* 1111-1115.

75. Osakai, T.; Maeda, K.; Ebina, K.; Hayamizu, H.; Hoshino, M.; Muto, K.; Himeno, S. *Bull. Chem. Soc. Jpn.* **1997,** *70,* 2473-2481.

76. Grigoriev, V. A.; Cheng, D.; Hill, C. L.; Weinstock, I. A. *J. Am. Chem. Soc.* **2001,** *123,* 5292-5307.

77. Grigoriev, V. A.; Hill, C. L.; Weinstock, I. A. *J. Am. Chem. Soc.* **2000,** *122,* 3544-3545.

78 López, X.; Nieto-Draghi, C.; Bo, C.; Avalos, J. B.; Poblet, J. M. *J. Phys. Chem. A* **2005,** *109,* 1216-1222.

79 Toth, J. E.; Anson, F. C. *J. Electroanal. Chem.* **1988,** *256,* 361-370.

80 Weinstock, I. A.; Grigoriev, V. A.; Cheng, D.; Hill, C. L. In *Polyoxometalate Chemistry for Nano-Composite Design*; Yamase, T., Pope, M. T., Eds.; Kluwer: New York, 2002; pp 103-127.

81 Bard, A. J.; Faulkner, L. R. *Electrochemical Methods: Fundamentals and Applications*, 2nd ed.; J. Wiley: New York, 2001.

82 Rohler, J. In *Handbook on the Physics and Chemistry of Rare Earths*; Gschneidner, K. A., Jr, Eyring, L., Hufner, S., Ed.; North-Holland: Amsterdam, 1987; Vol. 10 - High Energy Spectroscopy; pp 453-545.

83 Shannon, R. D. *Acta Crystallogr. Sect. A* **1976,** *32,* 751-767.

84. Moreau, G.; Helm, L.; Purans, J.; Merbach, A. E. *J. Phys. Chem. A* **2002,** *106,* 3034-3043.

85. Rakovan, J.; Newville, M.; Sutton, S. *Am. Miner.* **2001,** *86,* 697-700.

86. Mulazzani, Q. G.; Venturi, M.; Ballardini, R.; Gandolfi, M. T.; Balzani, V. *Isr. J. Chem.* **1985,** *25,* 183-188.

87. Kolitsch, U.; Holtstam, D. *Eur. J. Mineral.* **2004,** *16,* 117-126.

88. Wickleder, M. S. *Chem. Rev.* **2002,** *102,* 2011-2087.

89. Tanaka, F.; Yamashita, S. *Inorg. Chem.* **1984,** *23,* 2044-2046.

90. Vercouter, T.; Amekraz, B.; Moulin, C.; Giffaut, E.; Vitorge, P. *Inorg. Chem.* **2005,** *44,* 7570-7581.

91. Kido, J.; Okamoto, Y. *Chem. Rev.* **2002,** *102,* 2357-2368.

92. Richter, M. M.; Bard, A. J. *Anal. Chem.* **1996,** *68,* 2641-2650.

2.8 Supporting Information

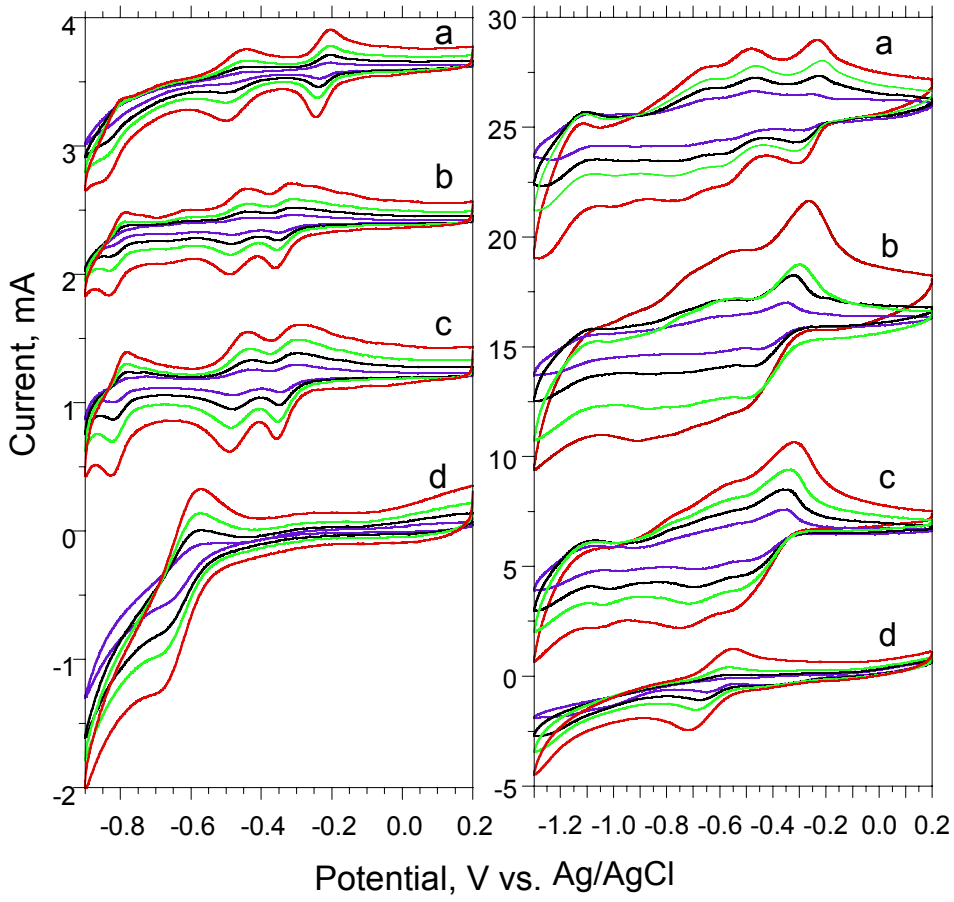

Figure S0. Cyclic voltammograms measured at the scan rates (a) 9 (blue line) (b) 25 (black line) (c) 49 (green line), and (d)100 mV s^{-1} (red line) for (a) $[\alpha\text{-1-}P_2W_{17}O_{61}]^{10-}$, (b) Eu-α-1, (c) Y-α-1, and (d) $Eu(ClO_4)_3$ in 0.2 M Li_2SO_4 aqueous electrolyte solution of pH = 3.0 by using GR working electrodes. The analyte concentrations are 0.25 (left panel) and 5.0 mM (right panel) for (a), (b) and (c); 1.0 (left panel) and 5.0 mM (right panel) for (d).

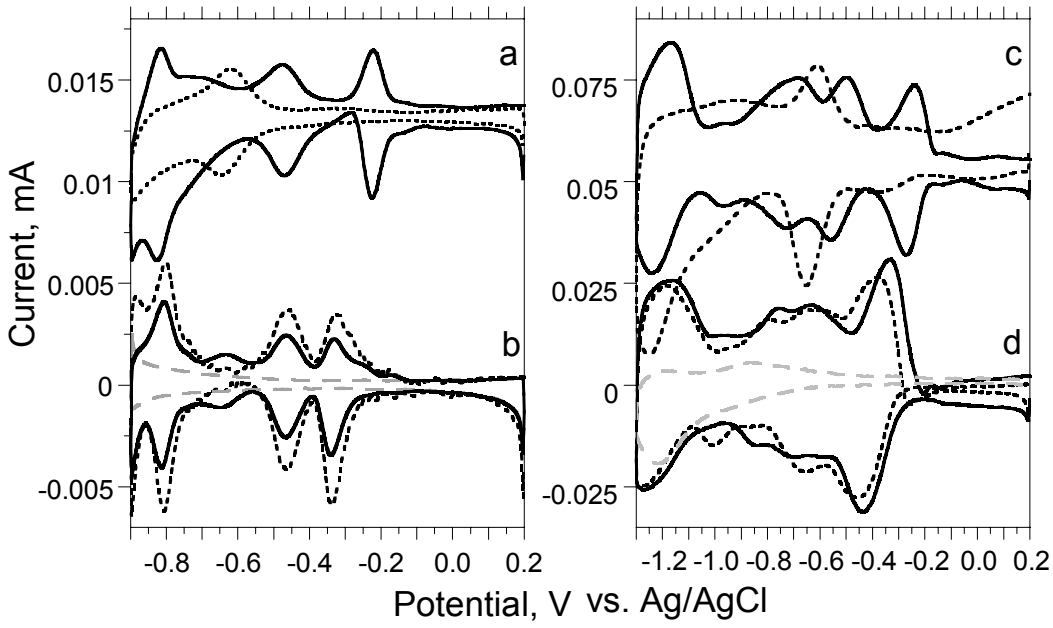

Figure S1. Semidifferential data of CVs of $[\alpha\text{-1-}P_2W_{17}O_{61}]^{10-}$ ligand, $Eu(ClO_4)_3$ and the $[Eu/Y(\alpha\text{-1-}P_2W_{17}O_{61})^{7-}]$ complexes, ν = 49 mV s^{-1}. (a) $[\alpha\text{-1-}P_2W_{17}O_{61}]^{10-}$ (solid line, 0.25 mM) and $Eu(ClO_4)_3$ (dashed line, 1.0mM); (c) $[\alpha\text{-1-}P_2W_{17}O_{61}]^{10-}$ (solid line,5.0 mM) and $Eu(ClO_4)_3$ (dashed line, 5.0 mM) (b) semidifferential data of CVs: background scan (grey dashed line), Eu-α-1, 0.25 mM (solid line), and Y-α-1, 0.25 mM (black dashed line) (d) semidifferential data: background scan (grey dashed line), Eu-α-1, (5.0 mM, solid line), and Y-α-1 (5.0 mM , black dashed line). Data for a, b, c, and d measured on GR electrodes in 0.2 M Li_2SO_4 electrolyte at pH = 3.0. The data in parts a and c are offset for clarity.

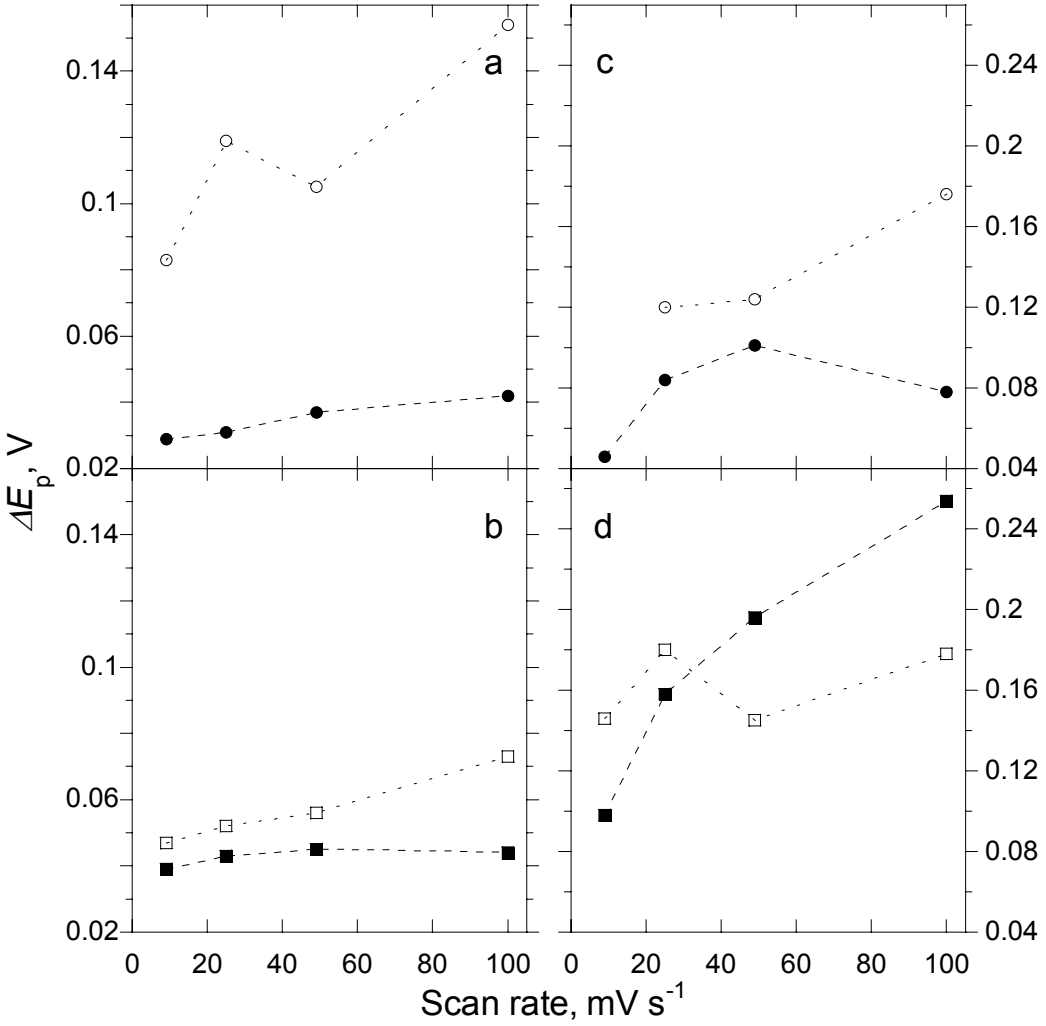

Figure S2. Peak separations, $\Delta E_p = E_{pa} - E_{pc}$, of the first redox couple (I) obtained from CV and their variations with scan rates, v = 9, 25, 49, and 100 mV s^{-1}. (a) 0.25 mM [α-1-$P_2W_{17}O_{61}]^{10-}$ (solid circles) and 1.0 mM $Eu(ClO_4)_3$ (open circles). (c) 5.0 mM [α-1-$P_2W_{17}O_{61}]^{10-}$ (solid circles) and 5.0 mM $Eu(ClO_4)_3$ (open circles). (b) Eu-α-1 (0.25 mM, solid squares) and Y-α-1 (0.25 mM, open squares). (d) Eu-α-1 (5.0 mM, solid squares) and Y-α-1 (5.0 mM, open squares). All data are measured on GR electrodes in 0.2 M Li_2SO_4 electrolyte at pH = 3.0.

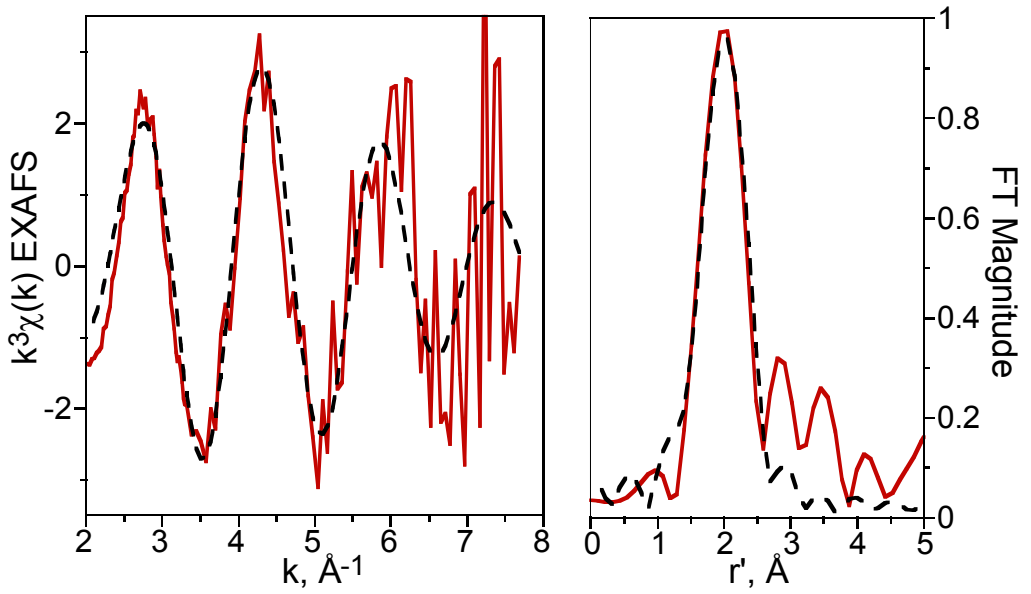

Figure S3. The experimental (red lines) Eu L_3-edge fluorescence EXAFS, $k^3\chi(k)$ left panel, and the Fourier transform data, right panel (without phase shift correction). The single peak in the FT data is attributed to O atoms in the immediate environment about Eu(II) in the multi-electron reduced Eu(II)-α-1 complex anion. Its metastable nature, particularly with regard to the rapid autooxidation of Eu(II), precludes the acquisition of higher-quality EXAFS spectra. Nevertheless, these data are sufficient for a conservative, single shell fit with 4 parameters. The best fit (black dashed lines) results exhibit good correspondence with the primary data and indicate that there are 7.7 ± 1.0 O atoms with an average Eu-O distance of 2.55(4) Å, a Debye-Waller factor, σ^2, 0.017(8) Å^2, and a ΔE_0 of 0.1(7) eV.

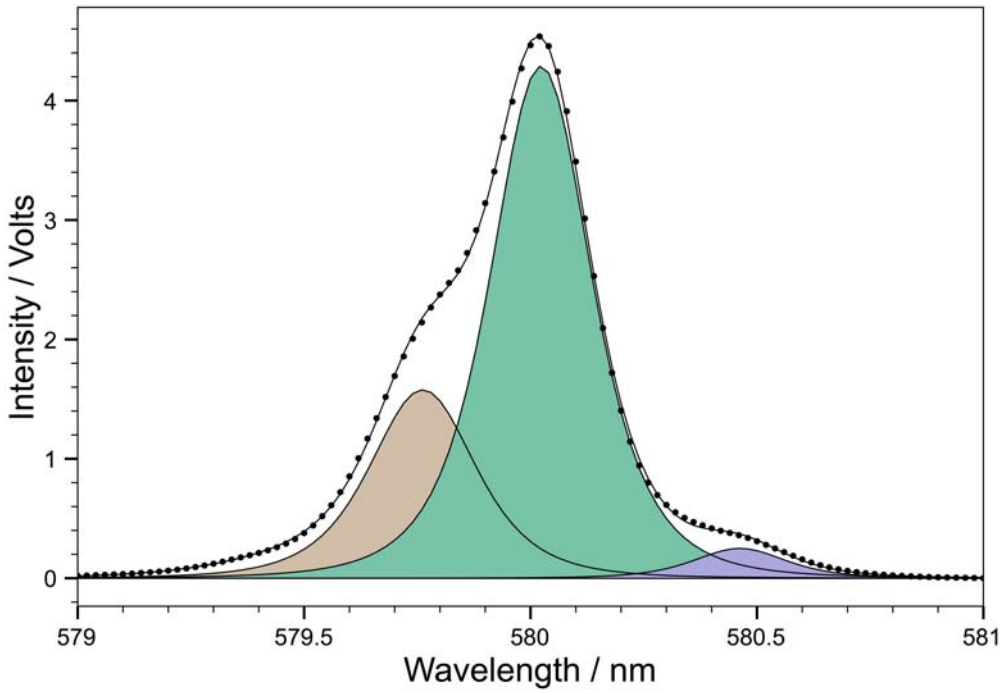

Figure S4. $^{7}F_0 \rightarrow {}^{5}D_0$ excitation spectrum of $[(H_2O)_4Eu(\alpha\text{-}1\text{-}P_2W_{17}O_{61})]^{7-}$ in 0.2 M Li_2SO_4 at pH = 3.0. Dots are observed intensity; solid line is the line of best fit. Each peak was fit to a Gauss-Lorentzian algorithm.

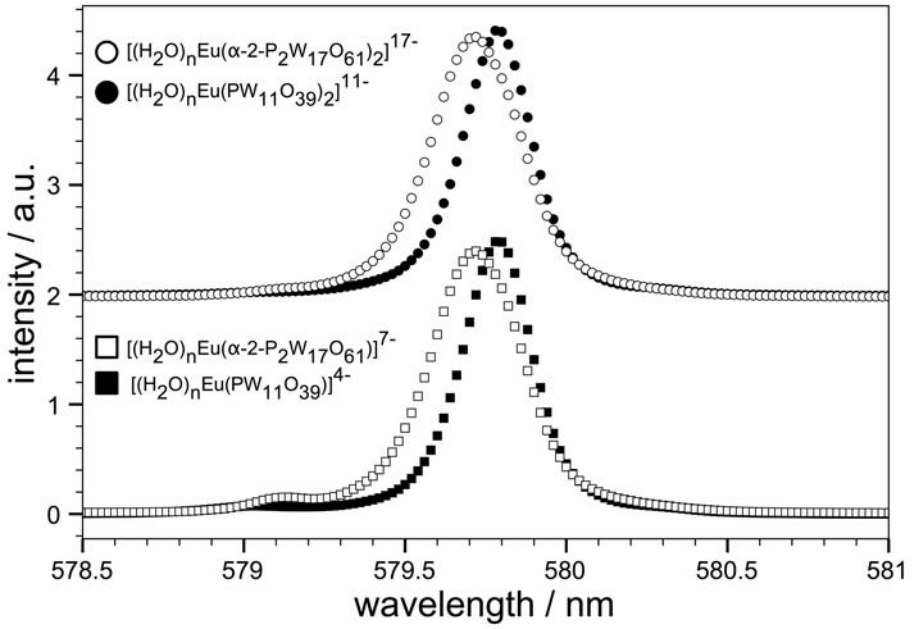

Figure S5. $^7F_0 \rightarrow {}^5D_0$ excitation spectra of 0.5 mM solutions of $[(H_2O)_nEu(PW_{11}O_{39})]^{4-}$, $[(H_2O)_nEu(PW_{11}O_{39})_2]^{11-}$, $[(H_2O)_nEu(\alpha\text{-}2\text{-}P_2W_{17}O_{61})]^{7-}$ and $[(H_2O)_nEu(\alpha\text{-}2\text{-}P_2W_{17}O_{61})_2]^{17-}$ in 0.2 M Li_2SO_4 at pH = 3.0. The 1:2 complexes have been offset for clarity.

Analysis of the $[\alpha\text{-}2\text{-}P_2W_{17}O_{61}]^{10-}$ and $[PW_{11}O_{39}]^{7-}$ complexes with Eu(III) show interesting discoveries regarding their own speciation. The $[\alpha\text{-}2\text{-}P_2W_{17}O_{61}]^{10-}$ complexes have been studied before in solution and have marked concentration dependent speciation. Here, the concentration is such that each species should have distinct differences in their excitation shifts, but the 1:2 complexes are not seen (or are in a very small concentration), this highlights a profound pH effect on the speciation where the 1:2 complexes dissociate upon dissolution in aqueous solutions at a pH of 3.0. The peak maxima for the $[\alpha\text{-}2\text{-}P_2W_{17}O_{61}]^{10-}$ and $[PW_{11}O_{39}]^{7-}$ complexes are very similar which comments on their isostructural similarities. $[PW_{11}O_{39}]^{7-}$ and $[\alpha\text{-}2\text{-}P_2W_{17}O_{61}]^{10-}$ POMs share the same local

structure around the vacancy site in which the lanthanide can bind. In theory, the total charge of the anion has a large nephelauxetic effect on the shift of the europium excitation spectrum.[1] The formal charges on the ligands go from -10 to -7 and the shifts are almost indistinguishable ($\Delta\lambda_{max}$ = 0.065 nm) because the local coordination environment is exceptionally similar and the number of coordinated water molecules is identical. What is unexpected its that the $^7F_0 \rightarrow {}^5D_0$ transition for $[(H_2O)_nEu(PW_{11}O_{39})]^{4-}$ is more red shifted than that of $[(H_2O)_nEu(\alpha\text{-}2\text{-}P_2W_{17}O_{61})]^{7-}$ which can be attributed to differences in the vacancy site basicities, i.e., the $[PW_{11}O_{39}]^{7-}$ defect site is the more basic of the two and can reduce the effective nuclear charge of Eu(III) more effectively. Lifetime analysis provides information on the coordination environment also and each of the environments possesses single exponential lifetimes between 215 and 256 μs which is typical for 4-coordinate polyoxometalates in aqueous solution. The data of Figure S5 highlights the difficulty in separating the signals responsible for samples where the environments are identical and the peak shapes are similar.

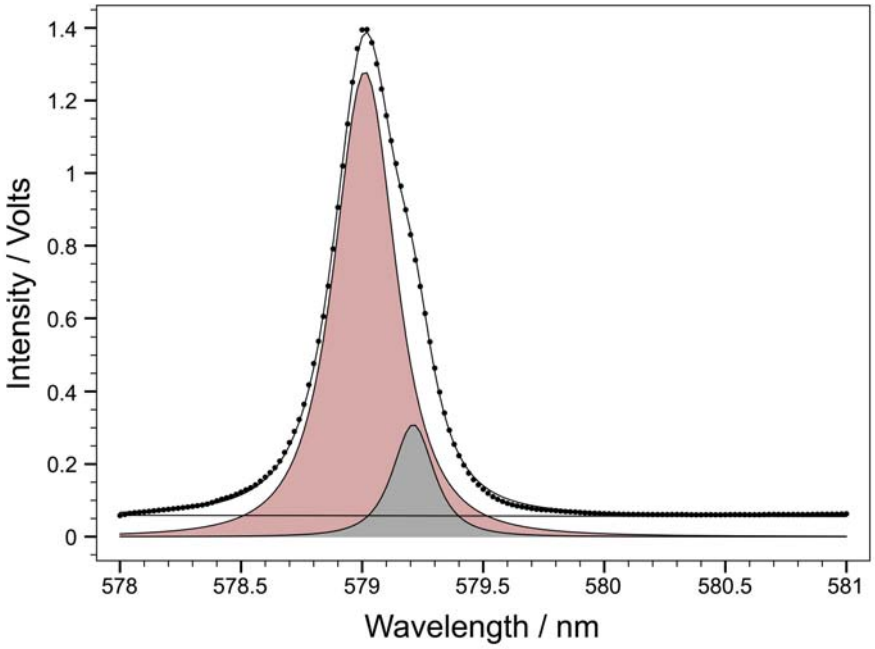

Figure S6. $^{7}F_{0} \rightarrow {}^{5}D_{0}$ excitation spectrum of $Eu_2[SO_4]_3$ in 0.2 M Li_2SO_4 at pH = 3.0. Dots are observed intensity; solid line is the line of best fit. Each peak was fit to a Gauss-Lorentzian algorithm.

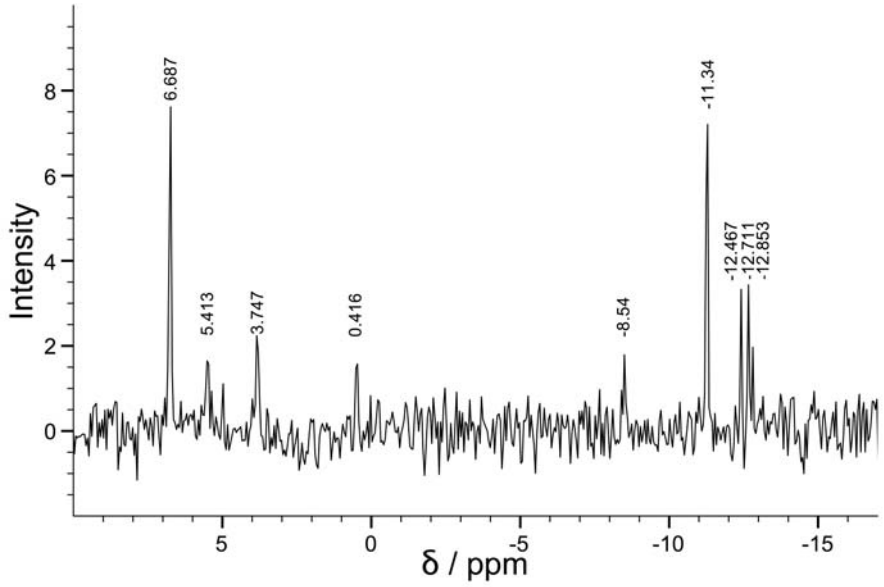

Figure S7. The ^{31}P NMR of Eu-α-1 solution produced by oxidation of the fully-reduced heteropoly blue solution showing peaks that are diagnostic of Eu-α-1 decomposition products, including $[Eu(\alpha\text{-}2\text{-}P_2W_{17}O_{61})_2]^{17-}$, $[(H_2O)_nEu(PW_{11}O_{39})]^{4-}$, $[Eu(PW_{11}O_{39})_2]^{11-}$ and $\alpha\text{-}[P_2W_{18}O_{62}]^{6-}$. The chemical shifts are collected in Table 3 of the manuscript.

Table S0. Slopes and regression coefficients of linear least squares fits to i_{pc} and i_{pa} vs. $v^{½}$ data of Figure 3.

Species	Conc., mM	i_p[a]	Slope, mA $s^{½}$ $mV^{-½}$	R^2
α-1	0.25	a	+0.027(2)	0.917
	0.25	c	-0.034(2)	0.938
	5.0	a	+0.354(5)	0.996
	5.0	c	-0.220(5)	0.990
Eu-α-1	0.25	a	+0.028(2)	0.950
	0.25	c	-0.032(2)	0.950
	5.0	a	+0.51(3)	0.940
	5.0	c	-0.387(3)	0.999
Y-α-1	0.25	a	+0.040(1)	0.984
	0.25	c	-0.048(1)	0.984
	5.0	a	+0.412(7)	0.995
	5.0	c	-0.33(2)	0.856

[a] Letters a and c denote anodic and cathodic peak current responses, respectively.

Table S1. Luminescence lifetimes for the standard solutions and electrolysis solutions summarizing the data for the various systems studied. Each excitation band predominately consists of contributions from two overlapping species as judged by the deconvolution of the excitation spectra. The lifetimes were obtained by fitting to a bi-exponential decay, and the goodness of fit was judged by the randomness of the residual and minimization of the residual squared. Error of measurement is ±10%. The weights are representative of the percentage contribution of each of the emitting species at that wavelength.

Compound	Wavelength (nm)	H_2O					
		weight	k_{obs1} (ms^{-1})	tau (ms)	weight	k_{obs2} (ms^{-1})	tau (ms)
$[(H_2O)_4Eu(\alpha\text{-}1\text{-}P_2W_{17}O_{61})]^{7-}$	579.82	0.560	4.42	**0.226**	0.440	4.42	**0.226**
	580.04	0.950	4.65	**0.215**	0.050	4.36	**0.229**
	580.46	0.690	4.23	**0.237**	0.310	0.59	**1.73**
$Eu_2(SO_4)_3$	579.00	0.974	7.92	**0.126**	0.026	0.35	**2.859**
$[(H_2O)_4Eu(\alpha\text{-}1\text{-}P_2W_{17}O_{61})]^{7-}$+ $Eu_2(SO_4)_3$	579.32	0.908	7.34	**0.136**	0.092	3.77	**0.265**
	579.72	0.790	3.55	**0.282**	0.210	7.86	**0.127**
	580.04	0.966	4.66	**0.215**	0.034	0.30	**3.380**
	580.46	0.959	4.88	**0.205**	0.041	0.56	**1.796**
$[(H_2O)_nEu(PW_{11}O_{39})]^{4-}$	579.06	0.943	7.11	**0.141**	0.057	0.33	**3.036**
	579.80	0.999	4.13	**0.242**	n/a	n/a	**n/a**
$[(H_2O)_nEu(PW_{11}O_{39})_2]^{4-}$	579.80	1.000	0.96	**0.252**	n/a	n/a	**n/a**
$[(H_2O)_4Eu(\alpha\text{-}1\text{-}P_2W_{17}O_{61})]^{7-}$ reduced solution	579.72	0.560	3.13	**0.320**	0.440	5.65	**0.177**
	580.04	0.962	4.65	**0.215**	0.038	0.28	**3.595**
	580.46	0.957	4.73	**0.211**	0.043	0.37	**2.722**

$[(H_2O)_4Eu(\alpha\text{-}1\text{-}P_2W_{17}O_{61})]^{7-}$ oxidized solution	579.80	0.890	3.87	**0.258**	0.110	4.67	**0.214**
	580.04	0.515	3.87	**0.258**	0.485	4.67	**0.214**
	580.46	0.031	0.53	**1.880**	0.969	4.71	**0.212**

Reference:

(1) Frey, S. T.; Horrocks, W. D. *Inorg. Chim. Acta* **1995**, *229*, 383-390.

Chapter 3. Series Behavior of Lanthanoid (III) Complexes with the α-1-Wells-Dawson Heteropolyoxoanion in Acetonitrile: Electrochemistry and Ln Coordination

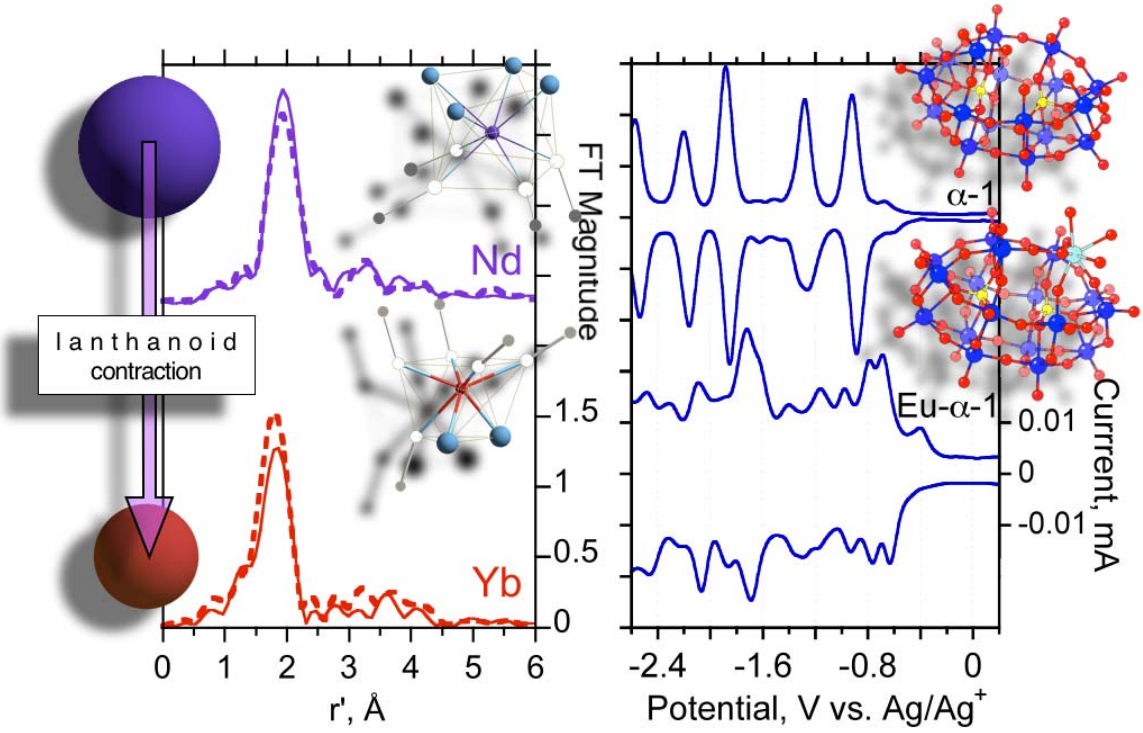

The Nd^{3+}, Sm^{3+}, Eu^{3+}, Tb^{3+}, Dy^{3+}, and Yb^{3+} complexes with α-1-$[P_2W_{17}O_{61}]^{7-}$ of 1:1 Ln:α-1-ligand stoichiometries, $[(H_2O)_nLn(\alpha\text{-}1\text{-}P_2W_{17}O_{61})]^{7-}$, as the tetra-*n*-butylammonium solid salts as well as their solutions in dry and wet acetonitrile were probed through use of voltammetry, electrolysis, and EXAFS to provide insights into electrochemical behaviors and hydration (n) phenomena across the 4f period.

3.1 Introduction

The intricacies and nuances of polyoxometalate (POM) chemistry that are driven by solvent and solute effects are renowned.[1] Even subtle variations of media and electrolytes can have pronounced impact on electrochemical equilibria and chemical speciation phenomena.[2, 3] For example, in aqueous reactions of selected lanthanoid cations, Ln(III), with the α-1 isomer of the Wells-Dawson heteropolyoxoanion, α-1-$[P_2W_{17}O_{61}]^{10-}$ (abbreviated hereafter as α-1), the formation of three, broadly different molecular anions results from concentration dependent sensitivities to the reactants.[4-8] These include complexes with 1:1, 2:2, and 1:2 Ln:α-1 stoichiometries in which the Ln(III) ions have O coordination environments with square antiprism (8 O) and monocapped square antiprism (9 O) geometries as illustrated in Figure 1. In each of these environments, one sterically-demanding α-1 ligand coordinates in tetradentate fashion with 4 basic O atoms (denoted $O_{\alpha\text{-}1}$ hereafter) as shown in Figure 1 with open black circles. For the 1:1 heteroleptic anion $[(H_2O)_4Lu(\alpha\text{-}1\text{-}P_2W_{17}O_{61})]^{7-}$ as the potassium salt,[6] the eight-O environment of Lu(III) is attained by the binding of 4 water molecules—their O atoms (denoted O_{H_2O} hereafter) are shown in Figure 1 as blue circles. The average Lu-O_{H_2O} bond distance is 0.12 Å longer than that for Lu-$O_{\alpha\text{-}1}$. The coordination environments for the 2:2 heteroleptic anions $[\{(H_2O)_4Ln(\alpha\text{-}1\text{-}P_2W_{17}O_{61})\}_2]^{14-}$ for Ln = La[9] and Ce[7] as the potassium and ammonium salts, respectively, also contain 4 water molecules, in addition to one terminal O atom of a second α-1 ligand that effectively serves to bridge two 1:1 species, thereby forming the 2:2 aggregates. In these nine-O coordination environments, the average Ln-O_{H_2O} bond distances are 0.11–0.12 Å longer than those for Ln-$O_{\alpha\text{-}1}$. The close resemblance of the Ln coordination environments is consistent with

the observation of a concentration-dependent equilibrium distribution of the two species in aqueous media that favors the 1:1 species on dilution,[7, 10] especially for the small, heavy Ln(III) ions.[9] The eight-O environments of Ln(III) in the 1:2 homoleptic anions $[Ln(\alpha\text{-}1\text{-}P_2W_{17}O_{61})_2]^{17-}$ for Ln = La, Nd, Eu, and Er as the mixed potassium-hydronium salts[8] as well as the 8-O environments of the tetravalent actinide (An) ions, Th and U, in the corresponding $[An(\alpha\text{-}1\text{-}P_2W_{17}O_{61})_2]^{16-}$ cluster anions as potassium salts[11] are free of water. The effect of which is that solution equilibria between the 1:2 and 1:1 as well as the 1:2 and 2:2 anions would involve the hydration (+ 4 H_2O) and dehydration (- 4 H_2O) of the Ln(III) ions. As such, these equilibria are either slow,[8] as for the former, or have not been observed, for the latter.

The fact that water figures so prominently in the Ln(III) coordination chemistry with the α-1 Wells-Dawson heteropolyoxoanion[12] in aqueous media led us to wonder about the corresponding system behavior in organic solvents. A comparison of the aqueous and acetonitrile (MeCN) soluble POM systems is particularly on point for the Eu(III) complex because the Eu(III) ion in the water-soluble potassium salt of composition $K_7[(H_2O)_4Eu(\alpha\text{-}1\text{-}P_2W_{17}O_{61})]\cdot xH_2O$, abbreviated hereafter as K^+-Eu-α-1, was shown to be reducible to Eu(II) in conjunction with the reduction of W in the α-1 ligand framework—the effects of which produce striking chemical instabilities and transformations.[13] Here we address the prospect of Eu-centered redox activity and its consequences in the corresponding MeCN-soluble tetra-*n*-butylammonium (abbreviated hereafter as TBA^+) salt of the Eu heteropolyoxoanion complex with the nominal composition $TBA_5H_2[(H_2O)_nEu(\alpha\text{-}1\text{-}P_2W_{17}O_{61})]\cdot xH_2O$, abbreviated hereafter as TBA^+-Eu-α-1. Previous electroanalytical studies of Ln(III) ions in MeCN demonstrate that the

homoleptic MeCN solvate of Eu(III), $[Eu(NCCH_3)_x]^{3+}$, is more easily reduced than Eu(III) as its homoleptic aqueous hydrate, $[Eu(OH_2)_y]^{3+}$. The Eu(III)/Eu(II) formal electrode potential in MeCN, +0.10—0.15 V vs. SCE,[14, 15] is some 0.7 V more positive than the standard electrode potential, -0.59 V vs. SCE,[16] in H_2O. Whether such a sizable shift carries over from the aqueous K^+-Eu-α-1 system to the TBA^+-Eu-α-1 one in MeCN is unknown. Insights into this issue as well as the Eu coordination environment of TBA^+-Eu-α-1 in MeCN serve to complement the extensive, by comparison, literature on the aqueous system chemistry. To put the results into a broader context, the organic-soluble TBA^+ salts of the α-1 heteropolyoxoanion complexes across the 4f period with Ln ≡ Nd—Yb were studied through use of voltammetry, bulk electrolysis, and XAS (X-ray absorption spectroscopy). In particular, the Ln L_3-edge XANES (X-ray absorption near edge structure) and EXAFS (extended X-ray absorption fine structure) were obtained for MeCN solutions of the TBA^+-Ln-α-1 salts and for their solid forms as well. This side-by-side comparative study of solid salts and their MeCN solutions provides information about the extent of hydration, n, and other metrical variations of the Ln(III) coordination environments that may be driven by two principal forces: (1) The effects of the lanthanoid contraction for a change of 10 units in Z and a 0.121 Å difference in ionic radius (IR)—from the large, light Nd (Z = 60, IR = 1.163 Å for CN = IX) to the small, heavy, Yb (Z = 70, IR = 1.042 Å for CN = IX).[17] (2) Effects of the dissolution itself, wherein the possibility of solvent (H_2O—CH_3CN) exchange for $0 \leq \delta \leq n$ as depicted in Eq. 1 (in which (s) and (o) designate the solid salt and the organic (MeCN) solubilized ions, respectively) may have a profound effect on electrochemical behaviors, especially with regard to Eu(III)/Eu(II) redox activity.

$TBA_5H_2[(H_2O)_nLn(\alpha\text{-}1\text{-}P_2W_{17}O_{61})](s) + xsCH_3CN \rightarrow$

$$[(H_2O)_{n-\delta}(CH_3CN)_\delta Ln(\alpha\text{-}1\text{-}P_2W_{17}O_{61})]^{7-}(o) + 5TBA^+(o) + 2H^+(o) \quad (1)$$

For both of these issues, the use of EXAFS provides access to metrical information that is otherwise not available about each of the six Ln(III) complexes studied (including Nd, Sm, Eu, Tb, Dy, and Yb) regardless of the physical state of the TBA^+-Ln-α-1 complexes and, therefore, obviates the need for growing crystals suitable for X-ray crystallography, a task that has eluded our preparative methodology. Other than the two reported structures of 2:2 Ln:α-1 complexes with La[9] and Ce[7], which are at the beginning of the period, and just one of the 1:1 complex with Lu,[6] which is at the end, we know only that EXAFS measurements of K^+-Eu-α-1[13] (representing the near middle of the period) in H_2O are in agreement with the 1:1 formulation of the $[(H_2O)_4Eu(\alpha\text{-}1\text{-}P_2W_{17}O_{61})]^{7-}$ complex wherein Eu(III) binds to four $O_{\alpha\text{-}1}$ and four O_{H_2O}, possibly with the stereochemistry that obtains for the K^+-Lu-α-1 crystal structure (Figure 1a). Moreover, in so far as EXAFS results provide a 1-D visualization of the coordination stereochemistry, the local environment of Eu with 8 O atoms at an average distance of 2.37–2.38 Å was shown to be the same in the solid K^+ salt and its aqueous solution.[13]

There are two geometric implications with precedence vis-à-vis the effects of the lanthanoid contraction upon the Ln coordination environments in Ln-α-1 complexes. The first concerns the period behaviors of the Ln(III) nonahydrates, $[Ln(OH_2)_9]^{3+}$ with monodentate water ligands,[18, 19] and the 1:2 Ln(III):Keggin complexes, $[Ln(\alpha\text{-}PMo_{11}O_{39})_2]^{11-}$ and $[Ln(\beta\text{-}2\text{-}SiW_{11}O_{39})_2]^{13-}$ with tetradentate heteropoly-molybdate[20, 21] and –tungstate ligands.[22] The O coordination numbers (CNs) determined from single-crystal X-ray diffraction remain constant at 9 and 8, respectively, and the average Ln-O_9

and Ln-O_8 bond lengths decrease smoothly in the expected quadratic fashion[23, 24] with increasing Z.[25] In the second, X-ray crystallography reveals that the homoleptic acetonitrile complexes of Ln(III) are 9 coordinate with N at the beginning of the period and 8 at the end.[26, 27] This effect mirrors that found for the *solution* behavior of the Ln(III) aqua ions, for which the O CN decreases from 9 for the large ions, like Nd, to 8 for the small ones, like Yb.[28-31] Similarly, both experimental[26, 32] and theoretical (molecular dynamics and quantum mechanical simulations)[33] research shows that the solution behavior of cationic acetonitrile solvates, $[Ln(NCCH_3)_x]^{3+}$, in anhydrous MeCN is likely to involve some variation of the Ln(III) ion coordination across the 4f period arising from two (or more) species in equilibrium that differ in either their coordination polyhedra or the number of coordinated MeCN molecules ($x = 9 \rightarrow 8$) and, in cases with coordinating anions, the influence of cation-anion interactions.

The Ln-α-1 series of complexes of interest here each contain bulky and space demanding TBA cations and tetradentate α-1 anions, which contribute 4 $O_{\alpha\text{-}1}$ atoms to each Ln(III), and an unknown number of significantly less bulky and far less space-demanding, monodentate water molecules. As such, the Ln period behavior is not easy to predict for either the solid TBA^+ salts, wherein crystal packing effects are in force, or for their acetonitrile solutions, wherein solvent exchange effects may contribute to the complicated current-voltage (*i–V*) behaviors that are observed. The effects of the lanthanoid contraction on the Ln coordination are discussed with particular focus on the EXAFS-determined Ln-O interatomic distances and O coordination numbers as well as with regard to the voltammetry data and the Eu XANES spectroelectrochemistry, which does not reveal Eu(III)/Eu(II) redox activity for TBA^+-Eu-α-1 in dry MeCN with a

$TBAPF_6$ electrolyte in contrast to the behavior of the K^+-Eu-α-1 salt in an aqueous electrolyte.

3.2 Experimental Section

3.2.1 Materials Preparation, Purity, and Voltammetry

The lacunary Wells-Dawson salt, $K_9Li[\alpha\text{-}1\text{-}P_2W_{17}O_{61}]\cdot 20H_2O$, was prepared following the method of Contant.[34] $LnCl_3\cdot nH_2O$ (Ln = Y, Nd, Sm, Eu, Tb, Dy, and Yb, from Aldrich Chemical Co.), Li_2SO_4 (from MP Biomedicals, Inc.), analytical grade tetra-*n*-butylammonium hexafluorophosphate (abbreviated $TBAPF_6$, from Avocado Research Chemicals), TBABr (from Acros Organics), and extra-dry acetonitrile (over molecular sieves with < 50 ppm H_2O, from Acros Organics) were used as received. $K_7[(H_2O)_nLn(\alpha\text{-}1\text{-}P_2W_{17}O_{61})]\cdot xH_2O$ (Ln = Y, Nd, Sm, Eu, Tb, Dy, and Yb) were synthesized in aqueous solutions as previously described. Phase purity was proven by ^{31}P NMR spectra of the K^+-Ln-α-1 salts dissolved in D_2O—the chemical shifts of the two P resonances shown in Table 1 are consistent with previous reports[4, 10, 13, 35, 36]—as described elsewhere.[4] The organic-soluble lacunary ligand, $TBA_9H[\alpha\text{-}1\text{-}P_2W_{17}O_{61}]$, and its Ln complexes, $TBA_5H_2[(H_2O)_nLn(\alpha\text{-}1\text{-}P_2W_{17}O_{61})]\cdot xH_2O$ (Ln = Y, Nd, Sm, Eu, Tb, Dy, and Yb), were obtained by means of metathesis of the corresponding K^+ salts in aqueous solution with TBABr. The preparation of isomerically-pure TBA^+-Ln-α-1 salts was established by their two-line ^{31}P NMR solution spectra obtained in D_3CCN with 10% D_2O—the chemical shifts shown in Table 1 are consistent with previous literature.[9] In the absence of D_2O, upon dissolution in dry acetonitrile alone, each TBA^+-Ln-α-1 salt exhibits a multi-line spectrum as shown in Figure S1 (ESI), suggesting the presence of different protonated

species (from the presence of adventitious water, xH_2O, in the solid salt hydrates upon their dissolution and solvolysis) and/or multiple diastereomers that do not interconvert on the NMR timescale—a phenomenon noted beforehand for K^+-U(IV)-α-1 (1:2) in aqueous media.[11] Upon the addition of 2-10 % vol. water, the resonances broaden and coalesce to resemble the two signals observed for the analogous compounds in aqueous solution. The simplification of the NMR spectra upon the addition of water can be explained by an amalgamation of effects, which are discussed elsewhere.[37] Nonetheless, the NMR establishes the phase purity and stability of the K^+-Ln-α-1 and TBA^+-Ln-α-1 systems in water and acetonitrile media, respectively. The latter of which were studied here by XAS as well as cyclic voltammetry (CV) and differential pulse voltammetry (DPV) in supporting electrolyte solutions of 0.1 M $TBAPF_6$ in MeCN at room temperature and under a N_2 atmosphere (all operations were performed in a glove box) with an Epsilon electrochemical workstation (BASi). The CV and DPV data for the MeCN solutions of TBA^+-Ln-α-1 were obtained in one-compartment glass vials using a standard three-electrode system consisting of a 3 mm diam. glassy carbon (GC) working electrodes (BASi MF-2012); 0.064 diam. Pt wire auxiliary electrodes; a Ag/Ag^+ reference electrode (BASi MF-2062) with which the ferrocene/ferrocenium half-wave electrode potential is observed at +0.090(5) V,[38] corresponding to +0.31 V vs. SCE.[39] Unless indicated otherwise, electrode potentials are quoted (± 0.005 V) with reference to the Ag/Ag^+ system. Bulk electrolysis (BE) data were acquired in three-compartment glass cells using 6.15 mm diam. graphite rods (GR) as the working and auxiliary electrodes (Alfa Aesar 14739) at -2.600 V vs. Ag/Ag^+ with a 100 B/W electrochemical analyzer (BASi).

3.2.2 XAS Data Collection, Analysis, and Spectroelectrochemistry

Ln L_3-edge (for Nd, Sm, Eu, Tb, Dy, and Yb) spectra were collected in fluorescence mode at beamline 12-BM-B[40] at the Advanced Photon Source (APS) at Argonne National Laboratory, using a multielement (Canberra) detector. The incident X-ray energy was calibrated against the first inflection point of the K-edge of Fe foil (7.112 keV). Fine powders of the six solid salts of TBA^+-Ln-α-1 (all with ca. 3 wt. % Ln) were compacted into micro X-ray cells (SPEX 3577) fitted with Prolene® X-ray film windows (4 μm gauge, Chemplex Industries) for measurements. The six 4.3 mM solutions of the TBA^+-Ln-α-1 salts in a nonaqueous electrolyte (24 mg in 1 mL of MeCN with 0.1 M $TBAPF_6$) were injected into the micro X-ray cells for data acquisition. Three one-hour scans to k_{max} = 10.5 $Å^{-1}$ were averaged for each of the 12 samples. All analyses of the $k^3\chi(k)$ EXAFS were performed in identical fashion in the usual manner with EXAFSPAK.[41] The curve-fitting with a fixed scale factor (S_0^2 = 1) entailed a series of step-wise fits of increasing complexity, including one-shell models of the nearest Ln-O interactions with and without cumulants (ESI, Tables S1–S3); a two-shell model of the Ln-O interactions (ESI, Tables S4 and S5), and; a three-shell coordination model that incorporated the distant Ln-O and Ln-W interactions (ESI, Table S6, based upon the known structure of $K_7[(H_2O)_4Lu(\alpha\text{-}1\text{-}P_2W_{17}O_{61})]^6$) as employed previously.[13] The addition of the distant interactions does not affect the metrical parameters of the nearest coordination sphere of O about Ln, indicating the absence of spectral congestion with the simplistic, one shell fits of the Ln(III)-O environments for which a detailed treatment of the Ln-O Debye-Waller factors is provided as Table S7 (ESI). All modeling employed the theoretical phase and amplitude functions calculated with FEFF8.01.[42] Based upon

the statistical information obtained for each fitting model—namely χ^2/ν, where χ^2 is the goodness-of-fit and ν is the number of degrees of freedom of the fit, and the F_χ test as applied in the manner of Lukens et al.[43], see Table S8 (ESI)—the O backscattering in the Ln EXAFS spectra for all samples were best modeled with two-shell fits that included contributions from the 4 nearest O atoms of the tetradentate α-1 ligand ($O_{\alpha\text{-}1}$) and the next nearest O atoms of water molecules (O_{H_2O}) that serve to complete the immediate coordination environments of the Ln(III) ions. In this model, six parameters were refined, including Ln-$O_{\alpha\text{-}1}$ and -O_{H_2O} interatomic distances, r (Å), and Debye-Waller factors, σ^2 (Å^2); O_{H_2O} coordination number (CN); energy threshold parameter, ΔE_0 (eV). The number of variables (6) was less than the number of relevant independent data points available in the primary spectra, which was estimated $N_I = (2\Delta k \Delta r)/\pi = (2\times 8.5\times 1.5)/\pi = 8$. The expected resolution of our EXAFS in r-space is approximated as 0.19 Å, meaning that shells of backscattering atoms about Ln with this (and smaller) interatomic separations are not resolved in the Fourier transform (FT) data. The XANES data were fit with WinXAS[44] using one pseudo-Voigt function to model the edge resonance and one arctangent function to model the edge jump. The fits are shown as Figure S2 (ESI) and the fitted parameters are available as Table S9 (ESI). The in situ Eu L_3-edge XANES spectroelectrochemical data for TBA^+-Eu-α-1 were collected on deaerated and continuously N_2-sparged MeCN solutions of the $[(H_2O)_nEu(III)(\alpha\text{-}1\text{-}P_2W_{17}O_{61})]^{7-}$ anion along with the 0.1 M $TBAPF_6$ electrolyte as contained in purpose-built electrochemical cells fitted with 6.1 mm diam. GR working and auxiliary electrodes.[13, 45, 46] Eu L_3-edge data were first acquired under open circuit conditions with a 100 B/W electrochemical

analyzer, followed by bulk electrolyses at electrode potentials of -1.200 to -1.500 V to produce heteropoly blue solutions of the reduced anion.

3.3 Results and Discussion

3.3.1 TBA^+-Eu-α-1 System Behavior

Electrochemistry. As shown in Figure 2, the polarization window available in dry MeCN with the 0.1 M $TBAPF_6$ electrolyte is flat and featureless over 2.80 V from the high limit switching potential (+0.200 V) to the low limit one (-2.600 V), wherein the ligand and Eu redox activity are expected. The CVs obtained for two concentrations—1.5 and 3.5 mM—of the lacunary, Ln-free, α-1 anion show four well-resolved processes with $E_{½}$ = -0.880, -1.252, -1.831 V, and -2.183 V as well as an unresolved one near the low-limit switching potential, all of which are attributed to W-based redox chemistry. The corresponding DPV data of Figure 3 demonstrate that the positions and shapes of the four peaks are essentially independent of the analyte concentration and, moreover, provide a well resolved response for a fifth process with $E_{½}$ = -2.554 V. Repetitive sweeps over the entire polarization window showed reproducible behavior even though the original, colorless solution turned blue, due to the reductive electrochemistry and delocalization of the added electrons in the LUMOs that consist of W and O character.[47-50] Throughout experimentation with different scan rates ($9 \leq \nu \leq 100$ mV s^{-1}, see Figure S3, ESI), we found that reduction does change the *i–V* response of the neat α-1 ligand over the course of time during repetitive sweeps between -2.6 and +0.2 V. In particular, two new couples grow in at $E_{½}$ = -1.47 and -0.63 V, and the peak currents for the anodic and cathodic processes (i_{pa} and i_{pc}, respectively) of the first reduction increase due to the growth of an

obscured, coincident response (see ESI Figure S4). In view of the known instabilities of the α-1-ligand in aqueous media,[13, 51] transformations to the α-2 isomer and the plenary Wells-Dawson anion are proposed to account for the changes. Analysis of the CV response for the initial reduction reveals a direct, linear correlation between the peak currents and $\nu^{1/2}$ for both analyte concentrations (see ESI Figure S5) wherein the data are adequately modeled by the Randles-Sevcik equation, indicating mass-transport controlled electron transfer kinetics.[13, 52] The less than unity $|i_{pa}/i_{pc}|$ ratios (0.86–0.92) as well as the concentration- and scan-rate-dependent values for peak separation (0.074–0.107 V) and $E_{1/2}$ (-0.88–-0.90 V), see ESI Figure S6, are indicators of irreversible behaviors, such as would arise from chemical instabilities. By use of controlled potential BE, freshly-prepared solutions of the fully-oxidized α-1 analyte were found to consume 11.4 ± 0.6 electrons/molecule upon exhaustive electrolysis at -2.600 V, forming heteropoly blue solutions.

The CV and DPV data of Figures 2 and 3, respectively, for two concentrations—1.5 and 3.5 mM—of the TBA^+-Eu-α-1 solution show multiple, poorly-resolved process over the polarization domain of -0.50 to -2.60 V. The complexation of Eu(III) with α-1 causes a significant perturbation of the reductive electrochemistry, turning the well-defined voltammograms of α-1 into a mass of redox congestion. The likes of such extensive and dense voltammetry in MeCN has been noted beforehand for α-$[P_2Mo_{18}O_{62}]^{6-}$ and α-$[S_2Mo_{18}O_{62}]^{4-}$,[53, 54] and stands in obvious contrast with the simple voltammogram of K^+-Eu-α-1 in an aqueous electrolyte.[13] Moreover, as with the aqueous voltammetry, there is a substantial concentration dependence to the peak shapes and positions. As such, it is impossible to attribute any single wave to a one-electron

Eu(III)/Eu(II) couple, which may be expected to occur at an electrode potential of ≤ -0.12 V, which is the value for the acetonitrile solvate of $Eu(ClO_4)_3$ in purified, anhydrous MeCN.[14] A shift to more negative values is typical, arising from stabilizing effects of strong complexation with Eu(III)[55, 56] although effects of the opposite nature are known,[45, 57] and the voltammetry of TBA^+-Eu-α-1 in MeCN may be an amalgamation of Eu- and ligand-centered redox activities, such as found for the voltammetry of K^+-Eu-α-1 in H_2O.[13]

To provide insight into this issue, the CV and DPV data of Figures 2 and 3, respectively, for two concentrations—1.5 and 3.5 mM—of TBA^+-Y-α-1 were obtained for comparison with TBA^+-Eu-α-1. Because Y(III) is not reducible to Y(II), the electrochemical response is that of the ligand alone as modified by Y(III) complexation, so that a difference between TBA^+-Y-α-1 and -Eu-α-1 stands to be an indicator of Eu redox activity. Remarkably, the voltammograms for TBA^+-Y-α-1 are every bit as complicated and concentration-dependent as those for TBA^+-Eu-α-1, and the differences between them are substantive, so much as to vitiate attempts to identify Eu redox activity amongst the bulk, W-based voltammetric response for TBA^+-Eu-α-1. The controlled potential BE data for TBA^+-Y-α-1 and -Eu-α-1 are also of little help in this regard, wherein a 1-electron difference is expected in the event of the 1-electron Eu(III) to Eu(II) reduction. Fresh solutions of the fully-oxidized analytes were found to consume 13.9 ± 0.7 and 13.5 ± 0.7 electrons/molecule, respectively, upon exhaustive electrolysis at -2.600 V, forming heteropoly blue solutions. The electron capacities of the TBA^+-Ln-α-1 clusters are statistically equivalent and greater that that of α-1 itself. Although it appears

that Eu is electrochemically-silent, a direct probe of Eu valence switching is provided through use of Eu XANES spectroelectrochemisty.[13]

Eu XANES spectroelectrochemistry. The normalized Eu L_3-edge XANES for a 0.25 mM TBA^+-Eu-α-1 solution in dry MeCN with 0.1 M $TBAPF_6$ electrolyte obtained under open circuit conditions is shown in Figure 4 (black dashed line). The intense L_3-edge peak observed at 6.9829 keV is characteristic of Eu(III).[6, 13, 46, 58] The blue curve in Figure 4 is the response for the same solution but following about 4 hours of BE with a controlled electrode potentials of -1.500 V vs. Ag/Ag^+, a value that is comparable to that (-1.300 V vs. Ag/AgCl) found to reduce Eu(III) in K^+-Eu-α-1 in an aqueous electrolyte.[13] There is no evidence for divalent Eu, which would give rise to a new peak appearing approximately 8 eV below the trivalent Eu edge peak. Instead, there is only minor broadening on the high-energy side (6.99—7.00 keV) of the edge peak that is attributable to a small perturbation of the Eu coordination environment induced by the reduction of W in the P-W-O framework. Otherwise, the responses for the colorless-oxidized and blue-reduced systems are essentially equivalent, indicating that Eu(III) is not reducible in TBA^+-Eu-α-1 as studied here. The reason for the contrasting behaviors in H_2O and MeCN may be driven by Eu-specific interactions with the different solvents. Precedence in this regard comes from electrochemical research demonstrating that homoleptic cationic acetonitrile solvates, $[Eu(NCCH_3)_x]^{3+}$, in dry MeCN are reduced at more positive electrode potentials than the corresponding aquated cations, $[Eu(OH_2)_y]^{3+}$, in H_2O.[14] This suggests that Eu(III) in TBA^+-Eu-α-1 in MeCN would be easier to reduce than Eu(III) in K^+-Eu-α-1 in H_2O. This is not the case, leading us to suspect that, unlike the homoleptic Eu solvate, MeCN does not fully-participate in coordination to Eu(III) in the POM

complex. To probe for possible structural variations in the coordination of Eu(III) between TBA^+-Eu-α-1 in MeCN, on the one hand, and K^+-Eu-α-1 in H_2O, on the other, EXAFS data were acquired for the nonaqueous system for comparison with the previously published results for the aqueous system[13] to account for the observed electrochemical differences.

EXAFS. The experimental $k^3\chi(k)$ EXAFS and the corresponding FT data (without phase correction) for the solid salt of TBA^+-Eu-α-1 and for a freshly prepared (4.3 mM) solution of it in MeCN are shown in Figure 5 as solid (red) and dashed (black) lines, respectively. The FTs reveal a single intense peak at 1.8–2.0 Å (before phase shift, right panel) containing the combined backscattering contributions from the 4 O atoms of the tetradentate α-1 ligand and O atoms from H_2O molecules (for the solid salt, which was precipitated from H_2O) and either O and/or N atoms from water and/or MeCN molecules (for the MeCN solution of TBA^+-Eu-α-1). The data for the MeCN solution are effectively superimposable with those from the solid salt, suggesting that the Eu coordination environment in the solid and the solution are comparable. The pivotal issue here is a proper accounting of the interactions that give rise to the strong, close peaks in the FT data. This was accomplished by means of curve fitting with different models of increasing structural complexity: the results from two are discussed below.

One-shell EXAFS model. The $k^3\chi(k)$ EXAFS for the solid salt and its MeCN solution were first fit with a conservative (4-parameter) single shell model of O about Eu(III). The best fit parameters are summarized in Table 2 and the fits show good correspondence with the experimental data, see Figure S7 (ESI), suggesting that the first coordination sphere about Eu(III) arises from O atoms. This is a chemically-sound

assignment for the TBA^+-Eu-α-1 salt, which was obtained metathetically from the corresponding aqueous solutions of the K^+-Eu-α-1 salt and, moreover, was never exposed to acetonitrile and, so, free of Ln-$NCCH_3$ coordination. Upon dissolution of the TBA^+-Eu-α-1 salt in dry MeCN (< 50 ppm H_2O), the average, single-shell distance is equivalent to within one esd (estimated standard deviation) of that for the solid, providing evidence for the same overall CN in both physical states. If solvent exchange were to occur as depicted in Eq. (1), the bond length for the solution sample is expected to be longer (on average) than that for the solid salt because of the presence of Eu-$NCCH_3$ interactions, which are longer than those for Eu-OH_2. For example, in the absence of X-ray crystallographic data for a homoleptic MeCN complex of Eu(III), comparisons of structural data for the corresponding complexes of the two adjacent elements Sm and Gd are on point. The average Ln-N_9 distances of 2.534(13) Å[27] and approximately 2.55 Å,[26] respectively, for the acetonitrile complexes $[Ln(NCMe)_9]^{3+}$ are 0.075 Å and 0.135 Å longer than the average Sm-O_9 and Gd-O_8 distances for the $[Sm(OH_2)_9]^{3+}$ and $[Gd(OH_2)_8]^{3+}$ aqua ions.[59] Instead, the average distances for the TBA^+ salt and solution of Eu-α-1 (2.40–2.41 Å) are consistent with the Eu-O_8 distances of 2.424(1), 2.39, and 2.40(3) Å for the homoleptic aqua $[Eu(OH_2)_8]^{3+}$ complex[19] as well as the $[Eu(\alpha\text{-}PMo_{11}O_{39})_2]^{11-}$ and $[Eu(\beta\text{-}2\text{-}SiW_{11}O_{39})_2]^{13-}$ complex anions, respectively.[20, 22] It follows that the Eu(III) ion appears to retain H_2O in its coordination sphere, even in dry MeCN, or, alternatively, that the acetonitrile CN (δ) is such that Eu is 8-coordinate, as $(H_2O)_{4-\delta}(CH_3CN)_\delta Eu(O_{\alpha\text{-}1})_4$ for $0 < \delta < 4$, which would result in shorter average bond lengths than for the 9-coordinate Ln nonasolvates. In this regard, EXAFS data alone are insufficient to directly distinguish between combinations of backscatterers that differ by

Z and Z ± 1, such as obtains for O and N, especially if the coordination environment contains an admixture of O (from the α-1 ligand and H_2O) and N (from MeCN). Nevertheless, additional insights about this issue for the solid TBA^+ salt and its solution in MeCN come from metrical results obtained with a different fitting model.

Two-shell EXAFS model. The distances obtained by use of the one-shell fitting model are valuable, initial results but the fits to the $k^3\chi(k)$ EXAFS are not truly descriptive of the system coordination chemistry. To extract more detailed metrical data and to avoid the possible under-determination of O CNs,[60] we employed a second curve fitting approach, which involved fitting the strong, single peak in the FT data with a 2-O shell model with 6 adjustable parameters. The central assumption in this model is that each Eu(III) is bound to one α-1 ligand through 4 $O_{\alpha\text{-}1}$ atoms, which serve to bridge between the Ln and W atoms, in the tetradentate manner of Figure 1a. This provides a coordination number of 4, which was fixed in the refinements. The oxophilic Eu(III) ions attain coordinative saturation through the bonding of H_2O molecules, in the conventional monodentate manner also of Figure 1a. The extent of bound H_2O (n) was obtained by refining the O_{H_2O} CNs. Without exception, this model provides statistically better fits than the 1-O shell model and, moreover, the reduced value of χ^2 for the two shell-modeling is significantly different, i.e., $P(F_\chi, b, \nu) < 0.05$, than that for the one-shell modeling (Table S8, ESI). The results, in terms of O_{H_2O} CNs as well as Eu-$O_{\alpha\text{-}1}$ and Eu-O_{H_2O} distances and Debye-Waller factors, are summarized in Table 2. The best fits are available as ESI Figure S8.

For the TBA^+-Eu-α-1 solid and its MeCN solution, the Eu-$(O_{\alpha\text{-}1})_4$ distances are shorter than the Eu-$(O_{H_2O})_n$ distances. Of these, the Eu-$O_{\alpha\text{-}1}$ distances for the TBA^+ solid

and solution are equivalent to within the statistical uncertainties of the measurements, indicating that the tetradentate coordination of α-1 to the Eu(III) ions is independent of physical state. In contrast, the 2.49(3) Å Eu-O_{H_2O} distance for the MeCN solution of the TBA^+ salt is 0.03 Å longer than that for the solid, and (in view of the esds) in proximity with the even longer 2.534(13) Å Sm-N_9 distance in $[Sm(NCMe)_9]^{3+}$.[19] This indirect, comparative evidence hints at the possibility that MeCN binds to Eu(III) in the TBA^+-Eu-α-1 complex dissolved in dry MeCN, and that the exchange of H_2O with CH_3CN according to Eq. (1) is a favorable process, leading to partial (δ) MeCN coordination and a mixed H_2O-MeCN solvate with a combination of Eu-OH_2 and Eu-$NCCH_3$ backscattering. This behavior was masked in the single-shell analyses of the Eu EXAFS, and an independent and substantive understanding of the issue is provided through direct methods, e.g., ^1H and ^{13}C NMR, FT-IR, luminescence, etc., as described elsewhere.[37] Concerning the O CNs for the TBA^+ solid and MeCN solution, the sums of $O_{\alpha\text{-}1}$ (4) and O_{H_2O} obtained from the 2 shell fits (7.8(11) and 7.6(9), respectively) are consistent with the values obtained for the K^+-Eu-α-1 salt and its aqueous solution.[13] These metrical results for the TBA^+-Eu-α-1 system when combined with those for other TBA^+-Ln(III)-α-1 systems across the 4f period provide a practical perspective on the variations of Ln(III) coordination in MeCN solutions, including solvent-exchange behaviors. The effects of the lanthanoid contraction have direct impact on the metrics of Ln-O bonding that, in turn, serve to complicate the MeCN solution electrochemistry as well.

3.3.2 System Behavior Across the 4f Period

Electrochemistry. Despite the research showing that the 1-e^- reduction of Eu(III) can be accomplished at a more positive electrode potential in MeCN than in H_2O,

corresponding to lower solvation energies in the nonaqueous solvent than in the aqueous one,[14, 15] the electroanalytical chemistry as well as the Eu XANES spectroelectrochemistry of TBA^+-Eu-α-1 provide no evidence for this process. The fact that we do not observe reduction of Eu(III) suggests an incomplete exchange of the approximately 4 H_2O coordinated to Eu in the solid salt upon its dissolution in dry MeCN, wherein the Eu-OH_2 interactions stabilize Eu(III) to reduction that otherwise occurs in aqueous media at comparable electrode potentials. The extreme complexity of the voltammetric data for the entire TBA^+-Ln-α-1 series (ESI Figures S9 and S10) that develops from the ideal, well-resolved response of the neat ligand (Figures 2 and 3) is a strong indicator of complicated equilibrium behaviors. As alluded to beforehand, these are most likely driven by the presence of multiple protonated species that arise from the release of adventitious water contained in the solid salts upon their dissolution in dry MeCN leading to coupled proton transfer processes.[8, 53, 54] The complexity, such as seen in Figures 2 and 3 for TBA^+-Eu(Y)-α-1, is also attributed to isomerization and solvolysis reactions, aggregation behaviors, including the possible formation of 2:2 dimers[7, 9] from the 1:1 monomer anions,[4] as well as fragmentation and reconstitution, all of which may be influenced by reduction[61, 62] as demonstrated for α-1 itself (ESI Figure S4). In the last regard, throughout the course of CV data acquisition between -2.6 and +0.2 V with different scan rates (9–100 mV s^{-1}) and the formation of heteropoly blue solutions, the *i*–*V* response (ESI Figures S11-S17) of the 1.5 and 3.5 mM solutions of the TBA^+-Ln-α-1 complexes shows less change over the course of time than the α-1 ligand itself.

In many respects, the multitude of *i*–*V* signals in dry MeCN is consistent with the complexity of the ^{31}P NMR data also obtained in dry MeCN. It is difficult to make

specific assignments in the voltammetry and spectroscopy of TBA^+-Ln-α-1. The fact that the deliberate addition of 4.7 % vol. D_2O enables proton exchange and sharpens the NMR resonances in organic solvents (like MeCN, ESI Figure S1) led us to wonder about its corresponding effects on the CV. The addition of 200 μL of H_2O to 1.5 mL of a 3.5 mM solution of α-1 results in (ESI Figure S4) three changes: (1) The waves become significantly broadened; (2) a high-current tail develops at the low switching potential, and; (3) the first reduction is shifted 150 mV to more positive electrode potentials, from $E_{½}$ = -0.88 to -0.74 V. The effects of the stepwise addition of 20, 100, and 200 μL of H_2O on the CV data are shown as ESI Figure S18. In contrast, previous work has shown that the addition of even small amounts of H_2O (up to 0.8 %) to otherwise dry MeCN solutions of $Eu(ClO_4)_3$ causes a significant *negative* shift (as much as 0.2 V) of the electrode potential for the Eu(III)→Eu(II) reduction and decreases the rate of the electrode reaction by controlled-potential BE. These effects have been attributed to Eu-OH_2 complexation and the formation of aquated Eu ions in MeCN as well as the influence of H_2O on the electrode surface.[14] In MeCN, which is a much weaker acid than H_2O, the Ln-α-1 anions are expected to have low solvation energies. Moreover, the bulky TBA countercations, which are inefficient at forming ion-pairs by attaching to the surface O atoms in the manner that alkali metal cations can do,[63] are unlikely to have a significant influence on the rich, reductive electrochemistry that coalesces into an unappealing amalgamation of poorly-resolved waves upon the deliberate addition of H_2O, which affects the Ln coordination in a much less significant manner. As shown in Figures 4 and 5, the addition of 200 μL of H_2O to 800 μL of a 4.3 mM solution of TBA^+-Eu-α-1 in otherwise dry MeCN produces minuscule effects on the Eu XANES and EXAFS,

respectively. Although water is a decisive factor with pronounced influences on the electroanalytical chemistry of TBA^+-Ln-α-1 in MeCN, its addition causes only minor perturbations of the Eu environment as judged by the metrical parameters of Table 2. This suggests that the Eu(III) ion is coordinately saturated with H_2O even before its further addition to the MeCN electrolyte. Information from electroanalysis is integrated with structural insights provided below through use of XAS.

XANES. The normalized Ln L_3-edge XANES for the 4.3 mM solutions of the TBA^+-Ln-α-1 salts in MeCN are shown in Figure 6. As with TBA^+-Eu-α-1, the intense L_3-edge peaks are characteristic of Ln(III)[6, 46, 58] and the responses are essentially equivalent, suggesting that the Ln(III) coordination environments in organic media are consistent across the period. Moreover, the XANES for the TBA^+-solid salts of Ln-α-1 (shown as ESI Figure S19) are qualitatively comparable. Quantitative details were extracted by use of curve fitting. The results, in terms of peak heights, positions, full widths at half-maximum (FWHM), areas, and inflection point energies, are listed in Table 3, and the fits are shown as Figure S2 (ESI). The plot of Figure 7 shows that the FWHM for the Ln L_3-edge peaks of the MeCN solutions (filled squares) of the TBA^+-Ln-α-1 salts increase with increasing Z as expected from the tabulations of natural widths by Krause and Oliver.[64] The experimental widths, which vary from ca. 5.5 to 7.0 eV, are some 1.5 × larger than the natural ones (filled circles), due to the broadening associated with the combination of beamline optics and instrumental resolution as well as the final-state (5d) bandwidths of the Ln(III) ions in the Ln-α-1 species. The X-axis at the top of Figure 7 shows the correlation of FWHM with the reciprocal ionic radius (IR),[46, 58] which is calculated here for CN = VIII from the tables of Shannon,[17] and the right-hand Y-axis

shows that the normalized peak height decreases with increasing Z and 1/IR. Both effects have been attributed to variations in the 2p → 5d oscillator strength,[46] which includes contributions from the radial dipole-moment integral and differences in the 5d densities of final states with appropriate symmetries. In so far as crystal field effects figure into the variations of 4f–5d orbital hybridization, a symmetry appropriate change in the Ln(III) coordination environment may be apparent in one (or more) of the parameters extracted from the XANES spectra. In this regard, the experimental variations of FWHM shown in Figure 7 are not as regular as expected from the corresponding plot of the natural L_3 level widths vs. Z, providing initial, indirect evidence that the environments about Ln(III) may be changing across the period between Nd and Yb for the TBA^+-Ln-α-1 salts and their solutions. Insights into this behavior are provided by analysis of the EXAFS data.

EXAFS. The experimental $k^3\chi(k)$ EXAFS and the corresponding FT data (without phase correction) for the solid salts of TBA^+-Ln-α-1 as well as their 4.3 mM solutions in MeCN are shown in Figure 8 as solid and dashed lines, respectively. The FTs reveal a single intense peak at 1.8–2.0 Å (right panel) containing the composite response from the 4 O atoms of the tetradentate α-1 ligand and O atoms from an unknown number of water molecules (for the solid salts) and either O and/or N atoms from H_2O and/or MeCN molecules (for the acetonitrile solutions). The subtle differences in the shapes and positions of the weak, distant peaks beyond 2.5 Å in the FT data for the solids and solutions are attributable to a combination of cation- and solvent-driven effects on the Ln-centered intra-atom interactions for which the results of the multi-shell modeling of the Ln $k^3\chi(k)$ EXAFS are available as ESI Figure S20. Of importance here is the one- and

two-shell fitting as previously discussed for TBA^+-Eu-α-1 in order to determine the extent and possible variation of Ln hydration across the period with and without MeCN.

One-shell EXAFS model. The best fit parameters, in terms of O CNs and Ln-O distances, from the one-O shell fits of the $k^3\chi(k)$ EXAFS for each of the TBA^+-Ln-α-1 solid salts and their MeCN solutions (Table 3) are displayed in Figure 9a. All the distances are within the range of those expected for 9- and 7-O coordination of Ln(III) across the period, as shown by the green and orange lines, respectively, wherein the average Ln-O_9 distances were obtained for the homoleptic series of aqua complexes, in which water has a denticity of 1 and an O CN of 1.[18, 19] In the absence of crystallographic information for homoleptic Ln(III) complexes with 7 O coordination across the period, the Ln-O_7 distances were calculated as the sum of the IR for Ln(III) (with CN = VII)[17] and O^{2-} (IR = 1.34 Å[65]). The average Ln-O_8 distances (shown as a red line in Figure 9a) were obtained from the crystallographic study[20] of the series of 1:2 Ln(III) [Ln(α-$PMo_{11}O_{39})_2]^{11-}$ complexes, in which α-$[PMo_{11}O_{39}]^{7-}$—like the α-1 ligand of interest here—has a denticity of 4 and an O CN of 4. The use of bond lengths as independent predictors of coordination numbers is a prudent reliability check of self-consistency with EXAFS.

As discussed for the TBA^+-Eu-α-1 EXAFS, the fact that the single-shell fits show good correspondence with the experimental data, see ESI Figure S7, suggests that the first coordination spheres about the Ln(III) ions arise from O atoms. This is a chemically-sound assignment for the TBA^+-Ln-α-1 salts. In contrast, the situation that obtains upon their dissolution in dry MeCN is the principal issue of attention here. The equivalence (within one esd) of the average, single-shell distances for the solids and solutions across

the period argues against the presence of Ln-$NCCH_3$ interactions, which are longer than those for Ln-OH_2. For example, at the high-Z end of the series, the average Yb-N_8 distance of 2.395(18) Å for the homoleptic MeCN complex $[Yb(NCMe)_8]^{3+}$ [27] is 0.078 Å longer than the average Yb-O_8 distance for the $[Yb(OH_2)_8]^{3+}$ aqua ion.[59] The Yb-O distances for the solid and MeCN solution, 2.27(1) and 2.25(1) Å, respectively, compare more favorably with O than N coordination. At the low-Z end, the 2.48(1) Å Nd-O distances for the solid and MeCN solution phases of TBA^+-Nd-α-1 compare favorably with the average Nd-O_9 distance in the aqua complex, $[Nd(OH_2)_9]^{3+}$, whereas in the middle of the series, the average distances for the TBA^+ salts and solutions of Sm-, Eu-, Tb-, and Dy-α-1 are consistent with the Ln-O_8 distances for the $[Ln(PMo_{11}O_{39})_2]^{11-}$ complex anions. The average distances for the TBA^+-Yb-α-1 solid and MeCN solution are essentially the same as expected for 7-O coordination. Moreover, the fact that the Yb-O distance for the solid TBA^+ salt, which is free of MeCN, is 0.02 Å longer than that found upon its dissolution in MeCN argues against the formation of an MeCN solvate of TBA^+-Yb-α-1. The interatomic distance variations with Z shown in Figure 9a suggest that the O coordination environment changes by 2 O across the TBA^+ series of solid salts and their MeCN solutions with a value of 9 O for Nd-α-1; effectively 8 O for Sm-, Eu-, Tb-, and Dy-α-1; 7 O for Yb-α-1.

The system-wide picture that emerges from the one-O shell analyses of the EXAFS data for the Ln-α-1 complexes is that the TBA^+ salts and their MeCN solutions have equivalent Ln-O distances. At the beginning of the period, the longer bond lengths for the TBA^+-Nd-α-1 samples may be an indicator of either higher overall CNs and/or, in the case of the MeCN solution, the participation of some MeCN in the Nd coordination

environment. Of relevance in this regard, is the observation that the residence times for MeCN molecules in the first coordination sphere of solvated Ln(III) ions decreases with increasing Z. In our series of Nd–Yb systems, this means that the lifetime of MeCN coordination is highest for Nd and lowest for Yb.[33] This trend is opposite of that for the residence times for H_2O molecules in the first coordination sphere of aquated Ln(III) ions, wherein the lifetime of H_2O coordination is lowest for Nd and highest for Yb.[33] For insight into these two competing issues, we turned to the use of two-shell fits, which allowed us to separate the short, tetradentate O coordination of the α-1 ligand from the long coordination of both H_2O and MeCN, which are treated together as Ln-O_{H_2O} interactions.

Two-shell EXAFS model. The best fit parameters from the two-O shell fits of the $k^3\chi(k)$ EXAFS for each of the TBA^+-Ln-α-1 solid salts and their MeCN solutions (Table 3) indicate that the Ln-$(O_{\alpha\text{-}1})_4$ distances are shorter than the Ln-$(O_{H_2O})_n$ ones. Both sets decrease across the period with increasing Z as shown by red symbols and blue filled symbols, respectively, in Figure 9b. The Ln-$O_{\alpha\text{-}1}$ distances for the TBA^+ solids and solutions alike are equivalent to within the statistical uncertainties of the measurements, indicating a period-wide consistency of the tetradentate coordination of α-1 to the Ln(III) ions. The Ln-O_{H_2O} distances for the MeCN solutions of the TBA^+ salts are consistently 0.02–0.06 Å longer (except for the equivalent Dy-O_{H_2O}) than those for the solids across the period. Moreover, the 2.51(3) Å Sm-O_{H_2O} distance is comparable (in view of the esds) with the longer 2.534(13) Å Sm-N_9 distance in $[Sm(NCMe)_9]^{3+}$.[19] As shown in Figure 9b with orange diamonds, the crystallographically-determined Nd-N_9 and Yb-N_8 distances of 2.64 and 2.395(18) for $[Nd(NCMe)_9]^{3+}$ and $[Yb(NCMe)_8]^{3+}$,[19, 26] respectively, are also

longer than, yet comparable with, the corresponding EXAFS results for the nominally Nd-O_{H_2O} and Yb-O_{H_2O} interactions. As for TBA^+-Eu-α-1 discussed above, this metrical data suggests that MeCN binds to the Ln(III) ions in the TBA^+-Ln-α-1 complexes dissolved in MeCN to form mixed ternary H_2O-MeCN-α-1 ligation with fluxional behaviors involving partial solvent exchange pursuant to Eq. (1). As concerns the O CNs for the TBA^+ solids and MeCN solutions, the sums of $O_{\alpha\text{-}1}$ (4) and O_{H_2O} (indicated with blue open symbols in Figure 9b) obtained from the 2 shell fits are generally consistent with the values obtained in the single shell approach (except for Nd), wherein it is found that Yb-α-1 contains 7-coordinate Yb (as 4 $O_{\alpha\text{-}1}$ + 3 O_{H_2O}), and that the CNs for the Nd-, Sm-, Eu-, Tb-, and Dy-α-1 complexes vary narrowly about 8 (as 4 $O_{\alpha\text{-}1}$ + 4 O_{H_2O}).

There is a final line of evidence that supports the case for partial MeCN coordination to Ln and the H_2O—CH_3CN solvent exchange depicted in Eq. (1). The Ln-O_{H_2O} bond lengths for the solution complexes in MeCN are consistently up to 0.05 Å longer than those for the aqueous solutions of the K^+ salts, see Table S10, ESI. This squares with the elongation anticipated upon substitution of one (or more) H_2O molecules with one (or more) CH_3CN molecules in the immediate coordination sphere of the Ln(III) ions upon the dissolution of the TBA^+-Ln-α-1 salts in MeCN. Even though the Ln(III) ions are more oxophilic than amminophilic and, clearly, retain water molecules coordinated to Ln(III), the excess of MeCN would favor solvent exchange. Other factors may also be at play. For example, the conformationally-flexible, space-demanding TBA^+ ion may drive changes in the bulk aggregation of the POM anions in MeCN more so than does the K^+ ion in aqueous solutions of corresponding K^+-Ln-α-1 salts. In this regard, previous NMR measurements have shown that 2:2 $[\{(H_2O)_4Ln(\alpha\text{-}1\text{-}P_2W_{17}O_{61})\}_2]^{14-}$

dimers exist in equilibrium with the 1:1 monomers in organic solution, particularly for the early Ln anions with tetraalkylammonium counterions.[9] From the atomic perspective of the Ln ion, the EXAFS results are insufficient to distinguish between a monomeric 1:1 formulation (with 8 O coordination) and a dimeric 2:2 stoichiometry (with 9 O coordination) in the style of Figures 1a and 1b, respectively. This issue is addressed in definitive fashion through use of direct measurements, including NMR spectroscopy, mass spectrometry, and small-angle X-ray scattering.[9, 37]

For the TBA^+-Ln-α-1 salts in which the coordination of MeCN is not possible and for the TBA^+-Yb-α-1 solution at the end of the series, the total O CNs obtained from all modeling of the Ln EXAFS present a consistent picture. For the Yb EXAFS in particular, this means that 7 O (4 $O_{\alpha\text{-}1}$ + 3 O_{H_2O}) are bound to Yb with an average distance of 2.27 ± 0.01 Å. In view of the similar IR for Yb(III) and Lu(III), 0.985 and 0.977Å, respectively, for CN = VIII.[17], why the Yb environment (with 7 O) in the TBA^+-Yb-α-1 solid should be different from that (with 8 O) in K^+-Lu-α-1 salt is not known. Despite the extensive, cumulative knowledge of this system,[4-8] including the complete assignment of the ^{183}W spectrum,[36] the intricacies and nuances of POM chemistry, in general, that are known to arise from solute and solvent effects on the molecular and crystal structures of Ln-POM complexes are always surprising, oftentimes unpredictable. Nevertheless, in the crystal structure,[6] the positional disorder of the Lu(III) ion over two sites in the P-W-O framework may account, in part, for the discrepancy. In this regard, the element-specificity of EXAFS has an advantage in that the metrical information is independent of the positional disorder of W but, a lack of site-specific sensitivity means that Yb EXAFS provides the site-averaged environment of Yb(III) ion. Despite this drawback, the lower

hydration number (3) for the TBA^+-Yb-α-1 complex when compared with those (4) for the TBA^+-Ln-α-1 complexes of the Ln(III) ions in the rest of the series, which was prepared and analyzed in identical fashion, is effectively rationalized in terms of spatial considerations. A larger ion, e.g., Nd(III), sits higher in the vacancy of the α-1 ligand and is more accessible to H_2O molecules than a smaller ion, e.g., Yb(III), which is bound deeper in the α-1 vacancy and is less accessible to H_2O, resulting in higher O CNs at the beginning of the 4f-period than at the end of it. In fact, steric arguments like these have been used to account for the presence of just 3.1±0.5 H_2O about Eu(III) in its 1:1 complex with $[GeW_{11}O_{39}]^{8-}$ (as determined by luminescence lifetime measurements)[66] and heptacoordinated Yb(III) in the 1:1 linear system built up with $[\alpha\text{-}SiW_{11}O_{39}]^{8-}$.[67] The 7-O, capped trigonal prism coordination environment of Yb(III) in $[(H_2O)_2Yb(\alpha\text{-}SiW_{11}O_{39})]^{5-}$ (illustrated in ESI Figure S21) has an average Yb-O distance of 2.31(4) Å, which is within one esd of the EXAFS results for the TBA^+-Yb-α-1 solid salt and its MeCN solution, providing ancillary support for 7 O coordination in the Yb-α-1 cluster anions. Additional precedence for a 1-O-lower CN for Yb than Nd is found in the situation that manifests itself in the coordination chemistry of Ce(III) in $[(H_2O)_3Ce(\alpha\text{-}2\text{-}As_2W_{17}O_{61})]^{7-}$ [68] and Er(III) in $[(H_2O)_2Er(\alpha\text{-}2\text{-}As_2W_{17}O_{61})]^{7-}$.[69] In the former, the large Ce ion is 8 coordinate with O (including 3 H_2O molecules) and, in the latter, the small Er ion is 7 coordinate with O (including 2 H_2O). Similar behavior is observed for the homoleptic Ln(III) aqua ion complexes, which are free of steric constraints from bulky ligands and in which the CN decreases from 9 to 8 across the period.[28-31] Even with the added steric complications of multidenticity of the α-1 ligand, the hydration of the Ln(III) ions in the Ln-α-1 complexes is more like that for the Ln aqua ions than for the solid salts of the

Ln(III) nonahydrates, which have a constant 9 O coordination across the entire period.[18, 19]

The O CN decrease with decreasing IR (increasing Z) is a simple steric effect, which applies equally well to the 1:1 species in MeCN media as studied here and the 2:2 dimers that form in aqueous media.[7, 70] With regard to the latter, one (or more) of the O atoms that our two-shell model has assumed as arising from water molecules (O_{H_2O}) may, in fact, be attributed to a terminal oxo interaction, consistent with Ce-O bond lengths for a 2:2 complex for the K^+-Ce-α-1 system.[7] Similarly, one of the O atoms that our models has assumed as arising from the α-1 ligand ($O_{\alpha\text{-}1}$) may include a scattering contribution to the terminal oxo interaction, consistent with La-O bond lengths for a 2:2 complex stoichiometry for K^+-La-α-1.[9] In either case, and in view of the well known complications of the Ln- and transition-metal-α-1 system chemistry with variations of countercation, anion concentration, solution pH and temperature,[7, 8, 10, 51, 71] the additional complication of monomer association and dimer dissociation equilibria in MeCN is not unexpected. Even simple, dilute solutions of salts of MeCN solvates, e.g., $[Ln(NCCH_3)_9](AlCl_4)_3$, in anhydrous MeCN reveal complicated equilibrium behaviors,[32] including Ln-$NCCH_3$ interactions of sizable strengths as judged by vibrational spectroscopy.[32, 72]

3.4 Conclusions

The prospect of Eu(III)/Eu(II) redox activity in the TBA^+-Eu-α-1 salt dissolved in MeCN, corresponding to the behavior of the K^+-Eu-α-1 salt dissolved in H_2O, was not realized under the experimental conditions of the work reported herein. Instead, the heterobinuclear molecular anion exhibits W-based redox activity of the electroactive

ligand, α-1-$[P_2W_{17}O_{61}]^{10-}$, that is strongly perturbed by complexation of Eu(III) and five other Ln(III) ions (for Z = 60–70) as well. Multielectron reduction leads to the formation of heteropoly blue species with chemical instabilities on time scales typical of voltammetric measurements and a significant concentration-dependence of the electroanalytical behaviors. The absence of a one-electron Eu(III) ⇆ Eu(II) couple suggests that the energetics of the 4f-orbital interactions with the LUMO of essentially W 5d-orbital character are unfavorable and uncooperative, a possible result of the Eu(III) ions' direct exposure to the MeCN solvent. In this regard, the comparative metrical data obtained about the inner-sphere Eu coordination environments in the solid salt of TBA^+-Eu-α-1 and upon its dissolution in dry MeCN with a 0.1 M $TBAPF_6$ electrolyte suggest that MeCN binds to Eu(III) in part ($0 < \delta < 4$) and in exchange with H_2O, forming a mixed H_2O-MeCN solvate. These results, in combination with the EXAFS results for the TBA^+-Ln-α-1 systems across the 4f period provide a fresh perspective on the variation of Ln(III) coordination in MeCN, including the effects of the lanthanoid contraction as well as known variations of MeCN and H_2O residence times. For example, a number of characteristic trends in interatomic distances and O CNs with Ln(III) ions for solid salts of TBA^+-Ln-α-1 and their solutions in MeCN reveal subtle alterations, indicating the absence of dramatic modifications to the O coordination environments of Ln(III) upon the dissolution of the salts. With the well-known variation of bond lengths that is characteristic of the lanthanoid contraction, we find that the Ln coordination number decreases by 1 O from 8 O for Ln = Nd–Dy to 7 O for Yb. This variation may be driven by the simple period behavior of decreasing ionic radii with increasing Z in association with a myriad of corresponding solution equilibria, especially solvent (H_2O—CH_3CN)

exchange. The long Nd-O distance obtained from the one-shell fitting model for the MeCN solution of TBA^+-Nd-α-1, although consistent with that for 9 O coordination, was shown through use of a two-shell fitting model to be a manifestation of MeCN coordination. In fact, the dissolution of the TBA^+-α-1 salts of both Nd and Sm in dry MeCN indicates that one (or more) H_2O molecules bound to each in the solid salts are exchanged with MeCN molecules pursuant to Eq. (1). This response is consistent with larger average residence times for MeCN coordination to the early, light Ln(III) ions than to the late, heavy ones. The systematic, interatomic variations of the metrical parameters, which provide an atomic-level perspective of the Ln(III) ions across the period, complement the exhaustive results obtained previously in aqueous media from the perspective of the framework P and W atoms by use of ^{31}P and ^{183}W NMR spectroscopy. The information obtained here for the MeCN solutions of TBA^+-Ln-α-1 with 0.1 M $TBAPF_6$ electrolyte is of prospective use on a number of active fronts, especially the continuing efforts to resolve the enantiomers of Ln-α-1 for their subsequent use in stereoselective reactions.[73, 74]

3.5 Figures

Figure 1. Ball and stick model of the O coordination environments of (a) Lu(III) with 8 O square antiprism geometry in $[(H_2O)_4Lu(\alpha\text{-}1\text{-}P_2W_{17}O_{61})]^{7-}$ as the K^+ salt;[6] (b) La(III) and Ce(III) with 9 O monocapped square antiprism geometry in $[\{(H_2O)_4Ln(\alpha\text{-}1\text{-}P_2W_{17}O_{61})\}_2]^{14-}$ as the K^+ and NH_4^+ salts, respectively;[7, 9] (c) La(III) with 8 O square antiprism geometry in $[La(\alpha\text{-}1\text{-}P_2W_{17}O_{61})_2]^{17-}$ as the K^+ salt.[8] The red circles are the Ln ions which are connected to terminal O_{H_2O} (blue circles) and $O_{\alpha\text{-}1}$ atoms (open circles) bridging to W atoms (gray circles). The insets show the entire molecular anions.

Figure 2. Cyclic voltammograms of 1.5 mM (black lines) and 3.5 mM (blue lines) TBA^+ salts of $\alpha\text{-}1\text{-}[P_2W_{17}O_{61}]^{10-}$ with background scan (grey dashed line); Eu-α-1; and Y-α-1 on GC electrodes in dry MeCN with 0.1 M $TBAPF_6$ electrolyte at ν = 100 mV s^{-1}, starting at +0.2 V.

Figure 3. Differential pulse voltammograms of 1.5 mM (black lines) and 3.5 mM (blue lines) TBA^+ salts of $\alpha\text{-}1\text{-}[P_2W_{17}O_{61}]^{10-}$; Eu-α-1; and Y-α-1 on GC electrodes in dry MeCN with 0.1 M $TBAPF_6$ electrolyte at ν = 20 mV s^{-1} from separate scans to negative electrode potentials (initial E = +0.2 V → final E = -2.6 V) and to positive electrode potentials (initial E = -2.6 V → final E = +0.2 V) providing the negative and the positive current responses, respectively.

Figure 4. Normalized Eu L_3-edge XANES spectra of a freshly prepared, fully-oxidized 4.3 mM TBA^+-Eu-α-1 solution at open circuit condition (dashed black line) in the in 0.1

M $TBAPF_6$ electrolyte in MeCN and its reduced, heteropoly blue form obtained with the GR electrode polarized at -1.50 V (blue line). The teal line shows the response after the deliberate addition of H_2O to a freshly prepared 4.3 mM TBA^+-Eu-α-1 solution in MeCN with added electrolyte.

Figure 5. Eu L_3-edge $k^3\chi(k)$ EXAFS data (left) and corresponding Fourier transform data (right) for the TBA^+-Eu-α-1 solid salt (solid red line) and its freshly prepared, fully-oxidized 4.3 mM solution (dashed line) at rest potential. The offset teal line shows the response after the deliberate addition of H_2O to a freshly prepared 4.3 mM TBA^+-Eu-α-1 solution l as described in Figure 4.

Figure 6. Normalized Ln L_3-edge XANES, I_f/I_0, for the 4.3 mM solutions of TBA^+-Ln-α-1 in MeCN with 0.1 M $TBAPF_6$ electrolyte. The inflection point energies obtained from the first differential XANES are given in Table 2.

Figure 7. The L_3-edge (2p → 5d) resonance FWHM and normalized peak intensities vs. atomic number for the 4.3 mM solutions of the TBA^+-Ln-α-1 salts in MeCN with 0.1 M $TBAPF_6$ (filled and open squares, respectively). The natural level widths are shown are shown as filled circles.

Figure 8. Left panel. The Ln L_3-edge $k^3\chi(k)$ EXAFS data for the TBA^+-Ln-α-1 solid salts (solid red lines) and their freshly-prepared 4.3 mM solutions in the MeCN electrolyte. Right panel. The corresponding FT data.

Figure 9. (a) Variation of O CNs (black symbols, left axis) and average Ln-O distances (blue symbols, right axis) vs. Z from the one-shell model fits to $k^3\chi(k)$ EXAFS data for the TBA^+-Ln-α-1 solid salts (squares) and their MeCN solutions (circles). Symbols connected with solid lines refer to the data obtained on the solids, whereas the symbols connected with dashed lines refer to the results obtained for the solutions. The red and green lines with the up and down triangle symbols are the average Ln-O_8 and Ln-O_9 distances for $[Ln(PMo_{11}O_{39})_2]^{11-}$ and $[Ln(OH_2)_9]^{3+}$, respectively.[19, 20] The orange line with the diamond symbols provides the Ln-O_7 distances calculated as the sum of Ln(III) and O^{2-} ionic radii. The magenta diamond at Z = 70 shows the average Yb-N_8 bond length for $[Yb(NCMe)_8]^{3+}$.[27] (b) Variation of O_{H_2O} CNs (blue open symbols, left axis) and average Ln-$O_{α-1}$ and Ln-O_{H_2O} distances (red open and blue filled symbols, respectively, right axis) vs. Z from the two-shell model fits to $k^3\chi(k)$ EXAFS data for the TBA^+-Ln-α-1 solid salts (squares) and their MeCN solutions (circles). Symbols connected with solid lines refer to the data obtained on the solids, whereas the symbols connected with dashed lines refer to the results obtained for the solutions. The Ln-$O_{α-1}$ distances shown (red open symbols) were obtained with a fixed $O_{α-1}$ CN = 4, indicated with a dotted red line. The magenta diamonds and dashed line show the average Ln-N_x bond lengths for acetonitrile solvates, $[Ln(NCCH_3)_x]^{3+}$ where x = 9 for Nd, Sm, Dy; x = 8 for Yb.[26, 27]

Figure 1

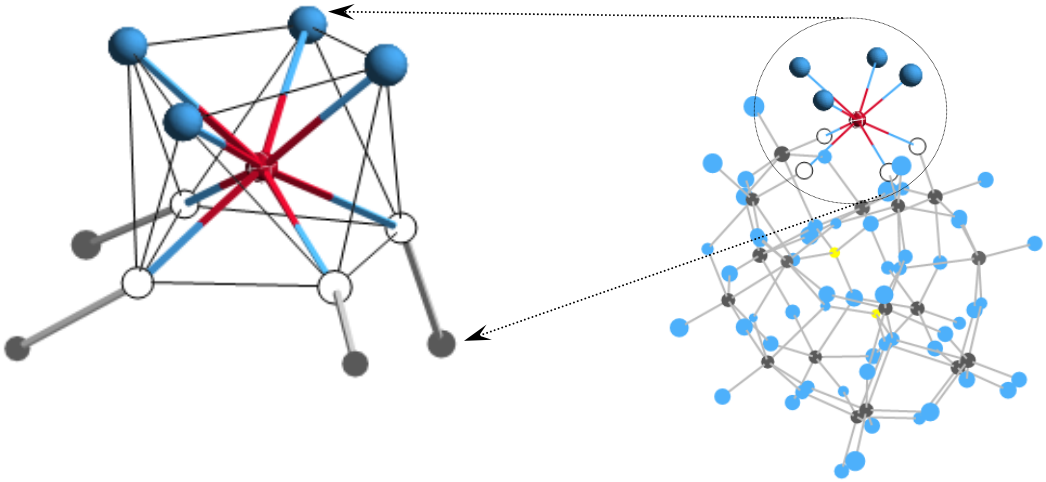

a

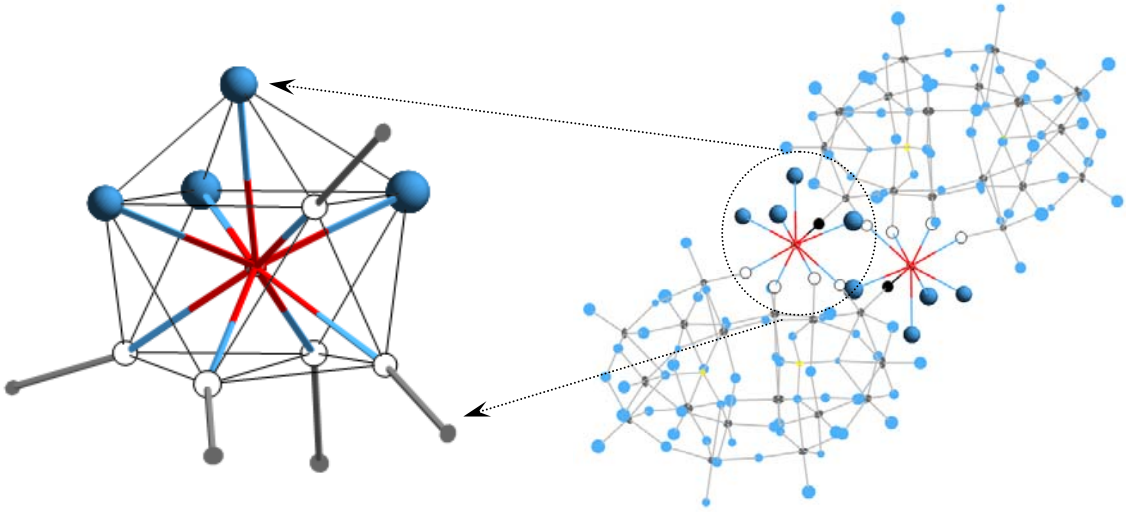

b

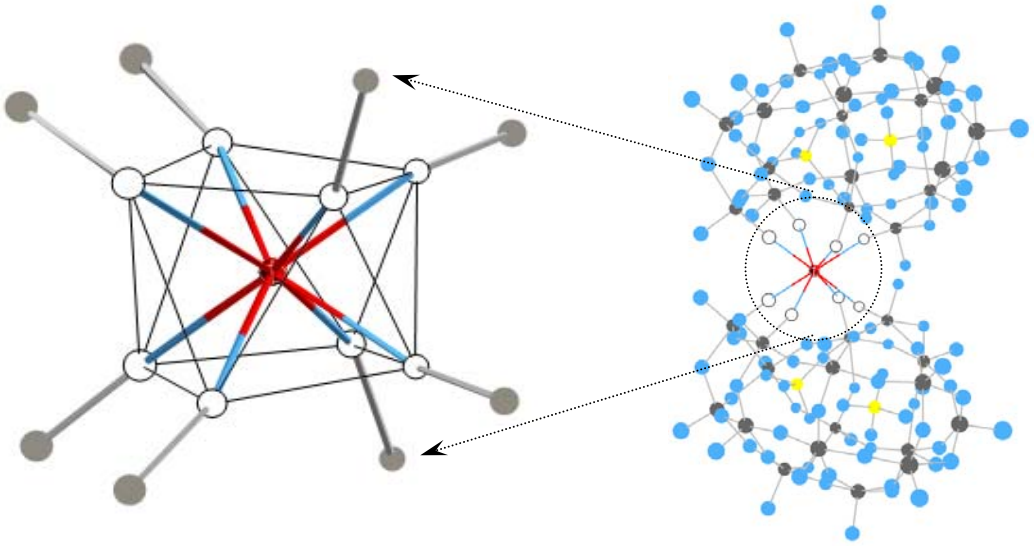

c

Figure 2

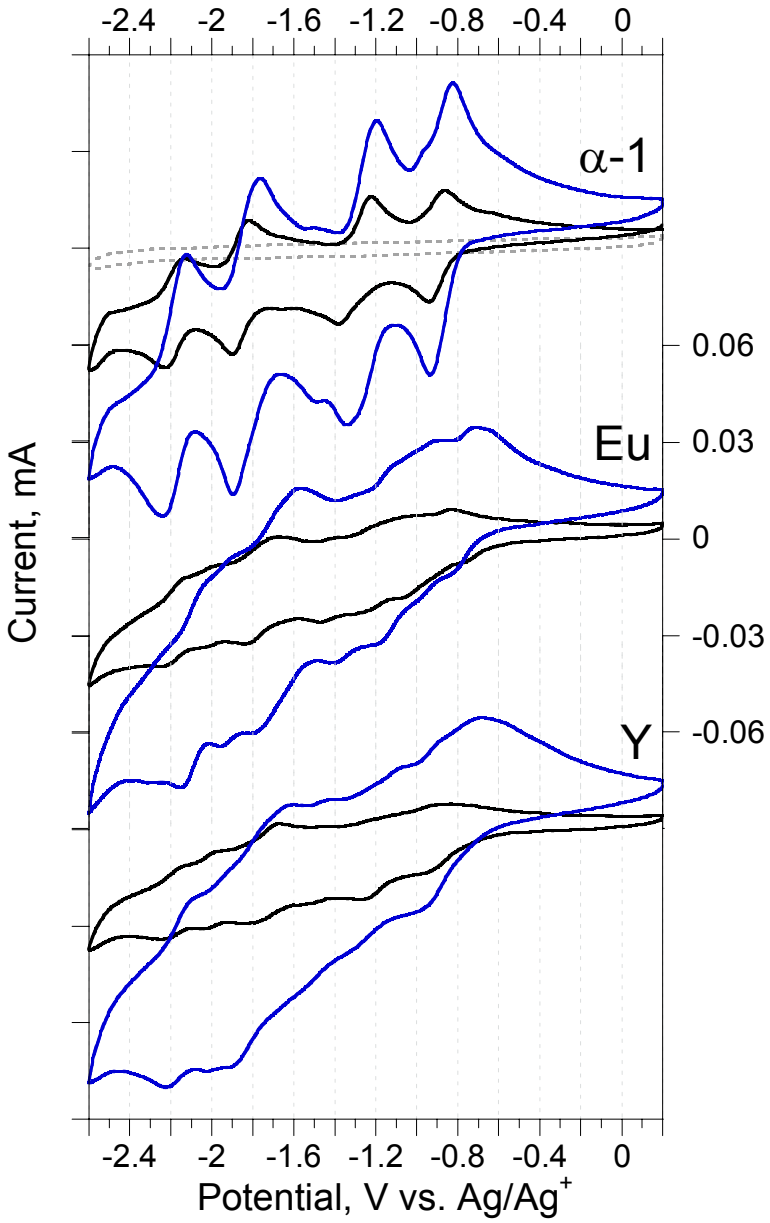
-2.4
-2
-1.6
-1.2
-0.8
-0.4
0
α-1
Eu
Y
0.06
0.03
0
-0.03
-0.06
Current, mA
Potential, V vs. Ag/Ag+

Figure 3

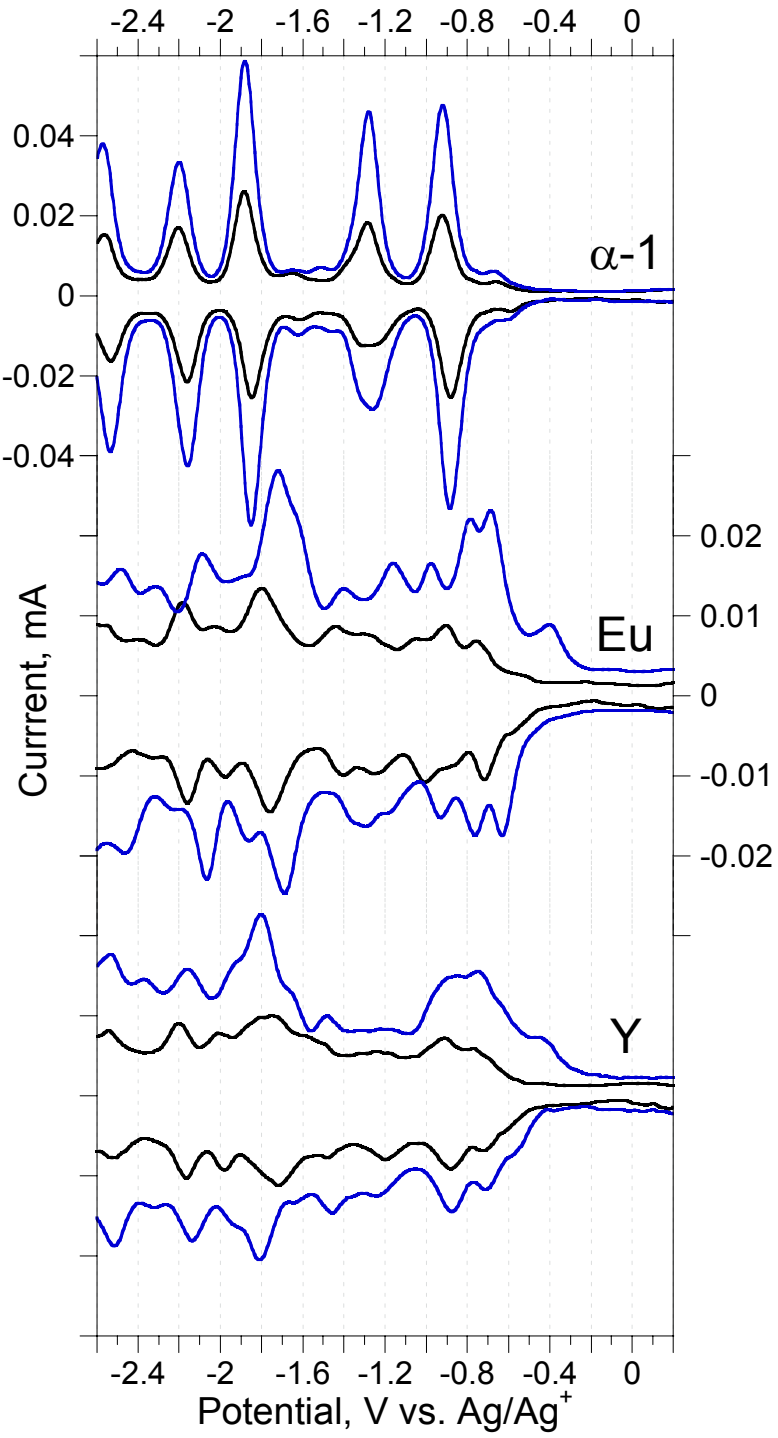
-2.4
-2
-1.6
-1.2
-0.8
-0.4
0
0.04
0.02
0
-0.02
-0.04
α-1
Eu
Y
0.02
0.01
0
-0.01
-0.02
Currrent, mA
Potential, V vs. Ag/Ag+

Figure 4

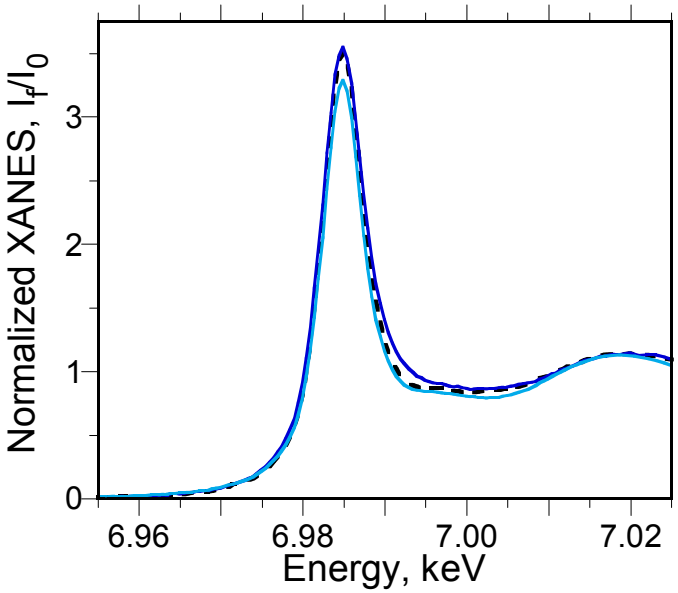

Figure 5

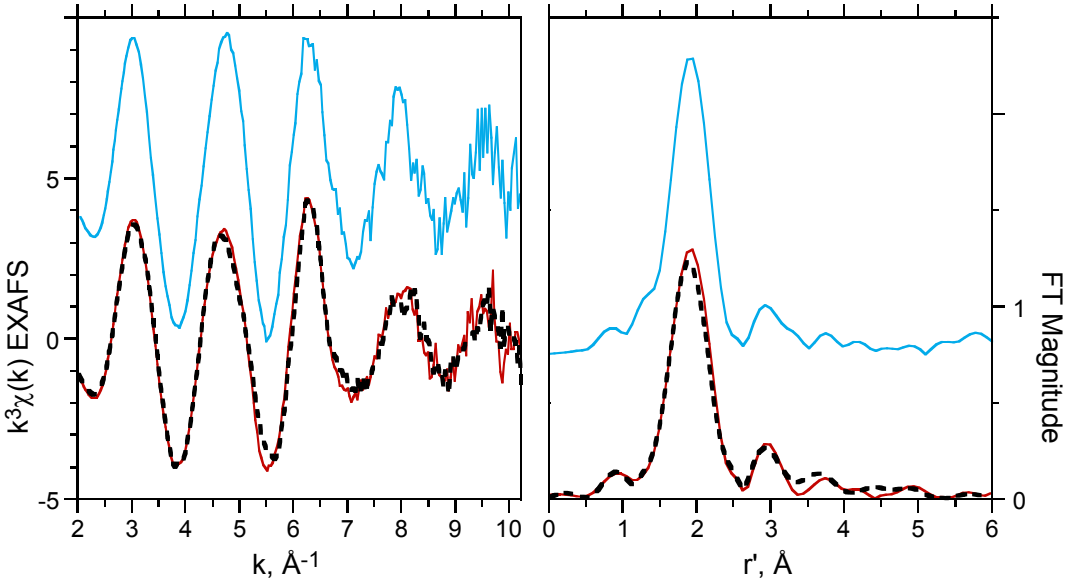

Figure 6

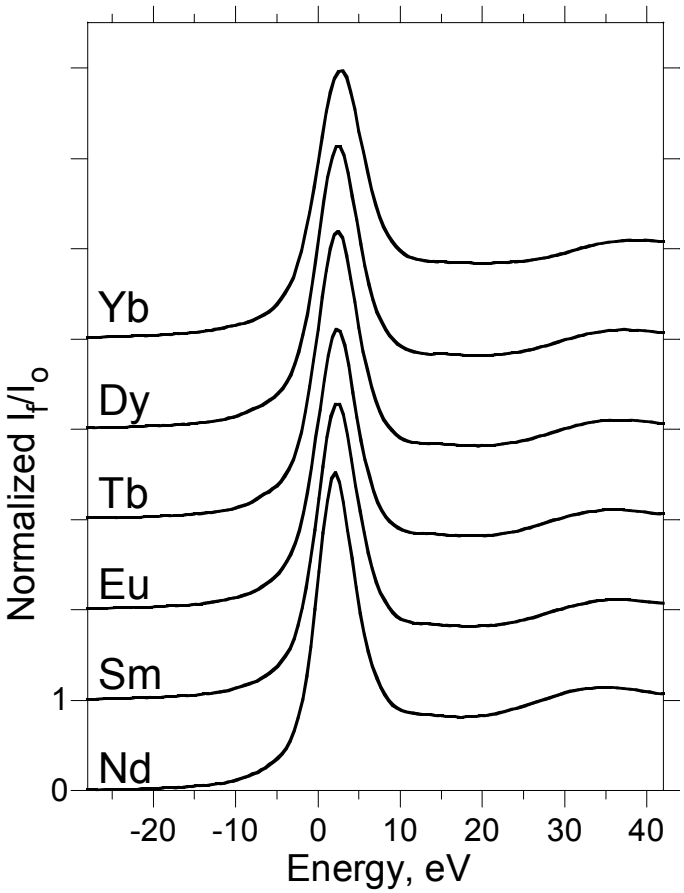

Figure 7

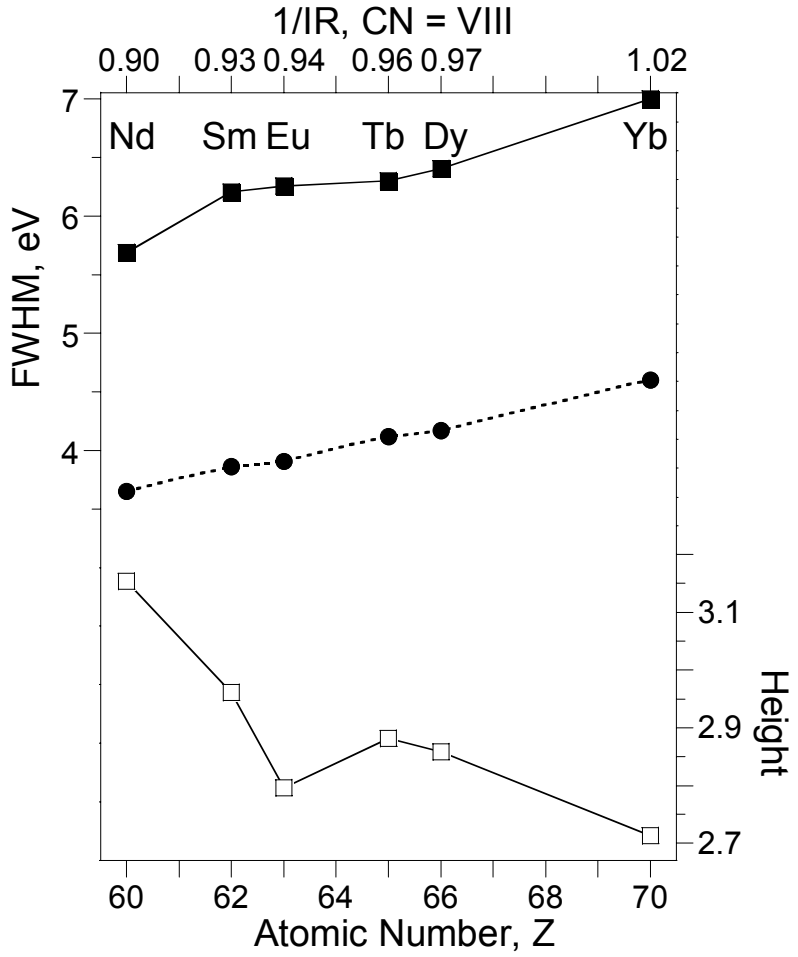
1/IR, CN = VIII
0.90
0.93
0.94
0.96
0.97
1.02
Nd
Sm
Eu
Tb
Dy
Yb
FWHM, eV
7
6
5
4
3.1
2.9
2.7
Height
60
62
64
66
68
70
Atomic Number, Z

Figure 8

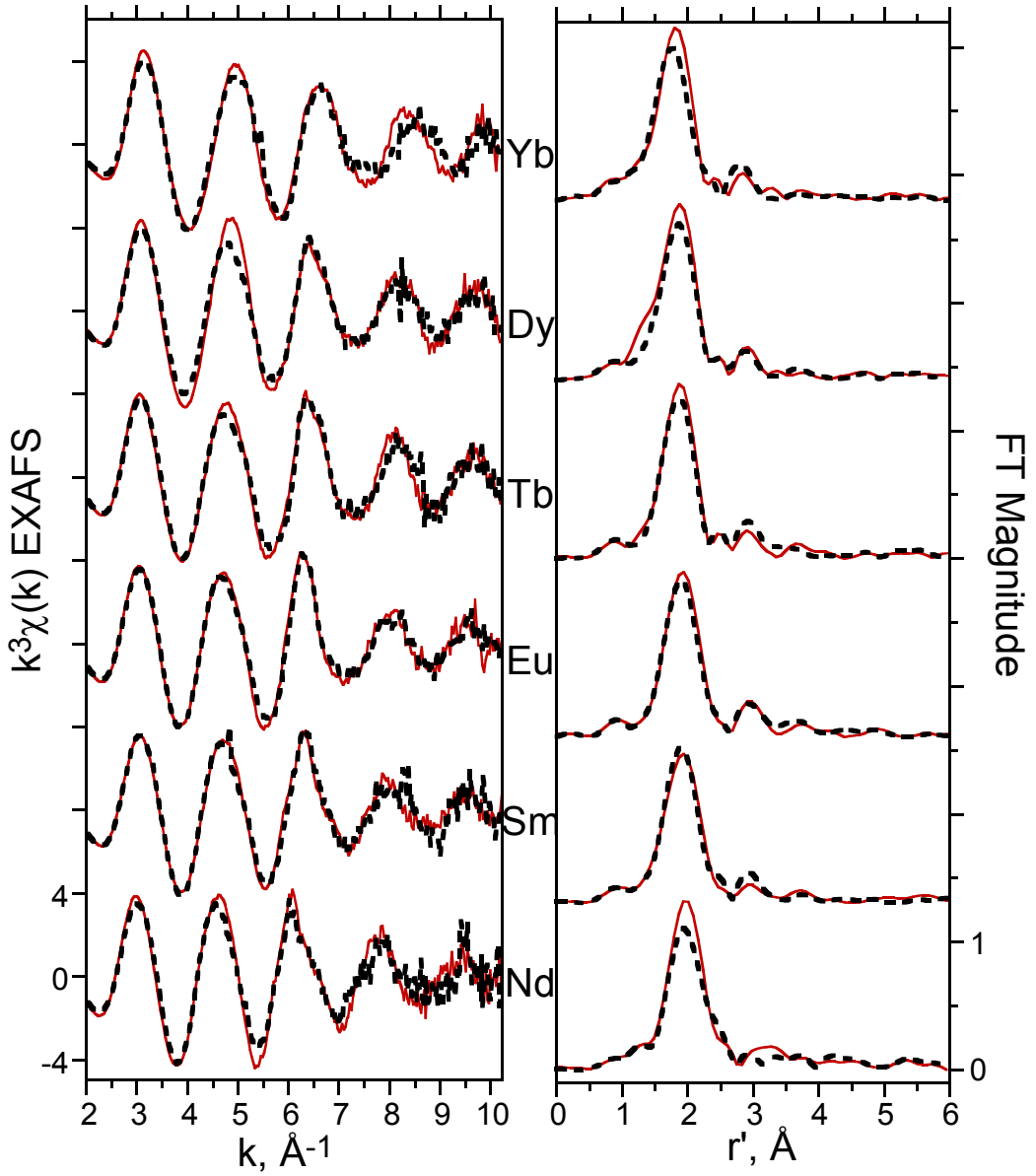
Yb
Dy
Tb
Eu
Sm
Nd
k$^3\chi$(k) EXAFS
FT Magnitude
k, Å^{-1}
r', Å
4
0
-4
1
0
2 3 4 5 6 7 8 9 10
0 1 2 3 4 5 6

Figure 9

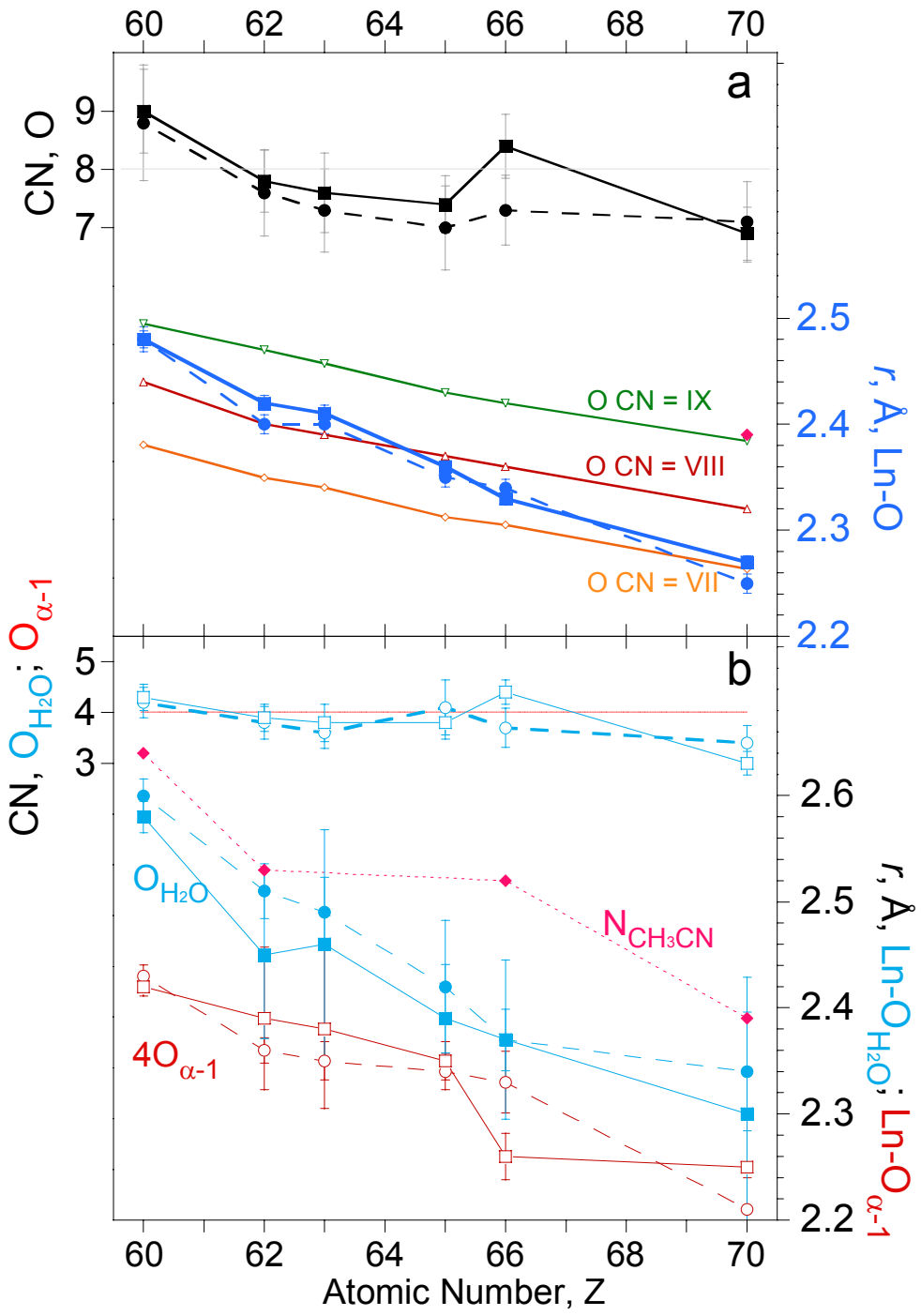
a
b
CN, O
r, Å, Ln-O
O CN = IX
O CN = VIII
O CN = VII
CN, O$_{H_2O}$; O$_{\alpha-1}$
r, Å, Ln-O$_{H_2O}$; Ln-O$_{\alpha-1}$
O$_{H_2O}$
N$_{CH_3CN}$
4O$_{\alpha-1}$
Atomic Number, Z

3.6 Tables

Table 1. ^{31}P NMR data for solutions (5 mM) of K^+-Ln-α-1 and TBA^+-Ln-α-1 salts.

Compound	Chemical Shift,[a] δ, ppm		Solvent
	P1	P2	
K^+-Nd-α-1	-14.5	-22.1	D_2O
K^+-Sm-α-1	-12.6	-13.5	D_2O
K^+-Eu-α-1	6.4	-11.4	D_2O
K^+-Tb-α-1	-176.2	-47.5	D_2O
K^+-Dy-α-1	-113.1	-29.2	D_2O
K^+-Yb-α-1	27.6	-6.2	D_2O
TBA^+-Nd-α-1	-16.9	-22.4	D_3CCN/10 % D_2O
TBA^+-Sm-α-1	-11.5	-12.1	D_3CCN/10 % D_2O
TBA^+-Eu-α-1	2.4	-14.2	D_3CCN/10 % D_2O
TBA^+-Tb-α-1	-198.7	-72.6	D_3CCN/10 % D_2O
TBA^+-Dy-α-1	-90.8	-42.2	D_3CCN/10 % D_2O
TBA^+-Yb-α-1	34.3	-1.7	D_3CCN/10 % D_2O

[a] P1 is the phosphorus atom near the vacancy; P2 is the phosphorus remote from the vacancy. All spectra were recorded at a concentration of 5.0 mM. ^{31}P spectra were referenced to 85% H_3PO_4.

Table 2. Results from one-O and two-O ($O_{\alpha\text{-}1}$ and O_{H_2O}) shell curve-fitting analyses of the Eu L_3-edge $k^3\chi(k)$ EXAFS of Figure 5 for the TBA^+-Eu-α-1 salt and its 4.3 mM solution in dry MeCN and with the deliberate addition of 20 % (vol.) H_2O.[a]

Sample form	Shell	CN[b]	r,[c] Å	σ^2,[d] Å^2	ΔE_0,[e] eV
Solid salt	O	7.6(7)	2.41(1)	0.011(1)	2.1
	$O_{\alpha\text{-}1}$	4	2.38(4)	0.008(3)	2.4
	O_{H_2O}	3.8(11)	2.46(5)	0.013(9)	/[f]
MeCN solution	O	7.3(7)	2.40(1)	0.012(2)	1.6
	$O_{\alpha\text{-}1}$	4	2.35(2)	0.006(4)	2.2
	O_{H_2O}	3.6(9)	2.49(3)	0.008(8)	/
MeCN solution + H_2O	O	7.5(8)	2.39(1)	0.010(2)	1.0
	$O_{\alpha\text{-}1}$	4	2.35(1)	0.001(1)	1.8
	O_{H_2O}	2.7(8)	2.51(2)	0.001(1)	/

[a] The number in the parentheses represent the estimated standard deviations (3σ) obtained from the least-squares fits. [b] Coordination number. [c] Interatomic distance. [d] The Debye-Waller factor, the root-mean-square deviation of the average Eu-X bond length, for X ≡ O, P, W. [e] The energy difference between the experimental and theoretical values of E_0. [f] Parameter fixed to value in column above.

Table 3. Results from the curve-fitting analyses of the normalized Ln L_3-edge XANES of the 4.3 mM TBA^+-Ln-α-1 MeCN solutions with a pseudo-Voight line shape to model the edge resonance and an arctangent function to model the edge jump. The corresponding data for the solid salts are provided as Table S9 (ESI).

Solution	Ln edge resonances				Edge steps			ip,[a] eV
	Height	Position	FWHM	Area	Height	Position	FWHM	
TBA^+-Nd-α-1	3.154	2.13	5.69	21.419	1.002	4.94	13.48	6213.7
TBA^+-Sm-α-1	2.961	2.36	6.21	21.918	1.011	6.19	16.31	6720.1
TBA^+-Eu-α-1	2.796	2.33	6.26	21.308	1.024	7.06	17.36	6980.6
TBA^+-Tb-α-1	2.881	2.37	6.30	21.886	0.991	6.30	15.81	7518.5
TBA^+-Dy-α-1	2.858	2.44	6.40	22.455	0.966	6.48	15.10	7795.4
TBA^+-Yb-α-1	2.713	2.67	7.00	22.992	0.952	6.56	14.10	8949.1

[a] Energy of the inflection point in the first differential XANES.

Table 4. Results from one-O and two-O ($O_{\alpha\text{-}1}$ and O_{H_2O}) shell curve-fitting analyses of the Ln L_3-edge $k^3\chi(k)$ EXAFS of Figure 8 for the 4.3 mM solutions of the TBA^+-Ln-α-1 salts in MeCN. The parameter definitions are the same as those in Table 2. The corresponding results for the solid salts are provided as Tables S1 and S4 (ESI).

Solution	Shell	CN	r, Å	σ^2, Å^2	ΔE_0, eV
TBA^+-Nd-α-1	O	8.8(9)	2.48(1)	0.016(2)	0.9
	$O_{\alpha\text{-}1}$	4	2.43(1)	0.003(2)	2.3
	O_{H_2O}	4.2(9)	2.60(2)	0.005(4)	/
TBA^+-Sm-α-1	O	7.6(7)	2.40(1)	0.012(2)	-0.3
	$O_{\alpha\text{-}1}$	4	2.36(1)	0.005(2)	1.13
	O_{H_2O}	3.8(10)	2.51(3)	0.009(7)	/
TBA^+-Tb-α-1	O	7.0(7)	2.35(1)	0.010(2)	-1.2
	$O_{\alpha\text{-}1}$	4	2.34(2)	0.006(1)	0.1
	O_{H_2O}	4.1(16)	2.42(6)	0.022(15)	/
TBA^+-Dy-α-1	O	7.3(6)	2.34(1)	0.012(1)	-0.8
	$O_{\alpha\text{-}1}$	4	2.33(3)	0.009(3)	-0.5
	O_{H_2O}	3.7(11)	2.37(8)	0.018(14)	/
TBA^+-Yb-α-1	O	7.1(7)	2.25(1)	0.013(2)	-0.9
	$O_{\alpha\text{-}1}$	4	2.21(3)	0.008(4)	-0.2
	O_{H_2O}	3.4(10)	2.34(6)	0.012(13)	/

3.7 References

1. C. L. Hill, in *Applications of Coordination Chemistry*, ed. M. Ward, Elsevier, Oxford, 2004, Vol. 4, pp. 679-759.
2. J. F. Kirby and L. C. W. Baker, *Inorg. Chem.*, 1998, **37**, 5537-5543.
3. C. Zhang, R. C. Howell, K. B. Scotland, F. G. Perez, L. Todaro and L. C. Francesconi, *Inorg. Chem.*, 2004, **43**, 7691-7701.
4. J. Bartis, M. Dankova, J. J. Lessmann, Q. H. Luo, W. D. Horrocks and L. C. Francesconi, *Inorg. Chem.*, 1999, **38**, 1042-1053.
5. J. P. Ciabrini and R. Contant, *J. Chem. Res.-S*, 1993, 391-391.
6. Q. H. Luo, R. C. Howell, M. Dankova, J. Bartis, C. W. Williams, W. D. Horrocks, V. G. Young, A. L. Rheingold, L. C. Francesconi and M. R. Antonio, *Inorg. Chem.*, 2001, **40**, 1894-1901.
7. M. Sadakane, M. H. Dickman and M. T. Pope, *Inorg. Chem.*, 2001, **40**, 2715-2719.
8. C. Zhang, R. C. Howell, Q. H. Luo, H. L. Fieselmann, L. J. Todaro and L. C. Francesconi, *Inorg. Chem.*, 2005, **44**, 3569-3578.
9. C. Boglio, G. Lenoble, C. Duhayon, B. Hasenknopf, R. Thouvenot, C. Zhang, C. Howell R., P. Burton-Pye B., C. Francesconi L., E. Lacote, S. Thorimbert, M. Malacria, C. Afonso and J.-C. Tabet, *Inorg. Chem.*, 2006, **45**, 1389-1398.
10. C. Boglio, B. Hasenknopf, G. Lenoble, P. Remy, P. Gouzerh, S. Thorimbert, E. Lacote, M. Malacria and R. Thouvenot, *Chem.-Eur. J.*, 2008, **14**, 1532-1540.
11. A. Ostuni, R. E. Bachman and M. T. Pope, *J. Clust. Sci.*, 2003, **14**, 431-446.
12. E. Derat, E. Lacote, B. Hasenknopf, S. Thorimbert and M. Malacria, *J. Phys. Chem. A*, 2008, **112**, 13002-13005.

13. J. Jing, B. P. Burton-Pye, L. C. Francesconi and M. R. Antonio, *Inorg. Chem.*, 2008, **47**, 6889-6899.

14. E. J. Cokal and E. N. Wise, *J. Electroanal. Chem.*, 1966, **11**, 406-415.

15. I. M. Kolthoff and J. F. Coetzee, *J. Am. Chem. Soc.*, 1957, **79**, 1852-1858.

16. S. G. Bratsch, *J. Phys. Chem. Ref. Data*, 1989, **18**, 1-21.

17. R. D. Shannon, *Acta Cryst.*, 1976, **A32**, 751-767.

18. A. Chatterjee, E. N. Maslen and K. J. Watson, *Acta Crystallogr. Sect. B-Structural Science*, 1988, **44**, 381-386.

19. R. E. Gerkin and W. J. Reppart, *Acta Crystallogr. Sect. C-Cryst. Struct. Commun.*, 1984, **40**, 781-786.

20. R. Copping, A. J. Gaunt, I. May, M. J. Sarsfield, D. Collison, M. Helliwell, I. S. Denniss and D. C. Apperley, *Dalton Trans.*, 2005, 1256-1262.

21. A. J. Gaunt, I. May, M. J. Sarsfield, D. Collison, M. Helliwell and I. S. Denniss, *Dalton Trans.*, 2003, 2767-2771.

22. B. S. Bassil, M. H. Dickman, B. von der Kammer and U. Kortz, *Inorg. Chem.*, 2007, **46**, 2452-2458.

23. E. A. Quadrelli, *Inorg. Chem.*, 2002, **41**, 167-169.

24. M. Seitz, A. G. Oliver and K. N. Raymond, *J. Am. Chem. Soc.*, 2007, **129**, 11153-11160.

25. Plots of the average Ln-O_9 distances of Gerkin and Reppart,[19] as well as the average Ln-O_8 distance of Copping et al.[20] are shown in Figure 9.

26. G. Bodizs, I. Raabe, R. Scopelliti, I. Krossing and L. Helm, *Dalton Trans.*, 2009, 5137-5147.

27. G. B. Deacon, B. Gortler, P. C. Junk, E. Lork, R. Mews, J. Petersen and B. Zemva, *J. Chem. Soc.-Dalton Trans.*, 1998, 3887-3891.

28. A. Abbasi, P. Lindqvist-Reis, L. Eriksson, D. Sandstrom, S. Lidin, I. Persson and M. Sandstrom, *Chem.-Eur. J.*, 2005, **11**, 4065-4077.

29. C. Cossy, L. Helm, D. H. Powell and A. E. Merbach, *New J. Chem.*, 1995, **19**, 27-35.

30. A. Habenschuss and F. H. Spedding, *J. Chem. Phys.*, 1979, **70**, 2797-2806.

31. A. Habenschuss and F. H. Spedding, *J. Chem. Phys.*, 1980, **73**, 442-450.

32. J.-C. G. Buenzli and A. Milicic-Tang, *Inorg. Chim. Acta*, 1996, **252**, 221-228.

33. M. Baaden, F. Berny, C. Madic and G. Wipff, *J. Phys. Chem. A*, 2000, **104**, 7659-7671.

34. R. Contant, in *Inorganic Syntheses*, ed. A. P. Ginsberg, Wiley-Interscience, New York, 1990, Vol. 27, pp. 104-107.

35. J. Bartis, Y. Kunina, M. Blumenstein and L. C. Francesconi, *Inorg. Chem.*, 1996, **35**, 1497-1501.

36. G. Lenoble, B. Hasenknopf and R. Thouvenot, *J. Am. Chem. Soc.*, 2006, **128**, 5735-5744.

37. B. P. Burton-Pye and L. C. Francesconi, *Dalton Trans.*, 2010, in preparation.

38. P. G. Rickert, M. R. Antonio, M. A. Firestone, K. A. Kubatko, T. Szreder, J. F. Wishart and M. L. Dietz, *Dalton Trans.*, 2007, 529-531.

39. A. J. Bard and L. R. Faulkner, *Electrochemical Methods: Fundamentals and Applications*, 2nd Edn., J. Wiley, New York, 2001.

40. M. A. Beno, M. Engbretson, G. Jennings, G. S. Knapp, J. Linton, C. Kurtz, U. Rütt and P. A. Montano, *Nucl. Instrum. Methods Phys. Res. A*, 2001, **467-468**, 699-702.

41. For documentaion and availability, see http://www-ssrl.slac.stanford.edu/exafspak.html

42. J. J. Rehr and R. C. Albers, *Rev. Mod. Phys.*, 2000, **72**, 621-654.

43. W. W. Lukens, J. J. Bucher, D. K. Shuh and N. M. Edelstein, *Environ. Sci. Technol.*, 2005, **39**, 8064-8070.

44. T. Ressler, *J. Phys. IV*, 1997, **7**, 269-270.

45. M. R. Antonio and L. Soderholm, *J. Cluster Sci.*, 1996, **7**, 585-591.

46. M. R. Antonio, L. Soderholm and I. Song, *J. Appl. Electrochem.*, 1997, **27**, 784-792.

47. E. Papaconstantinou and M. T. Pope, *Inorg. Chem.*, 1970, **9**, 667-669.

48. M. T. Pope, *NATO Advanced Study Institutes Series, Series C: Mathematical and Physical Sciences*, 1980, **58**, 365-386.

49. M. T. Pope and E. Papaconstantinou, *Inorg. Chem.*, 1967, **6**, 1147-1152.

50. G. M. Varga, Jr., E. Papaconstantinou and M. T. Pope, *Inorg. Chem.*, 1970, **9**, 662-667.

51. R. Contant, M. Richet, Y. W. Lu, B. Keita and L. Nadjo, *Eur. J. Inorg. Chem.*, 2002, 2587-2593.

52. M. R. Antonio and M. H. Chiang, *Inorg. Chem.*, 2008, **47**, 8278-8285.

53. D. M. Way, A. M. Bond and A. G. Wedd, *Inorg. Chem.*, 1997, **36**, 2826-2833.

54. J. N. Barrows and M. T. Pope, *Inorg. Chim. Acta*, 1993, **213**, 91-98.

55. H. R. Murner, E. Chassat, R. P. Thummel and J. C. G. Bunzli, *J. Chem. Soc.-Dalton Trans.*, 2000, 2809-2816.

56. S. Petoud, J. C. G. Bunzli, T. Glanzman, C. Piguet, Q. Xiang and R. P. Thummel, *J. Lumines.*, 1999, **82**, 69-79.

57. E. L. Yee, O. A. Gansow and M. J. Weaver, *J. Am. Chem. Soc.*, 1980, **102**, 2278-2285.

58. J. Röhler, in *Handbook on the Physics and Chemistry of Rare Earths*, eds. K. A. Gschneidner, Jr, L. Eyring and S. Hüfner, North-Holland, Amsterdam, 1987, Vol. 10 - High Energy Spectroscopy, pp. 453-545.

59. S. Ishiguro, Y. Umebayashi and M. Komiya, *Coord. Chem. Rev.*, 2002, **226**, 103-111.

60. S. Skanthakumar, M. R. Antonio, R. E. Wilson and L. Soderholm, *Inorg. Chem.*, 2007, **46**, 3485-3491.

61. M. H. Chiang, J. A. Dzielawa, M. L. Dietz and M. R. Antonio, *J. Electroanal. Chem.*, 2004, **567**, 77-84.

62. X. Lopez, C. Bo and J. M. Poblet, *Inorg. Chem.*, 2003, **42**, 2634-2638.

63. M. R. Antonio, M. Nyman and T. M. Anderson, *Angew. Chem., Int. Ed. Engl.*, 2009, **48**, 6136-6140.

64. M. O. Krause and J. H. Oliver, *J. Phys. Chem. Ref. Data*, 1979, **8**, 329-338.

65. J. K. Beattie, S. P. Best, B. W. Skelton and A. H. White, *J. Chem. Soc.-Dalton Trans.*, 1981, 2105-2111.

66. C. E. VanPelt, W. J. Crooks and G. R. Choppin, *Inorg. Chim. Acta*, 2003, **346**, 215-222.

67. P. Mialane, L. Lisnard, A. Mallard, J. Marrot, E. Antic-Fidancev, P. Aschehoug, D. Vivien and F. Secheresse, *Inorg. Chem.*, 2003, **42**, 2102-2108.

68. X. Y. Zhao, S. X. Liu, Y. H. Ren, J. F. Cao, R. G. Cao and K. Z. Shao, *J. Solid State Chem.*, 2008, **181**, 2488-2493.

69. L. Z. Liu, F. Y. Li, L. Xu, X. Z. Liu and G. G. Gao, *J. Solid State Chem.*, 2010, **183**, 350-355.

70. M. Sadakane, A. Ostuni and M. T. Pope, *J. Chem. Soc., Dalton Trans.*, 2002, 63-67.

71. B. Keita, F. Girard, L. Nadjo, R. Contant, J. Canny and M. Richet, *J. Electroanal. Chem.*, 1999, **478**, 76-82.

72. J. C. G. Bunzli and V. Kasparek, *Inorg. Chim. Acta*, 1991, **182**, 101-107.

73. C. Boglio, G. Lemiere, B. Hasenknopf, S. Thorimbert, E. Lacote and M. Malacria, *Angew. Chem., Int. Ed. Engl.*, 2006, **45**, 3324-3327.

74. B. Hasenknopf, K. Micoine, E. Lacote, S. Thorimbert, M. Malacria and R. Thouvenot, *Eur. J. Inorg. Chem.*, 2008, 5001-5013.

3.8 Supporting Information

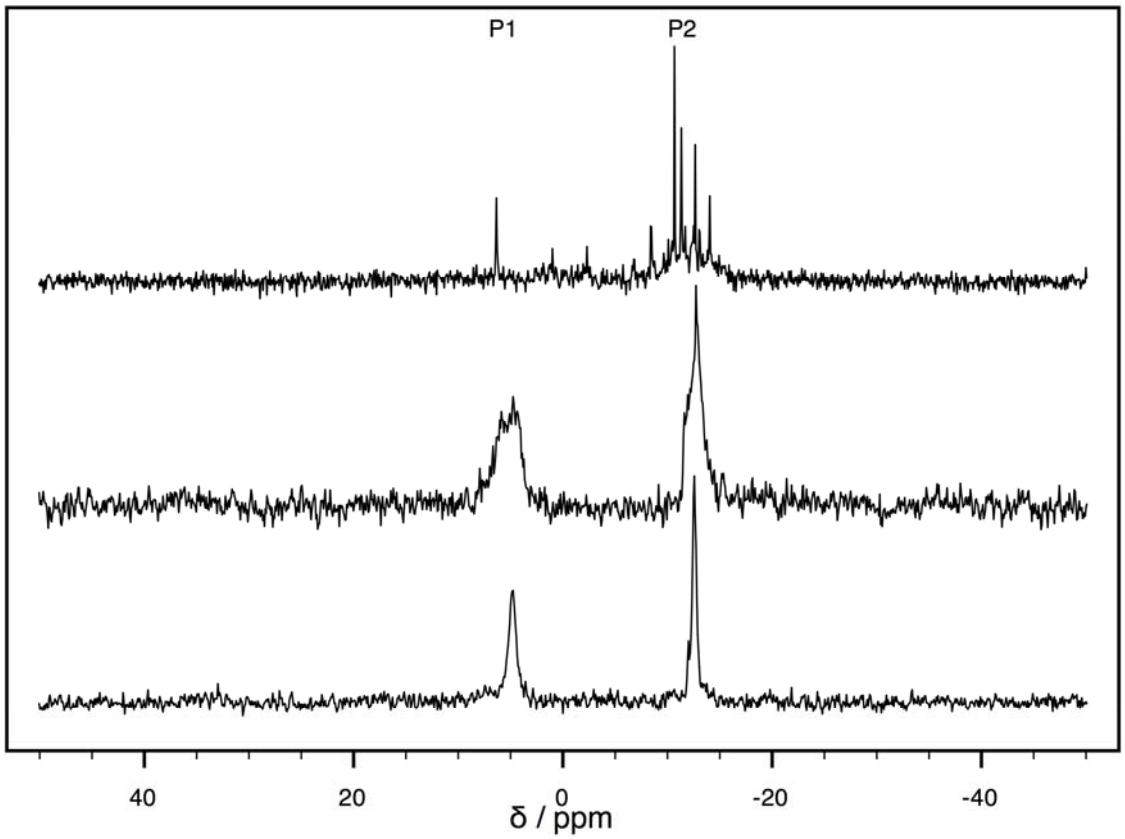

Figure S1. ^{31}P NMR spectrum of 20 mM TBA^{+}-Eu-α-1 in dry, d^3 acetonitrile (top), and after additions of 2% H_2O (middle), and 10% H_2O (bottom). P1 denotes the phosphate resonance near the lacuna and P2 denotes the remote phosphate resonance.

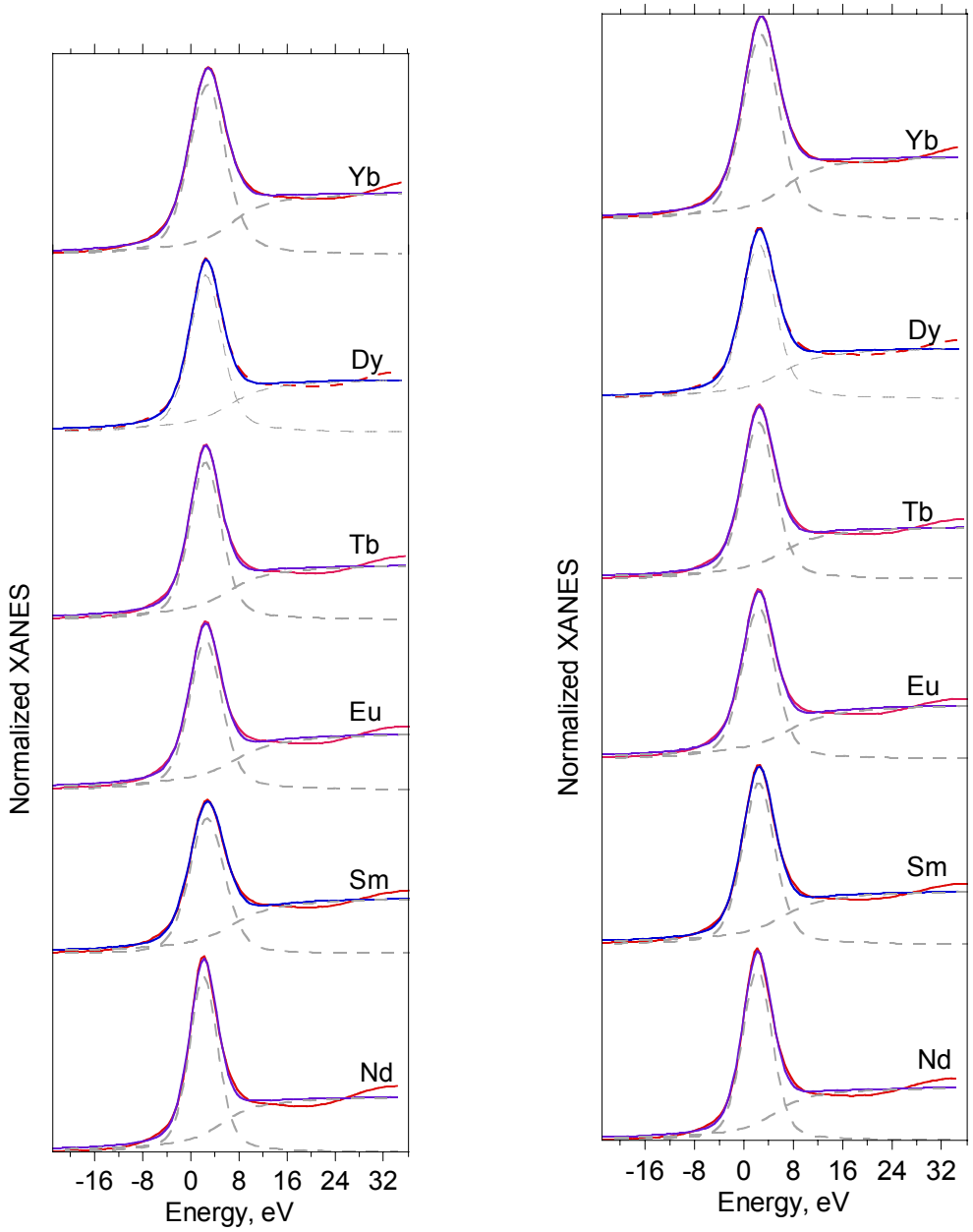

Figure S2. The normalized, experimental XANES (red solid line) for the TBA^{+}-Ln-α-1 solid salts (left) and their 4.3 mM solutions (right) in the acetonitrile electrolyte (0.1 M $TBAPF_6$). The fits to the data are shown as blue solid lines. The individual pseudo-Voigt and arctangent function of the fits are shown as grey dashed lines.

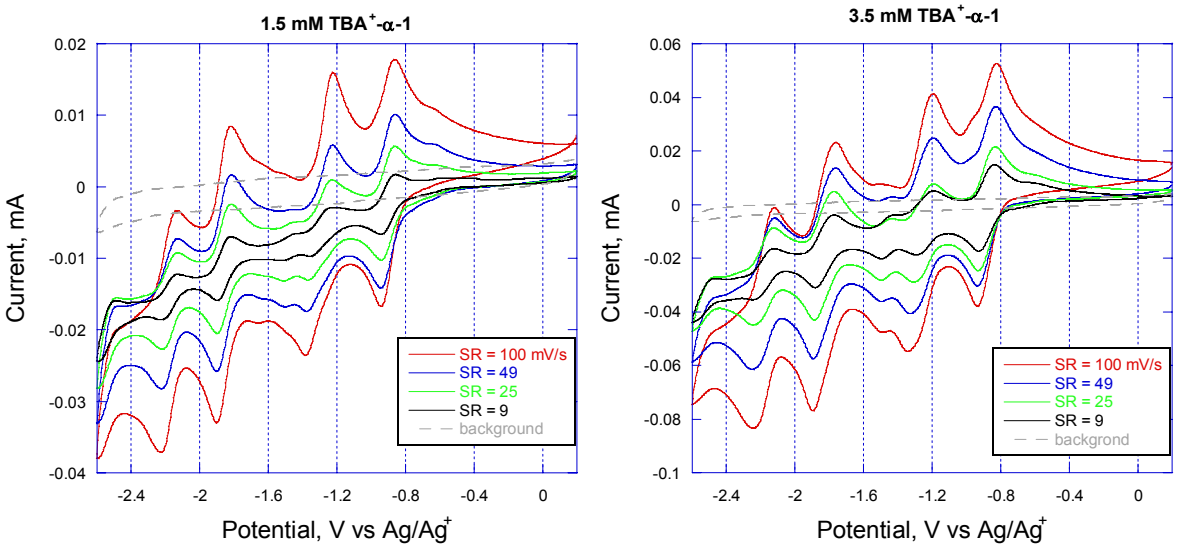

Figure S3. Cyclic voltammograms of 1.5 mM (left) and 3.5 mM (right) solution concentrations of the TBA^+ salt of α-1-$[P_2W_{17}O_{61}]^{10-}$ in dry CH_3CN with 0.1 M $TBAPF_6$ electrolyte obtained with a GC electrode working electrode and different scan rates in mV s^{-1}, starting at +0.2 V. The background scan in the absence of analyte is shown as the grey dashed line.

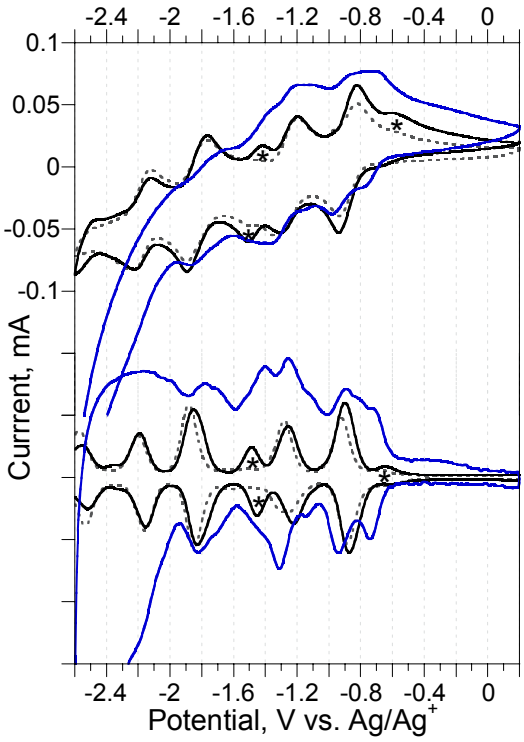

Figure S4. CV (top) and DPV (bottom) of the TBA^+ salt for a fresh 3.5 mM solution of α-1-$[P_2W_{17}O_{61}]^{10-}$ (dashed lines) in MeCN with 0.1 M $TBAPF_6$ electrolyte and after cycling for an hour (solid black lines) at ν = 20 mV s^{-1} showing the development of new couples (identified with asterisks) and after the deliberate addition of H_2O (blue lines) for which, in the absence of DPV data, the semi-differential (convolution) data of the CV are shown.

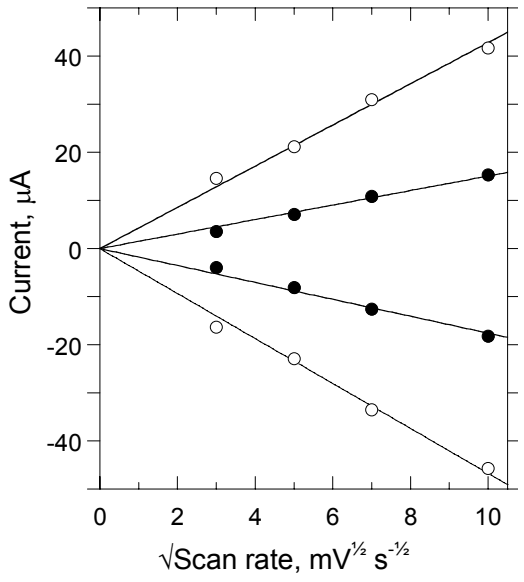

Figure S5. Anodic and cathodic peak current, i_{pa} and i_{pc}, variations of the first redox couple with the square roots of scan rates (v = 9, 25, 49, and 100 mV s^{-1}) from the CVs of Figure S3 for 1.5 mM (solid circles) and 3.5 mM (open circles) α1-$[P_2W_{17}O_{61}]^{10-}$ analyte concentrations. The fitted lines with intercepts of zero are based upon the Randles-Sevcik equation, $i_p = (5.02RT)^{-½}(nF)^{3/2}ACD^{½}v^{½}$ with the conventional symbol meanings.[1] The slopes are -1.76(7) and -4.7(1) for the i_{pc} response (1.5 and 3.5 mM, respectively) and 1.51(5) and 4.3(1) for i_{pa} (1.5 and 3.5 mM, respectively). The regression coefficients (R^2) for the fits are 0.976–0.987. At the 1.5 mM analyte concentration, the average i_{pa}/i_{pc} ratio is -0.86 and at 3.5 mM, the corresponding value is -0.92.

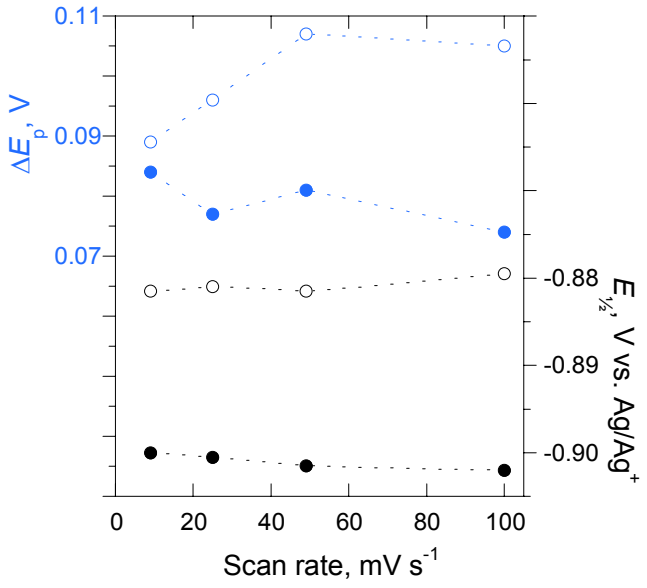

Figure S6. Peak separations, $\Delta E_p = E_{pa} - E_{pc}$ (left, blue ordinate), and half-wave potentials, $E_{½} = (E_{pa} + E_{pc})/2$ (right, black ordinate), for the first redox couple obtained from the CV data of Figure S3 and their variations with scan rates (v = 9, 25, 49, and 100 mV s^{-1}) for 1.5 mM (solid circles) and 3.5 mM (open circles) α1-$[P_2W_{17}O_{61}]^{10-}$ analyte concentrations.

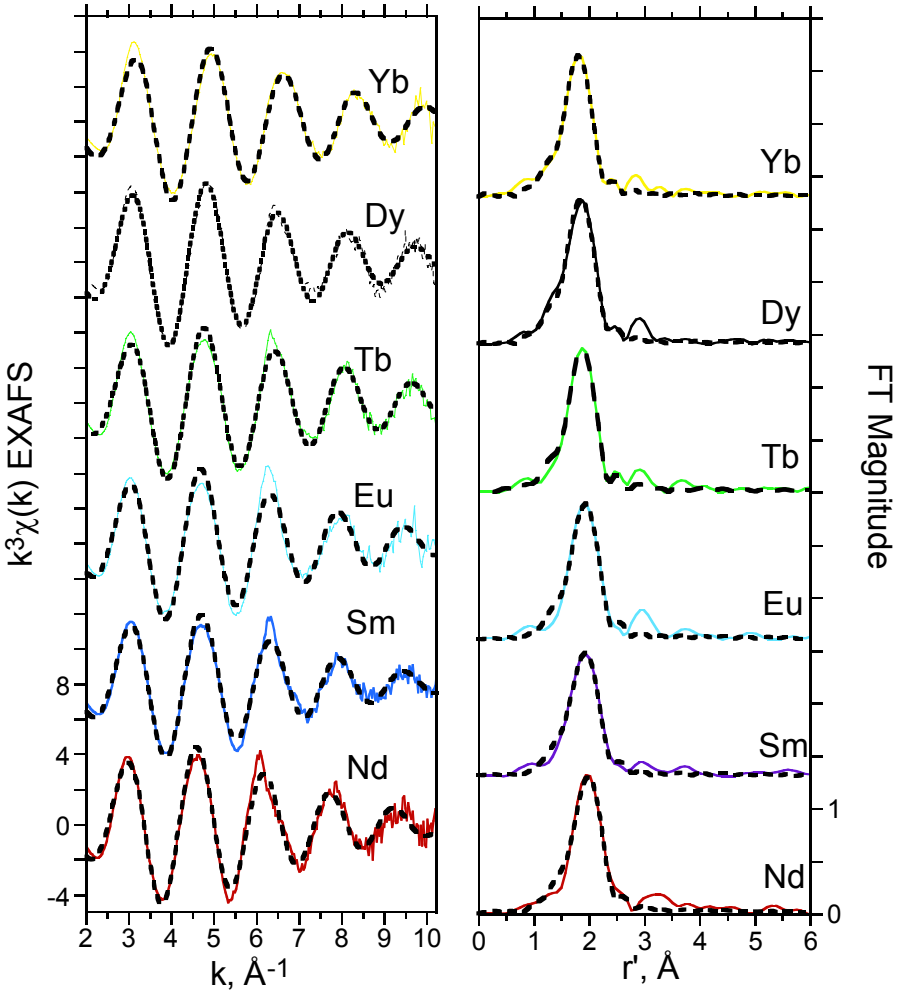

Figure S7a. The Ln L_3-edge $k^3\chi(k)$ EXAFS data and corresponding FT data for the neat TBA^+-Ln-α-1 salts. The experimental data are shown as solid lines and the fits obtained by using the one O-shell model are shown as dashed lines. The metrical parameters are provided in Table S1.

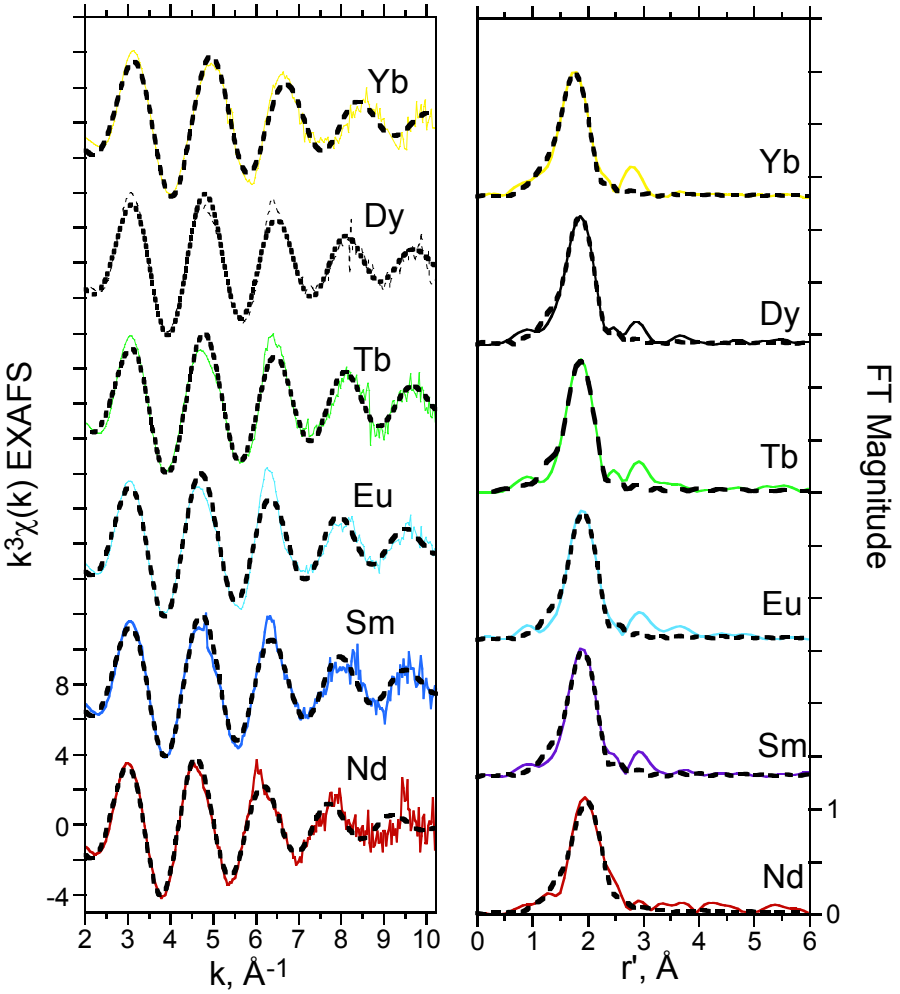

Figure S7b. The Ln L_3-edge $k^3\chi(k)$ EXAFS data and corresponding FT data for the 4.3 mM solutions of TBA^+-Ln-α-1 in the acetonitrile electrolyte (0.1 M $TBAPF_6$). The experimental data are shown as solid lines and the fits obtained by using the one O-shell model are shown as dashed lines. The metrical parameters are provided in the article itself, Tables 2 and 4.

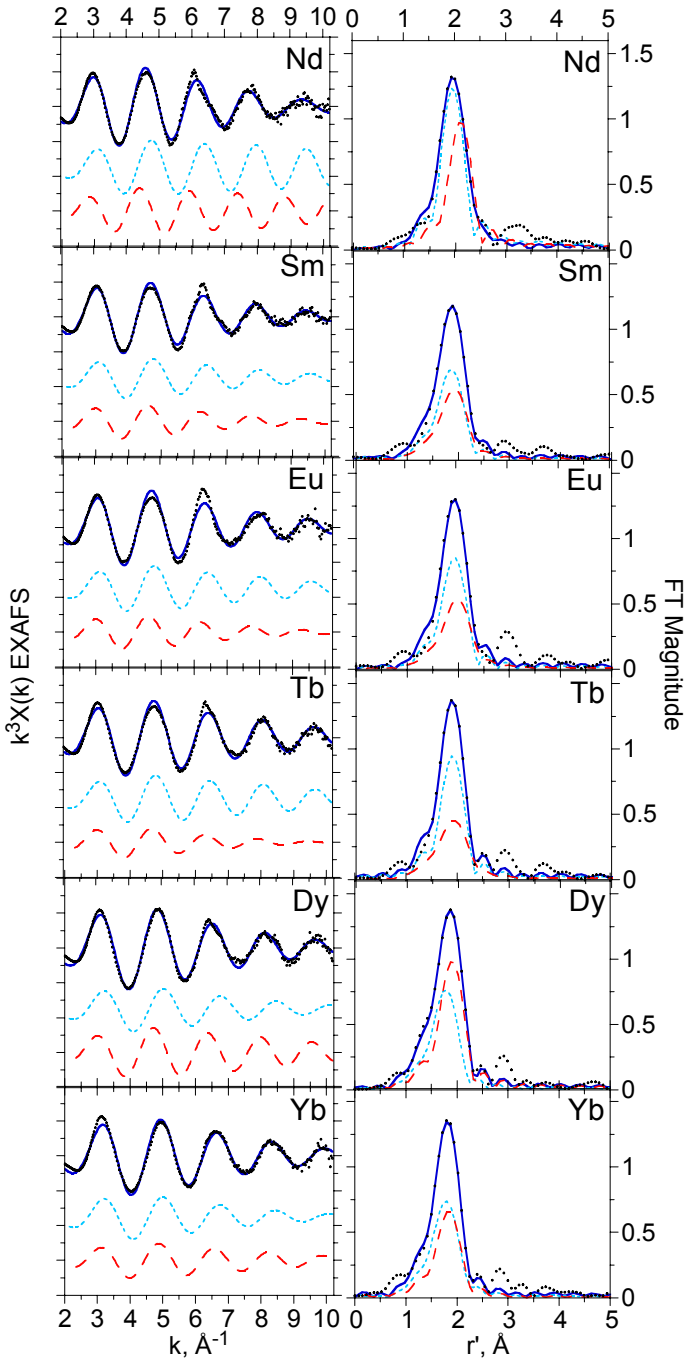

Figure S8a. The Ln L_3-edge $k^3\chi(k)$ EXAFS data and corresponding FT data for the neat TBA^+-Ln-α-1 salts (shown with points) as well as the fits by using the 2 shell model of $O_{\alpha\text{-}1}$ and O_{H_2O}, whose contributions are shown are teal and red dashed lines, respectively.

The composite best fits are shown as the solid blue lines, and the metrical parameters are provided in Table S4.

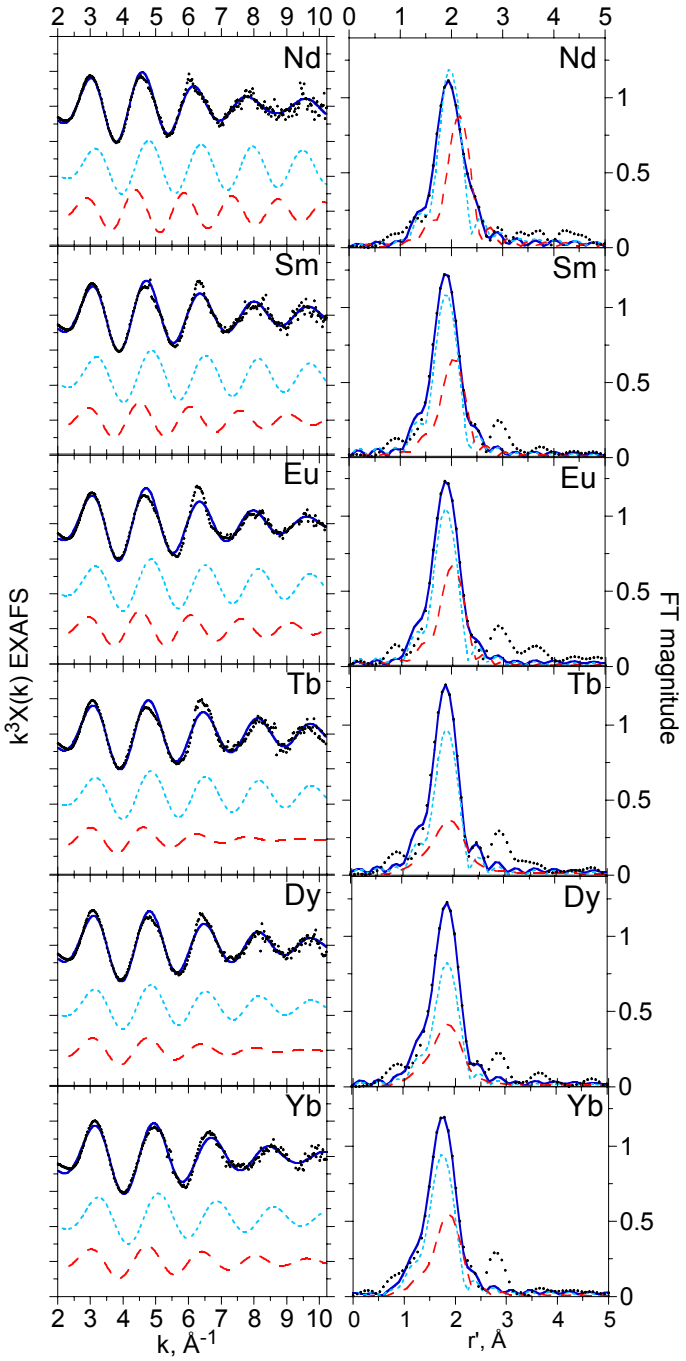

Figure S8b. The Ln L_3-edge $k^3\chi(k)$ EXAFS data and corresponding FT data for the 4.3 mM solutions of TBA^+-Ln-α-1 (shown with points) in the acetonitrile electrolyte (0.1 M

$TBAPF_6$) and the fits by using the 2 shell model of $O_{\alpha\text{-}1}$ and O_{H_2O}, whose contributions are shown as teal and red dashed lines, respectively. The composite best fits are shown as the solid blue lines, and the metrical parameters are provided in the article, Tables 2 and 4.

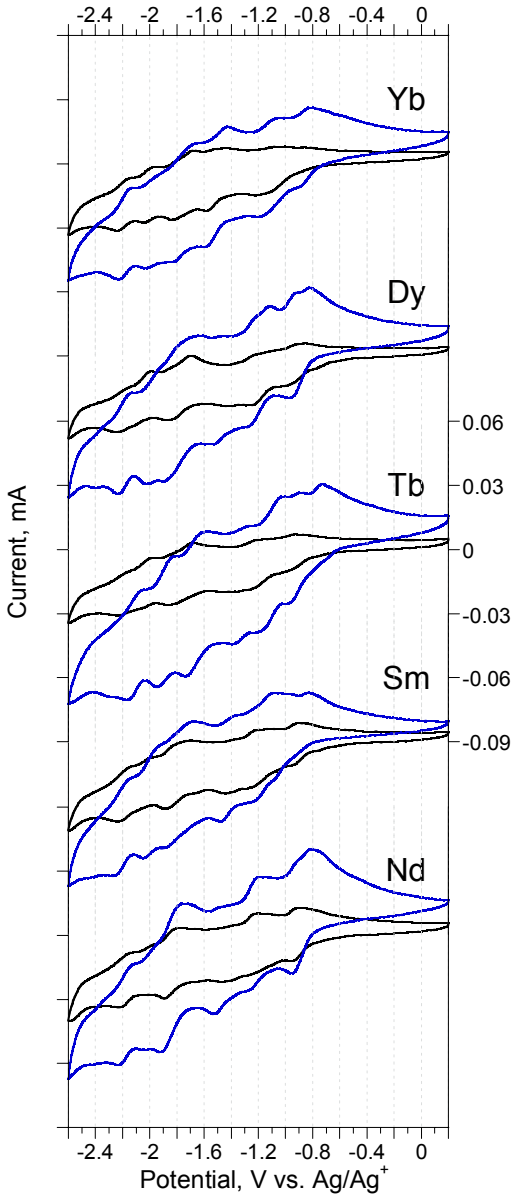

Figure S9. Cyclic voltammograms of 1.5 mM (black lines) and 3.5 mM (blue lines) solutions of the TBA^+ salts of Nd-α-1, Sm-α-1, Tb-α-1, Dy-α-1, and Yb-α-1 obtained

with GC electrodes in dry MeCN with 0.1 M $TBAPF_6$ electrolyte at ν = 100 mV s^{-1}, starting at +0.2 V.

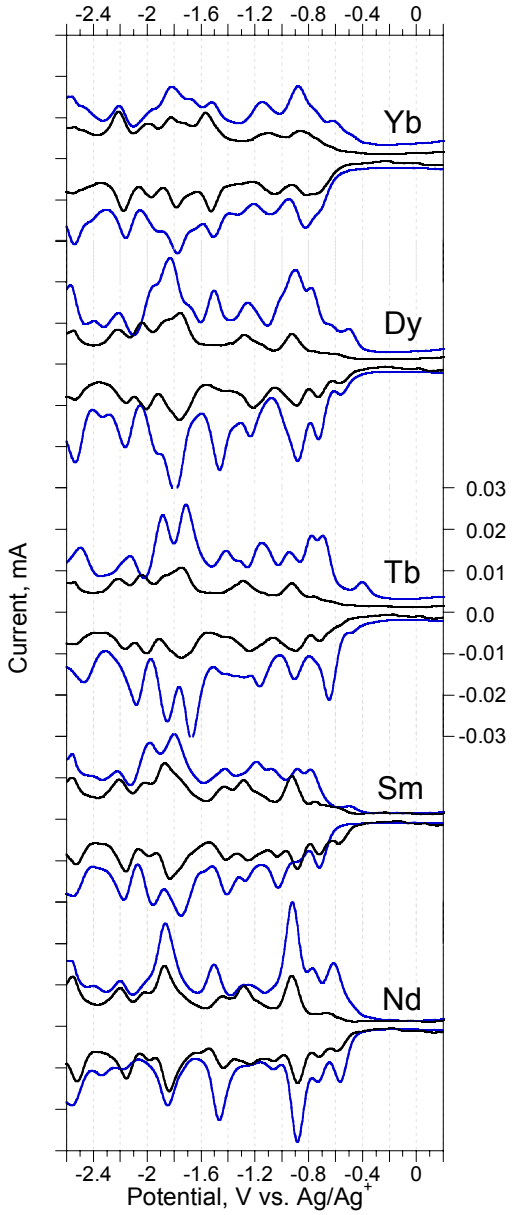

Figure S10. DPV data for 1.5 mM (black lines) and 3.5 mM (blue lines) TBA^+ salts of Nd-α-1, Sm-α-1, Tb-α-1, Dy-α-1, and Yb-α-1 obtained with GC electrodes in dry MeCN with 0.1 M $TBAPF_6$ electrolyte at ν = 20 mV s^{-1} from separate scans to negative and

positive electrode potentials (E) providing the negative (initial E = +0.2 V → final E = -2.6 V) and the positive (initial E = -2.6 V → final E = +0.2 V) current responses, respectively.

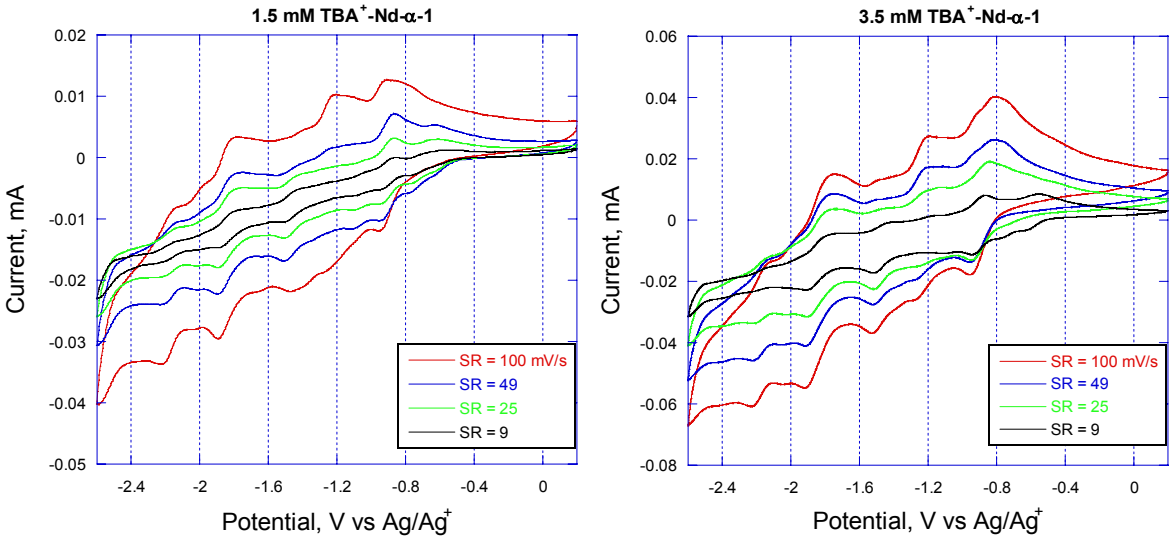

Figure S11. Cyclic voltammograms of 1.5 mM (left) and 3.5 mM (right) solution concentrations of the TBA^+ salt of the Nd(III) complex with α-1-$[P_2W_{17}O_{61}]^{10-}$ in dry acetonitrile with 0.1 M $TBAPF_6$ electrolyte obtained with a GC electrode working electrode and different scan rates in mV s^{-1}, starting at +0.2 V.

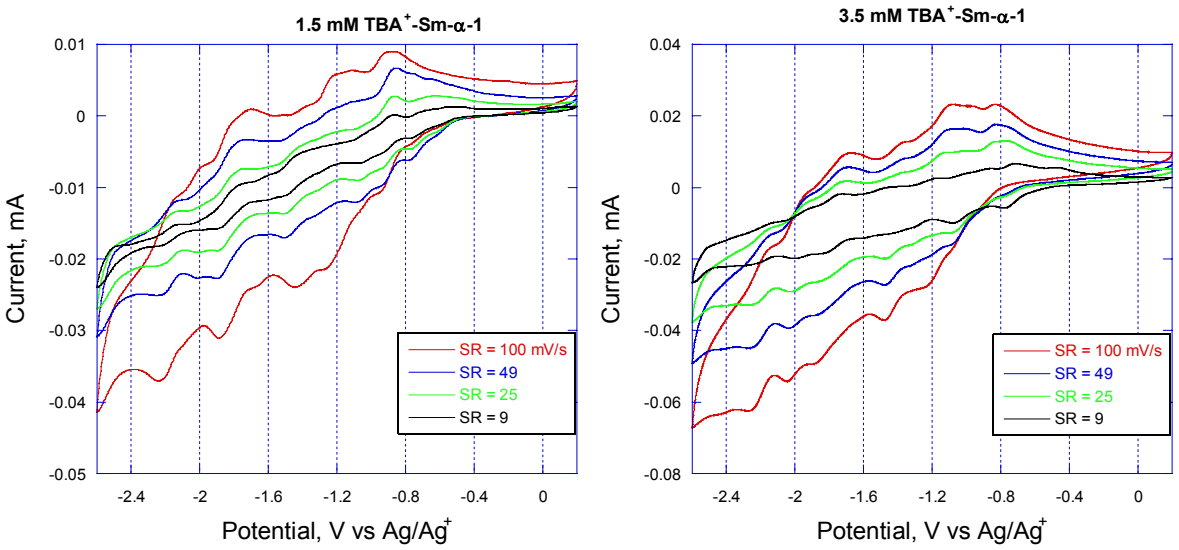

Figure S12. Cyclic voltammograms of 1.5 mM (left) and 3.5 mM (right) solution concentrations of the TBA^+ salt of the Sm(III) complex with α-1-$[P_2W_{17}O_{61}]^{10-}$ in dry acetonitrile with 0.1 M $TBAPF_6$ electrolyte obtained with a GC electrode working electrode and different scan rates in mV s^{-1}, starting at +0.2 V.

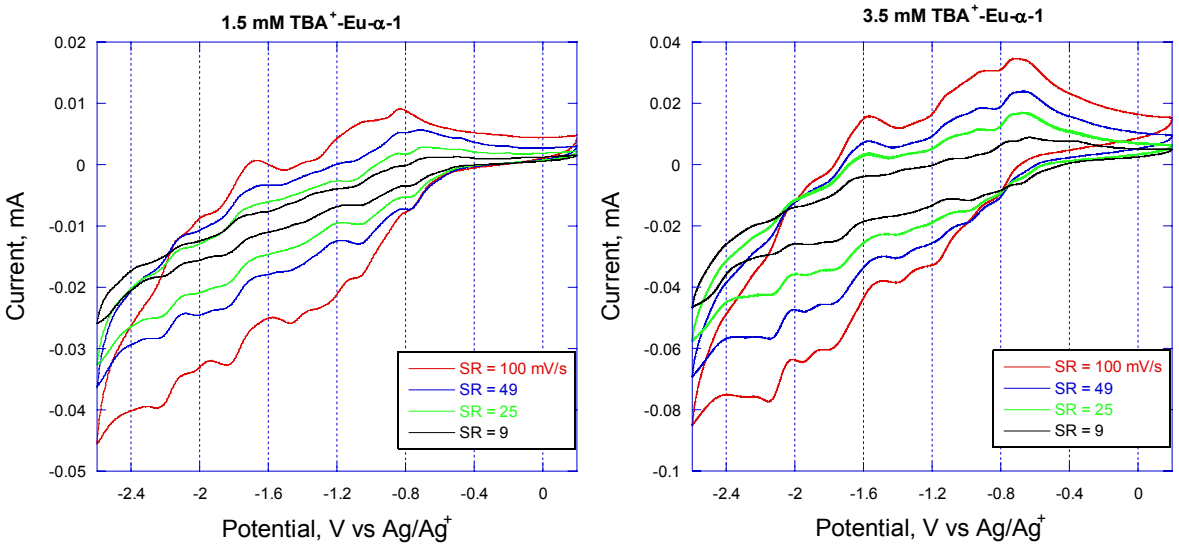

Figure S13. Cyclic voltammograms of 1.5 mM (left) and 3.5 mM (right) solution concentrations of the TBA^+ salt of the Eu(III) complex with α-1-$[P_2W_{17}O_{61}]^{10-}$ in dry

acetonitrile with 0.1 M $TBAPF_6$ electrolyte obtained with a GC electrode working electrode and different scan rates in mV s^{-1}, starting at +0.2 V.

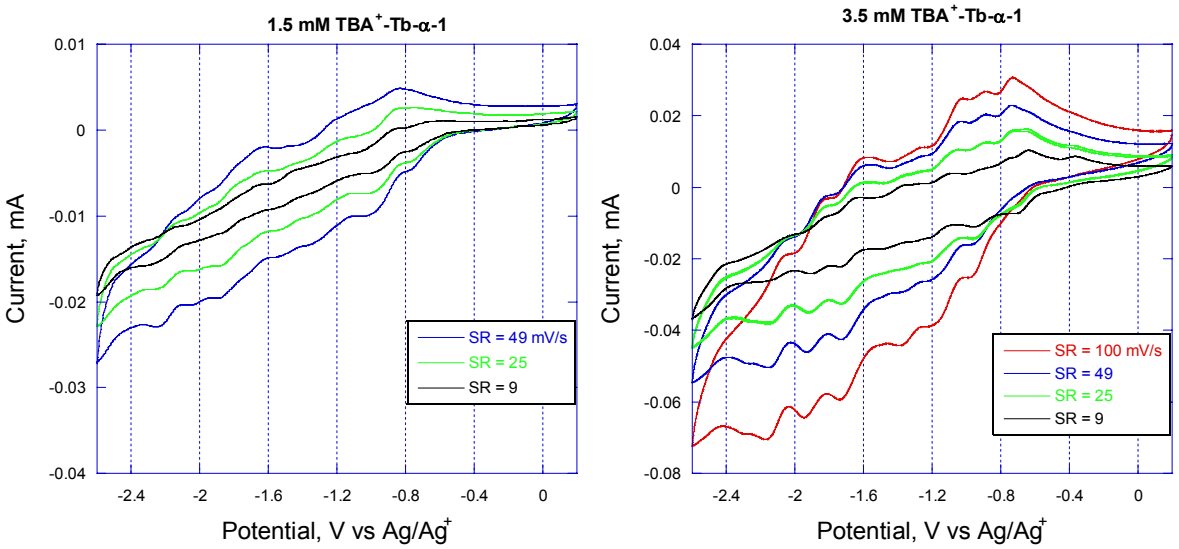

Figure S14. Cyclic voltammograms of 1.5 mM (left) and 3.5 mM (right) solution concentrations of the TBA^+ salt of the Tb(III) complex with α-1-$[P_2W_{17}O_{61}]^{10-}$ in dry acetonitrile with 0.1 M $TBAPF_6$ electrolyte obtained with a GC electrode working electrode and different scan rates in mV s^{-1}, starting at +0.2 V.

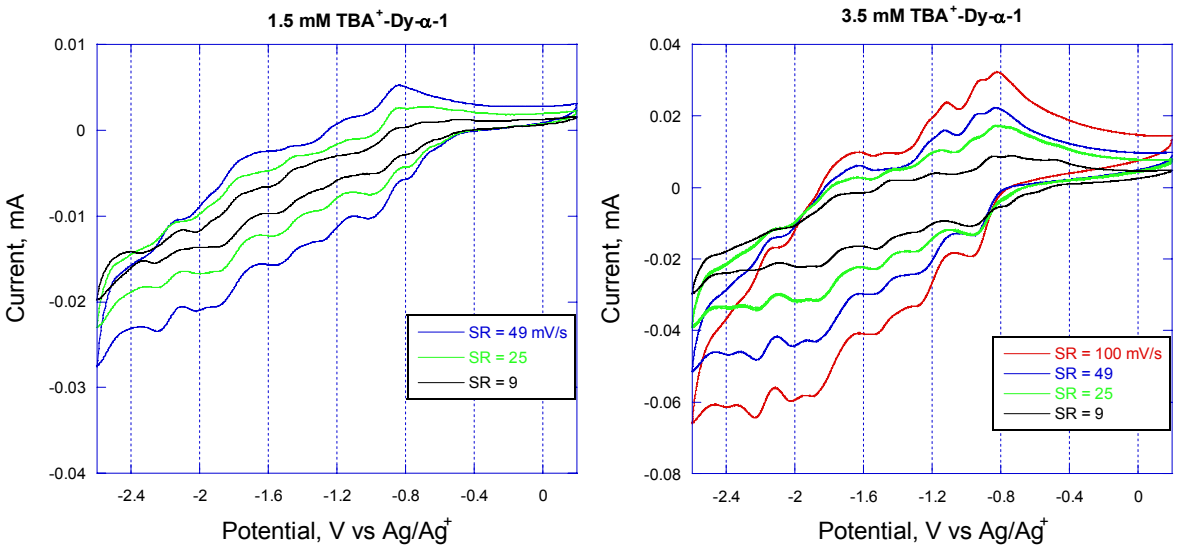

Figure S15. Cyclic voltammograms of 1.5 mM (left) and 3.5 mM (right) solution concentrations of the TBA^+ salt of the Dy(III) complex with α-1-$[P_2W_{17}O_{61}]^{10-}$ in dry acetonitrile with 0.1 M $TBAPF_6$ electrolyte obtained with a GC electrode working electrode and different scan rates in mV s^{-1}, starting at +0.2 V.

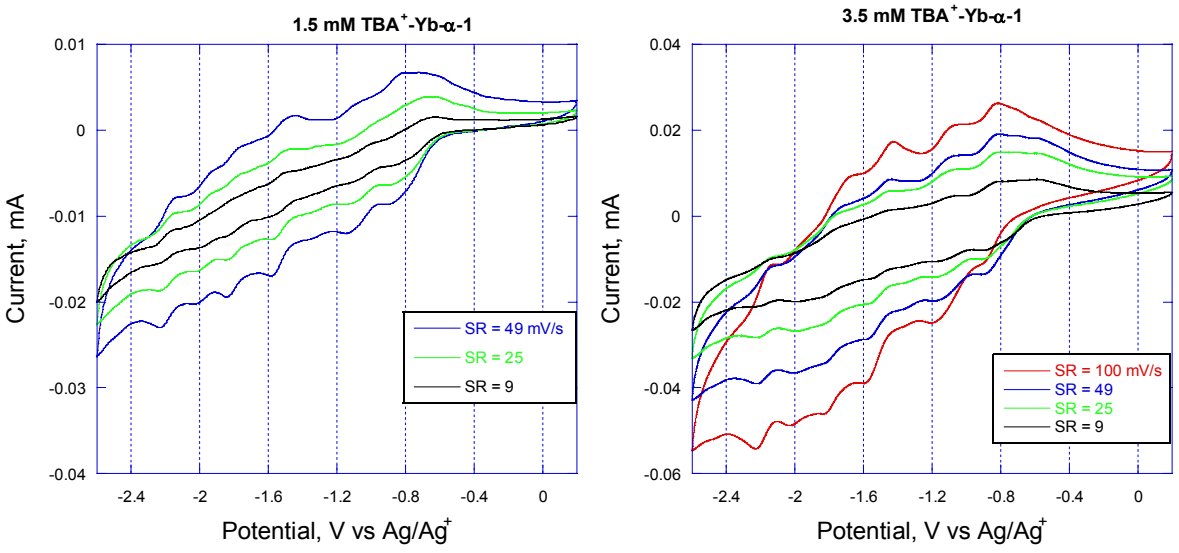

Figure S16. Cyclic voltammograms of 1.5 mM (left) and 3.5 mM (right) solution concentrations of the TBA^+ salt of the Yb(III) complex with α-1-$[P_2W_{17}O_{61}]^{10-}$ in dry

acetonitrile with 0.1 M $TBAPF_6$ electrolyte obtained with a GC electrode working electrode and different scan rates in mV s^{-1}, starting at +0.2 V.

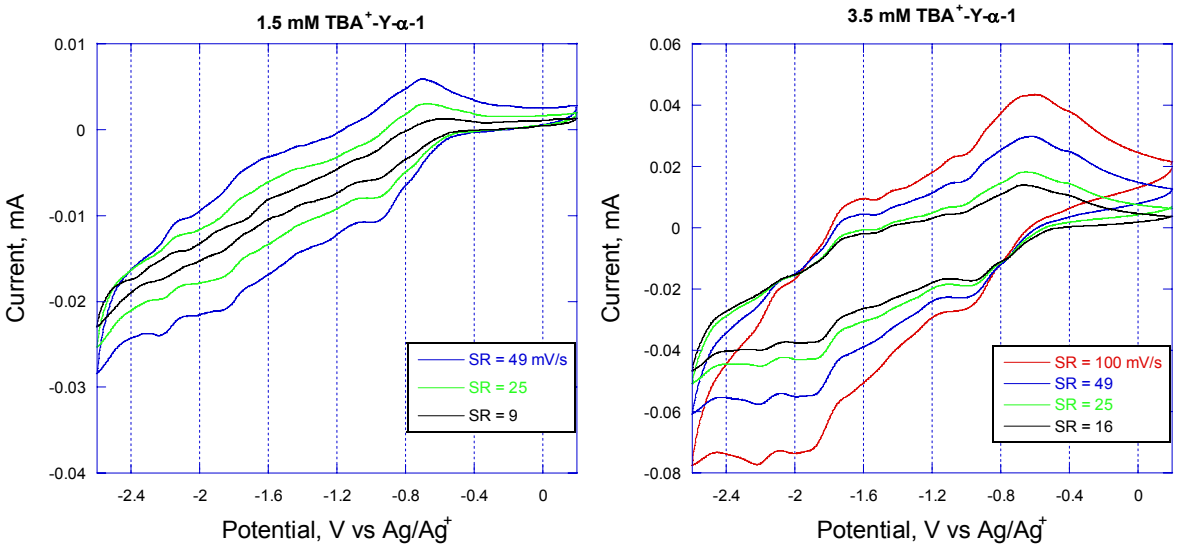

Figure S17. Cyclic voltammograms of 1.5 mM (left) and 3.5 mM (right) solution concentrations of the TBA^+ salt of the Y(III) complex with α-1-$[P_2W_{17}O_{61}]^{10-}$ in dry acetonitrile with 0.1 M $TBAPF_6$ electrolyte obtained with a GC electrode working electrode and different scan rates in mV s^{-1}, starting at +0.2 V.

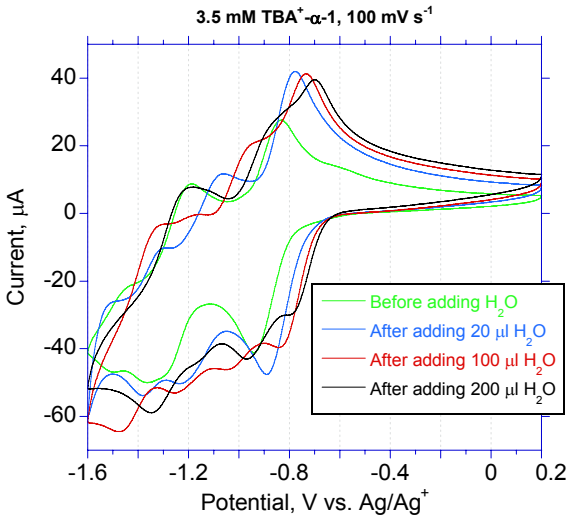

Figure S18. Cyclic voltammograms of the TBA^+ salt for a fresh 3.5 mM solution of α-1-$[P_2W_{17}O_{61}]^{10-}$ (lime color line) in MeCN with 0.1 M $TBAPF_6$ electrolyte and after the deliberate, successive addition of 20, 100, and 200 μL of H_2O.

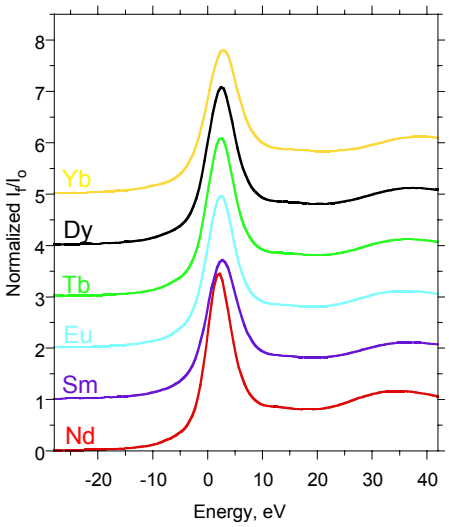

Figure S19. Normalized Ln L_3-edge XANES, I_f/I_0, for the neat, TBA^+-Ln-α-1 solid salts. The inflection point energies obtained from the first differential XANES are given in Table S9.

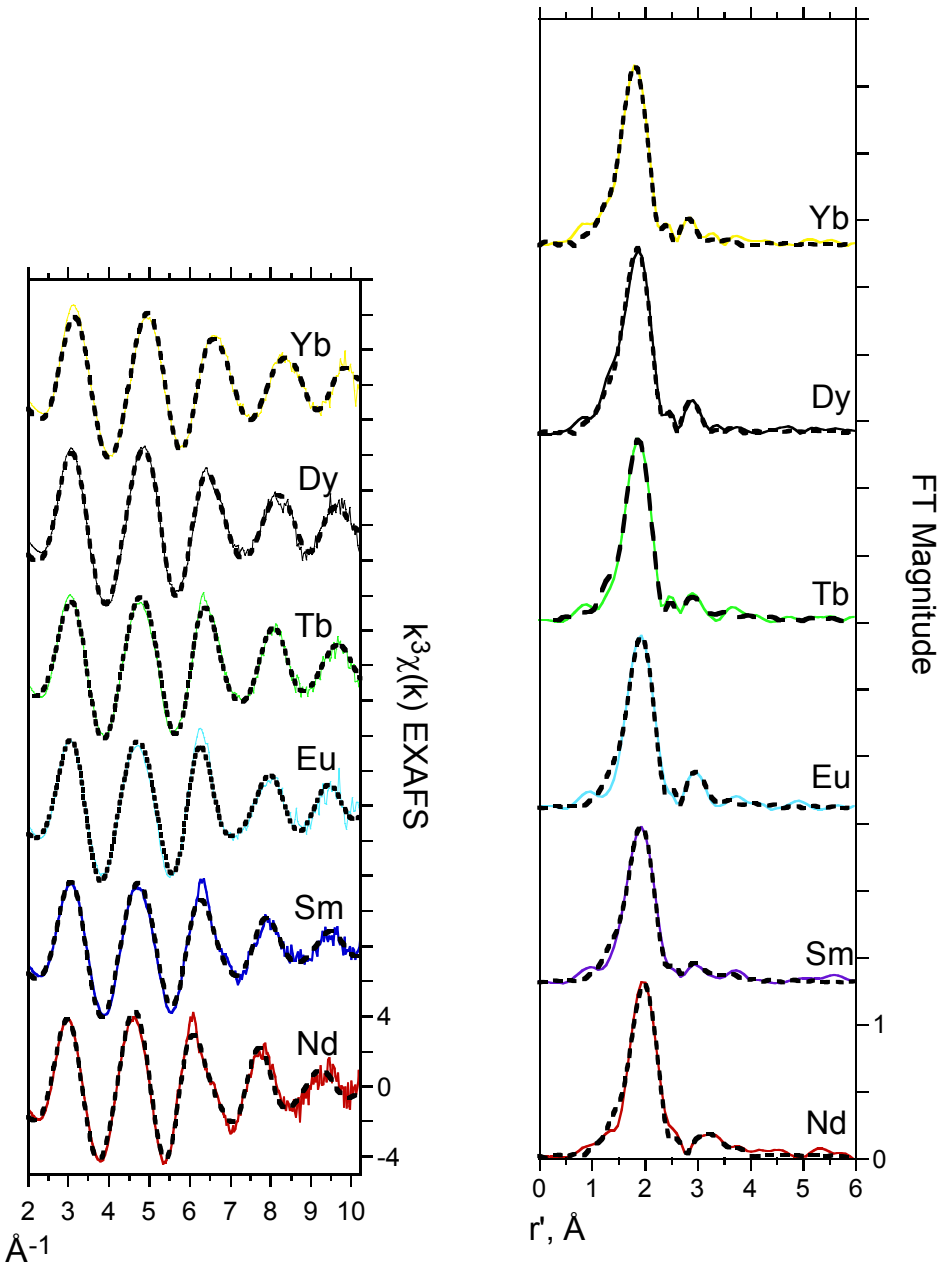

Figure S20a. Ln L_3-edge $k^3\chi(k)$ EXAFS data (left) and the corresponding FT data (right) for the neat TBA^+-Ln-α-1 solid salts. The solid lines illustrate the experimental data, and the dashed lines show the fits with the multishell model, which includes Ln-O, Ln-O, and Ln-W paths. The metrical parameters are provided in Table S6.

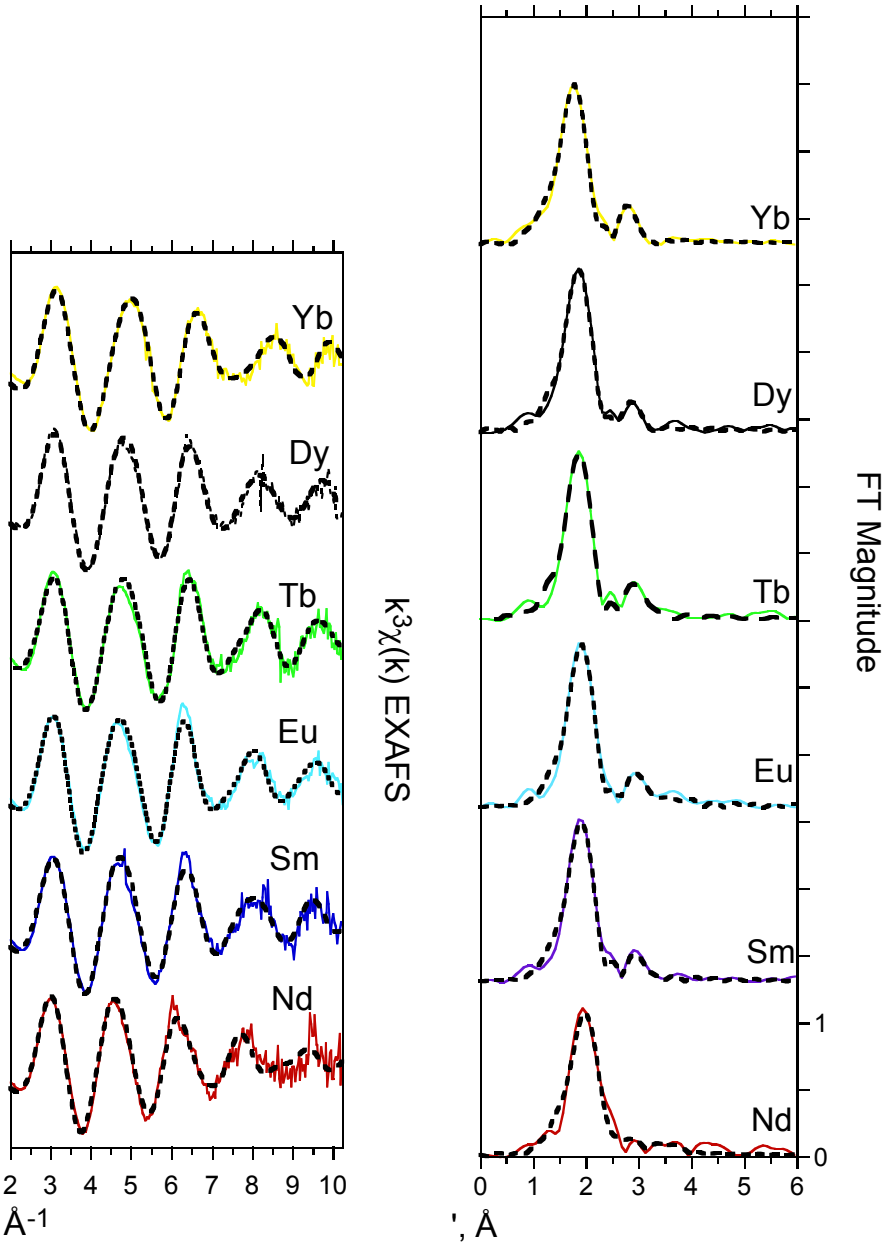

Figure S20b. Ln L_3-edge $k^3\chi(k)$ EXAFS data (left) and the corresponding FT data (right) for the 4.3 mM solutions of TBA^+-Ln-α-1 in the acetonitrile electrolyte (0.1 M $TBAPF_6$). The solid lines illustrate the experimental data, and the dashed lines show the fits with the multishell model, which includes Ln-O, Ln-O, and Ln-W paths. The metrical parameters are provided in Table S6.

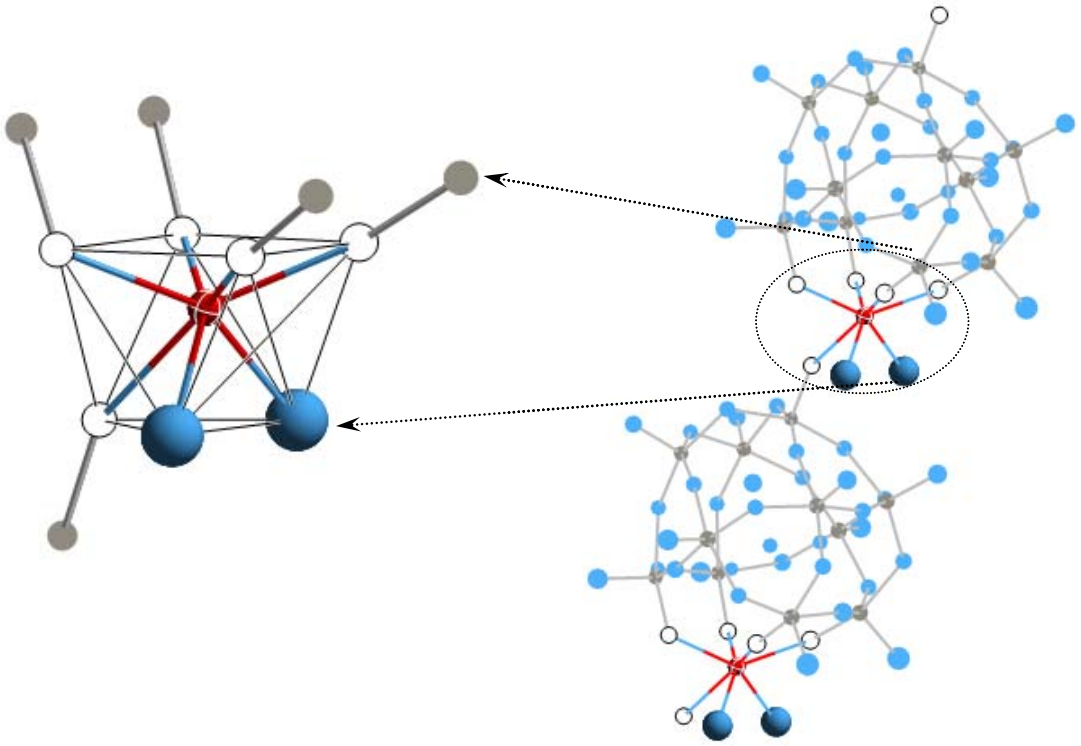

Figure S21. Ball and stick model of the 7 O coordination environment of Yb(III) with a capped trigonal prism geometry in $[(H_2O)_2Yb(\alpha\text{-}SiW_{11}O_{39})]^{5-}$ as the K-Cs_4 salt.[2] The red circle is the Yb ion which is connected to two terminal O_{H_2O} (blue circles) and $O_{\alpha\text{-}1}$ atoms (open circles) bridging to W atoms (gray circles). The inset shows a fraction of the infinite linear arrangement of the molecular anions.

Table S1. Results from the one-O shell fits of the Ln L_3-edge $k^3\chi(k)$ EXAFS for the TBA^+-Ln-α-1 solid salts.[a]

Powders	O CN[b]	r,[c] Å	σ^2,[d] Å^2	ΔE_0,[e] eV
TBA^+-Nd-α-1	9.0(7)	2.48(1)	0.012(1)	0.6
TBA^+-Sm-α-1	7.8(5)	2.42(1)	0.013(1)	0.7
TBA^+-Eu-α-1	7.6(7)	2.41(1)	0.011(1)	2.1
TBA^+-Tb-α-1	7.4(5)	2.36(1)	0.010(1)	-0.9
TBA^+-Dy-α-1	8.4(5)	2.33(1)	0.012(1)	-1.0
TBA^+-Yb-α-1	6.9(4)	2.27(1)	0.011(1)	1.0

[a] The numbers in the parentheses represent the estimated standard deviations (3σ) obtained from the least-squares fits. [b] Coordination number. [c] Interatomic distance. [d] The Debye-Waller factor, the root-mean-square deviation of the average Ln-O bond length. [e] The energy difference between the experimental and theoretical values of E_0.

Table S2. Results from the one-O shell of the Ln L_3-edge $k^3\chi(k)$ EXAFS of the aqueous solutions of 4.3 mM K^+-Ln-α-1 salts. The parameter definitions are given in the footnotes to Table S1.

Solution	O CN	r, Å	σ^2, Å^2	ΔE_0, eV
K^+-Nd-α-1	8.8(15)	2.45(2)	0.013(3)	0.7
K^+-Sm-α-1	8.8(9)	2.40(1)	0.012(2)	0.2
K^+-Eu-α-1	7.6(9)	2.38(1)	0.009(2)	0.6
K^+-Tb-α-1	8.1(6)	2.35(1)	0.010(1)	0.9
K^+-Dy-α-1	8.6(9)	2.33(1)	0.011(2)	-1.5
K^+-Yb-α-1	7.3(7)	2.26(1)	0.010(1)	0.8

Table S3. Results from the one-O shell fits of the Ln L_3-edge $k^3\chi(k)$ EXAFS of the TBA^+-Ln-α-1 solid salts and their 4.3 mM solutions in the acetonitrile electrolyte (0.1 M $TBAPF_6$). Fit results take the Ln-O pair distribution asymmetry into consideration by including the third cumulant σ' and the fourth cumulant σ''. Other parameter definitions are given in the footnotes to Table S1.

Sample	O CN	r, Å	σ^2, Å^2	σ'	σ''	ΔE_0
TBA^+-Nd-α-1 powder	8.0(4)	2.48(1)	0.006 (1)	0.0001(1)	-0.0002(1)	2.9
TBA^+-Nd-α-1 solution	7.6(2)	2.53(1)	0.006 (1)	0.0016(1)	-0.0004(1)	4.6
TBA^+-Sm-α-1 powder	9.0(2)	2.44(1)	0.014 (1)	0.0004(1)	0.00005(1)	4.0
TBA^+-Sm-α-1 solution	8.2(1)	2.43(1)	0.011 (1)	0.0007(1)	-0.00006(1)	3.4
TBA^+-Eu-α-1 powder	7.2(1)	2.46(1)	0.007 (1)	0.001(1)	-0.00014(1)	6.2
TBA^+-Eu-α-1 solution	7.1(1)	2.46(1)	0.007 (1)	0.001(1)	-0.00015(2)	6.0
TBA^+-Tb-α-1 powder	7.8(1)	2.38(1)	0.009 (1)	0.0002(1)	-0.000007(10)	2.0
TBA^+-Tb-α-1 solution	8.1(1)	2.38(1)	0.012 (1)	0.0006(1)	0.00005(1)	2.0
TBA^+-Dy-α-1 powder	8.8(2)	2.35(1)	0.012 (1)	0.000003(1)	0.00002(1)	1.7
TBA^+-Dy-α-1 solution	8.7(2)	2.38(1)	0.015 (1)	0.0007(1)	0.00012(1)	2.8
TBA^+-Yb-α-1 powder	7.1(1)	2.29(1)	0.010 (1)	0.0003(1)	0.00002(1)	3.9
TBA^+-Yb-α-1 solution	7.3(1)	2.32(1)	0.013 (1)	0.0015(1)	0.00008(1)	4.7

Table S4. Results from the two-O shell ($O_{\alpha\text{-}1}$ and O_{H_2O}) curve-fitting of the Ln L_3-edge $k^3\chi(k)$ EXAFS of the TBA^+-Ln-α-1 solid salts. The parameter definitions are given in the footnotes to Table S1.

Powders	Shell	CN	r, Å	σ^2, Å^2	ΔE_0, eV
TBA^+-Nd-α-1	$O_{\alpha\text{-}1}$	4	2.42(1)	0.003(2)	1.4
	O_{H_2O}	4.3(8)	2.58(2)	0.005(3)	/[a]
TBA^+-Sm-α-1	$O_{\alpha\text{-}1}$	4	2.39(20)	0.010(6)	0.8
	O_{H_2O}	3.9(8)	2.45(24)	0.013(29)	/
TBA^+-Eu-α-1	$O_{\alpha\text{-}1}$	4	2.38(8)	0.008(3)	2.4
	O_{H_2O}	3.8(11)	2.46(11)	0.013(20)	/
TBA^+-Tb-α-1	$O_{\alpha\text{-}1}$	4	2.35(2)	0.006(2)	-0.4
	O_{H_2O}	3.8(10)	2.39(5)	0.017(10)	/
TBA^+-Dy-α-1	$O_{\alpha\text{-}1}$	4	2.26(2)	0.010(6)	-1.9
	O_{H_2O}	4.4(7)	2.37(3)	0.006(3)	/
TBA^+-Yb-α-1	$O_{\alpha\text{-}1}$	4	2.25(9)	0.012(15)	0.7
	O_{H_2O}	3.0(7)	2.30(13)	0.008(4)	/

[a] The / notation indicates that the parameter was fixed to the value in the column above.

Table S5. Results from the two-O shell ($O_{\alpha\text{-}1}$and O_{H_2O}) curve-fitting of the Ln L_3-edge $k^3\chi(k)$ EXAFS for the 4.3 mM K^+-Ln-α-1 aqueous solutions. The parameter definitions are given in the footnotes to Table S1.

Solution	Shell	CN	r, Å	σ^2, Å^2	ΔE_0, eV
K^+-Nd-α-1	$O_{\alpha\text{-}1}$	4	2.40(2)	0.002(4)	1.8
	O_{H_2O}	4.4(16)	2.56(3)	0.005(7)	/[a]
K^+-Sm-α-1	$O_{\alpha\text{-}1}$	4	2.34(2)	0.004(4)	0.7
	O_{H_2O}	4.3(10)	2.48(3)	0.005(6)	/
K^+-Eu-α-1	$O_{\alpha\text{-}1}$	4	2.36(3)	0.004(3)	2.2
	O_{H_2O}	4.4(17)	2.48(5)	0.013(14)	/
K^+-Tb-α-1	$O_{\alpha\text{-}1}$	4	2.27(4)	0.007(8)	-2.3
	O_{H_2O}	4.8(15)	2.39(4)	0.008(8)	/
K^+-Dy-α-1	$O_{\alpha\text{-}1}$	4	2.24(6)	0.016(13)	-3.1
	O_{H_2O}	4.3(16)	2.35(3)	0.007(3)	/
K^+-Yb-α-1	$O_{\alpha\text{-}1}$	4	2.24(5)	0.009(15)	0.7
	O_{H_2O}	3.3(10)	2.29(7)	0.009(22)	/

[a] The / notation indicates that the parameter was fixed to the value in the column above.

Table S6. Parameters from curve-fitting analysis (multi-shell fit) of the Ln L_3-edge $k^3\chi(k)$ EXAFS of Figure S20. The parameters are defined in the footnotes to Table S1.

Sample	Shell	CN	r, Å	σ^2, Å^2	ΔE_0, eV
TBA^+-Nd-α-1 Powder	Nd-O	9.0(6)	2.48(1)	0.012(1)	0.6
	Nd-O	1	3.63(7)	0.007(10)	/[a]
	Nd-W	4	3.87(4)	0.018(5)	/
TBA^+-Sm-α-1 Powder	Sm-O	7.7(5)	2.42(1)	0.013(1)	0.6
	Sm-O	1	3.42(6)	0.010(9)	/
	Sm-W	4	3.75(4)	0.020(5)	/
TBA^+-Eu-α-1 Powder	Eu-O	7.7(5)	2.40(1)	0.011(1)	1.8
	Eu-O	1	3.44(3)	0.0005(11)	/
	Eu-W	4	3.71(4)	0.019(5)	/
TBA^+-Tb-α-1 Powder	Tb-O	7.4(4)	2.36(1)	0.009(1)	-1.0
	Tb-O	1	3.34(6)	0.010(9)	/
	Tb-W	4	3.63(3)	0.019(4)	/
TBA^+-Dy-α-1 Powder	Dy-O	8.5(5)	2.33(1)	0.012(1)	-1.2
	Dy-O	1	3.38(2)	0.0003(8)	/
	Dy-W	4	3.69(6)	0.028(11)	/
TBA^+-Yb-α-1 Powder	Yb-O	7.0(4)	2.27(1)	0.011(1)	0.8
	Yb-O	1	3.30(3)	0.002(3)	/
	Yb-W	4	3.66(5)	0.025(8)	/

[a] The / notation indicates that the parameter was fixed to the value in the column above.

Sample	Shell	CN	r, Å	σ^2, Å^2	ΔE_0, eV
TBA^+-Nd-α-1 Solution	Nd-O	8.7(10)	2.48(1)	0.015(2)	0.7
	Nd-O	1	3.41(6)	0.006(8)	/
	Nd-W	4	3.82(4)	0.018(6)	/
TBA^+-Sm-α-1 Solution	Sm-O	7.6(6)	2.40(1)	0.012(1)	-0.4
	Sm-O	1	3.41(3)	0.0005(11)	/
	Sm-W	4	3.4(3)	0.05(8)	/
TBA^+-Eu-α-1 Solution	Eu-O	7.4(5)	2.39(1)	0.012(1)	1.4
	Eu-O	1	3.39(3)	0.002(4)	/
	Eu-W	4	3.66(3)	0.016(4)	/
TBA^+-Tb-α-1 Solution	Tb-O	7.1(6)	2.35(1)	0.01(1)	-1.1
	Tb-O	1	3.35(4)	0.002(5)	/
	Tb-W	4	3.54(4)	0.019(5)	/
TBA^+-Dy-α-1 Solution	Dy-O	7.4(5)	2.34(1)	0.012(1)	-0.8
	Dy-O	1	3.32(3)	0.002(3)	/
	Dy-W	4	3.60(5)	0.023(7)	/
TBA^+-Yb-α-1 Solution	Yb-O	7.3(5)	2.25(1)	0.013(1)	-0.859
	Yb-O	1	3.26(2)	-0.001(2)	/
	Yb-W	4	3.50(6)	0.027(9)	/

Notes for Table S7:

The single-shell curve-fitting results for the Ln L_3-edge $k^3\chi(k)$ EXAFS presented in Tables 2 and 4 of the article text provide only average Ln-O distances for the Ln-α-1 complexes. Nevertheless, the two sets of individual distances, which are attributed to the 4 bridging O atoms from the α-1 ligand ($O_{\alpha\text{-}1}$) and n = 3–5 terminal O atoms from water molecules (O_{H_2O}) coordinated to the Ln(III) ions, can be estimated from the EXAFS-determined Debye-Waller factors, σ^2, which provide a measure of the total spread (δr) in the Ln-O distances, for the one-O shell fits. Through use of a procedure outlined previously,[3, 4] it was possible to determine the mean Ln-O_{H_2O} and Ln-$O_{\alpha\text{-}1}$ interatomic distances, r_n and r_m, respectively. The results are summarized here in Tables S7a and S7b, where we have assumed that the four Ln-$O_{\alpha\text{-}1}$ distances are shorter than all the Ln-O_{H_2O} ones (exactly as obtains in the crystal structures),[5-7] and assuming integer values for the hydration numbers, n, based upon the best fit CNs. The results are in excellent correspondence with the two sets of individual distances obtained from the two-shell model, presented in Tables 2 and 4 of the article text

Table S7a. Results for the acetonitrile solutions (4.3 mM) of the TBA^+-Ln-α-1 salts.

Solution	σ_{vib} [b]	σ_{exp} [c]	σ_{cal} [d]	n[a]	δr [e]	r_{exp} [f]	$r_{m,\,cal}$ [g]	$r_{n,\,cal}$ [g]	$r_{m,\,exp}$ [h]	$r_{n,\,exp}$ [h]
TBA^+-Nd-α-1	0.074	0.126	0.103	5	0.144	2.48	2.40	2.54	2.43	2.60
TBA^+-Sm-α-1	0.072	0.110	0.102	4	0.143	2.40	2.33	2.47	2.36	2.51
TBA^+-Eu-α-1	na	0.110	na	4	0.143	2.40	2.33	2.47	2.35	2.49
TBA^+-Tb-α-1	0.070	0.100	0.100	4	0.143	2.35	2.28	2.42	2.34	2.42
TBA^+-Dy-α-1	0.069	0.110	0.099	4	0.143	2.34	2.27	2.41	2.33	2.37
TBA^+-Yb-α-1	0.066	0.134	0.097	3	0.144	2.25	2.19	2.33	2.21	2.34

Table S7b. Results for the solid TBA^+-Ln-α-1 salts.

Powders	σ_{vib} [b]	σ_{exp} [c]	σ_{cal} [d]	n[a]	δr [e]	r_{exp} [f]	$r_{m,\,cal}$ [g]	$r_{n,\,cal}$ [g]	$r_{m,\,exp}$ [h]	$r_{n,\,exp}$ [h]
TBA^+-Nd-α-1	0.074	0.126	0.103	5	0.144	2.48	2.40	2.54	2.42	2.58
TBA^+-Sm-α-1	0.072	0.110	0.102	4	0.143	2.42	2.35	2.49	2.39	2.45
TBA^+-Eu-α-1	na[i]	0.110	na	4	0.143	2.41	2.34	2.48	2.38	2.46
TBA^+-Tb-α-1	0.070	0.100	0.100	4	0.143	2.36	2.29	2.43	2.35	2.39
TBA^+-Dy-α-1	0.069	0.110	0.099	4	0.143	2.33	2.26	2.40	2.26	2.37
TBA^+-Yb-α-1	0.066	0.114	0.097	3	0.144	2.27	2.21	2.35	2.25	2.30

[a] Value of n was obtained as the best integer CN for O_{H_2O} from the two O-shell fits; m was the fixed CN (4) for $O_{\alpha\text{-}1}$, which accounts for the tetradentate ligation of Ln with the α-1 ligand. [b] The vibrational contribution to the Debye-Waller factor, σ_{vib}, is calculated according to $\sigma_{vib} = 3.151 \times 10^{-3}[(v/K) \coth (y/2)]^{1/2}$, where $y = 1.441(v/T)$, the vibrational frequency, v, and the stretching force constant, *K*, are from Mink et al.,[8] and T is equal to 298 K. [c] The refined Debye-Waller factors from the single O-shell fitting model. [d] Calculated according to $\sigma_{cal} = (\sigma_{vib}^2 + \sigma_{stat}^2)^{½}$, where $\sigma_{stat}^2 = 0.0051$ Å^2 was calculated from the crystal structure of K^+-Lu-α-1,[6] according to $[\sum_{i=1}^{N}(r_i - r)^2 / N]^{1/2}$, where *r* is the mean crystallographic value (2.355 Å) of $N = 8$ distances. [e] δr is calculated from $\delta r = \sigma_{stat}(m + n)/(mn)^{½}$. [f] The refined, average Ln-O interatomic distances from the single O-shell fitting model. [g] Calculated according to $r_m = r - n\delta_r/(m + n)$, $r_n = r + m\delta_r/(m + n)$. [h] Interatomic distance from the two O-shell fits. [i] Not available.

Table S8. Statistical information—χ^2 is the goodness-of-fit and ν is the number of degrees of freedom of the fit—obtained from fitting with the one-O-shell (4 parameter) model (A) and the two-O-shell (6 parameter) model (C) to the data of the TBA^+-Ln-α-1 salts (powders) and their 4.3 mM solutions in the acetonitrile electrolyte (0.1 M $TBAPF_6$). The F_χ test was applied in the manner of Lukens et al.[9], where # ind. points = $2(r_{max} - r_{min})(k_{max} - k_{min})/\pi + 2 = 2(2.6 - 1.0)Å(10.2 – 2.0)(Å^{-1})/\pi + 2$; ν = # ind. Points - # params; $F_\chi = \nu_{(C)}[\chi^2_{(A)} - \chi^2_{(C)}]/b\chi^2_{(C)}$; $P(F_\chi, b, \nu)$ comes from function FDIST in Microsoft Excel.

1. TBA^+-Nd-α-1 Powder:

	Model A	Model C
# params	4	6
# ind. points	10	10
b	2	-
ν	6	4
χ^2	975	360
χ^2/ν	163	90
F_χ	3.4	
$P(F_\chi, b, \nu)$	0.103	

2. TBA^+-Sm-α-1 Powder:

	Model A	Model C
# params	4	6
# ind. points	10	10
b	2	-

ν	6	4
χ^2	897	27.8
χ^2/ν	150	<u>6.95</u>
F_χ	62.5	
$P(F_\chi, b, \nu)$	0.000096	

3. TBA^+-Eu-α-1 Powder:

	Model A	Model C
# params	4	6
# ind. points	10	10
b	2	-
ν	6	4
χ^2	18962	726.1
χ^2/ν	3160	<u>182</u>
F_χ	50.2	
$P(F_\chi, b, \nu)$	0.00018	

4. TBA^+-Tb-α-1 Powder:

	Model A	Model C
# params	4	6
# ind. points	10	10
b	2	-
ν	6	4
χ^2	1746	287.8
χ^2/ν	291	71.95
F_χ	10.13	
$P(F_\chi, b, \nu)$	0.0119	

5. TBA^+-Dy-α-1 Powder:

	Model A	Model C
# params	4	6
# ind. points	10	10
b	2	-
ν	6	4
χ^2	1872	286.5
χ^2/ν	312	71.6
F_χ	11.07	
$P(F_\chi, b, \nu)$	0.0097	

6. TBA^+-Yb-α-1 Powder:

	Model A	Model C
# params	4	6
# ind. points	10	10
b	2	-
ν	6	4
χ^2	2394	204.3
χ^2/ν	399	51.1
F_χ	21.4	
$P(F_\chi, b, \nu)$	0.0019	

7. TBA^+-Nd-α-1 Solution:

	Model A	Model C
# params	4	6
# ind. points	10	10
b	2	-
ν	6	4
χ^2	23082	5164
χ^2/ν	3847	1291
F_χ	6.94	
$P(F_\chi, b, \nu)$	0.0275	

8. TBA^+-Sm-α-1 Solution:

	Model A	Model C
# params	4	6
# ind. points	10	10
b	2	-
ν	6	4
χ^2	78642	6004
χ^2/ν	13107	1501
F_χ	24.2	
$P(F_\chi, b, \nu)$	0.0013	

9. TBA^+-Eu-α-1 Solution:

	Model A	Model C
# params	4	6
# ind. points	10	10
b	2	-
ν	6	4
χ^2	13999	587.5
χ^2/ν	2333	147
F_χ	45.7	
$P(F_\chi, b, \nu)$	0.00023	

10. TBA^+-Tb-α-1 Solution:

	Model A	Model C
# params	4	6
# ind. points	10	10
b	2	-
ν	6	4
χ^2	9956	80.1
χ^2/ν	1659	20
F_χ	247	
$P(F_\chi, b, \nu)$	1.7×10^{-6}	

11. TBA^+-Dy-α-1 Solution:

	Model A	Model C
# params	4	6
# ind. points	10	10
b	2	-
ν	6	4
χ^2	13546	73.1
χ^2/ν	2258	18
F_χ	369	
$P(F_\chi, b, \nu)$	5.2×10^{-7}	

12. TBA^+-Yb-α-1 Solution:

	Model A	Model C
# params	4	6
# ind. points	10	10
b	2	-
ν	6	4
χ^2	31189	97.2
χ^2/ν	5198	24.3
F_χ	640	
$P(F_\chi, b, \nu)$	1.0×10^{-7}	

Table S9. Results from the curve-fitting analyses of the normalized Ln L_3-edge XANES of the neat powders of the TBA^+-Ln-α-1 solid salts using XANES-Fit in WinXAS with a psedo-Voight line shape to model the edge resonance and an arctangent function to model the edge jump.

	Ln edge resonances				Edge steps			ip,[a] eV
Powders	Height	Position	FWHM	Area	Height	Position	FWHM	
TBA^+-Nd-α-1	3.096	2.09	5.57	20.981	1.009	5.07	14.21	6213.7
TBA^+-Sm-α-1	2.398	2.65	6.89	19.510	1.023	6.86	17.14	6720.0
TBA^+-Eu-α-1	2.651	2.39	6.36	20.637	1.026	7.14	17.71	6980.6
TBA^+-Tb-α-1	2.780	2.37	6.17	21.039	0.995	6.14	15.85	7518.4
TBA^+-Dy-α-1	2.771	2.46	6.35	21.714	0.969	6.13	15.39	7795.2
TBA^+-Yb-α-1	2.540	2.70	7.18	22.381	0.957	6.76	14.11	8948.8

[a] Energy of the inflection point in the first differential XANES.

Table S10. Ln-O_{H_2O} distances for the K^+-Ln-α-1 series of solid salts and aqueous solutions as well as the corresponding average Ln-O_{H_2O} distances for the TBA^+-Ln-α-1 series of solid salts and acetonitrile solutions as obtained from the two-shell EXAFS analyses. The intrasystem distance differences (δ = 0.00–+0.06 Å) between the MeCN solutions and the parent TBA^+ salts as well as the average intersystem differences (Δ = +0.01–+0.05 Å) between the MeCN solutions of TBA^+-Ln-α-1 and the corresponding aqueous solutions of K^+-Ln-α-1 support a fractional exchange of H_2O with MeCN pursuant to Eq. (1) in the article.

Ln-O_{H_2O} Distances and Distance Differences							Intersystem Differences[b]	
	K^+ systems			TBA^+ systems			Salts	Solns
Ln-α-1 (Z)	K^+ Salts	H_2O Solns	δ, Å[a]	TBA^+ Salts	MeCN Solns	δ, Å[a]	Δ, Å[b]	Δ, Å[b]
Nd (60)	2.55(2)	2.56(3)	+0.01	2.58(2)	2.60(2)	+0.02	+0.03	+0.04
Sm (62)	2.48(4)	2.48(3)	0.00	2.45(2)	2.51(3)	+0.06	-0.03	+0.03
Eu (63)	2.50(5)	2.48(5)	-0.02	2.46(1)	2.49(3)	+0.03	-0.04	+0.01
Tb (65)	2.37(2)	2.39(4)	+0.02	2.39(5)	2.42(6)	+0.03	+0.02	+0.03
Dy (66)	2.37(2)	2.35(3)	-0.02	2.37(3)	2.37(8)	0.00	0.00	+0.02
Yb (70)	2.31(2)	2.29(7)	-0.02	2.30(1)	2.34(6)	+0.04	-0.01	+0.05

[a] Distance difference = solution – salt. [b] Distance difference = TBA^+ – K^+.

References

1. W. R. Heineman and P. T. Kissinger, in *Laboratory Techniques in Electroanalytical Chemistry*, eds. P. T. Kissinger and W. R. Heineman, Marcel Dekker, New York, 1996, pp. 51-125.
2. P. Mialane, L. Lisnard, A. Mallard, J. Marrot, E. Antic-Fidancev, P. Aschehoug, D. Vivien and F. Secheresse, *Inorg. Chem.*, 2003, 42, 2102-2108.
3. M. R. Antonio, B. K. Teo and B. A. Averill, *J. Am. Chem. Soc.*, 1985, 107, 3583-3590.
4. B. K. Teo, M. R. Antonio and B. A. Averill, *J. Am. Chem. Soc.*, 1983, 105, 3751-3762.
5. C. Boglio, G. Lenoble, C. Duhayon, B. Hasenknopf, R. Thouvenot, C. Zhang, C. Howell R., P. Burton-Pye B., C. Francesconi L., E. Lacote, S. Thorimbert, M. Malacria, C. Afonso and J.-C. Tabet, *Inorg. Chem.*, 2006, 45, 1389-1398.
6. Q. H. Luo, R. C. Howell, M. Dankova, J. Bartis, C. W. Williams, W. D. Horrocks, V. G. Young, A. L. Rheingold, L. C. Francesconi and M. R. Antonio, *Inorg. Chem.*, 2001, 40, 1894-1901.
7. M. Sadakane, M. H. Dickman and M. T. Pope, *Inorg. Chem.*, 2001, 40, 2715-2719.
8. J. Mink, M. Y. Skripkin, L. Hajba, C. Nemeth, A. Abbasi and M. Sandstrom, *Spectroc. Acta Pt. A-Molec. Biomolec. Spectr.*, 2005, 61, 1639-1645.
9. W. W. Lukens, J. J. Bucher, D. K. Shuh and N. M. Edelstein, *Environ. Sci. Technol.*, 2005, 39, 8064-8070.

Appendix. Small-angle X-ray scattering (SAXS) of Ln-α-1-Wells-Dawson Heteropolyoxoanion

A.1 Introduction

Small angle scattering (SAS) is the collective name of three techniques: small angle X-ray (SAXS), neutron (SANS), and light (SALS) scattering. In these techniques elastic scattering of radiation by a sample is recorded at very low angles and the resulting scattering pattern is analyzed to determine the size, morphology and dispersion of materials. Scattering of X-rays is caused by differences in electron density. Scattering of neutrons is caused by differences in scattering power of different nuclei and scattering of light is caused by differences in refractive index (or dielectric constant).

As one of the small-angle scattering techniques, small-angle X-ray scattering (SAXS) is a powerful tool for structural characterization of particles in solid state and in solution. Before1970s, SAXS experiments were performed on instruments with laboratory X-ray tubes. The availability of synchrotron radiation sources increases the resolution of the experiments and decreases the acquisition times, making SAXS more widely used in various fields, from metal alloys to polymers in solution and in bulk, biological macromolecules in solution, porous materials, nanoparticles, etc. In comparison to other structure determination methods, SAXS allows us to overcome some restraints. For example, X-ray crystallography is limited to only work with crystalline solids, whereas SAXS is applicable to both crystalline and amorphous materials and the measurement is non-destructive.

SAXS is working in the procedure shown in Figure A1: irradiate a sample with a well-defined X-ray beam, measure the resulting intensity as a function of angle between the incoming beam and scattered beam, then determine the structure of the material that caused the observed pattern. As dictated by Bragg's Law: $2d \sin\theta = n\lambda$ (where d is the spacing between atomic planes, θ is the diffraction angle, λ is the wavelength of the X-ray beam and n is an integer), the larger the diffraction angle the smaller the length scale probed, therefore small-angle x-ray scattering (SAXS) is commonly used to probe relatively large-scale structures compared to wide angle x-ray scattering (WAXS) which mainly probes crystal structure on the atomic length scale.[1]

Gunier analysis is the analysis of the SAXS scattering curve at very small scattering angles. According to the Gunier law[2] which is given by the following equation,

$I(Q) = I(0) \exp(-Q^2R_g^2/3)$

two SAXS invariants were determined: the radius-of-gyration (R_g) and the extrapolated intensity at zero angle, I(0). The radius-of-gyration, R_g, indicating the size of the molecule, describes the mass distribution of the molecule around its center of gravity. It is the shape-independent, root-mean-square measure of all the mass-weighted distances in a particle from its center of mass.[3, 4] It can be directly calculated from the slope of the linear region of the *ln I*(*Q*) *versus* Q^2 plot(Guinier plot)[5] at low Q range:

$\ln[I(Q)]=\ln[I(0)]- Q^2R_g^2/3$

This approximation is valid for the region where $q * R_g < 1.3$.

I(0), the intensity measured at zero angle, is determined by extrapolation.

The Pair-distribution function, P(r), was determined from an indirect Fourier transform of the scattering curve: [6, 7]

$$P(r) = \frac{r}{2\pi^2}\int_0^\infty I(Q)Q\sin(Qr)dQ$$

P(r) function provides information about the shape of the scattering particle and the maximum dimension, D_{max} (r value where P(r) reaches zero). R_g and I(0) can also be calculated from P(r) function from the following two equations:

$$R_g^2 = \int_0^{D_{max}} r^2 P(r)dr \Big/ \int_0^{D_{max}} P(r)dr$$

$$I(0) = 4\pi\left(\int_0^{D_{max}} P(r)dr\right)$$

R_g value determined by P(r) function is obtained over the entire Q range. In contrast, R_g obtained from the Guinier fits is performed over the low Q range only, which is for identical, randomly-oriented, non-interacting particles.[8] Therefore, if both R_gs agree, it indicates that there are no interparticle effects in the system.

A.2 Experimental Section

A.2.1 Materials Preparation

Potassium salts of $[\alpha\text{-}1\text{-}P_2W_{17}O_{61}]^{10-}$, $[Eu(\alpha\text{-}1\text{-}P_2W_{17}O_{61})]^{7-}$ and $[Yb(\alpha\text{-}1\text{-}P_2W_{17}O_{61})]^{7-}$ (hereafter referred to as α-1, Eu-α-1, and Yb-α-1, respectively) were synthesized as previously published[9, 10]. α-1 ligand was prepared in 0.2 M Li_2SO_4 (pH=3.0) at concentration of 0.25mM, 0.75mM, 1.5mM, 2.5mM, 3.5mM, 4.25mM and 5mM. Eu-α1 ligand was prepared in 0.2 M Li_2SO_4 (pH=3.0) at concentration 0.25mM, 0.75mM, 1.5mM, 2.5mM, 4.25mM and 5mM. Yb-α1 ligand was prepared in 0.2 M Li_2SO_4 (pH=3.0) at concentraion of 1.5mM, 3.5mM, 4.25mM and 5mM.

A.2.2 SAXS Measurements and Data Treatment

SAXS measurements were performed at the Advanced Photon Source of Argonne National Laboratory on Beamline 12-BM-B.[11, 12] 18keV was chosen as the incident photon energy to provide good X-ray transmittance. Sample is diluted at different concentration and loaded in a capillary. The scattering vector amplitude Q is defined as $Q = (4\pi/\lambda)\sin\theta$, 2θ being the scattering angle and λ the X-ray wavelength. Data reduction to obtain I(Q) vs. Q was performed following standard procedure.[11, 13] R_gs were evaluated by the Igor program from Guinier analysis[5, 14, 15] and P(r) analysis [16] of the I(Q) data. Program CRYSOL[1] was used to evaluate the SAXS profiles from crystallographic structures.

A.3 Results and Discussion

The SAXS data for α-1 ligand, Eu-α-1 and Yb-α-1 at same concentration (5mM) are presented in Figure A2 as blue line, black line and red line, respectively. The three responses are very similar, implying that they maintain the same structural framework and are independent of Ln(III) ion. The teal line in Figure A2 is the SASX data calculated from crystallographic structure of 1:1 Lu-α-1[17], which has a dip at 0.76 $Å^{-1}$ and the small peak at 0.93 $Å^{-1}$. The grey line which is calculated from structure of 2:2 La-α-1[18] has a significant change in the range between 0.2 and 0.6 $Å^{-1}$, and the dip and peak shift to higher Q. By comparing my experimental SAXS data with 1:1 Lu-α-1 and 2:2 La-α-1, it shows Eu-α-1 and Yb-α-1 are all 1:1.

SASX data for of α1 ligand, Eu- α1 and Yb- α1 and their corresponding Guinier plots are shown in Figure A3. The Guinier plots in right panel for three compounds show

linear and parallel response, which indicates that the cluster size for each is independent of concentration and the clusters remain monodisperse without aggregation at high concentration.

The Pair-distribution function, P(r), for α1 ligand, Eu- α1 and Yb- α1 at different concentrations are displayed in Figure A4. The peak maximums are all at 6Å. The maximum dimension, D_{max}, is about 12Å. This value is consistent with the maximum linear dimension of 1:1 Lu-α-1 in true (crystallographic) distance, which is shown in Figure A5.

The peak position and FWHMs are listed in Table 1. It is obvious that the FWHM values are essentially equivalent within the statistical limitations of the measurements for α1 ligand, Eu- α1 and Yb- α1 at different concentrations.

The R_g obtained from the Guinier fit over the low Q range and P(r) analysis over the entire Q rang are listed in Table 2 and shown in Figure A6. The two sets of R_gs exhibit good consistence with each other, which again suggests that the clusters remain intact and monodisperse with no interparticle interactions and no aggregation at high concentration.

A.4 Figures

Figure A1. Schematic representation of SAXS experiment.
k_0 = excitation; k_T = transmitted beam; k_1 = scattered beam;
I(Q): Scattering intensity; Q: wavevector.

Figure A2. Top: SAXS data for α-1 ligand (blue line), Eu-α-1(black line) and Yb-α-1(red line) at concentration 5mM. The SXAS for 1:1 Lu-α-1(teal line) and 2:2 La-α-1(grey line) are calculated from the atomic coordinates in the structures shown in Bottom of Figure A2. Bottom: (a) Ball and stick model of 1:1 Lu-α-1 in $[(H_2O)_4Lu(\alpha\text{-}1\text{-}P_2W_{17}O_{61})]^{7-}$; (b) Ball and stick model of 2:2 La-α-1 in $[\{(H_2O)_4Ln(\alpha\text{-}1\text{-}P_2W_{17}O_{61})\}_2]^{14-}$. The red circles are the Lu/La ions which are connected to terminal O_{H_2O} (blue circles) and $O_{\alpha\text{-}1}$ atoms (open circles) bridging to W atoms (gray circles).

Figure A3. SAXS data of α1 ligand, Eu- α1 and Yb- α1 and their corresponding Guinier plots. Left: SAXS data of α1 ligand (a) at concentration 0.25mM, 0.75mM, 1.5mM, 2.5mM, 3.5mM, 4.25mM and 5mM; Eu- α1(b) at concentration 0.25mM, 0.75mM, 1.5mM, 2.5mM, 4.25mM and 5mM; and Yb- α1(c) at concentration 1.5mM, 3.5mM, 4.25mM and 5mM. Right: Corresponding plots of α1 ligand (a'), Eu- α1 (b') and Yb- α1(c').

Figure A4. The Pair-distribution function, P(r), for α1 ligand, Eu- α1 and Yb- α1 at different concentrations (concentrations are labelled on the graphs).

Figure A5. Stick model of 1:1 Lu-α-1 in $[(H_2O)_4Lu(\alpha\text{-}1\text{-}P_2W_{17}O_{61})]^{7-}$. Red is Lu; Blue is O; Gray is W, and yellow is P.

Figure A6. R_g value obtained from Guinier and P(r) analysis of the Experimental SAXS data for for (a) α1 ligand, (b) Eu- α1 and (c) Yb- α1 at different concentrations.

Figure A1

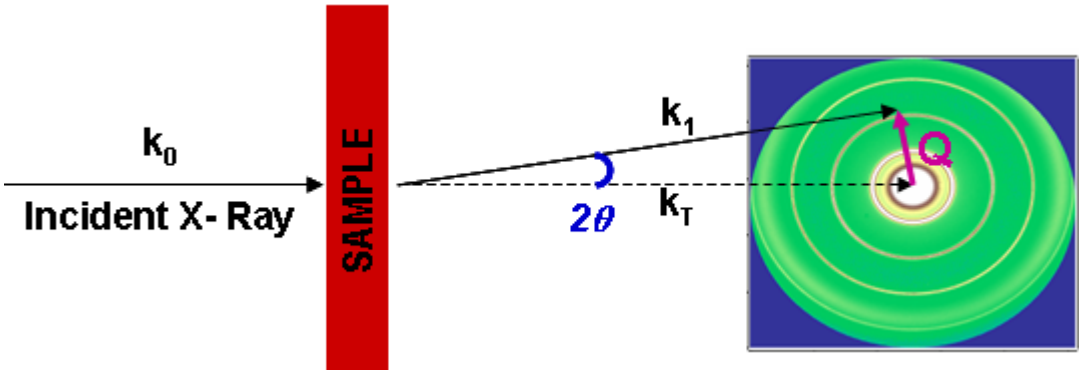

Figure A2

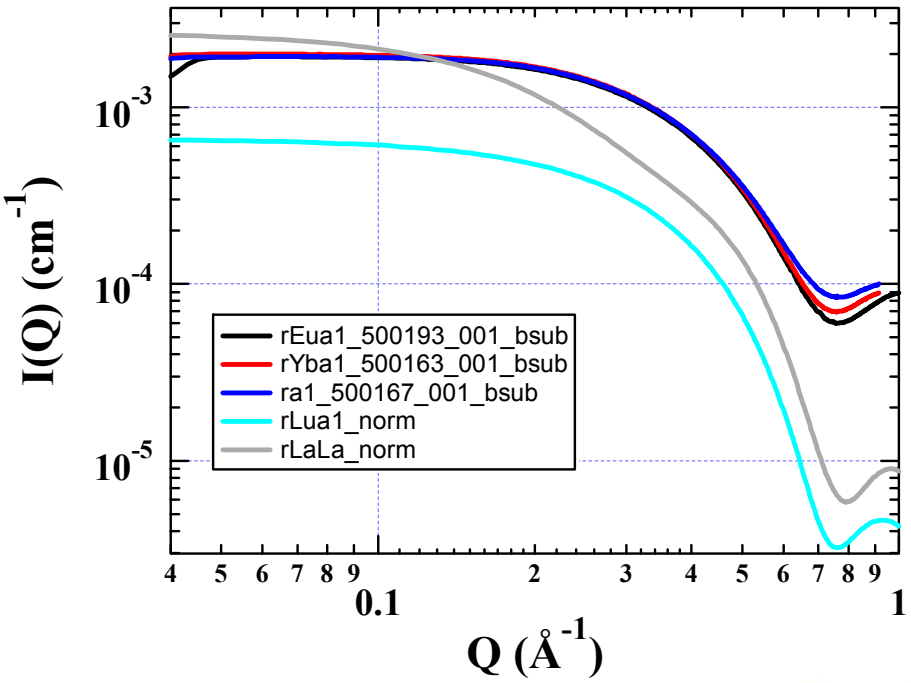

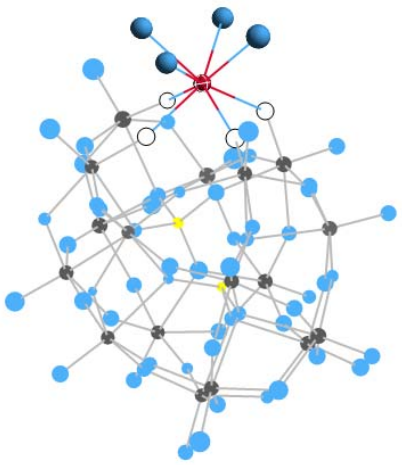

(a) Structure of 1:1 Lu-α-1

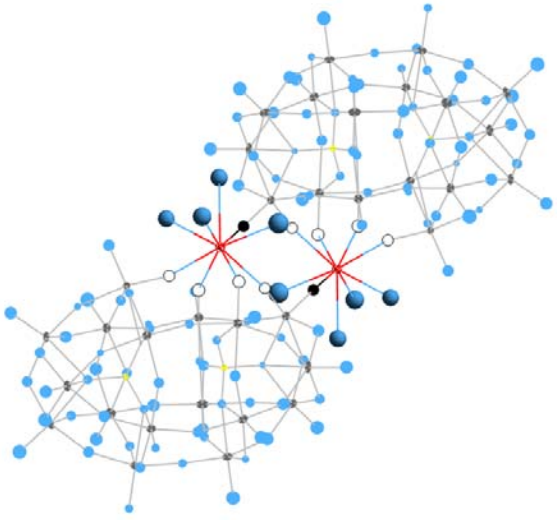

(b) Structure of 2:2 La-α-1

Figure A3

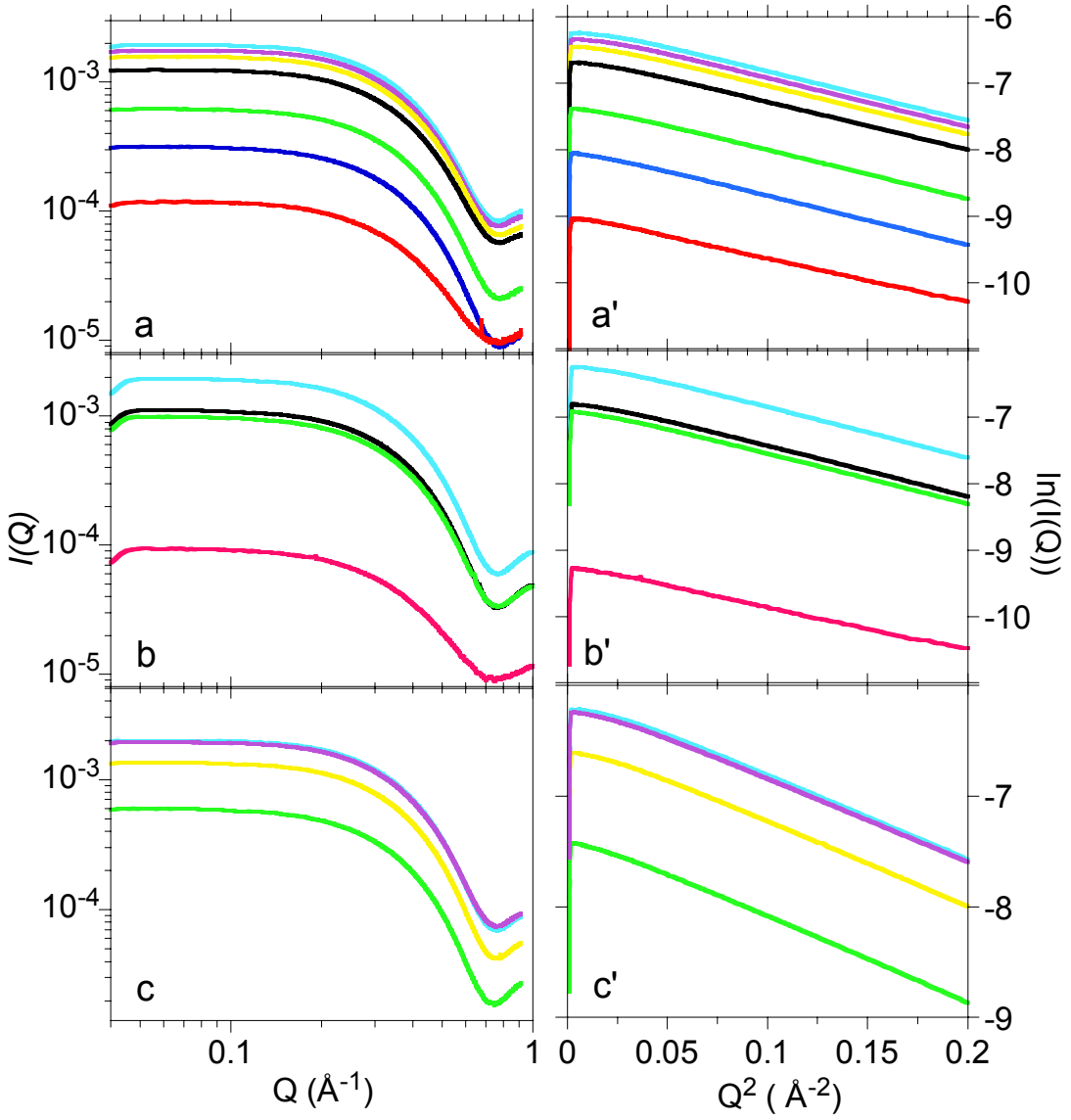

Figure A4

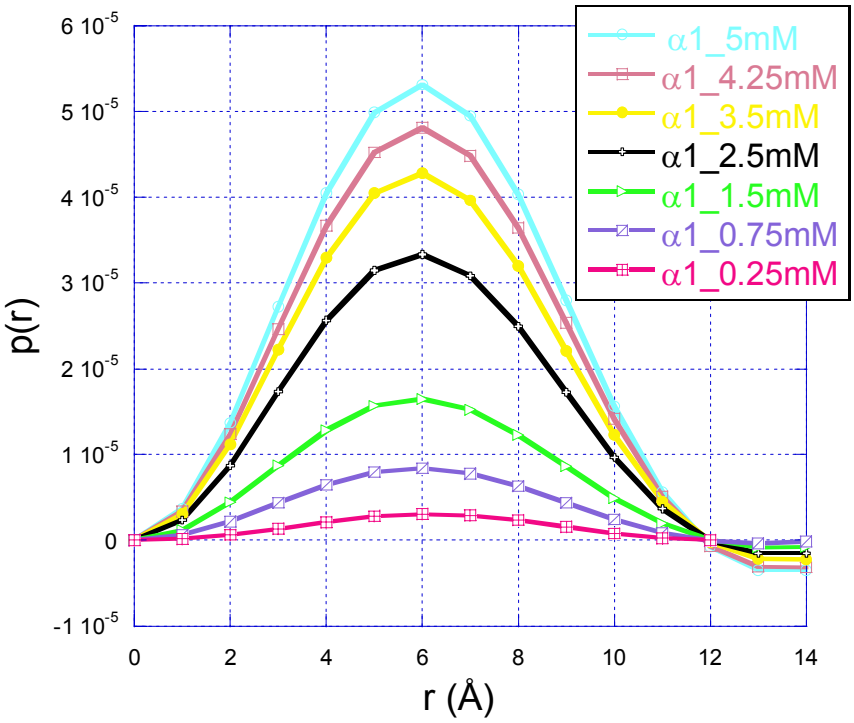
6 10-5
5 10-5
4 10-5
3 10-5
2 10-5
1 10-5
0
-1 10-5
p(r)
0
2
4
6
8
10
12
14
r (Å)
α1_5mM
α1_4.25mM
α1_3.5mM
α1_2.5mM
α1_1.5mM
α1_0.75mM
α1_0.25mM

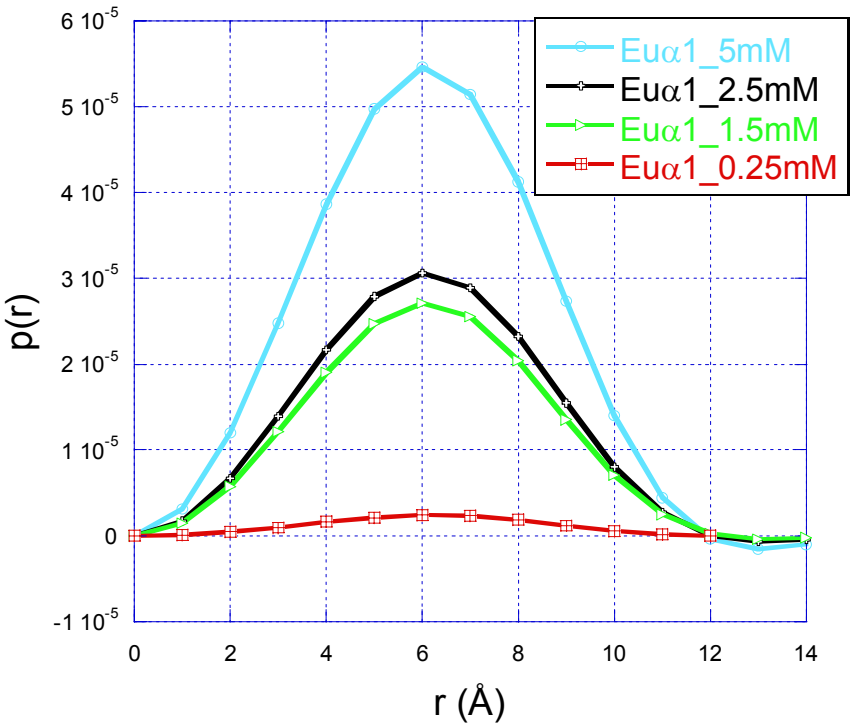
6 10-5
5 10-5
4 10-5
3 10-5
2 10-5
1 10-5
0
-1 10-5
p(r)
0
2
4
6
8
10
12
14
r (Å)
Euα1_5mM
Euα1_2.5mM
Euα1_1.5mM
Euα1_0.25mM

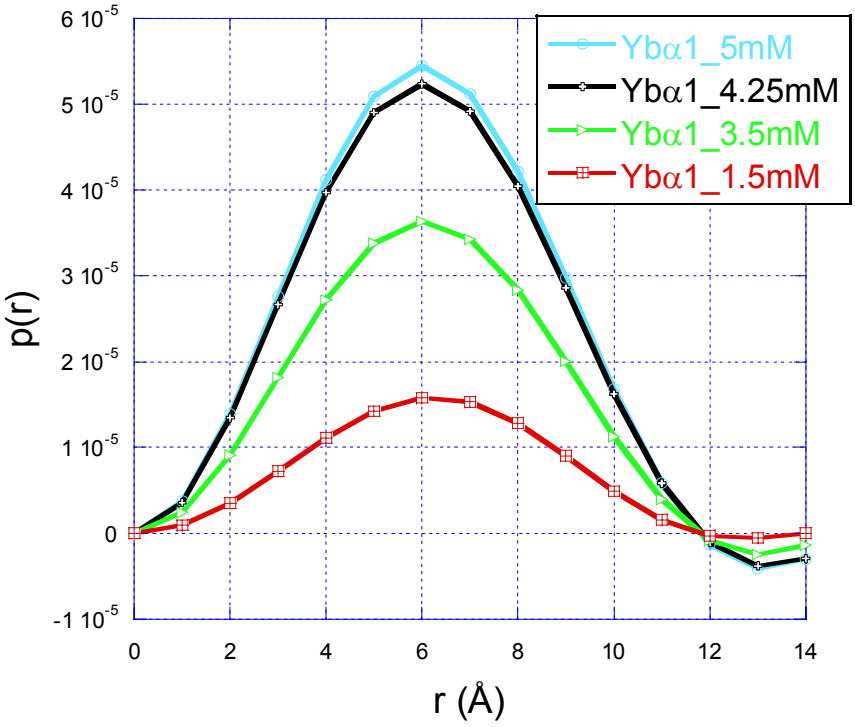
6 10-5
5 10-5
4 10-5
3 10-5
2 10-5
1 10-5
0
-1 10-5
p(r)
0
2
4
6
8
10
12
14
r (Å)
Ybα1_5mM
Ybα1_4.25mM
Ybα1_3.5mM
Ybα1_1.5mM

Figure A5

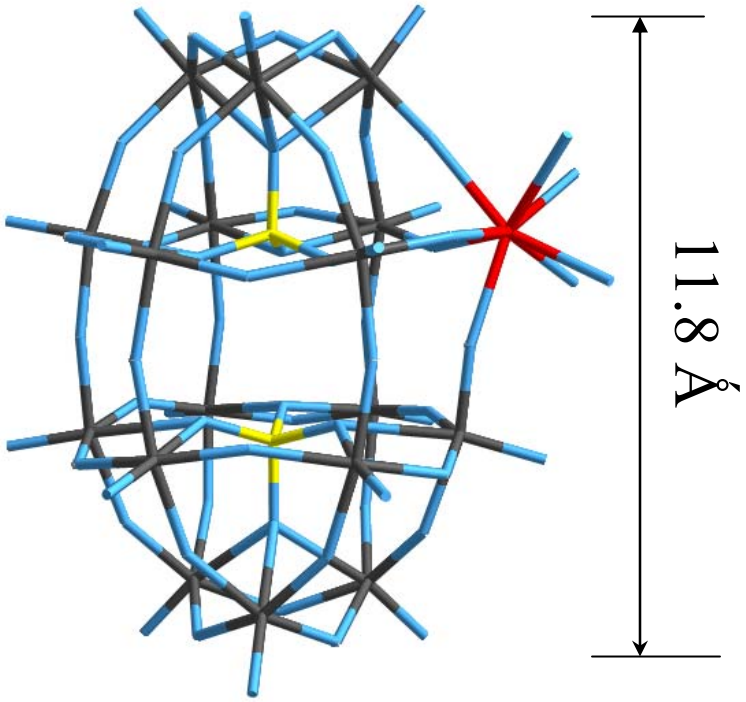
11.8 Å

Figure A6

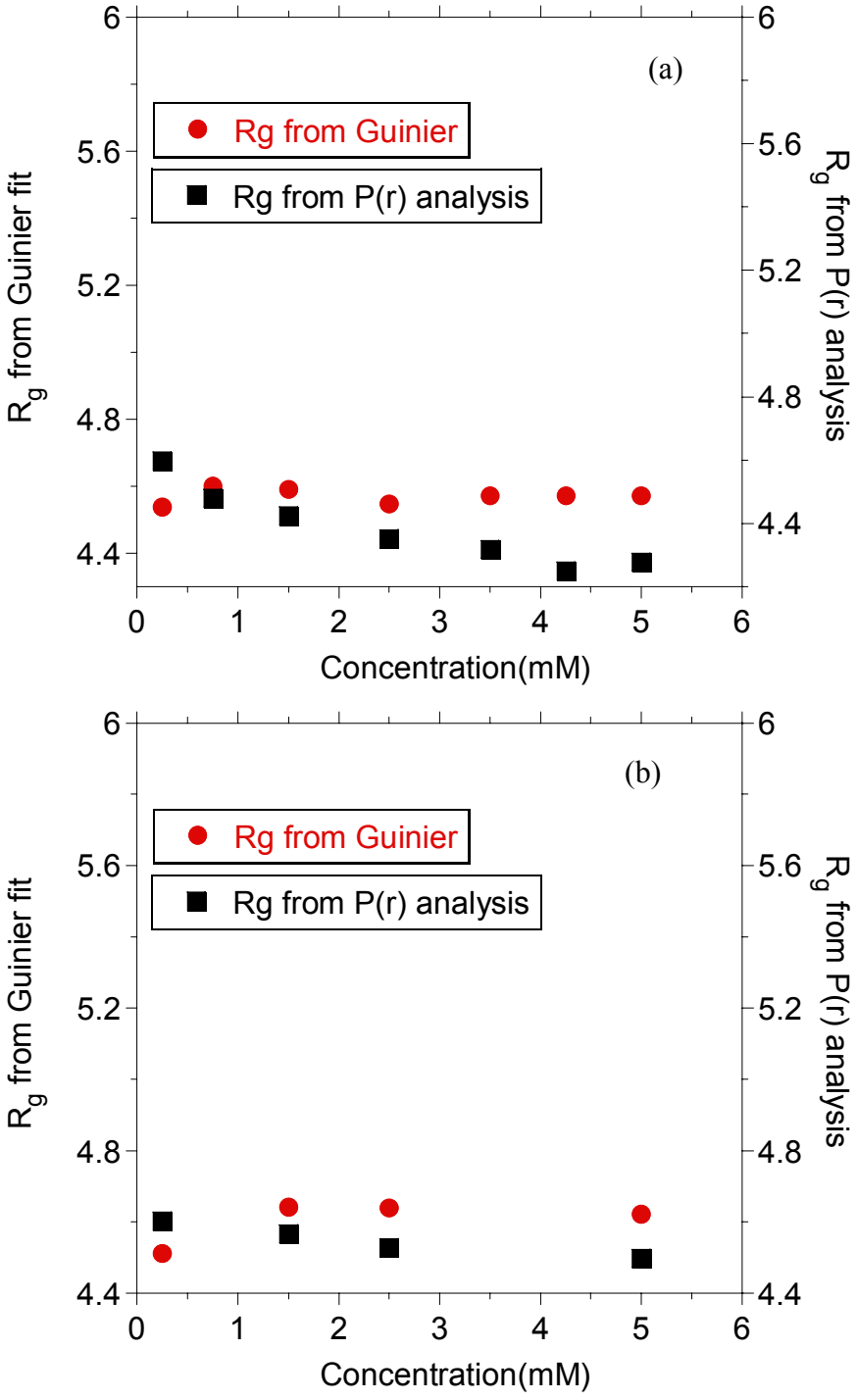
(a)
Rg from Guinier
Rg from P(r) analysis
R_g from Guinier fit
R_g from P(r) analysis
Concentration(mM)
(b)
Rg from Guinier
Rg from P(r) analysis
R_g from Guinier fit
R_g from P(r) analysis
Concentration(mM)

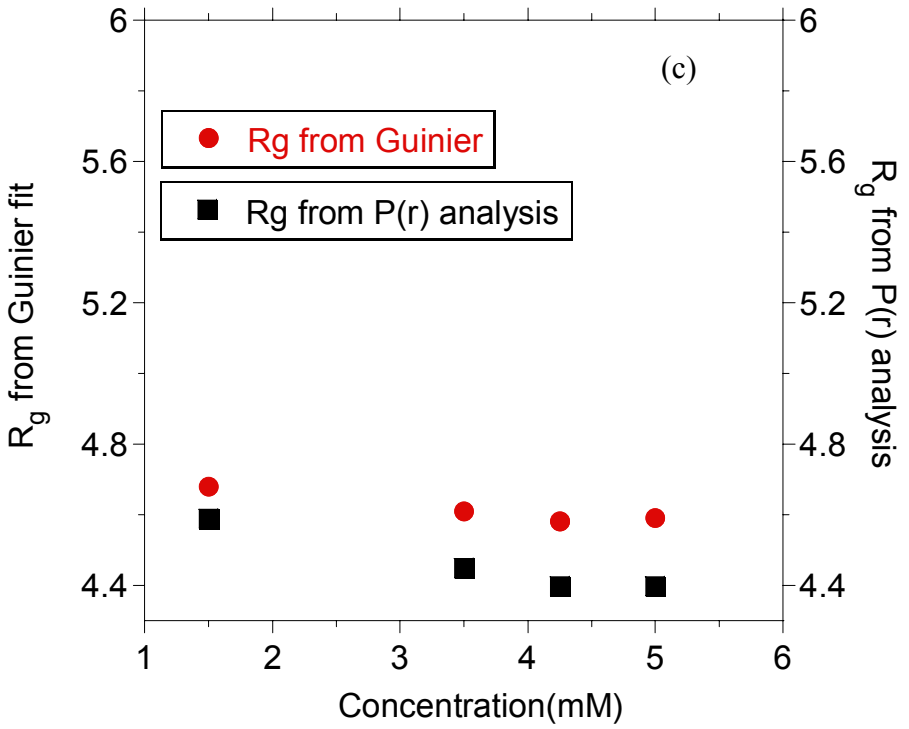

A.5 Tables

Table 1. Peak position and FWHMs(Full-Width Half-Maximum) of the Pair-distribution function, P(r), for α1 ligand, Eu- α1 and Yb- α1 at different concentrations.

		0.25mM	***0.75mM***	***1.5mM***	***2.5mM***	***3.5mM***	***4.25mM***	***5mM***
α 1 ligand	**Peak**	6.1 (1)	6.0 (1)	6.0 (1)	6.0 (1)	6.0 (1)	6.0 (1)	6.0 (1)
	FWHM	3.6 (1)	3.8 (3)	3.7 (3)	3.6 (2)	3.6(3)	3.7 (3)	3.7 (2)
Eu- α 1	**Peak**	6.2 (1)		6.1 (1)	6.1 (1)			6.1 (1)
	FWHM	3.4 (1)		3.4 (2)	3.5 (2)			3.5 (2)
Yb- α 1	**Peak**			6.2 (1)		6.1 (1)	6.1 (1)	6.1 (1)
	FWHM			3.7 (3)		3.7 (3)	3.8 (3)	3.8 (3)

Table 2. R_g value obtained from Guinier and P(r) analysis of the Experimental SAXS data for for α1 ligand, Eu- α1 and Yb- α1 at different concentrations.

(a) α1 ligand

Concentration of α1(mM)	R_g from Guinier fit	R_g from P(r) analysis
0.25	4.5	4.6
0.75	4.6	4.5
1.5	4.6	4.4
2.5	4.5	4.4
3.5	4.6	4.3
4.25	4.6	4.2
5.0	4.6	4.3

(b) Eu- α1

Concentration of Eu- α1	R_g from Guinier fit	R_g from P(r) analysis
0.25	4.5	4.6
1.5	4.6	4.6
2.5	4.6	4.5
5.0	4.6	4.5

(c) Yb-α1

Concentration of Yb-α1	R_g from Guinier fit	R_g from P(r) analysis
1.5	4.7	4.6
3.5	4.6	4.4
4.25	4.6	4.4
5.0	4.6	4.4

A.6 References

1. Svergun, D.; Barberato, C.; Koch, M. H. J. *J. Appl. Crystallogr.* **1995,** *28*, 768-773.
2. Feigin, L. A.; Svergun, D. I. *Structure Analysis by Small-Angle X-ray and Neutron Scattering*; Plenum Press: New York, 1987.
3. Antonio, M. R.; Nyman, M.; Anderson, T. M. *Angew. Chem.-Int. Edit.* **2009,** *48*, 6136-6140.
4. Putnam, C. D.; Hammel, M.; Hura, G. L.; Tainer, J. A. *Q. Rev. Biophys.* **2007,** *40*, 191-285.
5. Guinier, A.; Fournet, G. *Small-Angle Scattering of X-rays*; John Wiley & Sons: New York, 1955.
6. Glatter, O.; Kratky, O. *Small Angle X-rays Scattering*; Academic Press: London, 1982.
7. Glatter, O. *J. Appl. Crystallogr.* **1980,** *13*, 7-11.
8. G.Kostorz, Small Angle Scattering and its Application to Material Science. In *Neutron Scattering*, Academic Press: New York City, 1979; Vol. 15, pp 227-289.
9. Bartis, J.; Dankova, M.; Lessmann, J. J.; Luo, Q. H.; Horrocks, W. D.; Francesconi, L. C. *Inorg. Chem.* **1999,** *38*, 1042-1053.
10. Jing, J.; Burton-Pye, B. P.; Francesconi, L. C.; Antonio, M. R. *Inorg. Chem.* **2008,** *47*, 6889-6899.
11. Antonio, M. R.; Chiang, M. H.; Seifert, S.; Tiede, D. M.; Thiyagarajan, P. *J. Electroanal. Chem.* **2009,** *626*, 103-110.
12. Seifert, S.; Winans, R. E.; Tiede, D. M.; Thiyagarajan, P. *J. Appl. Crystallogr.* **2000,** *33*, 782-784.

13. Pigga, J. M.; Kistler, M. L.; Shew, C. Y.; Antonio, M. R.; Liu, T. B. *Angew. Chem.-Int. Edit.* **2009,** *48*, 6538-6542.

14. Thiyagarajan, P.; Zeng, F. W.; Ku, C. Y.; Zimmerman, S. C. *J. Mater. Chem.* **1997,** *7*, 1221-1226.

15. Thiyagarajan, P. *J. Appl. Crystallogr.* **2003,** *36*, 373-380.

16. Moore, P. B. *J. Appl. Crystallogr.* **1980,** *13*, 168-175.

17. Luo, Q. H.; Howell, R. C.; Dankova, M.; Bartis, J.; Williams, C. W.; Horrocks, W. D.; Young, V. G.; Rheingold, A. L.; Francesconi, L. C.; Antonio, M. R. *Inorg. Chem.* **2001,** *40*, 1894-1901.

18. Boglio, C.; Lenoble, G.; Duhayon, C.; Hasenknopf, B.; Thouvenot, R.; Zhang, C.; Howell, R. C.; Burton-Pye, B. P.; Francesconi, L. C.; Lacote, E.; Thorimbert, S.; Malacria, M.; Afonso, C.; Tabet, J. C. *Inorg. Chem.* **2006,** *45*, 1389-1398.

BIBLIOGRAPHY

1. Pope, M. T. *Heteropoly and Isopoly Oxometalates*; Springer-Verlag: Berlin, 1983.
2. Berzelius, J.; Poggendorfs, A. *Phys. Chem.* **1826,** *6,* 369-380.
3. Topical issue on polyoxometalates: Hill, C. L., Guest Ed. *Chem. Rev.* **1998,** *98,* 1-389.
4. Herve, G.; Teze, A. In *Polyoxometalate molecular science*; Borras-Almenar, J. J.; Coronado, E.; Muller, A.; Pope, M. T., Eds; Kluwer Academic Publishers: Dordrecht, 2001; Vol. 98; pp 33-54.
5. Pope, M. T. *Inorg. Chem.* **1976,** *15,* 2008-2010.
6. Baker, L. C. W.; Baker, V. S.; Eriks, K.; Pope, M. T.; Shibata, M.; Rollins, O. W.; Fang, J. H.; Koh, L. L. *J. Am. Chem. Soc.* **1966,** *88,* 2329-2331.
7. Rhule, J. T.; Hill, C. L.; Judd, D. A. *Chem. Rev.* **1998,** *98,* 327-357.
8. Jeannin, Y. P. *Chem. Rev.* **1998,** *98,* 51-76.
9. Kishore, P. S.; Viswanathan, B.; Varadarajan, T. K. In *Electrochemical Oxygen Reduction Reaction by Pt Nanoparticles on Carbon Support Stabilized by Polyoxometalates*, 2009; 2009; pp 5188-5197.
10. Hill, C. L.; Prossermccartha, C. M. *Coord. Chem. Rev.* **1995,** *143,* 407-455.
11. Keggin, J. F. *Nature* **1933,** *131,* 908-909.
12. Massart, R.; Contant, R.; Fruchart, J. M.; Ciabrini, J. P.; Fournier, M. *Inorg. Chem.* **1977,** *16,* 2916-2921.
13. Weinstock, I. A.; Cowan, J. J.; Barbuzzi, E. M. G.; Zeng, H. D.; Hill, C. L. *J. Am. Chem. Soc.* **1999,** *121,* 4608-4617.

14. Kozhevnikov, I.; Roberts, S. M. *Catalysis by polyoxometalates* John Wiley and Sons: Chichester, 2002.

15. Ciabrini, J. P.; Contant, R.; Fruchart, J. M. *Polyhedron* **1983,** *2,* 1229-1233.

16. Toth, J. E.; Anson, F. C. *J. Am. Chem. Soc.* **1989,** *111,* 2444-2451.

17. Toth, J. E.; Melton, J. D.; Cabelli, D.; Bielski, B. H. J.; Anson, F. C. *Inorg. Chem.* **1990,** *29,* 1952-1957.

18. Toth, J. E.; Anson, F. C. *J. Electroanal. Chem.* **1988,** *256,* 361-370.

19. Anderson, T. M.; Zhang, X.; Hardcastle, K. I.; Hill, C. L. *Inorg. Chem.* **2002,** *41,* 2477-2488.

20. Zhang, X.; Chen, Q.; Duncan, D. C.; Lachicotte, R. J.; Hill, C. L. *Inorg. Chem.* **1997,** *36,* 4381-4386.

21. Mizuno, N.; Nozaki, C.; Kiyoto, I.; Misono, M. *J. Am. Chem. Soc.* **1998,** *120,* 9267-9272.

22. Peacock, R. D.; Weakley, T. J. R. *J. Chem. Soc. A* **1971,** 1836-1838.

23. Soderholm, L.; Liu, G. K.; Muntean, J.; Malinsky, J.; Antonio, M. R. *J. Phys. Chem.* **1995,** *99,* 9611-9616.

24. Zhang, C.; Howell, R. C.; McGregor, D.; Bensaid, L.; Rahyab, S.; Nayshtut, M.; Lekperic, S.; Francesconi, L. C. *C. R. Chim.* **2005,** *8,* 1035-1044.

25. Binnemans, K. *Chem. Rev.* **2009,** *109,* 4283-4374.

26. Blasse, G. *Eur. J. Solid State Inorg. Chem.* **1991,** *28,* 719-726.

27. Lis, S. *J. Alloy. Compd.* **2000,** *300,* 88-94.

28. AlDamen, M. A.; Clemente-Juan, J. M.; Coronado, E.; Marti-Gastaldo, C.; Gaita-Arino, A. *J. Am. Chem. Soc.* **2008,** *130,* 8874-8875.

29. AlDamen, M. A.; Cardona-Serra, S.; Clemente-Juan, J. M.; Coronado, E.; Gaita-Arino, A.; Marti-Gastaldo, C.; Luis, F.; Montero, O. *Inorg. Chem.* **2009,** *48,* 3467-3479.

30. Corma, A. *Chem. Rev.* **1995,** *95,* 559-614.

31. Kozhevnikov, I. V. *Chem. Rev.* **1998,** *98,* 171-198.

32. Sadakane, M.; Steckhan, E. *Chem. Rev.* **1998,** *98,* 219-237.

33. Okuhara, T.; Mizuno, N.; Misono, M. Catalytic chemistry of heteropoly compounds. In *Advances in Catalysis, Vol 41*; Academic Press Inc: San Diego, 1996; Vol. 41; pp 113-252.

34. Raynaud, M.; Chermann, J. C.; Plata, F.; Jasmin, C.; Mathe, G. **1971,** *272,* 347-348.

35. Liu, S. Q.; Kurth, D. G.; Mohwald, H.; Volkmer, D. *Adv. Mater.* **2002,** *14,* 225-227.

36. Groenendaal, B. L.; Jonas, F.; Freitag, D.; Pielartzik, H.; Reynolds, J. R. *Adv. Mater.* **2000,** *12,* 481-494.

37. DeLongchamp, D. M.; Hammond, P. T. *Adv. Funct. Mater.* **2004,** *14,* 224-232.

38. Trombach, N.; Hild, O.; Schlettwein, D.; Wohrle, D. *J. Mater. Chem.* **2002,** *12,* 879-885.

39. Gao, G. G.; Xu, L.; Wang, W. J.; An, W. J.; Qiu, Y. F. *J. Mater. Chem.* **2004,** *14,* 2024-2029.

40. Liu, S. Q.; Mohwald, H.; Volkmer, D.; Kurth, D. G. *Langmuir* **2006,** *22,* 1949-1951.

41. Xu, B. B.; Xu, L.; Gao, G. G.; Jin, Y. N. *Appl. Surf. Sci.* **2007,** *253,* 3190-3195.

42. Kawata, S.; Kawata, Y. *Chem. Rev.* **2000,** *100,* 1777-1788.

43. Rosseinsky, D. R.; Mortimer, R. J. *Adv. Mater.* **2001,** *13,* 783-789.

44. Bard, A. J.; Faulkner, L. R. *Electrochemical Methods: Fundamentals and Applications*; John Wiley & Sons: New York, 1980.

45. Kissinger, P. T.; Heineman, W. R. *Laboratory Techniques in Electroanalytical Chemistry*; Marcel Dekker: New York, 1984.

46. Rudolph, M.; Reddy, D. P.; Feldberg, S. W. **1994,** *66,* A589-A600.

47. Kissinger, P. T.; Heineman, W. R. *J. Chem. Educ.* **1983,** *60,* 702-706.

48. Teze, A.; Canny, J.; Gurban, L.; Thouvenot, R.; Herve, G. *Inorg. Chem.* **1996,** *35,* 1001-1005.

49. Pope, M. T.; Muller, A. *Angew. Chem.-Int. Edit. Engl.* **1991,** *30,* 34-48.

50. Altenau, J. J.; Pope, M. T.; Prados, R. A.; So, H. *Inorg. Chem.* **1975,** *14,* 417-421.

51. Maeda, K.; Katano, H.; Osakai, T.; Himeno, S.; Saito, A. *J. Electroanal. Chem.* **1995,** *389,* 167-173.

52. Keita, B.; Nadjo, L. *J. Electroanal. Chem.* **1987,** *227,* 77-98.

53. Xi, X. D.; Dong, S. J. *J. Mol. Catal. A-Chem.* **1996,** *114,* 257-265.

54. Keita, B.; Nadjo, L.; Krier, G.; Muller, J. F. *J. Electroanal. Chem.* **1987,** *223,* 287-294.

55. Shen, Y.; Liu, J. Y.; Jiang, J. G.; Liu, B. F.; Dong, S. J. *J. Phys. Chem. B* **2003,** *107,* 9744-9748.

56. Papadakis, A.; Souliotis, A.; Papaconstantinou, E. *J. Electroanal. Chem.* **1997,** *435,* 17-21.

57. Teo, B. K. *EXAFS: Basic Principles and Data Analysis*; Springger-Verlag: Berlin, 1985.

58. Antonio, M. R.; Soderholm, L. X-ray absorption spectrocopy of the actinides. In *The Chemistry of the Actinide and Transactinide Elements*; Morss, L. R.; Edelstein, N. M.; Fuger, J., Eds; Springer: Dordrecht, 2006; Vol. 5; pp 3086-3198.

59. Chiang, M. H.; Soderholm, L.; Antonio, M. R. *Eur. J. Inorg. Chem.* **2003,** 2929-2936.

60. http://www.aps.anl.gov/.

61. Chiang, M. H.; Williams, C. W.; Soderholm, L.; Antonio, M. R. *Eur. J. Inorg. Chem.* **2003,** 2663-2669.

62. Yano, J.; Yachandra, V. K. *Photosynth. Res.* **2009,** *102,* 241-254.

63. Bressler, C.; Chergui, M. *Chem. Rev.* **2004,** *104,* 1781-1812.

64. Teo, B. K.; Antonio, M. R.; Averill, B. A. *J. Am. Chem. Soc.* **1983,** *105,* 3751-3762.

65. Antonio, M. R.; Teo, B. K.; Averill, B. A. *J. Am. Chem. Soc.* **1985,** *107,* 3583-3590.

66. Sharpe, L. R.; Heineman, W. R.; Elder, R. C. *Chem. Rev.* **1990,** *90,* 705-722.

67. Antonio, M. R. *Mat. Res. Soc. Symp. Proc.* **2004,** *8002,* 157-168.

68. Cronin, L.; Beugholt, C.; Krickemeyer, E.; Schmidtmann, M.; Bogge, H.; Kogerler, P.; Luong, T. K. K.; Muller, A. *Angew. Chem., Int. Ed.* **2002,** *41,* 2805-2808.

69. Fukaya, K.; Yamase, T. *Angew. Chem., Int. Ed.* **2003,** *42,* 654-658.

70. Howell, R. C.; Perez, F. G.; Jain, S.; Horrocks, W. D.; Rheingold, A. L.; Francesconi, L. C. *Angew. Chem., Int. Ed.* **2001,** *40,* 4031-4034.

71. Muller, A.; Beugholt, C.; Bogge, H.; Schmidtmann, M. *Inorg. Chem.* **2000,** *39,* 3112-3113.

72. Muller, A.; Peters, F.; Pope, M. T.; Gatteschi, D. *Chem. Rev.* **1998,** *98,* 239-272.

73. Ostuni, A.; Pope, M. T. *Comptes Rendus Acad. Sci. Ser. II C* **2000,** *3,* 199-204.

74. Wassermann, K.; Dickman, M. H.; Pope, M. T. *Angew. Chem., Int. Ed.* **1997,** *36,* 1445-1448.

75. Zimmermann, M.; Belai, N.; Butcher, R. J.; Pope, M. T.; Chubarova, E. V.; Dickman, M. H.; Kortz, U. *Inorg. Chem.* **2007,** *46,* 1737-1740.

76. Bassil, B. S.; Dickman, M. H.; Von Kammer, B.; Kortz, U. *Inorg. Chem.* **2007,** *46,* 2452-2458.

77. Belai, N.; Sadakane, M.; Pope, M. T. *J. Am. Chem. Soc.* **2001,** *123,* 2087-2088.

78. Copping, R.; Gaunt, A. J.; May, I.; Sarsfield, M. J.; Collison, D.; Helliwell, M.; Denniss, I. S.; Apperley, D. C. *Dalton Trans.* **2005,** 1256-1262.

79. Lu, Y. W.; Keita, B.; Nadjo, L. *Polyhedron* **2004,** *23,* 1579-1586.

80. Mialane, P.; Lisnard, L.; Mallard, A.; Marrot, J.; Antic-Fidancev, E.; Aschehoug, P.; Vivien, D.; Secheresse, F. *Inorg. Chem.* **2003,** *42,* 2102-2108.

81. Ozeki, T.; Yamase, T. *Acta Crystallogr. Sect. B-Struct. Commun.* **1994,** *50,* 128-134.

82. Sadakane, M.; Dickman, M. H.; Pope, M. T. *Angew. Chem., Int. Ed.* **2000,** *39,* 2914-2916.

83. Shiozaki, R.; Inagaki, A.; Nishino, A.; Nishio, E.; Maekawa, M.; Kominami, H.; Kera, Y. *J. Alloys Compd.* **1996,** *234,* 193-198.

84. Sousa, F. L.; Ferreira, A.; Ferreira, R. A. S.; Cavaleiro, A. M. V.; Carlos, L. D.; Nogueira, H. I. S.; Rocha, J.; Trindade, T. *J. Nanosci. Nanotechnol.* **2004,** *4,* 214-220.

85. Yamase, T. *Chem. Rev.* **1998,** *98,* 307-326.

86. Yamase, T.; Kobayashi, T.; Sugeta, M.; Naruke, H. *J. Phys. Chem. A* **1997,** *101,* 5046-5053.

87. Boglio, C.; Lemiere, G.; Hasenknopf, B.; Thorimbert, S.; Lacote, E.; Malacria, M. *Angew. Chem., Int. Ed.* **2006,** *45,* 3324-3327.

88. Boglio, C.; Lenoble, G.; Duhayon, C.; Hasenknopf, B.; Thouvenot, R.; Zhang, C.; Howell R., C.; Burton-Pye B., P.; Francesconi L., C.; Lacote, E.; Thorimbert, S.; Malacria, M.; Afonso, C.; Tabet, J.-C. *Inorg. Chem.* **2006,** *45,* 1389-1398.

89. Keita, B.; Nadjo, L. In *Encyclopedia of Electrochemistry*; Scholz, F., Pickett, C. J., Eds.; Wiley-VCH: Weiheim, 2006; Vol. 7b; pp 607-700.

90. Weinstock, I. A. *Chem. Rev.* **1998,** *98,* 113-170.

91. Guldi, D. M.; Rahman, G. M. A.; Marczak, R.; Matsuo, Y.; Yamanaka, M.; Nakamura, E. *J. Am. Chem. Soc.* **2006,** *128,* 9420-9427.

92. Matsuo, Y.; Muramatsu, A.; Kamikawa, Y.; Kato, T.; Nakamura, E. *J. Am. Chem. Soc.* **2006,** *128,* 9586-9587.

93. Park, B. K.; Lee, G.; Kim, K. H.; Kang, H.; Lee, C. Y.; Miah, M. A.; Jung, J.; Han, Y. K.; Park, J. T. *J. Am. Chem. Soc.* **2006,** *128,* 11160-11172.

94. Zhang, C.; Howell, R. C.; Scotland, K. B.; Perez, F. G.; Todaro, L.; Francesconi, L. C. *Inorg. Chem.* **2004,** *43,* 7691-7701.

95. Zhang, C.; Howell, R. C.; McGregor, D.; Bensaid, L.; Rahyab, S.; Nayshtut, M.; Lekperic, S.; Francesconi, L. C. *C. R. Chim.* **2005,** *8,* 1035-1044.

96. Fukaya, K.; Yamase, T. *J. Alloy. Compd.* **2006,** *408,* 915-920.

97. Bartis, J.; Dankova, M.; Lessmann, J. J.; Luo, Q.-H.; De Horrocks, W., Jr.; Francesconi, L. C. *Inorg. Chem.* **1999,** *38,* 1042-1053.

98. Ozeki, T.; Yamase, T.; Naruke, H.; Sasaki, Y. *Inorg. Chem.* **1994,** *33,* 409-410.

99. Antonio, M. R.; Soderholm, L. *J. Cluster Sci.* **1996,** *7,* 585-591.

100. Antonio, M. R.; Soderholm, L.; Jennings, G.; Francesconi, L. C.; Dankova, M.; Bartis, J. *J. Alloys Compd.* **1998,** *275-277,* 827-830.

101. Soderholm, L.; Antonio, M. R.; Skanthakumar, S.; Williams, C. W. *J. Am. Chem. Soc.* **2002,** *124,* 7290-7291.

102. Antonio, M. R.; Soderholm, L.; Williams, C. W.; Ullah, N.; Francesconi, L. C. *Dalton Trans.* **1999,** 3825-3830.

103. Chiang, M. H.; Antonio, M. R.; Soderholm, L. *Dalton Trans.* **2004,** 3562-3567.

104. Fernandez, J. A.; Lopez, X.; Bo, C.; de Graaft, C.; Baerends, E. J.; Poblet, J. M. *J. Am. Chem. Soc.* **2007,** *129,* 12244-12253.

105. Bartis, J.; Kunina, Y.; Blumenstein, M.; Francesconi, L. C. *Inorg. Chem.* **1996,** *35,* 1497-1501.

106. Bartis, J.; Sukal, S.; Dankova, M.; Kraft, E.; Kronzon, R.; Blumenstein, M.; Francesconi, L. C. *Dalton Trans.* **1997,** 1937-1944.

107. Luo, Q.; Howell, R. C.; Bartis, J.; Dankova, M.; Horrocks, W. D., Jr.; Rheingold, A. L.; Francesconi, L. C. *Inorg. Chem.* **2002,** *41,* 6112-6117.

108. Lenoble, G.; Hasenknopf, B.; Thouvenot, R. *J. Am. Chem. Soc.* **2006,** *128,* 5735-5744.

109. Kozik, M.; Baker, L. C. W. *J. Am. Chem. Soc.* **1990,** *112,* 7604-7611.

110. Kozik, M.; Hammer, C. F.; Baker, L. C. W. *J. Am. Chem. Soc.* **1986,** *108,* 2748-2749.

111. Contant, R.; Abbessi, M.; Canny, J.; Belhouari, A.; Keita, B.; Nadjo, L. *Inorg. Chem.* **1997,** *36,* 4961-4967.

112. Contant, R.; Richet, M.; Lu, Y. W.; Keita, B.; Nadjo, L. **2002,** 2587-2593.

113. Keita, B.; Belhouari, A.; Nadjo, L.; Contant, R. *J. Electroanal. Chem.* **1998,** *442,* 49-57.

114. Keita, B.; Girard, F.; Nadjo, L.; Contant, R.; Canny, J.; Richet, M. *J. Electroanal. Chem.* **1999,** *478,* 76-82.

115. Keita, B.; Lu, Y. W.; Nadjo, L.; Contant, R. *Eur. J. Inorg. Chem.* **2000,** 2463-2471.

116. Keita, B.; Mbomekalle, I. M.; Nadjo, L.; Contant, R. *Eur. J. Inorg. Chem.* **2002,** 473-479.

117. Keita, B.; Jean, Y.; Levy, B.; Nadjo, L.; Contant, R. *New J. Chem.* **2002,** *26,* 1314-1319.

118. Lopez, X.; Bo, C.; Poblet, J. M. *J. Am. Chem. Soc.* **2002,** *124,* 12574-12582.

119. Lopez, X.; Bo, C.; Poblet, J. M. *Inorg. Chem.* **2003,** *42,* 2634-2638.

120. Xi, X. D.; Wang, G.; Liu, B. F.; Dong, S. J. *Electrochim. Acta* **1995,** *40,* 1025-1029.

121. Contant, R. Inorganic Syntheses; Ginsberg, A. P., Ed.; Wiley-Interscience: New York, 1990; Vol. 27; pp 104-107.

122. Beno, M. A.; Engbretson, M.; Jennings, G.; Knapp, G. S.; Linton, J.; Kurtz, C.; Rütt, U.; Montano, P. A. *Nucl. Instrum. Methods Phys. Res. A* **2001,** *467-468,* 699-702.

123. Soderholm, L.; Antonio, M. R.; Williams, C.; Wasserman, S. R. *Anal. Chem.* **1999,** *71,* 4622-4628.

124. Antonio, M. R.; Soderholm, L.; Song, I. *J. Appl. Electrochem.* **1997,** *27,* 784-792.

125. Gannaz, B.; Antonio, M. R.; Chiarizia, R.; Hill, C.; Cote, G. *Dalton Trans.* **2006,** 4553-4562.

126. George, G. N.; Hilton, J.; Temple, C.; Prince, R. C.; Rajagopalan, K. V. *J. Am. Chem. Soc.* **1999,** *121,* 1256-1266.

127. Ressler, T. *J. Phys. IV* **1997,** *7,* 269-270.

128. Rehr, J. J.; Albers, R. C. *Rev. Mod. Phys.* **2000,** *72,* 621-654.

129. Luo, Q. H.; Howell, R. C.; Dankova, M.; Bartis, J.; Williams, C. W.; Horrocks, W. D.; Young, V. G.; Rheingold, A. L.; Francesconi, L. C.; Antonio, M. R. *Inorg. Chem.* **2001,** *40,* 1894-1901.

130. Stern, E. A. *Phys. Rev. B* **1993,** *48,* 9825-9827.

131. Nwe, K.; Richard, J. P.; Morrow, J. R. *Dalton Trans.* **2007,** 5171-5178.

132. Contant, R.; Ciabrini, J. P. *J. Chem. Res. (S)* **1977,** 222.

133. Pope, M. T. In *Mixed-Valence Compounds. Theory and Applications in Chemistry, Physics, Geology, and Biology;* Brown, D.B., Ed.; D.Reidel: Dordrecht, 1980; pp 365-386

134. Papaconstantinou, E.; Pope, M. T. *Inorg. Chem.* **1970,** *9,* 667-669.

135. Varga, G. M., Jr.; Papaconstantinou, E.; Pope, M. T. *Inorg. Chem.* **1970,** *9,* 662-667.

136. Pope, M. T.; Papaconstantinou, E. *Inorg. Chem.* **1967,** *6,* 1147-1152.

137. Bratsch, S. G. *J. Phys. Chem. Ref. Data* **1989,** *18,* 1-21.

138. Wadsworth, E.; Duke, F. R.; Goetz, C. A. *Anal. Chem.* **1957,** *29,* 1824-1825.

139. Keita, B.; Nadjo, L. *Mater. Chem. Phys.* **1989,** *22,* 77-103.

140. Maeda, K.; Katano, H.; Osakai, T.; Himeno, S.; Saito, A. *J. Electroanal. Chem.* **1995,** *389,* 167-173.

141. Osakai, T.; Katano, H.; Maeda, K.; Himeno, S.; Saito, A. *Bull. Chem. Soc. Jpn.* **1993,** *66,* 1111-1115.

142. Osakai, T.; Maeda, K.; Ebina, K.; Hayamizu, H.; Hoshino, M.; Muto, K.; Himeno, S. *Bull. Chem. Soc. Jpn.* **1997,** *70,* 2473-2481.

143. Grigoriev, V. A.; Cheng, D.; Hill, C. L.; Weinstock, I. A. *J. Am. Chem. Soc.* **2001,** *123,* 5292-5307.

144. Grigoriev, V. A.; Hill, C. L.; Weinstock, I. A. *J. Am. Chem. Soc.* **2000,** *122,* 3544-3545.

145. López, X.; Nieto-Draghi, C.; Bo, C.; Avalos, J. B.; Poblet, J. M. *J. Phys. Chem. A* **2005,** *109,* 1216-1222.

146. Toth, J. E.; Anson, F. C. *J. Electroanal. Chem.* **1988,** *256,* 361-370.

147. Weinstock, I. A.; Grigoriev, V. A.; Cheng, D.; Hill, C. L. In *Polyoxometalate Chemistry for Nano-Composite Design*; Yamase, T., Pope, M. T., Eds.; Kluwer: New York, 2002; pp 103-127.

148. Bard, A. J.; Faulkner, L. R. *Electrochemical Methods: Fundamentals and Applications*, 2nd ed.; J. Wiley: New York, 2001.

149. Rohler, J. In *Handbook on the Physics and Chemistry of Rare Earths*; Gschneidner, K. A., Jr, Eyring, L., Hufner, S., Ed.; North-Holland: Amsterdam, 1987; Vol. 10 - High Energy Spectroscopy; pp 453-545.

150. Shannon, R. D. *Acta Crystallogr. Sect. A* **1976,** *32,* 751-767.

151. Moreau, G.; Helm, L.; Purans, J.; Merbach, A. E. *J. Phys. Chem. A* **2002,** *106,* 3034-3043.

152. Rakovan, J.; Newville, M.; Sutton, S. *Am. Miner.* **2001,** *86,* 697-700.

153. Mulazzani, Q. G.; Venturi, M.; Ballardini, R.; Gandolfi, M. T.; Balzani, V. *Isr. J. Chem.* **1985,** *25,* 183-188.

154. Kolitsch, U.; Holtstam, D. *Eur. J. Mineral.* **2004,** *16,* 117-126.

155. Wickleder, M. S. *Chem. Rev.* **2002,** *102,* 2011-2087.

156. Tanaka, F.; Yamashita, S. *Inorg. Chem.* **1984,** *23,* 2044-2046.

157. Vercouter, T.; Amekraz, B.; Moulin, C.; Giffaut, E.; Vitorge, P. *Inorg. Chem.* **2005,** *44,* 7570-7581.

158. Kido, J.; Okamoto, Y. *Chem. Rev.* **2002,** *102,* 2357-2368.

159. Richter, M. M.; Bard, A. J. *Anal. Chem.* **1996,** *68,* 2641-2650.

160. C. L. Hill, in *Applications of Coordination Chemistry*, ed. M. Ward, Elsevier, Oxford, 2004, Vol. 4, pp. 679-759.

161. J. F. Kirby and L. C. W. Baker, *Inorg. Chem.*, 1998, **37**, 5537-5543.

162. C. Zhang, R. C. Howell, K. B. Scotland, F. G. Perez, L. Todaro and L. C. Francesconi, *Inorg. Chem.*, 2004, **43**, 7691-7701.

163. J. Bartis, M. Dankova, J. J. Lessmann, Q. H. Luo, W. D. Horrocks and L. C. Francesconi, *Inorg. Chem.*, 1999, **38**, 1042-1053.

164. J. P. Ciabrini and R. Contant, *J. Chem. Res.-S*, 1993, 391-391.

165. Q. H. Luo, R. C. Howell, M. Dankova, J. Bartis, C. W. Williams, W. D. Horrocks, V. G. Young, A. L. Rheingold, L. C. Francesconi and M. R. Antonio, *Inorg. Chem.*, 2001, **40**, 1894-1901.

166. M. Sadakane, M. H. Dickman and M. T. Pope, *Inorg. Chem.*, 2001, **40**, 2715-2719.

167. C. Zhang, R. C. Howell, Q. H. Luo, H. L. Fieselmann, L. J. Todaro and L. C. Francesconi, *Inorg. Chem.*, 2005, **44**, 3569-3578.

168. C. Boglio, G. Lenoble, C. Duhayon, B. Hasenknopf, R. Thouvenot, C. Zhang, C. Howell R., P. Burton-Pye B., C. Francesconi L., E. Lacote, S. Thorimbert, M. Malacria, C. Afonso and J.-C. Tabet, *Inorg. Chem.*, 2006, **45**, 1389-1398.

169. C. Boglio, B. Hasenknopf, G. Lenoble, P. Remy, P. Gouzerh, S. Thorimbert, E. Lacote, M. Malacria and R. Thouvenot, *Chem.-Eur. J.*, 2008, **14**, 1532-1540.

170. A. Ostuni, R. E. Bachman and M. T. Pope, *J. Clust. Sci.*, 2003, **14**, 431-446.

171. E. Derat, E. Lacote, B. Hasenknopf, S. Thorimbert and M. Malacria, *J. Phys. Chem. A*, 2008, **112**, 13002-13005.

172. J. Jing, B. P. Burton-Pye, L. C. Francesconi and M. R. Antonio, *Inorg. Chem.*, 2008, **47**, 6889-6899.

173. E. J. Cokal and E. N. Wise, *J. Electroanal. Chem.*, 1966, **11**, 406-415.

174. I. M. Kolthoff and J. F. Coetzee, *J. Am. Chem. Soc.*, 1957, **79**, 1852-1858.

175. S. G. Bratsch, *J. Phys. Chem. Ref. Data*, 1989, **18**, 1-21.

176. R. D. Shannon, *Acta Cryst.*, 1976, **A32**, 751-767.

177. A. Chatterjee, E. N. Maslen and K. J. Watson, *Acta Crystallogr. Sect. B-Structural Science*, 1988, **44**, 381-386.

178. R. E. Gerkin and W. J. Reppart, *Acta Crystallogr. Sect. C-Cryst. Struct. Commun.*, 1984, **40**, 781-786.

179. R. Copping, A. J. Gaunt, I. May, M. J. Sarsfield, D. Collison, M. Helliwell, I. S. Denniss and D. C. Apperley, *Dalton Trans.*, 2005, 1256-1262.

180. A. J. Gaunt, I. May, M. J. Sarsfield, D. Collison, M. Helliwell and I. S. Denniss, *Dalton Trans.*, 2003, 2767-2771.

181. B. S. Bassil, M. H. Dickman, B. von der Kammer and U. Kortz, *Inorg. Chem.*, 2007, **46**, 2452-2458.

182. E. A. Quadrelli, *Inorg. Chem.*, 2002, **41**, 167-169.

183. M. Seitz, A. G. Oliver and K. N. Raymond, *J. Am. Chem. Soc.*, 2007, **129**, 11153-11160.

184. Plots of the average Ln-O_9 distances of Gerkin and Reppart,[19] as well as the average Ln-O_8 distance of Copping et al.[20] are shown in Figure 9.

185. G. Bodizs, I. Raabe, R. Scopelliti, I. Krossing and L. Helm, *Dalton Trans.*, 2009, 5137-5147.

186. G. B. Deacon, B. Gortler, P. C. Junk, E. Lork, R. Mews, J. Petersen and B. Zemva, *J. Chem. Soc.-Dalton Trans.*, 1998, 3887-3891.

187. A. Abbasi, P. Lindqvist-Reis, L. Eriksson, D. Sandstrom, S. Lidin, I. Persson and M. Sandstrom, *Chem.-Eur. J.*, 2005, **11**, 4065-4077.

188. C. Cossy, L. Helm, D. H. Powell and A. E. Merbach, *New J. Chem.*, 1995, **19**, 27-35.

189. A. Habenschuss and F. H. Spedding, *J. Chem. Phys.*, 1979, **70**, 2797-2806.

190. A. Habenschuss and F. H. Spedding, *J. Chem. Phys.*, 1980, **73**, 442-450.

191. J.-C. G. Buenzli and A. Milicic-Tang, *Inorg. Chim. Acta*, 1996, **252**, 221-228.

192. M. Baaden, F. Berny, C. Madic and G. Wipff, *J. Phys. Chem. A*, 2000, **104**, 7659-7671.

193. R. Contant, in *Inorganic Syntheses*, ed. A. P. Ginsberg, Wiley-Interscience, New York, 1990, Vol. 27, pp. 104-107.

194. J. Bartis, Y. Kunina, M. Blumenstein and L. C. Francesconi, *Inorg. Chem.*, 1996, **35**, 1497-1501.

195. G. Lenoble, B. Hasenknopf and R. Thouvenot, *J. Am. Chem. Soc.*, 2006, **128**, 5735-5744.

196. B. P. Burton-Pye and L. C. Francesconi, *Dalton Trans.*, 2010, in preparation.

197. P. G. Rickert, M. R. Antonio, M. A. Firestone, K. A. Kubatko, T. Szreder, J. F. Wishart and M. L. Dietz, *Dalton Trans.*, 2007, 529-531.

198. A. J. Bard and L. R. Faulkner, *Electrochemical Methods: Fundamentals and Applications*, 2nd Edn., J. Wiley, New York, 2001.

199. M. A. Beno, M. Engbretson, G. Jennings, G. S. Knapp, J. Linton, C. Kurtz, U. Rütt and P. A. Montano, *Nucl. Instrum. Methods Phys. Res. A*, 2001, **467-468**, 699-702.

200. For documentaion and availability, see http://www-ssrl.slac.stanford.edu/exafspak.html

201. J. J. Rehr and R. C. Albers, *Rev. Mod. Phys.*, 2000, **72**, 621-654.

202. W. W. Lukens, J. J. Bucher, D. K. Shuh and N. M. Edelstein, *Environ. Sci. Technol.*, 2005, **39**, 8064-8070.

203. T. Ressler, *J. Phys. IV*, 1997, **7**, 269-270.

204. M. R. Antonio and L. Soderholm, *J. Cluster Sci.*, 1996, **7**, 585-591.

205. M. R. Antonio, L. Soderholm and I. Song, *J. Appl. Electrochem.*, 1997, **27**, 784-792.

206. E. Papaconstantinou and M. T. Pope, *Inorg. Chem.*, 1970, **9**, 667-669.

207. M. T. Pope, *NATO Advanced Study Institutes Series, Series C: Mathematical and Physical Sciences*, 1980, **58**, 365-386.

208. M. T. Pope and E. Papaconstantinou, *Inorg. Chem.*, 1967, **6**, 1147-1152.

209. G. M. Varga, Jr., E. Papaconstantinou and M. T. Pope, *Inorg. Chem.*, 1970, **9**, 662-667.

210. R. Contant, M. Richet, Y. W. Lu, B. Keita and L. Nadjo, *Eur. J. Inorg. Chem.*, 2002, 2587-2593.

211. M. R. Antonio and M. H. Chiang, *Inorg. Chem.*, 2008, **47**, 8278-8285.

212. D. M. Way, A. M. Bond and A. G. Wedd, *Inorg. Chem.*, 1997, **36**, 2826-2833.

213. J. N. Barrows and M. T. Pope, *Inorg. Chim. Acta*, 1993, **213**, 91-98.

214. H. R. Murner, E. Chassat, R. P. Thummel and J. C. G. Bunzli, *J. Chem. Soc.-Dalton Trans.*, 2000, 2809-2816.

215. S. Petoud, J. C. G. Bunzli, T. Glanzman, C. Piguet, Q. Xiang and R. P. Thummel, *J. Lumines.*, 1999, **82**, 69-79.

216. E. L. Yee, O. A. Gansow and M. J. Weaver, *J. Am. Chem. Soc.*, 1980, **102**, 2278-2285.

217. J. Röhler, in *Handbook on the Physics and Chemistry of Rare Earths*, eds. K. A. Gschneidner, Jr, L. Eyring and S. Hüfner, North-Holland, Amsterdam, 1987, Vol. 10 - High Energy Spectroscopy, pp. 453-545.

218. S. Ishiguro, Y. Umebayashi and M. Komiya, *Coord. Chem. Rev.*, 2002, **226**, 103-111.

219. S. Skanthakumar, M. R. Antonio, R. E. Wilson and L. Soderholm, *Inorg. Chem.*, 2007, **46**, 3485-3491.

220. M. H. Chiang, J. A. Dzielawa, M. L. Dietz and M. R. Antonio, *J. Electroanal. Chem.*, 2004, **567**, 77-84.

221. X. Lopez, C. Bo and J. M. Poblet, *Inorg. Chem.*, 2003, **42**, 2634-2638.

222. M. R. Antonio, M. Nyman and T. M. Anderson, *Angew. Chem., Int. Ed. Engl.*, 2009, **48**, 6136-6140.

223. M. O. Krause and J. H. Oliver, *J. Phys. Chem. Ref. Data*, 1979, **8**, 329-338.

224. J. K. Beattie, S. P. Best, B. W. Skelton and A. H. White, *J. Chem. Soc.-Dalton Trans.*, 1981, 2105-2111.

225. C. E. VanPelt, W. J. Crooks and G. R. Choppin, *Inorg. Chim. Acta*, 2003, **346**, 215-222.

226. P. Mialane, L. Lisnard, A. Mallard, J. Marrot, E. Antic-Fidancev, P. Aschehoug, D. Vivien and F. Secheresse, *Inorg. Chem.*, 2003, **42**, 2102-2108.

227. X. Y. Zhao, S. X. Liu, Y. H. Ren, J. F. Cao, R. G. Cao and K. Z. Shao, *J. Solid State Chem.*, 2008, **181**, 2488-2493.

228. L. Z. Liu, F. Y. Li, L. Xu, X. Z. Liu and G. G. Gao, *J. Solid State Chem.*, 2010, **183**, 350-355.

229. M. Sadakane, A. Ostuni and M. T. Pope, *J. Chem. Soc., Dalton Trans.*, 2002, 63-67.

230. B. Keita, F. Girard, L. Nadjo, R. Contant, J. Canny and M. Richet, *J. Electroanal. Chem.*, 1999, **478**, 76-82.

231. J. C. G. Bunzli and V. Kasparek, *Inorg. Chim. Acta*, 1991, **182**, 101-107.

232. C. Boglio, G. Lemiere, B. Hasenknopf, S. Thorimbert, E. Lacote and M. Malacria, *Angew. Chem., Int. Ed. Engl.*, 2006, **45**, 3324-3327.

233. B. Hasenknopf, K. Micoine, E. Lacote, S. Thorimbert, M. Malacria and R. Thouvenot, *Eur. J. Inorg. Chem.*, 2008, 5001-5013.

234. Svergun, D.; Barberato, C.; Koch, M. H. J. *J. Appl. Crystallogr.* **1995,** *28*, 768-773.

235. Feigin, L. A.; Svergun, D. I. *Structure Analysis by Small-Angle X-ray and Neutron Scattering*; Plenum Press: New York, 1987.

236. Antonio, M. R.; Nyman, M.; Anderson, T. M. *Angew. Chem.-Int. Edit.* **2009,** *48*, 6136-6140.

237. Putnam, C. D.; Hammel, M.; Hura, G. L.; Tainer, J. A. *Q. Rev. Biophys.* **2007,** *40*, 191-285.

238. Guinier, A.; Fournet, G. *Small-Angle Scattering of X-rays*; John Wiley & Sons: New York, 1955.

239. Glatter, O.; Kratky, O. *Small Angle X-rays Scattering*; Academic Press: London, 1982.

240. Glatter, O. *J. Appl. Crystallogr.* **1980,** *13*, 7-11.

241. G.Kostorz, Small Angle Scattering and its Application to Material Science. In *Neutron Scattering*, Academic Press: New York City, 1979; Vol. 15, pp 227-289.

242. Bartis, J.; Dankova, M.; Lessmann, J. J.; Luo, Q. H.; Horrocks, W. D.; Francesconi, L. C. *Inorg. Chem.* **1999,** *38*, 1042-1053.

243. Jing, J.; Burton-Pye, B. P.; Francesconi, L. C.; Antonio, M. R. *Inorg. Chem.* **2008,** *47*, 6889-6899.

244. Antonio, M. R.; Chiang, M. H.; Seifert, S.; Tiede, D. M.; Thiyagarajan, P. *J. Electroanal. Chem.* **2009,** *626*, 103-110.

245. Seifert, S.; Winans, R. E.; Tiede, D. M.; Thiyagarajan, P. *J. Appl. Crystallogr.* **2000,** *33*, 782-784.

246. Pigga, J. M.; Kistler, M. L.; Shew, C. Y.; Antonio, M. R.; Liu, T. B. *Angew. Chem.-Int. Edit.* **2009,** *48*, 6538-6542.

247. Thiyagarajan, P.; Zeng, F. W.; Ku, C. Y.; Zimmerman, S. C. *J. Mater. Chem.* **1997,** *7*, 1221-1226.

248. Thiyagarajan, P. *J. Appl. Crystallogr.* **2003,** *36*, 373-380.

249. Moore, P. B. *J. Appl. Crystallogr.* **1980,** *13*, 168-175.

250. Luo, Q. H.; Howell, R. C.; Dankova, M.; Bartis, J.; Williams, C. W.; Horrocks, W. D.; Young, V. G.; Rheingold, A. L.; Francesconi, L. C.; Antonio, M. R. *Inorg. Chem.* **2001,** *40*, 1894-1901.

251. Boglio, C.; Lenoble, G.; Duhayon, C.; Hasenknopf, B.; Thouvenot, R.; Zhang, C.; Howell, R. C.; Burton-Pye, B. P.; Francesconi, L. C.; Lacote, E.; Thorimbert, S.; Malacria, M.; Afonso, C.; Tabet, J. C. *Inorg. Chem.* **2006,** *45*, 1389-1398.